Probing Gravity with High-Precision Pulsar Timing

Dissertation
zur
Erlangung des Doktorgrades (Dr. rer. nat.)
der
Mathematisch-Naturwissenschaftlichen Fakultät
der
Rheinischen Friedrich-Wilhelms-Universität Bonn

von
Ricardo Nicolaos Caballero Pouroutidou
aus
David, Panama

Submitted: Bonn, 31.03.2016

Dieser Forschungsbericht wurde als Dissertation von der Mathematisch-Naturwissenschaftlichen Fakultät der Universität Bonn angenommen und ist auf dem Hochschulschriftenserver der ULB Bonn http://hss.ulb.uni-bonn.de/diss_online elektronisch publiziert.

1. Gutachter:	Prof. Dr. Michael Kramer
2. Gutachter:	Prof. Dr. Norbert Langer
Tag der Promotion:	19.07.2016
Erscheinungsjahr:	2016

Abstract

Pulsars are highly magnetised neutron stars which spin tremendously fast, at periods that are as low as a few milliseconds. Chapter 1 gives an overview of their basic observational properties and applications. Pulsars are observed as sources with periodic, broadband and highly polarised signals, which are thought to be formed by rotating, beamed electromagnetic radiation emitted from their magnetic poles. This simple geometric picture, known as the *lighthouse model*, is the basis of the *pulsar timing* technique. Pulsar timing, which is explained in Chapter 2, makes use of the clock-like stability of pulsars' rotations to create a model of the rotational and orbital (if in a binary) parameters of pulsars, which are compared to the observed pulse times-of-arrival. Modern pulsar-timing instrumentation can record of pulse arrival times with precision as high as a few hundreds of nanoseconds. The comparison of the high-precision pulsar-timing data with the predictions of the equations-of-motion of General Relativity and alternative theories of gravity allows, among others, accurate tests of gravity theories in the strong-field regime of gravity. Pulsars are also employed as high-precision cosmic clocks which can trace space-time perturbations caused by propagating gravitational waves. This application requires the use of data from an ensemble of *millisecond pulsars*, the fastest and most rotationally stable pulsars, known as *Pulsar Timing Array*.

The Effelsberg 100-m radio telescope in Germany, is part of a network of telescopes conducting regular pulsar-timing observations. In Chapter 3, I first present the reduction and analysis of timing data from recorded at Effelsberg in the period 1996-2013. The chapter then focuses on the combination of the Effelsberg data with the that from the other telescopes that are part of the *European Pulsar Timing Array*, and the timing analysis of the resulting data set, which includes 42 millisecond pulsars. This work was highlighted by the employment new analysis methods, the first measurements of a significant amount of astrometric and orbital parameters and an in-depth analysis of pulsar distance estimations.

Chapter 4 extends the analysis of the 42 millisecond pulsars, focusing on the characterisation of the noise in the individual-pulsar data. The noise levels present in the timing data have a direct impact on the sensitivity of a timing array to gravitational waves, and the detailed characterisation of the noise is necessary prior to any searches for spatially correlated gravitational-wave signals in the timing data. This work marked the first ever comprehensive comparison of two independent methods for characterising the low-frequency, stochastic and achromatic noise component. The study also focused on searching for instrumental or analysis-systematics noise. Finally, the analysis quantifies the impact low-frequency noise on the data set's sensitivity to gravitational waves.

Chapter 5 presents two tests of gravity theories using timing data from individual millisecond pulsars. The first test is based on data from solitary millisecond pulsars to place the best-to-date limits on one of the three *post-Newtonian* parameters that describe *preferred-frame effects*, generally predicted by theories that include isotropic violations of local Lorentz invariance of gravity. The test was based on upper limits of variations in the pulsar pulse profiles. Pulse profiles are predicted to change over time due to a precession of their spin axis in the presence of preferred-frame effects. The second test uses data from a binary millisecond pulsars to perform a *radiation damping* test. These tests focus on the change of orbital parameters due to energy loss by gravitational wave emission from the system. Focusing on the predictions by the physically motivated mono-scalar-tensor theories of gravity, this work places a stringent upper limit on the existence of dipole gravitational waves which is predicted by a variety of alternative theories of gravity.

Finally, Chapter 6 concludes the thesis with an overview of the research and the results, and a discussion on further work being made in the framework of these research topics.

Acknowledgements

> "If I have seen further it is by standing on the shoulders of giants"
>
> *Sir Isaac Newton*

Making it to the end of a PhD, takes much more than what you did during the years you were a PhD student. It's all you did during your life that led you to become a person who would pursue this path. If I were to thank every person who contributed throughout my life into helping me get to this point, it would take me many pages. And I would certainly forget many. As I probably did, when writing these lines, while trying to at least remember all those who played a key role the past years. So let me say in advance, thanks to all who have helped me become who I am today.

First in the list, is of course my academic family. I feel privileged and honoured to have worked together with these great minds. I want like to wholeheartedly thank my supervisors, Prof. Michael Kramer and Dr. David J. Champion. A big thanks to Michael, for accepting me in this fantastic research group and for supporting me every step of the way. He has been a big source of inspiration for me all these years, through his example of a great scientist, advisor and group leader. Without his generous financial support that got me to participate in so many meetings and conferences around the globe, it would had been much harder indeed to network with the rest of the pulsar community. Thanks to David, for supervising me on a regular basis, always worrying about my progress and pushing me to perform better. I'm grateful for all the support and protection he has provided within our collaborations, which allowed me to focus on my research with a minimum amount of concerns. If there's something I really appreciate from my supervisors, is the fact that they always expected more for me, but always gave me enough space to solve the problems on my own. Though I know I sometimes disappointed them, I hope that I managed to justify my selection for this PhD position.

Special thanks goes to Dr. Kejia Lee, Dr. Joris Verbiest, Dr. Norbert Wex and Dr. Gregory Desvignes with whom I worked closely over these years. KJ, you have been nothing less than a true mentor to me the past years. Through our collaboration, not only have I learned so much about our research field, but my interest in scientific research was truly reborn. Thank you for all the help and support, without which I would have never finished all my research in time. I really look forward to many more years of working together. Joris, next to you I learned what pulsar timing is. You took me by the hand like a big brother when I first started my PhD and you made sure that I never was lost for too long. Your example of professional integrity will always be in my mind. Thanks for everything. Norbert, thanks for being so kind with me and for so patiently explaining to a novice what gravity really is and how to use pulsar timing to test gravity theories. I feel really lucky I had the chance to work with you. Because of all I have learned with you over the past years, I finally feel that it is possible to one day really understand General Relativity. A special thanks goes also to Gregory, for really spending a

lot of time helping me out, especially with coding problems and use of the computer clusters. During our work together for the EPTA, I really learned a lot.

I thank the members of the Fundamental Physics in Radio Astronomy group with whom I had the great honour, to work and hang out. It's really hard to think of a single person from which I haven't learned something. Thanks to Patrick L., John A., Ewan B. and Alessandro R. for tolerating me as their officemate and the nice discussions we had in the office. Lijing S., it was great to have you here for two years. We did some cool work together, didn't we? Paulo F., it was great discussing pulsar timing, polyhedra and so many other cool stuff with you. Ramesh K., thanks for all the discussions we had on instrumentation and all the help when having problems during observations. Kuo L., thanks for helping out with wide-band data analysis and for all the insightful discussions. Axel J., thanks for teaching me the fine details of the EBPP. Stefan O., thanks for the tips on PSRchive. To Dominic S., Laura S., and Weiwei Z., thanks for helping me out when preparing postdoc applications, despite your very busy schedules. Olaf W., thanks for reading my paper on such short notice when I needed it. A great thanks also to Jason W., Eleni G., Nataliya P., Joey M., Leon H., Pablo T., Ralph E., Golam S., and Amit B., for all the great times we had. They really kept me sane! Also, a big thank you to the operators at the Effelsberg observatory for all their help, insightful conversations and of course, their company during on-site observations!

I'd like to acknowledge the support from our group's assistants and administration. To Gabi Breuer, who sadly left us so unexpectedly, I'm grateful for the warm welcome, the huge amount of time she saved me and all our little chats in her office that helped me understand how to best behave in my new social environment. The same gratitude extends to the group's new assistant, Kira Kühn, who takes care of the paperwork which I so much dislike. A huge thanks also to Ms. Tuyet-Le Tran, Ms. Barbara Menten and Ms. Simone Pott for taking care of so many things, which would have taken me so much time, especially with my poor German, as well as to Viola Tegethoff, for the amazing support and help. Thanks also to Manolis Angelakis, for his warm welcome as the IMPRS co-ordinator.

My gratitude extends to my PTA colleagues and friends around the globe. Special thanks go to my fellow EPTAers, from which I have learned so much, and with whom we had some fun times: Gemma J., Alberto S., Lindley L., Marta B., Andrea P., Sotiris S., Stas B., Ben S., Alberto V., Caterina T., Delphine P. Ismael C., Jason H., Antoine L., Pablo R., James M., Rutger vH., Gilles T. et al. I would like to thank Bill Coles, for all he taught me on spectral analysis during his summer visit in Bonn, Mike Keith and George Hobbs for their useful advice and discussions. I'd also like to thank Prof. Jim Cordes and Dr. Shami Chatterjee for their support and insightful conversations.

I thank all those who have given me strength to keep going one way or another. For all their love, understanding, friendship, support and inspiration over my academic life, I thank my 'bizaro family' in Melbourne, Hananeh S., Alex S., Marios M., Markos L., Nandia L., Lysandros D., Kallia G., Marinos K., Vasilis K., Jeff H., Silvia S. Angela V., Marcus B. Senol Y., Rik vL., Arjen S., Tullio B., Tresa, Antonio C., Chris M., Amit B., Lisa Z., Michael. T. L., George P. T. and Dimitra K. I want to especially thank my long-standing close friends, Panagiotis 'Quendi' Antonopoulos, Nantia Pythara, Yianna Shamma, Yiannis Pasisis, Stella Sarafi, Costas Anastasiou, Nikos Nikoloudakis and Kostas Gourgouliatos. Although for many years we have long distances separating us, you guys are always there when I need you. And I needed you many times over the years. Especially to Q, I owe an enormous extra thank you, for constantly being the first person I turned to whenever I had to face a personal challenge, for over a decade. Finishing my PhD through all the difficulties, would had been a lot more difficult without you.

Finally, I want to offer my greatest thanks to my family, for being my constant support during my

whole life. My siblings Monica and Petros, who always believe in me and unconditionally support me. My grandparents Petros and Panagiota, who did so much to help my parents raise us. My brother-in-law Martin, my nephews Kimi and Sonny, for being such a great inspiration. And finally, my parents, Anastasia and Hector. For their unconditional love, for raising me through so many difficulties and for always making sure I had food on my table and a roof above my head, and much more than that. Thank you for all your love, moral and financial support throughout the years. Without you, I may had never reached this point in my life.

Contents

CHAPTER 1

Pulsars: Discovery, Properties and Applications

> "I switched on the high-speed recorder and it came blip.... blip.... blip.... blip.... blip... Clearly the same family, the same sort of stuff and that was great, that was really sweet [...] It has to be some new kind of star, not seen before, and that then cleared the way for us publishing, going public!"
>
> *Dame Jocelyn Bell Burnell*

Pulsars are rapidly spinning, highly magnetised neutron stars (NSs), one of the three types of stellar remnants, alongside white dwarves (WDs) and black holes (BHs). After the explosive death (a supernova explosion) of a progenitor massive star (i.e. with mass higher than about 8 solar masses), the remaining mass gravitationally collapses to a core composed almost entirely of neutrons and whose self-gravity is balanced only by the quantum-mechanical effect of neutron degeneracy pressure. Having inherited the angular momentum its progenitor but now with a radius a million times smaller, the NS acquires tremendous spin periods, which can be as short as a few milliseconds. The NS magnetic fields have large flux densities that can exceed 10^{14} G. The origin of these strong magnetic fields is still poorly understood. Scenarios have been theorised in which either the magnetic field is inherited from the progenitor star, owing their strength to the conservation of magnetic flux, or field amplification during the core-collapse precess (e.g. Spruit 2008).

The term "pulsar" was introduced as an abbreviation to "pulsating (radio) star". From a purely observational point of view, a pulsar is a celestial source from which we record periodic, pulsed, broadband and highly polarised signals, with periods between milliseconds to seconds. The pulsed emission is thought to originate from radiation beams, emitted from above the magnetic-field poles by charged particles accelerated to relativistic velocities along open magnetic-field lines. The magnetic poles are not aligned with the rotational axis, causing the radiation beams to sweep across space, and be detectable as a pulse each time they cross the observer's line-of-sight (LOS). This configuration is known as the "lighthouse model" (Figure 1.1).

Some pulsars exhibit very stable rotations and can therefore be used as precise celestial clocks. By measuring the times-of-arrival (TOAs) of the pulses it is possible to probe with high precision the pulsar's rotational and orbital characteristics, as well as the ionised interstellar medium (IISM) through which the signals propagate. The clock-like behaviour of pulsars turns them into a powerful tool, with applications in astrophysics and fundamental physics. In this chapter I will overview the discovery of pulsars, their basic observational properties and their applications.

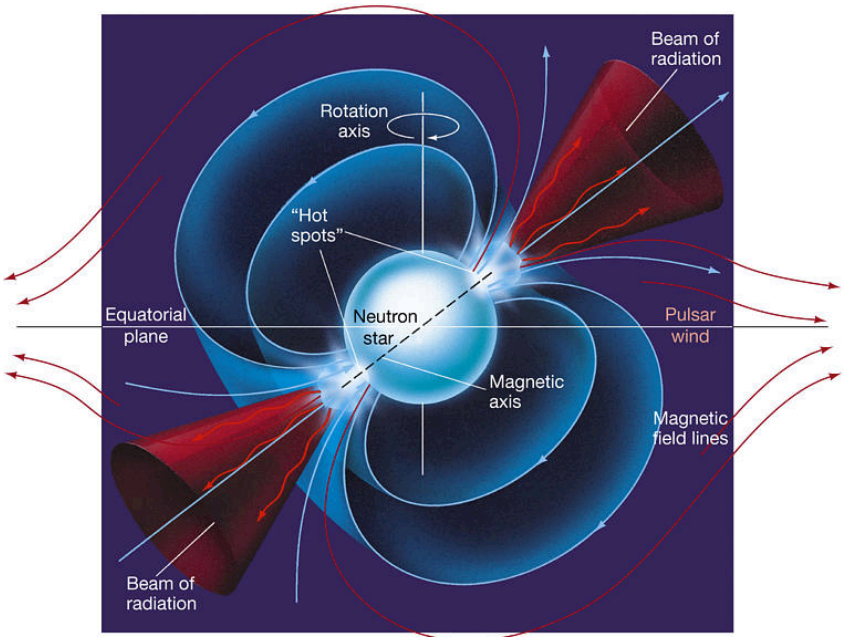

Figure 1.1: The lighthouse model for pulsars: The pulsar is a highly magnetised neutron star, with a dipolar magnetic field. Particles accelerated across open field lines emit beamed radiation along the field line, owing to their relativistic velocities. The "hot spots" are within the *velocity-of-light cylinder*, defined by the radial distance where the magnetosphere rotates with the angular velocity that the pulsar would have at the same distance (Lyne & Graham-Smith 1998). The misalignment between the rotation and magnetic-field axes result in the radiation beam to sweep space like a lighthouse, viewed by a distant observer as a periodic pulsation. Particles accelerated by the outward energy flow from the rotating magnetic dipole form the pulsar wind.
Image Copyrights: 2005 Pearson Prentice Hall, Inc.

1.1 Discovery of Pulsars

Pulsars were first discovered in 1967. Not unlike other big scientific discoveries, pulsars were discovered by first observing them accidentally. Antony Hewish and his research team constructed the Mullard Radio Astronomy Observatory with the aim of finding quasars by making use of the effects of interplanetary scintillation. Dame Jocelyn Bell Burnell, a graduate student at that time at the University of Cambridge, was analysing the data. She noticed in the data some distinct signals, 'scruffs' which at first appeared as sporadic interference. Their true nature came to light through a systematic investigation of those signals and to a large degree, thanks to Bell's determination to solve the mystery and her persistent work to do exactly that. High-speed recordings eventually resolved the scruffs to a periodical pulsed signal, with a period of 1.3 seconds, always coming from the same sky position.

Long before their discovery, and only two and a half years after the discovery of the neutron[1] (Chadwick 1932), Baade & Zwicky (1934) predicted the existence of NSs, as the end result of stars undergoing supernova explosions. Pacini (1967), theorised that if a NS has a strong magnetic field, its rotational energy can power supernova remnants (SNRs) with strong thermal emission. An example was the Crab Pulsar, the archetype of what we now classify as "pulsar wind nebulae" or "plerions".

[1] For the discovery of the neutron, James Chadwick received the 1935 Nobel prize in physics (http://www.nobelprize.org/nobel_prizes/physics/laureates/1935/)

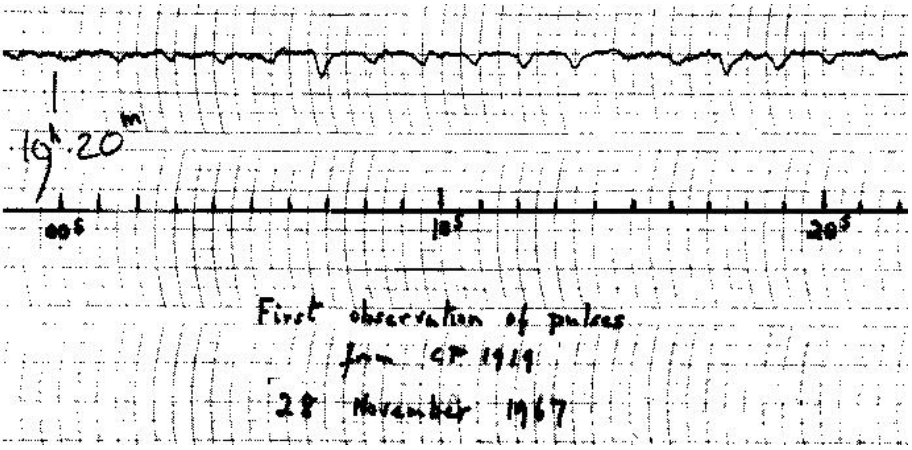

Figure 1.2: The first ever observations of time-resolved pulses from a radio pulsar, on November 28th, 1967. It is designated as "CP 1919", which stands for "Cambridge Pulsar" and the source's Right Ascension. The time is noted on the lower line of the chart with a small tick per second and a large tick per ten seconds. One can see the pulses on the top of the chart, appearing periodically every 1.3 seconds.
Image from: http://www.cv.nrao.edu/course/astr534/Pulsars.html

Studies of the Crab Nebula brought scientists one step from discovering pulsars, when Hewish & Okoye (1965) reported an "unusual source of high radio brightness temperature in the Crab Nebula". The small size of the source made the very high observed radio flux difficult to be explained by synchrotron emission, but noted that it could be explained by the active remnant of the supernova explosion, as was already suggested by Oort & Walraven (1956), to explain the optical radiation brightness and polarisation from the region.

On November 27th, 1967, the first high-speed recordings which resolved a pulsar's periodic signal were performed at the Mullard Radio Astronomy Observatory. The pulsar observed was was PSR B1919+21 (Figure 1.2). After a process of confirming the observations with a different telescope as well as the celestial origin of the regular pulses, the discovery was announced in Hewish et al. (1968). The discovery of this new type of celestial object had a huge impact in astronomy and physics, and Hewish was awarded the 1974 Nobel Prize in Physics[2] "for his decisive role in the discovery of pulsars" .

Pulsar Astronomy has grown over the decades to become a fascinating research branch. Many more pulsars have been discovered, and more applications for these remarkable objects were conceptualised along with new ways of observing them. At the moment of writing these lines, 2536 pulsars are registered in the ATNF Pulsar Catalogue, one of the most complete databases of confirmed pulsars[3] (Manchester et al. 2005). This number is growing fast and will undoubtably be outdated already when the writing of this thesis is over.

[2] The prize was jointly awarded to Hewish and Sir Martin Ryle, "for his observations and inventions, in particular of the aperture synthesis technique" (http://www.nobelprize.org/nobel_prizes/physics/laureates/1974/).
[3] http://www.atnf.csiro.au/people/pulsar/psrcat/

1.2 Basic Observational Properties of Pulsars

Although pulsars are observed throughout the electromagnetic spectrum, it is at radio wavelengths that they are most prominently observed. As we will see, the combination of the typical flux density distribution of radio pulsar emission and effects of the IISM on the pulsed-signal propagation, results in most pulsars being easier observed at the frequency range of 1-2 GHz. Throughout this thesis, unless explicitly stated, I will be referring to radio observations of pulsars.

1.2.1 Pulse Profiles

For each rotation we can, in principle, record one pulse as the emission beam sweeps past the telescope's field-of-view (FOV). The pulse from each rotation is called a "single pulse". For many pulsars, however, single pulses are too weak for contemporary instrumentation to record them. For those pulsars where it is possible to detect single pulses, we observe that these show stochastic variability in shape and phase. The pulse phase variability is known as pulse phase jitter and becomes a limiting factor for the precision we can measure the TOAs at high signal-to-noise ratio (S/N) observations (e.g. Shannon et al. 2014). It is also observed, however, that the average (or integrated) profiles which result from adding (in phase) thousands of single pulses, are very stable. Figure 1.3 shows a comparison of the single pulses and the average pulse profile of PSR B1133+16. The stability of the average profile has an important use. As discussed later in this chapter and elsewhere in this thesis, it allows long-term monitoring of the pulsar's rotation, since the TOA of each recorded average profile can be compared to a single reference profile. Average profiles are widely used in pulsar astronomy not only because of their stability, but also because by adding many single pulses we can increase S/N, which for single pulses is typically very low. Henceforth, when referring to pulse profiles, I will refer to the average profile and explicitly state when discussing single pulses.

Pulse profiles show a wealth of structures. While some have only a single component, others may include interpulses (secondary component separated from the main component by ~180°), two main components or multiple components, in some cases resulting in rather complex profiles. Assuming the validity of the lighthouse model for pulsars, the profile shapes reflect the pattern of the two-dimensional cross-section of the radiation beam. Single-component profiles could at the simplest (geometrically speaking) case be produced by a pencil beam along the magnetic axis (Backer 1976). In this model, interpulses can be explained as the pulse from the second magnetic axis, which we can observe if the magnetic and rotational axes are (almost) perpendicular. Alternatively, we can also attribute single- and two-component profiles to a hollow-cone shaped beam (Komesaroff 1970). In this case, a double-component profile results from the telescope beam cutting through the radiation beam more centrally to also pass through the central void, while the single-component profile forms when the cut happens only through the outer part of the cone. The final example we discuss, assumes pencil beam but with patchy emission pattern (Lyne & Manchester 1988). Depending on the line of intersection with the telescope beam, simple or complicated profiles can be observed.

As discussed in the introduction of this chapter, pulsar emission is broadband and polarised. The shape of the pulse profiles show frequency evolution. Although there are cases where the profile shape is quite stable over large frequency ranges, the general trend is to have different shapes at different frequencies. In Figure 1.4, we show two cases, one in which the profile evolves strongly with frequency (PSR J1022+1001) and one with moderate evolution (PSR J1713+0747). The profile of PSR J1022+1001 evolves significantly, starting with two hardly distinguished peaks at 370 MHz, to a profile with two

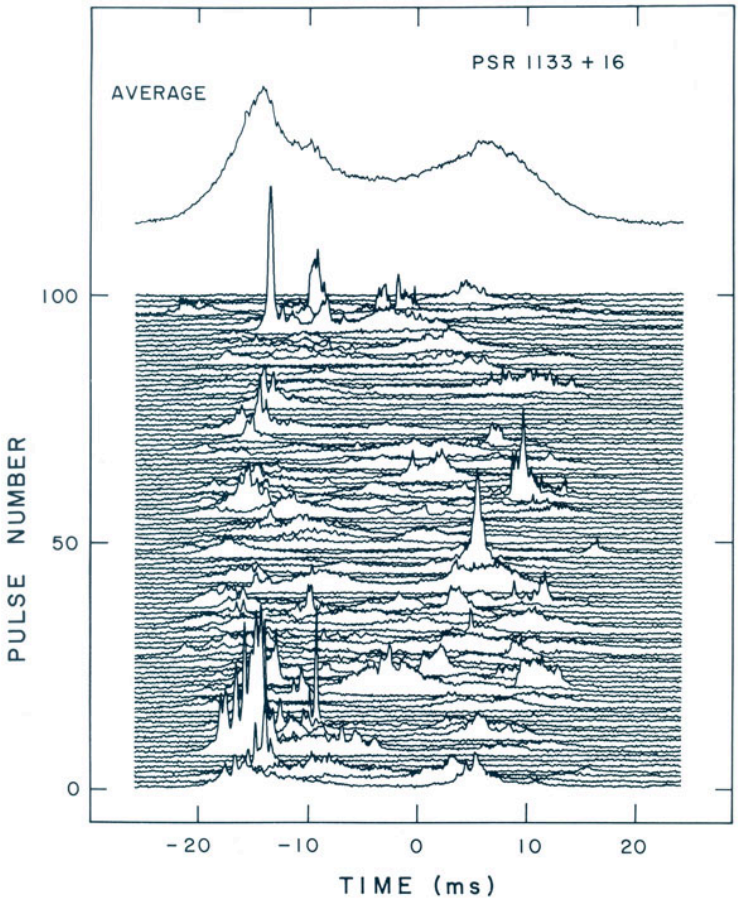

Figure 1.3: Observed single pulses from PSR B1133+16, and at the top of the image, the average profile after adding all single pulses. Despite the variability of single pulses in shape and phase, the average profiles are remarkably stable and unique for each pulsar.
Image credit: http://arecibo.tc.cornell.edu/PALFA/images.aspx

distinct, sharp peaks at 1410 MHz and eventually to an almost single-component profile at ~5 GHz. In contrast, PSR J1713+0747 has a profile that hardly changes across the same frequency range. Some general trends are observed when it comes to the frequency evolution of pulse profiles (e.g. Xilouris et al. 1996, and references therein). For example with increasing observing frequency we observe a decrease both in the widths of pulses and in the separation between components. These effects are proposed to be a consequence of the details of the emission mechanisms for pulsar radio emission. For example, the aforementioned effects are proposed to reflect the fact that radiation at different frequencies is formed at different heights above the pulsar surface. This effect is known as the *radius-to-frequency mapping* and suggests that the higher the frequency, the closer to the pulsar surface is the emission region (e.g. Komesaroff 1970; Cordes 1978).

Although the shape of the average pulse profiles are extremely stable in time by comparison to the single pulses, average profiles can also show temporal variations. Apart from possible changes due to instrumental instabilities or imperfections in the polarisation calibration of the data (e.g. Hotan et al. 2004a; van Straten 2006), temporal profile variations can occur from geometrical processes such as the

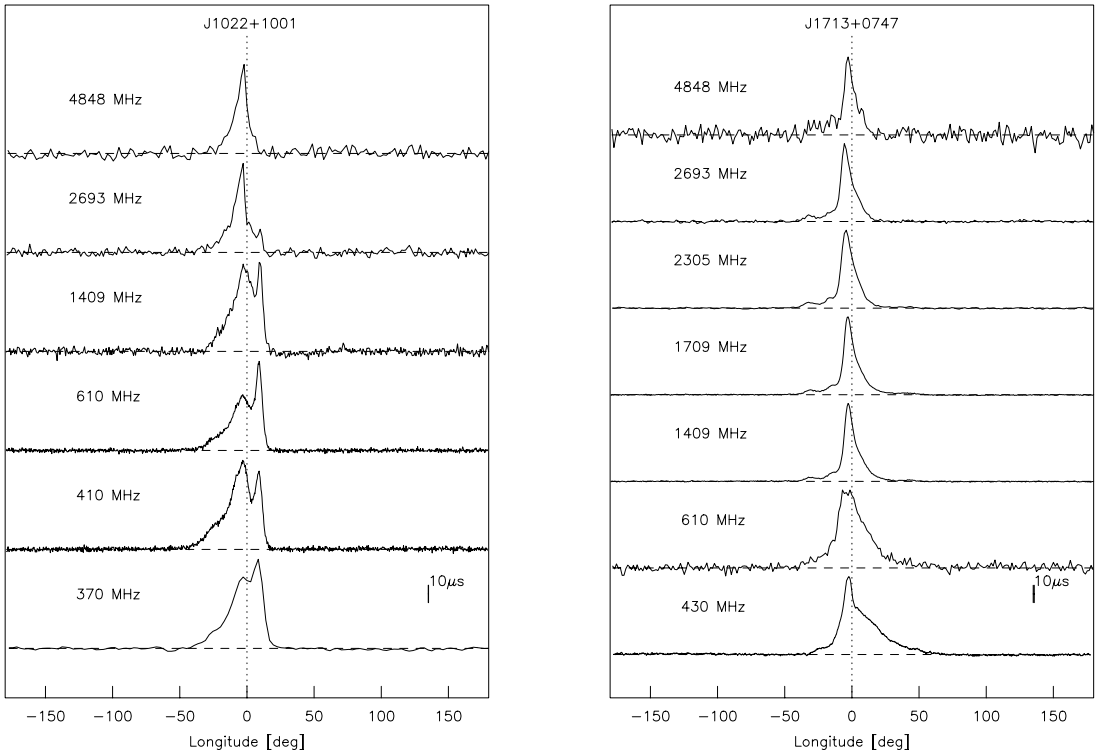

Figure 1.4: Examples of a pulsar profile evolution with observing frequency for PSRs J1022+1001 (left) and J1713+0747 (right), with periods of 16.4 and 4.5 milliseconds respectively. The profiles are aligned using the phase predictions of an accurate timing model. Figures from Kramer et al. (1999).

precession of the spin axis of pulsars in highly relativistic orbits (e.g. Weisberg et al. 1989; Kramer 1998) or *mode-changes*, events during which the profile suddenly switches back and forth between two to three shapes and are most likely connected with changes in the pulsar's magnetosphere (e.g. Lyne et al. 2010).

To conclude the discussion on pulsar profiles, we note that a pulsar's profile can differ in intensity and/or in shape significantly at different polarisations. Observations of pulsars with strongly polarised emission need to be calibrated to ensure that the two polarisation components are properly weighted when forming the total intensity profiles. The relative strength of the linear polarisation components change, for example, with the parallactic angle (e.g. van Straten 2003). In cases where the pulsar is bright enough to not require a total intensity profile to get the necessary S/N for a given application, it may be more beneficial to use the polarised components. For example, polarised components may contain sharp features that allow better determination of the pulse TOA (van Straten 2006).

1.2.2 Flux Density

The intensity of an observed pulse profile as a function of its phase is given in arbitrary units. One can convert this in physical units, with a number of methods. One way is to use the radiometer equation

(Eq. 2.1, see Chapter 3 for a definition), i.e. the relation of the signal's flux density and the S/N (see e.g. Bilous et al. 2015). This method requires good measurement of the total system temperature, $T_{\rm sys}$, which is the sum of the antenna temperature[4] and equivalent terms from the sky background, atmospheric emission and radiation from the ground. Calibration for these factors can be attempted by comparing the measurement counts when observing a standard calibrator, i.e. a radio continuum source with known flux density, and a nearby region of the sky clear of strong radio sources. More accurate flux measurements can be performed by conducting flux calibration observations with every observation of the pulsar, using a noise diode switched on and of with some periodicity (see e.g. Lazarus et al. 2016, for an application). These observations are made on and just off the calibration source and give a calibration factor for the flux that can be used to scale the pulsar profile in physical units.

Generally, pulsars are relatively weak radio sources. The median mean flux density (i.e. the integrated flux density of pulsar emission over one rotation and averaged over the period) at 1.4 GHz of all pulsars documented in the ATNF Pulsar Catalogue with measured fluxes (1676 out of 2536 pulsars) is only 0.42 mJy However, by keeping in mind that this flux density originates from narrow beamed emission, the corresponding brightness temperature, T_b, is large. The latter, is the corresponding temperature that a black body in thermal equilibrium must have in order to have the observed flux density. At radio frequencies, the brightness temperature is well described by the Rayleigh-Jeans approximation. As such, following Lorimer & Kramer (2005), the surface brightness, in Kelvin, of a pulsar can be approximated by:

$$T_b \simeq 10^{30}\mathrm{K}\left(\frac{S}{\mathrm{Jy}}\right)\left(\frac{\nu}{\mathrm{GHz}}\right)^{-2}\left(\frac{\Delta t}{\mu\mathrm{s}}\right)^{-2}\left(\frac{d}{\mathrm{kpc}}\right)^{2}, \tag{1.1}$$

where k_B is the Boltzmann constant, ν the observing frequency, Δt the pulse duration and d is the distance to the pulsar. Here, the flux density, S, can refer to any measure of the quantity, e.g. the mean or the peak. The mean flux density, $\langle S \rangle$, is the equivalent flux density that the pulsar would have if it were a continuum radio source and it is used in pulsar astronomy as the standard quantity for the measure of the pulse signal strength. Using the above quoted median flux density, a typical distance of observed pulsars at 1 kpc, and a pulse duration of 11 μs, we derive a brightness temperature of order 10^{32} K. The highest flux density reported in the ATNF catalogue is 1.1×10^3 mJy and belongs to the Vela Pulsar (PSR B0833-45), located at a distance of 294 pc. The corresponding brightness temperature for a pulse of is then of the order of 10^{34} K. Moreover, intense single pulses from the Crab Pulsar (PSR B0531+21), with flux densities that are thousands of times its average flux density, known as *giant pulses*, imply a brightness temperature of the order 10^{35} K (e.g. Bhat et al. 2008). Such high brightness-temperature values rule out the possibility that pulsar radiation derives from any incoherent emission mechanism, and must originate from a coherent emission mechanism.

1.2.2.1 Flux Density Distribution

A basic property of any type of astronomical objects with broadband emission is the flux energy distribution, which shows how much energy is emitted at each frequency band. This information, combined with other radiation properties, for example the polarisation or absolute luminosity when the distance is

[4] The random fluctuations noise of a radio receiver, is usually quantified by the so called antenna temperature, T_A, defined as the temperature of a resistor with resistance k that has the same power as the output of the antenna in power, W, i.e. $W = kT_A$ (see e.g. Rohlfs & Wilson 2004).

known, provides insights into the emission mechanisms.

At radio frequencies, pulsars are generally brighter at lower frequencies. Various independent studies have examined the flux density distributions of pulsar in radio frequencies. For younger pulsars (see below in §1.3 for the different pulsar populations) these studies show the same general trend. The mean flux density follows a negative power-law with respect to the observing frequency, ν and shows a turnover at about 100 MHz to lower frequencies. It is therefore usually described by $\langle S \rangle \propto \nu^{\beta}$, with β the spectral index. For frequencies above ~100 MHz, Maron et al. (2000) report a mean spectral index of $\beta = -1.8 \pm 0.2$ in a study using 281 pulsars.

For about 90% of the sources, the mean flux density distributions are sufficiently described by a single power-law and the flux densities of the rest either show evidence or are clearly better fitted by a two-component broken power-law. Similar results were already derived by e.g. Sieber (1973), Malofeev & Malov (1980) and Izvekova et al. (1981). These latter studies also pointed out to the turnover of the flux density below 100 MHz. More recently, Bilous et al. (2015) have more clearly demonstrated the turn-over at low frequencies using observations of 194 young pulsars at low frequencies (110-188 MHz). There are also evidence for a flattening or even a turn-up of the spectral index at very high ($\gtrsim$ 30 GHz) frequencies (Kramer et al. 1996).

"Recycled" pulsars, which have accreted mass from their binary companions (see §1.4) are typically fainter and a larger fraction of this population appears to have flux density distributions that are sufficiently described by a single, rather than a multi-component, power-law up to frequencies of 5 GHz (e.g. Kramer et al. 1998, 1999). A flux turnover at low frequencies, however, has not been observed for this pulsar population (e.g. Kuzmin & Losovsky 1999; Kondratiev et al. 2016).

The flux density distribution of pulsars has direct consequences of the choices of frequencies at which we search for, and observe pulsars. Since the flux drops fast with increasing frequency for most pulsars, the usefulness of very high frequency observations ($\gtrsim$5 GHz) is limited. However, pulsars have been detected up to frequencies of 225 GHz (Torne et al. 2015) and clearly more observations are needed to understand the flux energy distribution at very high frequencies. Although at low frequencies ($\lesssim$0.6 GHz) the flux is typically stronger, their use is complicated by the fact that signals at these frequencies are strongly affected by the propagation through the IISM, as we shall see in the next section.

1.2.3 Interstellar Medium Effects

The beamed emission from the pulsar travels through the IISM and suffers from dispersion, scattering and scintillation. Proper modelling of these effects and and mitigation of their effects when possible, are necessary for being able to detect and subsequently observe pulsars. In most cases, unless these effects are corrected for, the pulse is smeared out and potentially undetectable. In this section, I overview the main effects on the pulsar's signal from propagating through the IISM.

1.2.3.1 Dispersion and Faraday Rotation

It is well known that the group velocity of electromagnetic waves propagating through a medium, depends on the wave's frequency, a phenomenon known in optics as *dispersion*. For a broadband signal, such as the radio emission of pulsars, this means that the propagating signal arrives first at higher and later at lower frequencies. The propagation of electromagnetic waves through the IISM results in their

interactions with free electrons causing a frequency dependent delay to the signal which scales with the inverse of the frequency squared. In more detail, modelling the IISM as cold and homogeneous plasma, the difference in the arrival time of the signal at observing frequencies ν_1 and ν_2 due to the dispersion from the IISM is (e.g. Landau & Lifshitz 1960):

$$\Delta T_{\rm DM} = K \frac{\rm DM}{\rm pc\,cm^{-3}} \left[\left(\frac{\nu_1}{\rm GHz} \right)^{-2} - \left(\frac{\nu_2}{\rm GHz} \right)^{-2} \right]. \tag{1.2}$$

Here, $K = 4.15 \times 10^{-3}\,s$, is the dispersion constant. DM, is the dispersion measure, defined as the integrated column density of free electrons along the LOS, i.e.:

$$\rm DM = \int_{l=0}^{l=d_p} n_e\, dl, \tag{1.3}$$

where n_e is the mean free-electron density and $d_{\rm p}$ is the distance to the pulsar. DM values for pulsars vary from less than ten, to about 10^3. Figure 1.5 shows an example of the effect of dispersion to the propagation of the signal and on the shape of the pulse profile. The median DM value of all entries in the ATNF catalogue is 149 $\rm cm^{-3}$pc. Using this DM value, we can see that the arrival time of the signal at observing frequencies of 0.5 and 1.5 GHz differs by 2.2 seconds and 6.8 seconds if we change the observing frequencies to 0.2 and 2.6 GHz. The frequencies used in these examples are representative of the frequency coverage used in pulsar observing campaigns in order to mitigate dispersive DM delays effects.

The IISM, is also magnetised, and therefore the propagating pulsar signal also experiences Faraday rotation, i.e. rotation of the radio wave's linear polarisation planes. The origin of the phenomenon lies in the different propagation velocities of the two circular polarisations of the signal through the IISM. The rotating electric field of each of these polarisations exerts a force on the interstellar free electrons which inducing a circular motion, causing the free electrons to produce locally a magnetic field additional to the Galactic field. For one circular polarisation the local magnetic field will have the same direction as the Galactic, while for the other circular polarisation, the locally induced filed will oppose the Galactic. The enhancement and decrease of the magnetic field in the two cases is the reason behind the difference in their propagation velocities, which leads to a differential phase rotation between the two circular polarisations. The rotation of the wave's linear polarisation planes is a consequence of the fact that any linear polarisation component is equivalent to the superposition of a right and a left circular-polarisation components of the same amplitude but different phase. Therefore the differential phase rotation between the two circular polarisations is equivalent to a rotation of the linear polarisation components. Based on this principle, the equation describing RM can be derived.

For signals propagating through the IISM, the effect is proportional to ν^{-2} and to the proportionality constant, known as the rotation measure (RM). The equation describing RM is (see e.g. Lorimer & Kramer 2005, for a derivation):

$$\rm RM = \frac{e^3}{2\pi_e^2 c^4} \int_{l=0}^{l=d_p} B_{\|} n_e dl, \tag{1.4}$$

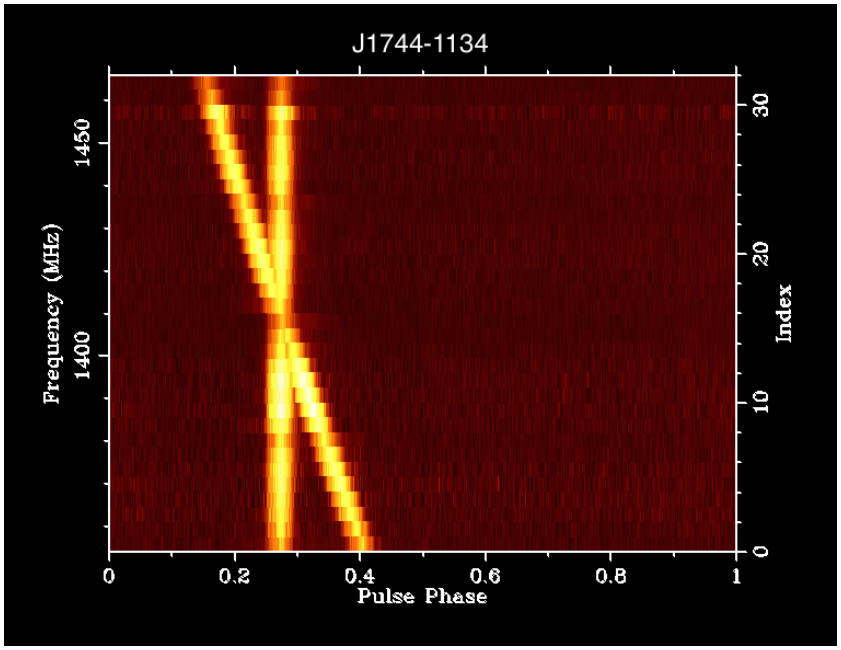

Figure 1.5: Overlaid pulse phase vs observing frequency plots for PSR J1744-1134. The intensity is colour coded, with the pulse clearly seen as a bright line. Before correcting for the dispersion, the pulse sweeps across the frequency as the signal arrives earlier at higher observing frequencies as predicted by the dispersion law (Eq. 1.2). After de-dispersion, the pulse arrives at all frequencies simultaneously. Plots created using Effelsberg data described in Chapter 3.

where e is the electron charge and $B_{\parallel}$ is the magnetic-field component in the LOS, e.g. the Galactic magnetic field. Already before the discovery of pulsars, RMs of extra-Galactic sources were used to probe the Galactic magnetic field (Gardner & Davies 1966, e.g.). However, two complications prevented secure estimations of $B_{\parallel}$. The first was the unknown value of the electron density and the second was the presence of RM internal to the sources themselves. Pulsars lack such internal RMs, and a measure of the electron content at the LOS can be derived directly from the DM measurement. The combined DM and RM measurements allow therefore the estimation of the mean magnetic-field flux density along the LOS, by combining Equations 1.3 and 1.4:

$$\langle B_{\parallel} \rangle \equiv \frac{\int_{l=0}^{l=d_{\rm p}} B_{\parallel} n_e dl}{\int_{l=0}^{l=d_{\rm p}} n_e \, dl}. \tag{1.5}$$

1.2.3.2 Scattering, Scintillation and DM Variations

Although the approximation of the IISM as a homogeneous medium predicts a dispersion-frequency dependence which appears to describe the data of a given epoch to a large degree, the interstellar medium is neither homogeneous, nor stationary. At the same time, the LOS to the pulsar is constantly changing due to the pulsar's own motion and the Earth's orbital motion. The inhomogeneities in the IISM result in multi-path propagation of the signal. Together with the relative motion between the observer and the

pulsar and the turbulent nature of the IISM, they induce scattering, scintillation effects on pulsar data and temporal changes in the DM of pulsars.

A simple model used to derive analytic expressions of the intensity's variations is one where the irregularities of the IISM are treated as a moving thin screen of turbulent plasma between the pulsar and the observer (see e.g. Lorimer & Kramer 2005). For the calculations, one needs to consider the type of the inhomogeneities. A good first, and simple approximation is to assume they follow a Kolmogorov spectrum. The propagating radiation wavefront is then distorted randomly, changing the phase of the wave multiple times. This effect is equivalent to the wave changing direction by an effective angle θ. The net result is various rays arriving at the observer at this angle, but from multiple paths, others without being bent, and others bent by various degrees. The more scattering a ray has undergone, the later it arrives, having undergone a geometric delay equal to $\Delta t(\theta) = \theta^2 d/c$, where d is the distance between the observer and the turbulence screen (here, half the distance to the pulsar) and c is the speed of light. The intensity of the emission is then found to modulate with time as:

$$I(t) \propto e^{-c\Delta t(\theta)/(\theta_d^2 d)} \equiv e^{(-\Delta t/\tau_s)}, \tag{1.6}$$

The pulse profile will therefore be broadened due to scattering by a one-sided exponential function with a characteristic *scattering timescale*, τ_s, given by:

$$\tau_s = \frac{\theta_d^2 d}{c} \propto d^2 \nu^{-4}. \tag{1.7}$$

The timescale itself is strongly dependent on the observing frequency, following a negative power-law twice as steep as the one for dispersion, making this effect more difficult to detect already at lower frequencies, than in the case of dispersion delay.

Scattering delay tails have been observed in some studies to follow this relation (e.g. Johnston et al. 1998; Cordes et al. 1985). In other studies, however, the scattering timescale has been observed to have a less steep dependence on the frequency, implying deviations of the IISM's turbulence from a pure Kolmogorov spectrum (e.g. Löhmer et al. 2001; Bhat et al. 2004). The observed profile can be fitted by a template which is constructed as a convolution of a profile template fitted to a high-frequency profile (largely unaffected by scattering) and a scattering pulse broadening (impulse response) function (see e.g. Löhmer et al. 2001). An example of such observations and the respective fitted models can be seen in Figure 1.6 for observations of PSR J1745−2900.

Pulse broadening by scattering imposes strong limitations on pulsar surveys. When searching for periodic signals of pulsars at trial spin periods in time-domain data, one needs to perform signal de-dispersions at many trial DM values (based on Eq. 1.2) in order to reveal the pulse, which otherwise is smeared out. The effects of scattering, however, cannot be removed. Therefore, surveys are scattering limited, making it difficult to detect pulsars with pulse widths narrower than the scattering timescale. Very short period pulsars, which can serve as excellent tools for applications such as testing gravity theories (see Chapter 5), become very difficult to find, along the Galactic plane where the DM increases rapidly with distance.

The radiation from pulsars is also subject to interstellar scintillation, modulations in the observed emission intensity on various scales of time and bandwidth. In the case of multi-path scattering, diffract-

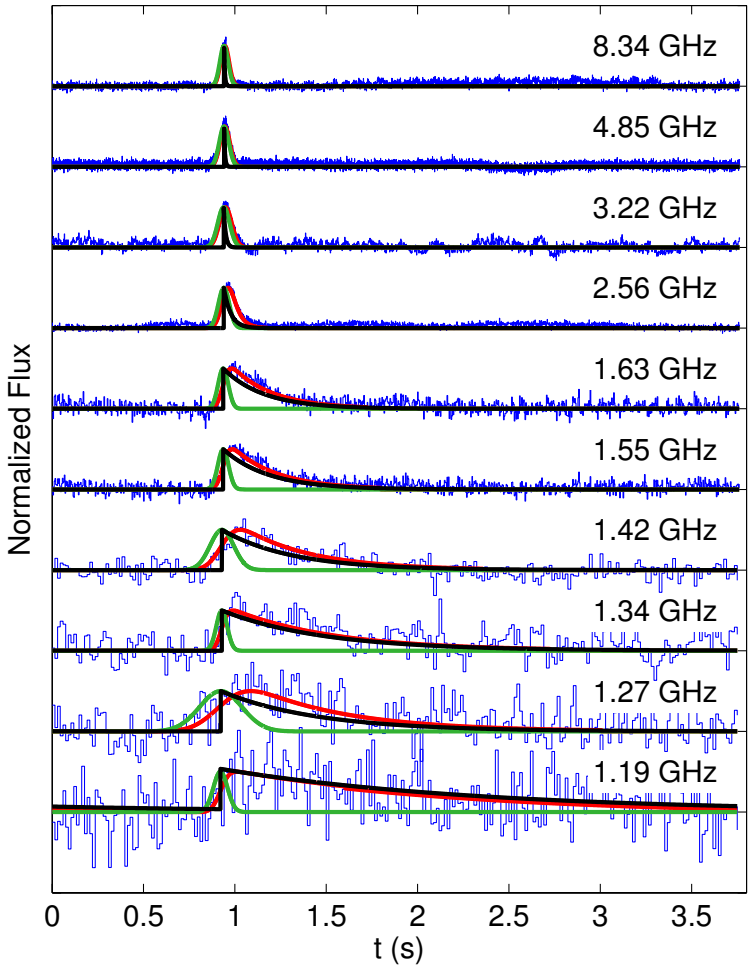

Figure 1.6: Scattering-dominated pulse broadening effects at various observing frequencies (denoted in GHz in each panel) for PSR J1745−2900, in the direction to the Galactic centre. The blue lines are the observed profiles. These are fitted with a model (red lines) described by the convolution of a Gaussian profile (green lines) and a pulse broadening function (black lines). Figure from Spitler et al. (2014).

ive scintillation takes place due to the random frequency changes that the radiation wavefronts experience, and which are of the order $2\pi\nu\tau_s$ (Lorimer & Kramer 2005). The interaction of wavefronts that have undergone different scattering paths creates wave interference patterns, obviously with intensity variations that are observed due to the observer-pulsar relative motion. The timescale of these intensity variations, τ_{sc} will naturally depend on this relative velocity. An important aspect, is that interference occurs only under the condition that the frequency difference between the interacting waves are below about 1 radian, i.e., $2\pi\Delta\nu\tau_s \lesssim 1$, where $\Delta\nu$ is the scintillation bandwidth. One can easily deduce that scintillation causes intensity variations not only as a function of time but also of the observing frequency as:

$$\Delta\nu \propto 1/\tau_s \propto \nu^4 \tag{1.8}$$

Pulsar emission also exhibits intensity variations on much longer time-scales, of the order of months. These are induced by refractive scintillation, caused by the refraction of the signal by large scale irregularities of the IISM structure, as first pointed out by Rickett et al. (1984). The first strong evidence to the origin of long-timescale intensity fluctuation arising from interstellar medium effects (and not from the pulsar radiation mechanism) was the correlation between the time-scales of the intensity variation and the DM values (Sieber 1982). Indeed, the large scale structure irregularities of the IISM, together with its turbulent nature and the change of the LOS to the pulsar due to our relative motion, results in well observed temporal variations of the DM (e.g. You et al. 2007). As we shall see in Chapter 4, DM temporal variations add stochastic noise to the time series of TOAs if not properly corrected and great efforts are being made to mitigate these effects.

1.2.4 Period and Period Derivative

Two of the most fundamental pulsar observational properties are its period, P and period derivative, $\dot{P}$. The latter term, reflects the loss of rotational energy through various mechanisms. Part of this energy is converted to the observed radio emission. The rotating magnetic field generates an electric filed which accelerates (to relativistic velocities) particles from the pulsar surface along the magnetic-field lines, producing the observed emission. Only a small fraction of this energy is converted to radio emission. The majority of the rotational energy is converted to high-energy dipolar radiation and to the kinetic energy of the pulsar wind (see Fig. 1.1), outflow of particles at relativistic speeds (see e.g. Lyne & Graham-Smith 1998).

One can combine the relations for the rotational energy loss and the energy loss from a rotating magnetic dipole to construct a relation that connects the period and the period derivative with the pulsar's age, under certain assumptions (e.g. Lorimer & Kramer 2005). We can relate the spin-down with the loss of rotational energy, $E_{\rm rot}$, as:

$$\dot{\rm E} = -\frac{dE_{\rm rot}}{dt} = -\frac{{\rm d}(I\Omega^2/2)}{{\rm d}t}. \tag{1.9}$$

Here, I is the moment of inertia and $\Omega = 2\pi/P$ is the rotational angular frequency. The energy loss from a strong, magnetic dipole can be written as:

$$\dot{\rm E}_{\rm dip} = -\frac{2}{3c^3}|{\rm m}|^2\Omega^4\sin^2\alpha, \tag{1.10}$$

where c is the light-speed, $\mathbf{m}$ is the magnetic dipole moment and α is the angle between the dipole moment and the rotation axis. One can then express the latter relation in terms of P and $\dot{P}$, in the form of a power-law as:

$$\dot{P} = KP^{2-n},\ K = \frac{8\pi^2|{\rm m}|\sin^2\alpha}{3Ic^3} = \text{constant}. \tag{1.11}$$

The term n is called the *breaking index*. In the example of a pure magnetic dipole, n =3 (as in Eq. 1.10). One can integrate Eq. 1.11 to construct an equation for the age of the pulsar, $T_{\rm p}$:

$$T_{\rm p} = \int_{P_0}^{P} P^{n-2} dP = \frac{P}{(n-1)\dot{P}}\left[1 - \left(\frac{P_0}{P}\right)^{n-1}\right], \tag{1.12}$$

where P_0 is the rotational period at formation.

From the latter equation, we introduce the *characteristic age* of the pulsars, $\tau_{\rm c}$, which is the age calculated under the assumption that the pulsar has spun-down sufficiently so that $P << P_0$ and $n = 3$:

$$\tau_{\rm c} \equiv (1/2) P \dot{P}^{-1}. \tag{1.13}$$

Expanding on the magnetic dipole model for the pulsar, it is useful to derive an expression to connect direct observables, such as P and $\dot{P}$ with the hard-to-measure magnetic-field strength. The basis for the derivation is the relation of the magnetic-field flux density, B, with the magnetic moment, $\mathbf{m}$. For the case of a magnetic dipole this relation is approximated by $B \approx |\mathbf{m}| r^{-3}$. We use this relation to substitute $\mathbf{m}$ in Equation 1.9 and derive that at the pulsar's surface, $B \propto \sqrt{P\dot{P}}$. A typical value of the magnetic-field flux density can be derived for a pulsar of given P and $\dot{P}$, with an assumption of the pulsar's radius, R, moment of inertia, I, and the angle between the dipole moment and the rotation axis, α. By assigning values typical to pulsars, we can get the *characteristic magnetic field*, which serves as an estimate of B. By setting $R = 10\,\mathrm{km}$, $\alpha = 90°$, $I = 10^{45}\,\mathrm{g\,cm^2}$, we derive the characteristic magnetic-field strength (Lorimer & Kramer 2005):

$$B_{\rm c} = 3.2 \times 10^{19} \mathrm{G} \sqrt{P\dot{P}}. \tag{1.14}$$

As already stressed, the characteristic age and magnetic field of a pulsar, are only useful approximations. The calculations have assumed that the emission is produced by a perfect dipole, and the magnetic-field strength and the angle between the magnetic and the rotational axis to be time-invariant. It is known that these simple assumptions do not hold. Measured breaking indices are consistently smaller than 3 (e.g. Livingstone et al. 2007), implying additional torque forces contributing to the spin-down, beyond the magnetic dipole radiation; for example, by the presence of magnetic dipole in plasma instead of the vacuum. Variations in the magnetic-field strength, is also proposed as a mechanism to explain the breaking index values smaller than three (Blandford & Romani 1988). Such variations can happen for example during mass accretion from the pulsar's companion (see e.g. §1.4).

Calculating the characteristic age also assumes that $P << P_0$, which a weak approximation for very young pulsars. The true age of the pulsar can be inferred, in some cases, from historical information on the associated SNR and compared with their characteristic ages. Examples of very young pulsars are the Crab Pulsar, located in the Crab Nebula which is associated with the supernova SN 1054, and PSR J0205+6449, associated with the supernova SN 1181. The number in the supernovae names are the year of discovery, so their true ages are 962 and 835 years respectively. By comparison, the derived characteristic age using the period and period derivative values from the ATNF pulsar catalogue are 1257 and 5366 years respectively.

1.3 The $P - \dot{P}$ diagram

Although the characteristic ages derived with the measured periods and period derivatives do not provide a reliable estimate of the true ages of pulsars, the latter two quantities can be used to classify pulsars in groups. The period, period derivative and characteristic ages and magnetic fields are often presented on the $P - \dot{P}$ diagram, which in pulsar astronomy is the equivalent of the Hertzprung-Russell diagram in stellar evolution. Figure 1.7 shows the $P - \dot{P}$ diagram for a sample of pulsars. The diagram shows a clear

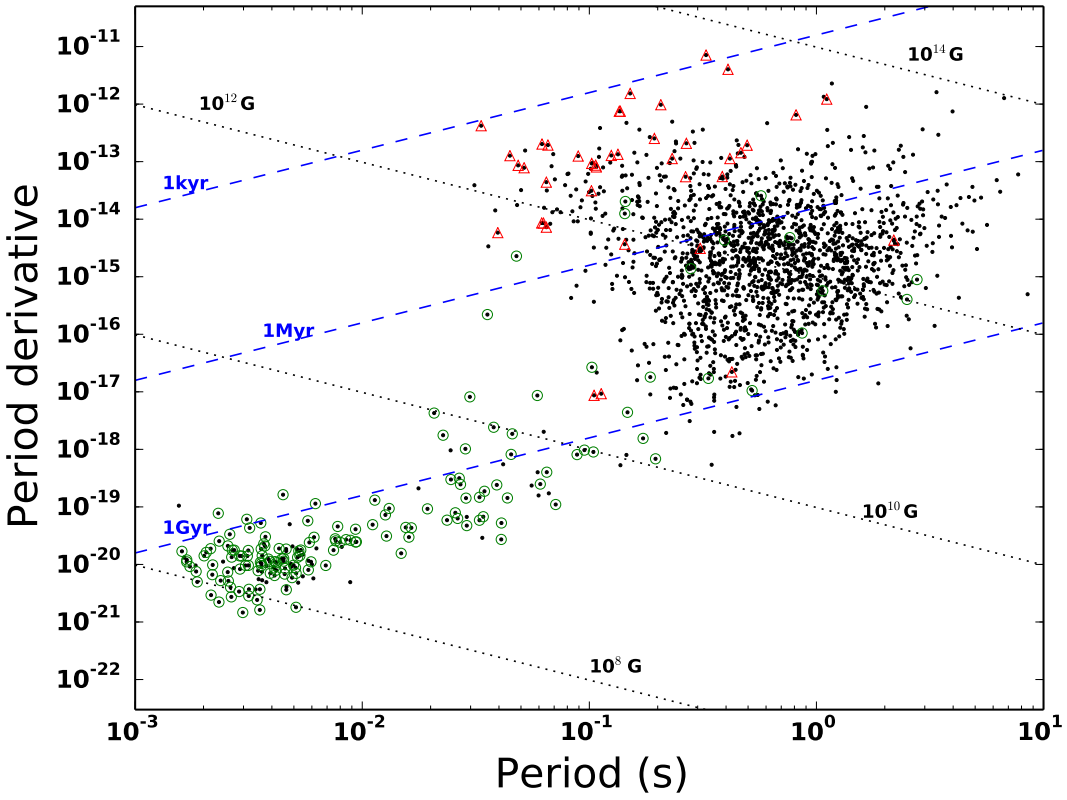

Figure 1.7: A $P - \dot{P}$ diagram, created using information from the ATNF pulsar catalogue. The black points show Galactic pulsars, excluding those in globular clusters (due to their different evolution, owing to multiple interactions with other cluster members). Binary pulsars are noted with green circles. Pulsars with SNR associations, are noted with red triangles. The black, dotted lines show constant characteristic ages (Eq.1.13), while the blue dashed lines show the areas of constant characteristic magnetic fields (Eq. 1.14). There is a clear separation in the diagram between solitary and binary pulsars populations, with the latter typically having spin periods roughly two orders of magnitude shorter than solitary pulsars and spin-down rates about five orders of magnitude smaller.

division into two main populations. The first consists of pulsars with periods of order of seconds and period derivatives of $\sim 10^{-15}$. These are typically solitary pulsars and almost all pulsars with SNR associations (red triangles) belong to this population. This population is referred to as "canonical" pulsars in the literature. The SNR associations are evidence of their younger ages. Their characteristic ages and magnetic-field strengths are of order $\sim$1 Myrs and $\sim 10^{12}\,G$, respectively. Long-term monitoring of these pulsars has revealed that they suffer significantly from rotational instabilities (e.g. Hobbs et al.

2010). Glitches, sudden increases of the spin frequency which are sometimes followed by slow recoveries on time-scales that can vary from days to years (e.g. Link et al. 1992), are predominantly observed in canonical pulsars (e.g. Espinoza et al. 2011; Yu et al. 2013). It is theorised that glitches are caused by transfer of angular momentum from the superfluid in the pulsars interior to the outer crust (e.g. Anderson & Itoh 1975). Canonical pulsars are also characterised by other types of instabilities in the rotation and the emission mechanism, which are discussed in more detail in Chapter 4.

The lower left part of the $P - \dot{P}$ diagram is populated by a class of pulsars known as "Millisecond pulsars" (MSPs), due to their remarkably fast rotations with millisecond-order periods. Period derivatives are of the order 10^{-20}, over four orders of magnitude smaller than canonical pulsars. Their characteristic ages and magnetic-field strengths are of order Gyrs and $\sim 10^8\,G$, respectively. MSPs are the most stable pulsars known, with TOAs stable at the ns level over decadal time-scales (e.g. Verbiest et al. 2009, see also Chapter 4). For this reason, MSPs have become the most-widely used pulsars for precision-timing applications. Due to the central role of MSPs in the work for this dissertation, I overview their properties and formation theory in the next section.

1.4 Millisecond Pulsars

Soon after the first discovery of an MSP (Backer et al. 1982), it was theorised that they are formed via mass accretion from their companion star (Alpar et al. 1982; Radhakrishnan & Srinivasan 1982). This process transfers angular momentum to the pulsar, spinning it up to millisecond periods. After the end of the mass transfer, they return to the state of a rotationally-powered pulsar with a spin-down. This evolutionary scenario, which is widely accepted today, explains their extremely fast rotations, their weaker magnetic fields and the fact that the vast majority of MSPs are located in binary systems (see e.g. Tauris 2011, for a review). Solitary MSPs could result from disruption to the binary caused by e.g. a subsequent supernova explosion of the companion (if massive enough) or its tidal break-up.

The companions of MSPs in binary systems are WDs (neutron star-white dwarf systems or NS-WDs), another NS (double neutron star systems or DNSs) and substellar, semi-degenerate companions. During the accretion process, binary MSPs are observed as X-ray binaries. Low- and intermediate-mass X-ray binaries evolve to NS-WD systems while high-mass X-ray binaries are the predecessors to DNSs. This connection is strongly supported by observations in agreement with theoretical predictions (see e.g. Bhattacharya & van den Heuvel 1991) such as the evidence for a past present of an accretion disc in a radio MSP (Archibald et al. 2009), X-ray MSPs, i.e. MSPs powered by accretion with observable millisecond periodicities in X-rays (e.g. Wijnands & van der Klis 1998) and perhaps more importantly, by observations of systems transitioning from a radio to an X-ray MSP (e.g. Papitto et al. 2013).

MSPs have proven to be excellent tools for a wealth of studies in astrophysics and fundamental physics. Their short periods allows higher precision in the TOA calculations (see e.g. van Straten 2006). While, as we mentioned, MSPs show remarkable rotational stability, their weak magnetic fields result in smaller amount of energy loss through their rotation (hence the small period derivatives, see Equation 1.14) and can therefore rotate at ms periods for billions of years (e.g. Alpar et al. 1982). The pulse profiles of MSPs exhibit much less frequency evolution (Kramer et al. 1999) and time variability (e.g. Shao et al. 2013).

The properties of MSPs have led to a wealth of applications and cutting-edge scientific results, especially via the pulsar timing technique, which uses precise measurements of the TOAs to construct an accurate timing model of the (binary) pulsar's rotational and orbital parameters and of the free electrons

content of the interstellar medium between the pulsar and Earth. Pulsar timing is a central topic of this dissertation and will be discussed in detail in Chapter 2.

1.5 Pulsar Astronomy: Applications and Highlights

Pulsar astronomy has been active for only four decades, but has produced a remarkable number of scientific highlights. The combined properties of pulsars, make them a very useful tool for observational astrophysics. Thanks to their huge densities and self-gravity, pulsars are excellent laboratories for studying the physics of supra-dense matter and the nature of gravity in the strong-field regime. The high polarisation degree and broadband nature of their emission, allow to probe the electron content and the magnetic fields along the LOS. The usefulness of pulsars are amplified by their stable rotations and the high precision by which we can measure their TOAs.

Undoubtably, one of the biggest breakthroughs of the field is the opportunity that binary pulsars provided to test the predictions of General Relativity (GR) and other theories of gravity beyond the weak gravitational field of the Solar system. The first ever binary pulsar discovered, was B1913+16 (or J1915+1606), also known as the *Hulse-Taylor pulsar* (Hulse & Taylor 1975). Its timing analysis provided the first evidence of the existence of Gravitational Waves (GWs) through the precise measurement of its orbital decay, which agreed with the prediction of GR for the orbital decay from energy loss by GW emission (Taylor & Weisberg 1989, see also Figure 1.8). It then became clear, that binary pulsars were a huge asset in the toolbox of experimental gravity and Russell A. Hulse and Joseph H. Taylor Jr. were awarded the 1993 Nobel prize in physics [5] "for the discovery of a new type of pulsar, a discovery that has opened up new possibilities for the study of gravitation".

Many more binary pulsars have been found since, most of which contain MSPs. Their timing has indeed provided with some of the most stringent tests of GR and alternative theories of gravity in the strong-field regime. The *Double Pulsar*, PSR J0737−3039A/B (Burgay et al. 2003; Lyne et al. 2004), is the only DNS so far, where both members have been observed as radio pulsars. It has provided with the best tests of the predictions of GR in strong gravitational fields (Kramer et al. 2006b). Other MSPs have been used to limit the parameter space of different classes of alternative gravity theories, for example scalar-tensor gravity (see e.g. Freire et al. 2012b). More details on experimental gravity with precision pulsar timing are discussed in Chapter 5.

As we shall see in the next chapter, pulsar timing can be very sensitive to any process affecting the TOAs that is not included in the timing model. In this way, pulsar timing provided the first ever detection of exoplanets (e.g. Wolszczan & Frail 1992). One of these planets, in orbit around PSR B1257+12, is the least massive exoplanet known (Figure 1.8), with an estimated mass only about twice the lunar (Wolszczan 1994). Proper motion measurements of pulsars, performed via timing, interferometric imaging or optical observations provided information for pulsar-SNR associations, pulsar birth-periods and supernova-kick mechanisms (e.g. Hobbs et al. 2005; Noutsos et al. 2013).

The measurement of pulsar physical parameters, can shed light to the physics of its super-dense interior. Proposed equations-of-state (EOSs) of matter at supra-nuclear densities impose upper limits on NS masses. High-mass pulsars such as J1614−2230 and J0348+0432, have placed constraints on the possible EOSs (Demorest et al. 2010; Antoniadis et al. 2013). These high-mass NSs, are also important in that they provide observational evidence on the lowest necessary mass of a supernova's remnant to become a BH.

[5] http://www.nobelprize.org/nobel_prizes/physics/laureates/1993/

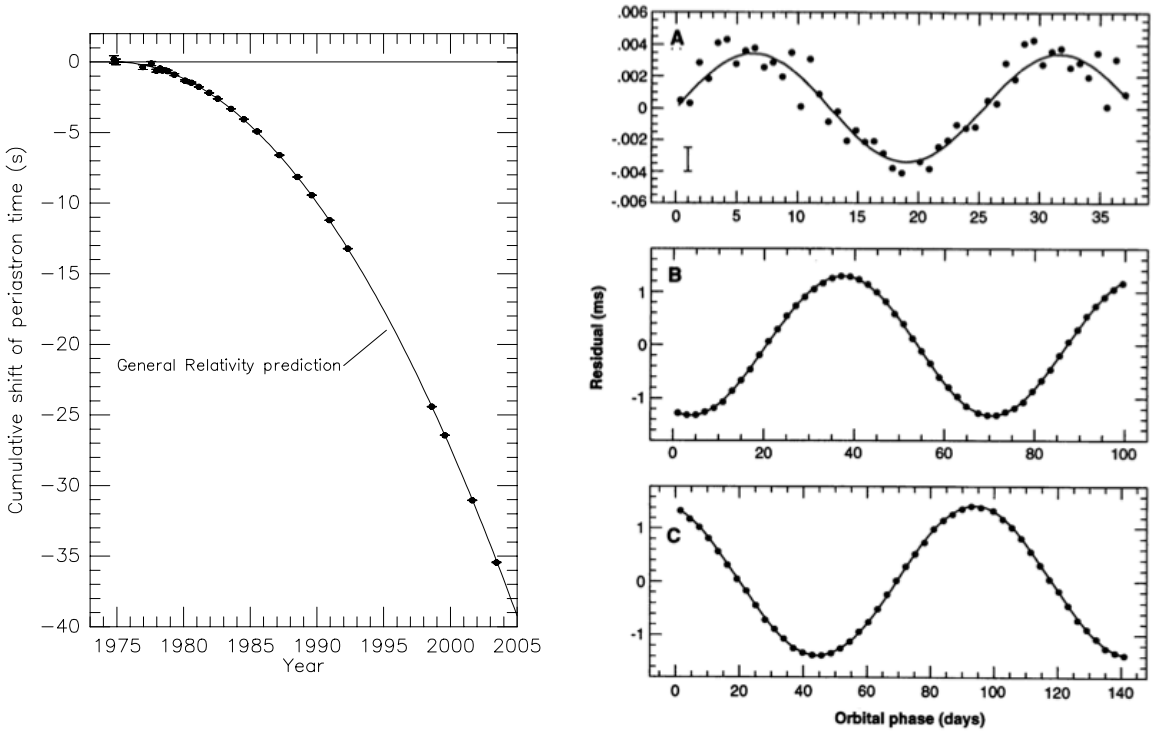

Figure 1.8: *Left Panel:* Evidence for the existence of gravitational waves from precision timing of the binary pulsar B1913+16. The data points show the observed change in the epoch of periastron, expressed as the cumulative change over time. The uncertainties on the data points are smaller than the dots and difficult to see. The solid line is the prediction of General Relativity and agreed with the data to within about 0.2%. Figure from Weisberg & Taylor (2005). *Right Panel:* Detection of exoplanets using pulsar timing observation. Each panel shows the timing 'signature' from the orbit of one of the planets, i.e. the residual signal when fitting for all parameters, except the orbit of the planet, with respect to their orbital periods. Planets A, B, and C are in increasing distance to the pulsar. Figure from Wolszczan (1994)

Measurements of the DMs in many different LOSs, provides prior information to calibrate models of the Galactic distribution of free electrons (e.g. Cordes & Lazio 2003; Schnitzeler 2012). These models can then serve as a basis for estimating pulsar distances and deviations from independent measurements can provide further constraints to the electron distribution models (e.g. Desvignes et al. 2016, see §3.3.3). The combined information from DM and RM measurements have been used to constrain the strength of the Galactic magnetic field (Mitra et al. 2003; Noutsos et al. 2008). More recently, these type of measurements were used to demonstrate the existence of a dynamically important magnetic field in the vicinity of the supermassive BH at the Galactic centre (Eatough et al. 2013). The measured magnetic flux can explain the radio-to-X-rays observations from the Galactic centre, attributed to accretion by the BH.

Pulsars are also used in the efforts for direct detection of low-frequeny GWs, primarily at nHz frequencies, via long-term timing of an ensemble of MSPs in random sky positions, known as a Pulsar Timing Array (PTA; Foster & Backer 1990). A PTA acts as a multi-arm Galactic-scale detector, used to measure the pulsar TOA delays induced by the space-time distortion caused by propagating GWs. The

pursuit of GW detection using pulsar timing is co-ordinated by three consortia; the European Pulsar Timing Array (EPTA; Kramer & Champion 2013) in Europe, the North-American Nanohertz Observatory for Gravitational Waves (NANOGrav; McLaughlin 2013) in North America and the Parkes Pulsar Timing Array (PPTA; Hobbs 2013) in Australia. PTAs employ in total eight large single-dish radio telescopes. The EPTA uses five telescopes, namely the Effelsberg Radio Telescope, the Nançay Radio Telescope, the Lovell Telescope, the Westerbork Radio Synthesis Telescope and the Sardinia Radio Telescope. NANOGrav uses two telescopes, the Green Bank Telescope and the Arecibo Radio Telescope, while the PPTA uses the Parkes Radio Telescope. The three consortia co-operate under the International Pulsar Timing Array (IPTA) consortium, maximising the observing efficiency and data set sensitivity (Verbiest et al. 2016). Much of the work presented for this thesis, was conducted in the framework of the EPTA. Further details on GWs searches with PTAs are discussed in Chapter 3.

1.6 Thesis Structure

This thesis is organised as follows: Chapter 2 presents in detail the pulsar timing technique. In Chapter 3, an overview of the instrumentation for pulsar timing observations is presented, followed by a presentation of the Effelsberg-Berkeley Pulsar Processor which has been employed at the Effelsberg radio telescope for almost two decades. I will describe my work reducing and analysing these data, followed by a presentation of their combination with data from another three European telescopes and the results from the timing of 42 MSPs. Chapter 4 presents the principles of detecting GWs with PTAs and the analysis of the noise properties of the 42 EPTA MSPs. The measured noise properties are then used to quantify the impact of MSP noise on the PTA community's efforts for direct nHz-GW detection. In Chapter 5, I will introduce the methods used for testing gravity theories using pulsar timing data and present work and results such tests using timing data of three MSP, namely PSRs B1937+21, J1744-1134 and J1012+5307. Finally, in Chapter 6, I will conclude with an overview and discussion of the results presented in this thesis and an outlook to future perspectives of pulsar-timing applications.

CHAPTER 2

Pulsar Timing

> ”Observe due measure, for (right) timing is in all things the most important (factor).”
>
> *Hesiod*

The previous chapter concluded with an outline of the pulsar-timing technique and a brief discussion which included some of the method's most important applications. In this chapter, I will describe pulsar timing in more detail. I first review how we form the TOAs from the recorded timing data and the TOA fitting routine. I then discuss in more detail the various signal delay terms and reference system transformations in the pulsar timing before providing an overview on the fitted timing-model parameters. I will conclude this chapter with a brief discussion on the fundamental assumptions of the timing method, how they often break down and how we take these into account in our data analyses.

2.1 Basics of Pulsar Timing

As discussed in §1.4, pulsar timing is the technique where TOAs from pulsars are regularly recorded with high precision and are then fitted with a model of the (binary) pulsar's rotational and orbital parameters and of the free electrons content between the pulsar and Earth. The difference between the observed and the model-predicted TOAs are called *timing residuals*. A non-optimal fit of individual parameters induces specific signatures in the residuals, allowing for the detection and measurement of a number of processes affecting the observed system. The stability of the pulsar rotation allows these models to predict the future TOAs with high precision. Iteratively, more data can be added in order to update and improve the model.

In order to demonstrate the power of pulsar timing as a tool to probe the physics that governs their motions, let us consider a binary MSP at a typical distance of 1 kpc and with a typical orbit size of 10 light-seconds (3×10^9 m). A typical MSP TOA measurement precision with contemporary observing systems of 1 μs, translates into $\sim$ 100 m precision in the pulsars's position, or a 0.001% precision of the position relative to the size of the orbit. For the brightest MSPs measurement precisions of $\sim$ 200ns can be achieved, which gives a 0.000001% precision of the position relative to the size of the orbit.

Pulsar timing is, in essence, a precision comparison of clocks: terrestrial time-standards compared against the pulsar time-standard, defined by the periodic pulse arrival times. To the precision that this

experiment takes place, where the most precise terrestrial time standards are used, Newtonian gravity is by far insufficient. Relative velocities between the various reference frames require special-relativistic time-dilation corrections. Furthermore, the effects of gravitational redshift and time-dilation must be corrected for. For example, Global Positioning System (GPS) clocks require relativistic corrections for the difference in time keeping by clocks at the surface of the Earth and on orbit.

The field equations of GR, which describe the gravitational interaction, are non-linear and do not have exact solutions for the two-body problem. In order to study problems such as the orbit of a binary system, a framework in which approximate solutions are formed with correction terms of increasing-order deviations from Newton's law of universal gravitation, was first introduced for GR by Sir Arthur Eddington (Eddington 1922). This framework, named the *post-Newtonian (PN) approximation* was later re-formulated in the *Parametrised post-Newtonian* (PPN) formalism, where the parametrisation of the PN terms allows to compare the predictions by different boost-invariant[1] gravity theories (Will 1981).

Further discussion on the PPN formalism is made in §5.1. What is important to note here, is the fact that for objects in the vicinity of Solar system bodies, which have weak gravitational fields and move with velocities well below that of the speed of light, the predictions of GR and other physically motivated alternative theories of gravity are the same. Relativistic time-dilations between reference frames and gravitational time-dilation and red-shift effects taking place in the Solar system (§2.2.1) can therefore be calculated using the PN approximation of GR. On the other hand, the orbital motion of a binary pulsar is affected by the strong gravitational field of the NS and higher-order PN corrections, that can differ significantly in alternative theories of gravity, become important. For this reason, the PPN formalism has been used to develop the *parametrised post-Keplerian* (PPK) formalism (Damour & Deruelle 1985, 1986), in which the relativistic effects of the binary orbit are parametrised by a set of all the observable effects in a phenomenological, theory-independent way. Details of the PPK formalism will be discussed in §2.3.3.

2.1.1 Recording and Time-stamping the Incoming Signal

Let us now see the basic steps of pulsar timing, which are schematically presented in Fig. 2.1. This description begins from the moment the pulsar signal reaches the data processor, or *backend*. The details on how the signal is processed by the receiver, or *frontend*, and more details on the signal processing by the backend, will be discussed in the next chapter.

The first step in pulsar timing is recording of the TOAs with the highest possible precision. This is shown in the steps (i) to (iii) in Fig. 2.1 (henceforth in this section, roman numerals in parentheses will refer to the corresponding stages in Fig. 2.1). As explained in §1.2.1, average profiles are constructed by adding single pulses in phase in order to increase the S/N. To perform this process, which is known as *folding* (step i), the observatory's backend uses a parameter file containing the basic properties of the pulsar; its position, spin period and period derivative, its DM and its Keplerian orbital parameters (§2.3.3). The position, period and DM are initially know from the pulsar's discovery. During observations, the DM information is used to de-disperse the recorded signals (see Equation 1.2) and the rest of the information is used to correctly predict the phase of the pulses in order to be properly aligned for folding. In principle, short sub-integration times are preferred, in order to reduce the effects of small errors in timing parameters. Subsequently, the recorded sub-integrations can be folded to increase the S/N, using more up-to-date timing models.

[1] This means that the outcome of an experiment is not influenced by the change of the reference frame, therefore are invariant under the Lorentz transformations. Certain classes of alternative theories of gravity violate this principle (see e.g. §5.2).

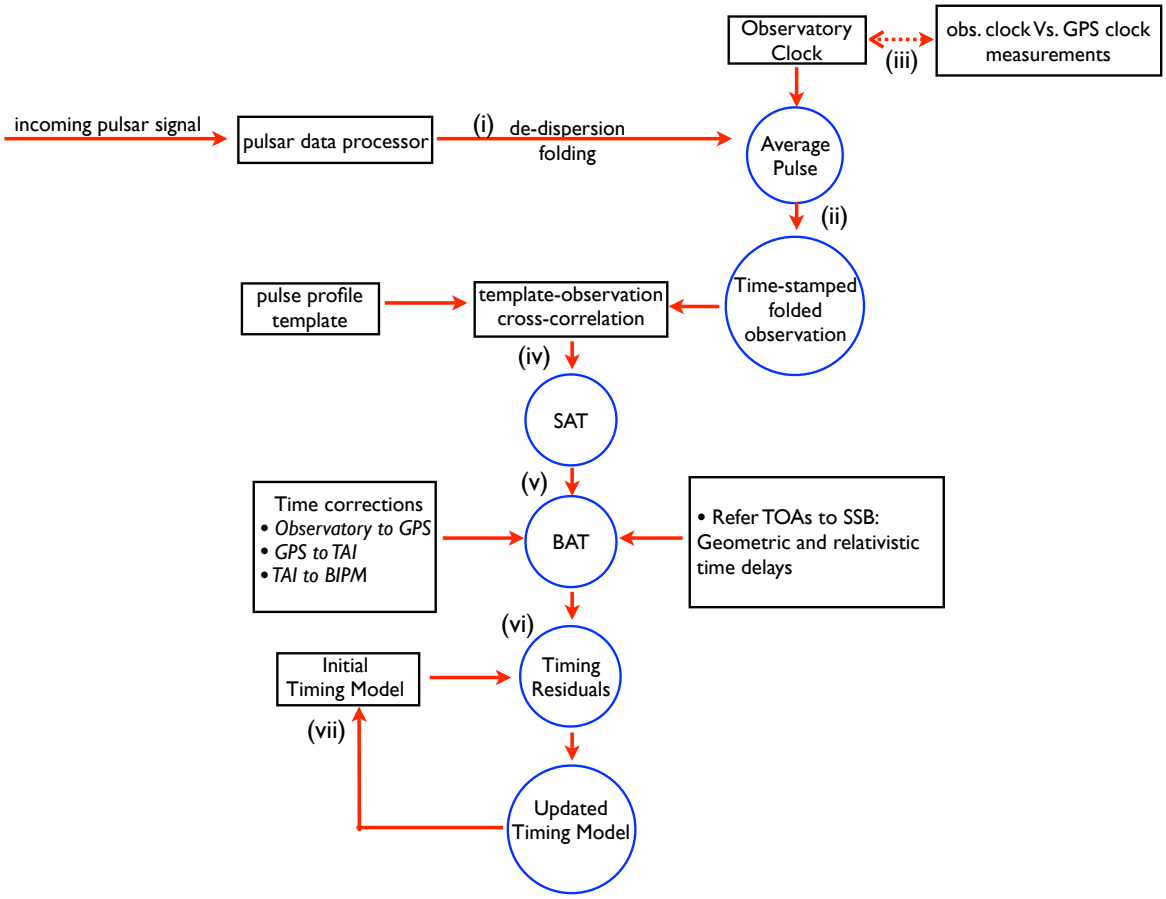

Figure 2.1: Schematic overview of the pulsar-timing technique. See discussion in §2.1

The uncertainty of the TOA measurement can be approximated by the ratio of the pulse width (or width of the sharpest component) to the S/N, which is in turn defined as the ratio of the peak pulse flux density, $S_{\rm p}$, to the off-pulse fluctuation levels. The theoretical minimum of these fluctuations is derived using the radiometer equation. By applying this equation to pulsed signals, one can derive the pulse maximum S/N (see e.g. Lorimer & Kramer 2005, Appendix 1) and express the TOA uncertainty as :

$$\sigma_{\rm TOA} \approx \frac{W}{S/N} = \frac{WS_{\rm p}P}{T_{\rm sys}[n_{\rm sp}\Delta t \Delta\nu W(W-P)]^{1/2}}\,, \tag{2.1}$$

where W is the pulse width, $n_{\rm sp}$ is the number of integrated single pulses, Δt is the length of the observation, $\Delta\nu$ is the receiver bandwidth and P is the pulse period.

During observations, each output profile file is time-stamped with the observatory's clock (step ii), which is usually a high-precision clock, either an atomic clock (e.g. Hydrogen maser clock) or a GPS clock. Time-stamps refer to the start time of the observation. The atomic clocks used at the observatories are very precise standards on timescales of days to weeks, but show instabilities on timescales of months to years and therefore cannot serve as stable long-term standards. Therefore, the observatories keep

measurements of the offsets of their local atomic clocks with that of a GPS clock (step iii) for later corrections.

2.1.2 Forming the Topocentric TOAs

The time-stamped profiles are then used to derive the average TOA of the integrated pulse. In order to form a TOA, one needs to specify the time that the pulse arrived relative to a reference time. For this purpose, all observations are cross-correlated with a template profile, which can have any arbitrary phase (step iv). The procedure assumes that at a given time, t, the template, $T(t)$, is a shifted and scaled version of each observed pulse, $P(t)$. Noting the phase offset as a, the scaling factor as b and the pulse's sampling noise as $N(t)$, the template matching equation can be written in time domain as (e.g Taylor 1992; Lorimer & Kramer 2005):

$$P(t) = a + bT(t - \tau) + N(t) \tag{2.2}$$

The time shift, τ, is the topocentric TOA or site-arrival-time (SAT) relative to the template. When the template matching is performed in time domain, the precision is limited by the size of the sampling bins. The precision can be improved by performing the template matching in the frequency domain, using the Fourier transforms of the pulses and the template. The timing precision can then be smaller than a tenth of the sampling bin size (e.g Rawley 1986; Taylor 1992).

All profiles are referred to the same template, and therefore the temporal stability of the pulsar's pulse profile is critical for achieving long-term high-precision timing. A high-S/N pulse profile can serve as the template, although it is now common practice to construct analytic, noiseless templates by fitting the high S/N profile with analytic functions (e.g. Kramer 1994) or by smoothing the data (Demorest et al. 2013). Analytic templates are preferred in order to avoid the effect of *noise locking*, i.e. the positive correlation between noise components of the two profiles. We note that due to the frequency evolution of the profiles (as discussed in §1.2.1), different templates are typically used for data obtained at different frequency bands. More recently, due to the advancement of wide-band receivers, new 2-dimensional (in phase and observing frequency) template-matching techniques have been developed to account for the pulse profile's frequency evolution and dispersive delays across the receiver's band (e.g Liu et al. 2014; Pennucci et al. 2014).

2.1.3 Forming the Timing Residuals

In order to model the observed TOAs, we choose to make use of inertial reference frames for both the observations and the model predictions. In practice, we refer the TOAs to the quasi-inertial reference frame of the Solar system Barycentre (SSB) to form the barycentric TOAs (BATs) which are then used as input by the model to predict the time of pulse emission at the inertial pulsar's co-moving reference frame. The choice of referring the TOAs to the SSB becomes even more important with the use of data sets with data from multiple telescopes at different Earth locations, since it additionally acts as a convenient common reference frame for all the TOAs.

Denoting the SATs as t_{sat} and the pulse emission time at as t_{em}, and following Edwards et al. (2006),

we can write the timing equation in a compact way, with various terms grouped as:

$$t_{em} = t_{sat} - \Delta_{\odot} - \Delta_{IS} - \Delta_{B}. \tag{2.3}$$

Here, $\Delta_{\odot}$, Δ_{IS} and Δ_{B} describe the signal delays from the details of the signal propagation across the solar system, the interstellar medium and the binary orbit, respectively. They contain the terms that successively transform the TOAs from SATs to BATs, then to the arrival time at the BB, t_{bb}, and finally to the pulsar's proper emission time.

Once the pulse emission time is derived, we use the timing model to predict the pulse's phase evolution with time. As discussed in §1.2.4, the pulsar's rotational phase evolution is mainly characterised by spin-down due to the energy loss from the emitted radiation. Due to this stable behaviour, the phase evolution can be modelled as a smooth function and can be well approximated by a Taylor expansion of the phase as function of time as (see e.g. Lorimer & Kramer 2005; Hobbs et al. 2006):

$$\phi(t) = \sum_{n \geq 1} \frac{(d\phi/dt)^{(n-1)}}{n!} (t_{em} - t_0)^n + \phi_0. \tag{2.4}$$

Here, $d\phi/dt$, is equal to the rotational frequency of the pulsar, and the $(n-1)$ superscript denotes the $(n-1)$th-order time derivatives of the rotational frequency. The latter are fitted timing parameters, while t_0 and ϕ_0 are the reference time and phase. The two first terms of the series (i.e. $1/P$ and $1/\dot{P}$) are usually sufficient for solutions of rotationally stable pulsars such as the MSPs. Higher-order terms can be used to describe rotational instabilities with stationary signals. However, it is becoming common practice to model such instabilities separately, as we explain in §2.4, especially in applications like GW detection, where the noise is important to be characterised (Chapter 5). Glitches, which as discussed (§1.3) mostly characterise young pulsars, can be modelled by added terms to Eq. (2.4) (see e.g. Edwards et al. 2006).

Under the assumption of the lighthouse model for the pulsar emission (Fig. 1.1) every single pulse corresponds to one rotation. Therefore, the difference in the phases corresponding to any two TOAs, must contain an integer number of rotations. This is then the case also for average pulses. The importance of this statement is that Eq. 2.4 can be used to predict the pulse number at a given time, $N(t)$, with respect to the pulse number at reference time, N_0. The timing residual corresponding to the fit of i-th TOA, R_i, is then calculated in terms of integer numbers as:

$$R_i = N_i - \mathbb{Z}_i \,, \tag{2.5}$$

where $\mathbb{Z}$ is the nearest integer to N_i. The predictive power of the timing model can be evaluated by using a statistical estimator, typically the reduced chi-squared of the residuals, which should be unity for a model fully describing the data and is defined as:

$$\chi^2_{red} = \frac{1}{n_{free}} \sum_i^N \left(\frac{R_i}{\sigma_i}\right)^2, \tag{2.6}$$

where σ_i is the TOA uncertainty and n_{free} is the number of free parameters, equal to the sum of the number of data points and the number of fitted timing parameters. The sum is performed over the total number of TOAs. An iterative procedure is performed to converge to a solution by re-fitting the timing parameters to minimise the chi-squared. If the data are fully described by the timing model, the timing residuals will deviate randomly around the mean value within the measurement uncertainties, or equivalently, the residuals will have a white power-spectrum (see Fig. 2.3).

2.2 From Topocentric Arrival Times to Pulse Emission Time

Let us now discuss the components of the delay terms in Equation 2.3 in more detail. Each sub-section discusses one of the sub-equations separately, in order to follow the referencing of the TOAs to each reference frame. To do so, $\Delta_\odot$, Δ_{IS} and Δ_B will be expanded to the individual terms of which they are composed.

To facilitate the discussion, I introduce in Fig. 2.1 the general geometry of the pulsar timing problem. The diagram shows the geometric relations between the telescope coordinates (OBS), the Solar system barycentre (SSB), the binary's barycentre at reference and observing times (BB_0 and BB) and the pulsar position (P). The displacement vectors connecting these points are noted with boldface letters. The subscripts $\parallel$ and $\perp$ are used to denote the parallel and transverse components of the vectors with respect to the vector of the initial barycentric position of the BB, $\mathbf{R_0}$. The hat notation above vectors is used to denote unit vectors.

The topocentric position of the pulsar (i.e. position observed from the observatory) is defined by the vector $\mathbf{R}$. The vectors $\mathbf{R_0}$ and $\mathbf{R_{BB}}$ are the barycentric (i.e. with respect to the SSB) positions of the BB at reference and observing epoch, t_0 and t, and $\mathbf{r}$ is the observatory's barycentric position. The displacement of the BB due to the binary's motion in space in the time interval $t - t_0$, is described by $\mathbf{k}$ while the displacement of the pulsar due to the orbital motion is described by $\mathbf{b}$.

2.2.1 Forming the Barycentric TOAs

We expand the term $\Delta_\odot$ in Eq. (2.3) and derive a relation that describes the conversion of the TOA's reference system, from the observatory's coordinates to that of the SSB, as:

$$t_{bat} = t_{sat} - \Delta_\odot = t_{sat} + \Delta_{clk} - (\Delta_{\mathrm{R}\odot} + \Delta_{\mathrm{D}\odot} + \Delta_{\mathrm{E}\odot} + \Delta_{\mathrm{S}\odot} + \Delta_{\mathrm{px}} + \Delta_{\mathrm{Atm}}). \tag{2.7}$$

The first step in deriving the BATs, described with the term Δ_{clk}, is to perform the necessary clock corrections to the SATs, in order to counteract the inherit long-term instabilities of the observatory's local clock. The clock correction files (step (iii) in Fig. 2.1) are used for the first step in a series of corrections, which refer the SATs to GPS-based Coordinated Universal Time (UTC), then to the

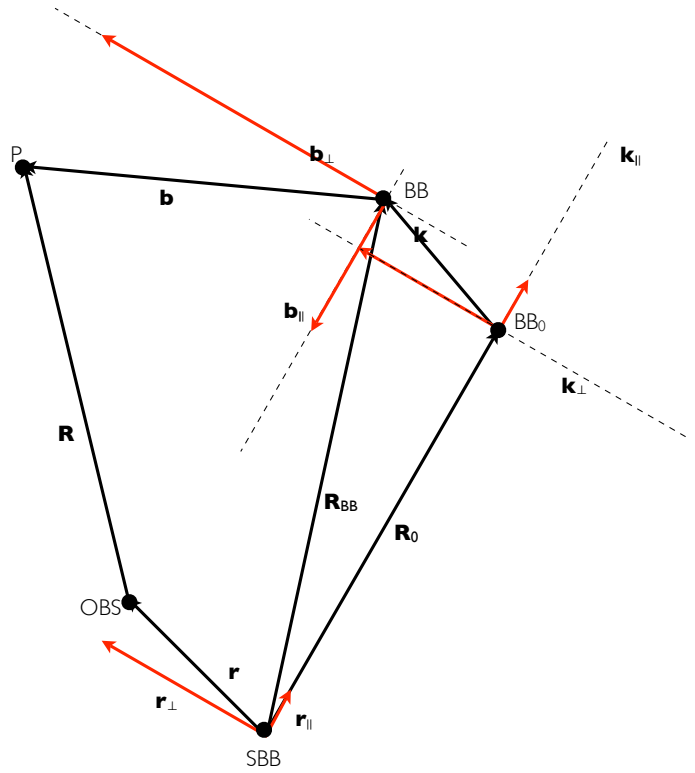

Figure 2.2: The displacement vectors used to construct the equations of the delay terms in pulsar timing. The vectors, noted with boldface letters, relate the positions of the telescope (OBS), the solar system barycentre (SSB), the initial and current position of the binary's barycentre (BB_0 and BB) and the current position of the pulsar (P). Parallel (subscript ||) and transverse (subscript $\perp$) components (red-coloured vectors) are with respect to the initial barycentric position (i.e. position observed from the SSB) of the binary (i.e. the vector $\mathbf{R_0}$). Dashed lines show the parallel and transverse directions at different points.

International Atomic Time (TAI) standard and finally to the most up-to-date Bureau International des Poids et Mesures (BIPM) time standard. Further details on clock corrections are discussed in §4.6.

The first delay term, $\Delta_{R\odot} = \mathbf{r} \cdot \hat{\mathbf{R}}_{BB}/c$, is the Solar system Roemer delay, which corrects for the geometric vacuum delay between the pulse's TOA at the observatory and at the SSB. The $\Delta_{D\odot}$ term calculates the signal dispersion while propagating through the ionised interplanetary medium, much like the case of dispersion of the signal by free electrons in the interstellar medium (§1.2.3). This is mainly caused by the electron content of the solar wind. From in situ measurements by the *Ulysses* mission, the solar system electron density is measured to have a radial profile as $n_{e,\odot} \propto n^{-2.003\pm0.015}$ (Issautier et al. 1998). Equation 1.3 is therefore modified to calculate the solar system DM as (Edwards et al. 2006):

$$DM_\odot = \int_{l=0}^{l=d_\infty} n_0 \, [1\mathrm{AU}/r(l)]^2 dl. \tag{2.8}$$

Here, $n_0 = 4\,\mathrm{cm}^{-3}$, is the electron density at $r = 1\mathrm{AU}$, and r is the heliocentric distance. The integral is

evaluated across the LOS (parameterised by l).

The Einstein delay term, $\Delta_{\mathrm{E}\odot}$, corrects the effects of the transformation of the reference frame, from that of the observatory to that of the SSB. The time dilation between the two reference frames is calculated as:

$$\Delta_{\mathrm{E}\odot} = \frac{1}{c^2}\int_{t=t_0}^{t}\left[U_\oplus + \frac{u_\oplus^2}{2} + \Delta L_{\mathrm{C}}^{(\mathrm{PN})} + \Delta L_{\mathrm{C}}^{(\mathrm{A})}\right]dt + \frac{\mathbf{s}\cdot\mathbf{v}_\oplus + W_0 t_{sat}}{c^2}. \tag{2.9}$$

The integral is the relativistic time dilation between the SSB and the Geocentre. The gravitational potential at the geocentre is $U_\oplus$, taking into account all Solar system bodies but the Earth. The rest of the integral's terms, $u_\oplus$, $\Delta L^{(\mathrm{PN})}$ and $\Delta L_{\mathrm{C}}^{(\mathrm{A})}$ are the Geocentre's velocity relative to the SSB, higher-order relativistic corrections and a mean correction for the effects of the asteroids, respectively. The second term on Equation's 2.9 right-hand-side, refers the time at the geocentre to the observatory's position, due to the time dilation and gravitational redshift between the Earth's centre and surface. The terms $\mathbf{s}$, $\mathbf{v}_\oplus$ and W_0 are the vector for the Geocentric position of the observatory, the barycentric velocity of the geocentre and the sum of the gravitational and spin potential at the geoid. For these calculations, it is necessary to know the positions of the Solar system bodies at any given time. This is achieved by using one of the Solar system ephemerides available. In pulsar timing software, the Einstein delay is calculated analytically (see Irwin & Fukushima 1999).

The Shapiro delay term, $\Delta_{\mathrm{S}\odot}$, describes the excess travel-time of the electromagnetic waves when propagating through the curved space-time in the vicinity of Solar system bodies. For this, an up-to-date Solar system ephemeris is required. The two main families of ephemerides updated regularly and used by the pulsar astronomy community are the DE and the INPOP, published by the Jet Propulsion Laboratory (e.g. Folkner et al. 2014) and the Paris Observatory (e.g. Fienga et al. 2012) respectively. The Shapiro delay corrections in the Solar system are dominated by first-order terms, since the self-gravity and velocities of planets is relatively small (see §5.1 for further discussion on the various gravity/velocity regimes). As derived by Backer & Hellings (1986), the Solar system Shapiro delay term is calculated as:

$$\Delta_{\mathrm{S}\odot} = -2\sum_i \frac{Gm_i}{c^3}\ln(\hat{\mathbf{R}}\cdot\mathbf{r_i} + r_i) + O^2\,, \tag{2.10}$$

where the index i denotes the different Solar system bodies, m is the body's mass, G is the gravitational constant and O^2 is a second-order relativistic correction, used only for rays passing from very near the Sun.

The parallax delay, Δ_{px}, describes the periodic variations of the SATs from the change of the Earth's position as a result of its orbital motion and will be discussed later in §2.3.2.

Finally, the term Δ_{Atm} describes the signal's delay from its propagation through the Earth's atmosphere, where the refractive index differs from that of the vacuum. The refractive index values in the atmosphere also changes between the ionosphere and the non-ionised troposphere. Correction methods are described, for example, in Davis et al. (1995). Atmospheric propagation delays can be influenced by the variable amount of water vapours and dispersion effects in the ionosphere, but these effects are small compared to the rest and are not necessarily corrected (Edwards et al. 2006).

2.2.2 Forming the TOAs at the Binary Barycentre

The relation between the BATs and the arrival times at the BB can be constructed by expanding the Δ_{IS} term of Eq. 2.3. We the get:

$$t_{bb} = t_{bat} - \Delta_{IS} = t_{bat} - (\Delta_{\mathrm{R}IS} + \Delta_{\mathrm{D}IS} + \Delta_{\overline{\mathrm{D}IS}} + \Delta_{\mathrm{E}IS}) \,. \tag{2.11}$$

The first term, is the interstellar Roemer delay. Just as in the case of the Solar system, it is the vacuum propagation delay, this time for the difference of the pulse's TOA between the SSB and the BB. The frequency-dependent delay from the dispersion by the IISM ($\Delta_{\mathrm{D}I}$), is based on the description of the DM dispersion law as defined by Equations 1.2 and 1.3. However, we are referring the TOAs to the BB from the SSB, so we need to convert the observing frequencies at the observatory (ν_1 and ν_2 in the dispersion equations) to the corresponding frequencies at the SSB, $\nu_1^{(SSB)}$ and $\nu_2^{(SSB)}$. This is required because of the effects of Doppler shift and gravitational red-shift on the signal. The conversion is (Edwards et al. 2006):

$$\nu^{(SSB)} = \left(1 + \frac{\mathrm{d}\Delta_{\mathrm{R}\odot}}{\mathrm{d}t} + \frac{\mathrm{d}\Delta_{\mathrm{E}\odot}}{\mathrm{d}t}\right)\nu \tag{2.12}$$

Frequency-dependent delays that do not follow the ν^{-2} law can in principle be modelled separately with the $\Delta_{\overline{\mathrm{D}IS}}$ term. Such terms could be, for example, delays from multi-path scattering as discussed in §1.2.3.2.

Finally, the latter term of the right-hand-side, is the interstellar Einstein delay which accounts for the special relativistic time-dilation due to the relative velocity of the SSB to the BB, according to the Lorentz transformation.

2.2.3 Forming the Pulse Emission Time

For pulsars in binary systems, the orbital motion induces additional delays that need to be considered. Most MSPs are in binary systems and their use as laboratories for testing gravity theories largely depends on calculating the orbital parameters. Time delays from binary parameters can become more prominent under certain orientations of the binary with respect to the observer, and/or when the system is highly relativistic, e.g. DNSs in close orbits. The relation between the TOAs at BB and the pulse emission time is expressed as:

$$t_{em} = t_{bb} - \Delta_B = t_{bb} - (\Delta_{\mathrm{R}B} + \Delta_{\mathrm{E}B} + \Delta_{\mathrm{S}B} + \Delta_{\mathrm{A}B}) \,. \tag{2.13}$$

Similarly to the terms of converting the time reference for the observatory to the SSB, this transformation also includes a Roemer delay ($\Delta_{\mathrm{R}B}$), an Einstein delay ($\Delta_{\mathrm{E}B}$) and a Shapiro delay term ($\Delta_{\mathrm{S}B}$). The Roemer delay accounts for the additional travel time of the signal due to the pulsar's displacement caused by the orbital motion. The Einstein delay here is related to the added effects of gravitational redshift due to the pulsar's gravitational potential and special relativistic time dilation. The Shapiro delay term accounts for the excess in the signal's travel time when it propagates through the gravitational

potential of the companion. Finally, Δ_{AB}, is a term which accounts for the aberration of the radio beam due to the pulsar's relative transverse velocity with respect to the observer. This correction is derived form the Lorentz transformation that relates the observer's and the pulsar's co-moving reference frames (Damour & Deruelle 1986). Expansion and discussion of these terms is made below in §2.3.3.

2.3 The Fitted Pulsar Timing Parameters

When fitting the timing model, the end goal is to use the timing data to measure the pulsar's astronomical parameters. In this section, I overview the rotational, astrometric and orbital parameters. Due to the strong gravitational potential of the pulsar, the delay of the signal propagation within the binary orbit requires higher order corrections compared to the interstellar and Solar system terms. For this reason, the binary parameters are discussed within the framework of the introduction to the PPK formalism, in §2.3.3

2.3.1 Rotational Parameters

As we have already discussed in §2.1.3, the time evolution of the pulsar's spin frequency can be described by a Taylor series of the rotational phase around a reference time. (Eq. 2.4). This relation includes the rotational frequency and its time derivatives with respect to the reference time. The most important, which are used in the timing model of any pulsar without exception, are the rotational frequency and the first derivative. As fitted parameters, they are a linear and a quadratic polynomial term respectively. Figure 2.3 shows the frequency derivative residual signature using simulated data.

2.3.2 Astrometric Parameters

Pulsar timing models contain 5 astrometric parameters, namely the sky co-ordinates, the proper motion parameters and the timing parallax. The celestial co-ordinates are first derived from the pulsar's discovery and subsequent timing of the pulsar will improve the precision of the localisation. Typically, timing models use the equatorial system co-ordinates, namely the right ascension, α, and declination, δ. For pulsars very close to the ecliptic, the ecliptic co-ordinates are used, namely the ecliptic longitude and latitude.

Pulsars have significant proper motion values, μ, with transverse velocities of order 10^2 km s^{-1} (e.g. Hobbs et al. 2005), mainly thought to be produced by the kick from the asymmetry of the progenitor supernova explosion (e.g. Lyne & Lorimer 1994). The proper motion is fitted in a timing model using two parameters, one for the change in each position co-ordinate. The last astrometric parameter is the timing parallax, i.e. the timing equivalent to the usual astronomical parallax. In astronomical imaging, parallax is calculated by measuring the difference in the angular separation between the object and a very distant object[2] at two opposite points of the Earth's orbit. In pulsar astronomy, the timing parallax is a measurement of the difference in the measured TOAs at different positions of the Earth's orbit, due to the curvature of the signal's waveform. It is apparent, that measuring the time parallax can be very challenging for the most distant pulsars. It has been shown that parallax measurements with certainties below 95% are significantly affected by the Lutz-Kelker bias (Verbiest et al. 2010). This bias refers to the systematic overestimation of parallax by failure to reflect the effect of the larger space volume

[2] typically extra-Galactic objects such as quasars; their large distance means they appear stationary despite the Earth's rotation

sampled at smaller parallaxes (Lutz & Kelker 1973). Application of the necessary correction (see e.g. Chapter 5) leads to a larger distance estimate than the measured value and asymmetric errors.

The astrometric parameters rise naturally from the calculations of the geometric, vacuum propagation delays. Using the notation from Fig. 2.1 and following the discussion in §2.2, the total geometric delay, $\Delta_{g,tot}$, is given by:

$$\Delta_{g,tot} = \Delta_{\mathrm{R}\odot} + \Delta_{\mathrm{px}} + \Delta_{\mathrm{R}IS} + \Delta_{\mathrm{R}B} \tag{2.14}$$

From Fig. 2.2, we see that the vector $\mathbf{R}$, defining the topocentric pulsar position, can be expressed as:

$$\mathbf{R} = \mathbf{R_0} - \mathbf{r} + \mathbf{k} + \mathbf{b}. \tag{2.15}$$

Here, $\mathbf{R_0}$ is the pulsar's topocentric position at reference epoch, t_0, and the vectors $\mathbf{r}$, $\mathbf{k}$ and $\mathbf{b}$ are the observatory's position with respect to the SSB, the displacement of the BB in time $t - t_0$ due to the binary's motion and the displacement of the pulsar position due to the orbital motion, respectively. The magnitude of $|\mathbf{R}| = R$ defines the geometric length. Following Edwards et al. (2006), it can be derived by performing a Taylor expansion of the square root of R^2 (i.e. $(\mathbf{R}\cdot\mathbf{R})^{1/2}$). Neglecting the terms of order R_0^{-3} and smaller, we get:

$$R = R_0 + b_{\parallel} + k_{\parallel} - r_{\parallel} + \frac{1}{R_0}\left(\frac{k_{\perp}^2}{2} - \mathbf{k}_{\perp}\cdot\mathbf{r}_{\perp} + \mathbf{k}_{\perp}\cdot\mathbf{b}_{\perp} + \frac{r_{\perp}^2}{2} - \mathbf{r}_{\perp}\cdot\mathbf{b}_{\perp} + \frac{b_{\perp}^2}{2}\right)\left(1 - \frac{k_{\parallel}}{R_0} + \frac{r_{\parallel}}{R_0} - \frac{b_{\parallel}}{R_0}\right) \tag{2.16}$$

The terms in the second parenthesis define higher order terms which induce variations to the terms in the first parenthesis due to the radial motion of the pulsar and the Earth's orbit. The term R_0 is not directly measurable and plays the role of a Doppler shift which can be absorbed in redefinitions of orbital parameters (see §2.3.3).

To focus on the astrometric parameters in this section, we neglect the orbital effects by setting $\mathbf{b} = 0$. The $r_{\parallel}$ term measures the contribution to the Roemer delay due to the orbital motion of Earth ($\Delta_{R\odot}$). The delay induced by $k_{\parallel}$, i.e. by the radial motion of the pulsar due to its velocity, is absorbed in the measurement of the spin frequency. Note that other radial motion contribution, such as that from the system's acceleration by the Galactic gravitational potential, can be included in $k_{\parallel}$ (see also §3.3.4). The term $\tilde{\mu} \equiv (1/R_0)\mathbf{k}_{\perp}\cdot\mathbf{r}_{\perp}$, corresponds to the change in the path due to the pulsar's proper motion. We can rewrite $\mathbf{k}_{\perp}$ in terms of the proper motion, μ, and the reference and observing epochs as $\mathbf{k}_{\perp} = (t - t_0)\boldsymbol{\mu}$. The $\varpi \equiv (1/R_0)r_{\perp}^2/2$ term, represents the change in R due to the Earth's orbit, therefore is the annual timing parallax. The other remaining term, $(1/R_0)k_{\perp}^2/2 \equiv \mathcal{S}$ is the Shklovskii effect (Shklovskii 1970), a quadratic apparent radial motion component, induced by the binary's transverse motion.

Due to the Earth's orbit, $r_{\perp}$ and $r_{\parallel}$ have annual, sinusoidal signatures. Therefore, errors in the pulsar position parameters will induce residuals with these characteristics (see Fig. 2.3). The time delay term from the proper motion shows that erroneous proper motion values, will induce annual, sinusoidal residuals (effect of $\mathbf{r}_{\perp}$) with the amplitude increasing linearly with time ($t - t_0$ factor; see Fig. 2.3)). The timing parallax signature is a squared sinusoid, with a period of half a year. Errors in the position or proper motion, induces additional variations in the other astrometric parameters. We can use the derived terms and introduced notation to describe the non-binary terms in Equation 2.14. The Solar system

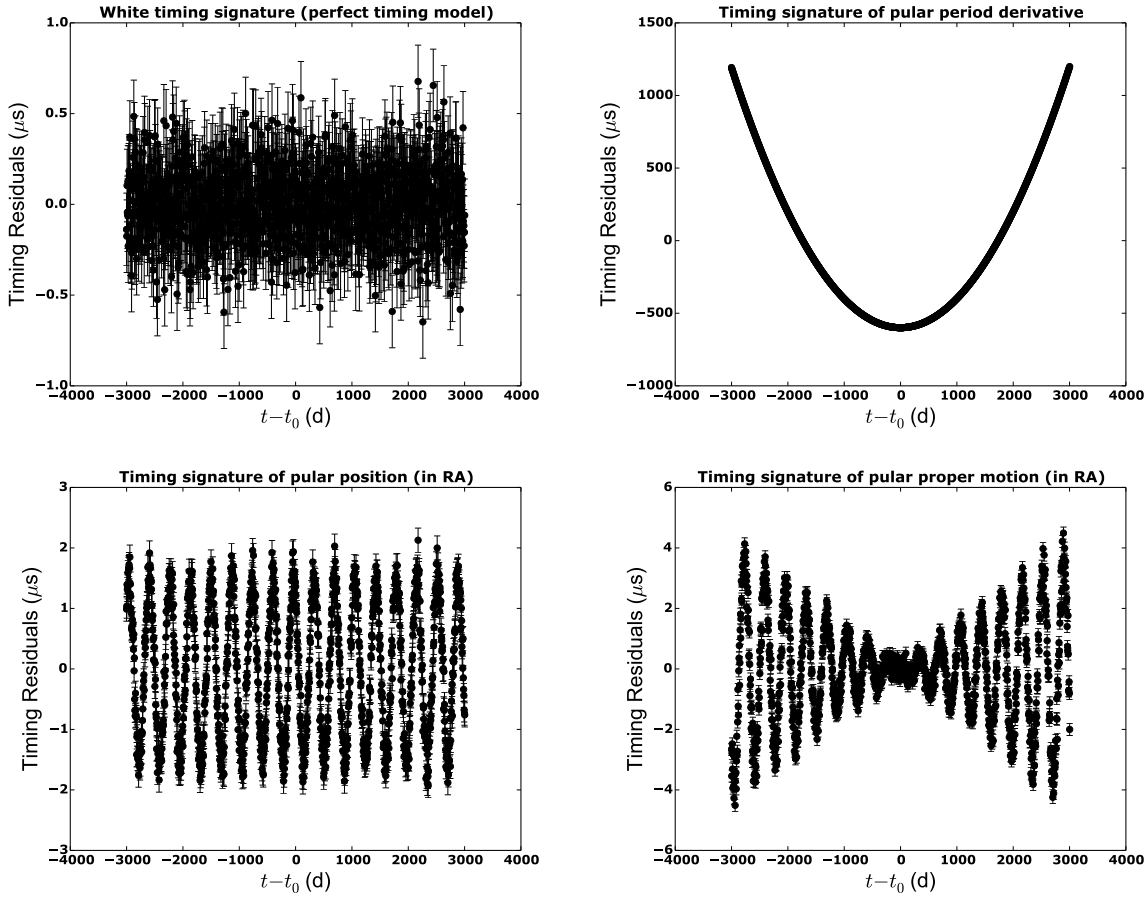

Figure 2.3: Timing residuals for simulated data based on the timing parameters of PSR J1012+5307. Residuals are centred around the reference epoch, t_0. See §2.3.2 for a discussion on these parameters. *Top Left Panel:* White residuals resulting from a timing model which fully describes the data. *Top Right Panel:* The timing signature of the pulsar's rotation period derivative. The residuals are induced by an incorrect value of the parameter in the model. *Bottom Left Panel:* The annual-sinusoid timing signature of the pulsar's right ascension *Bottom Right Panel:* The timing signature of proper motion, an annual sinusoid with an amplitude increasing linearly in time.

Roemer delay, parallax delay, and interstellar Roemer delay are then (Edwards et al. 2006):

$$\Delta_{R\odot} = (1/c)\Big(r_\parallel + \tilde{\mu} + \mathcal{S}\frac{r_\parallel}{R_0} + \tilde{\mu}\frac{k_\parallel}{R_0}\Big) \tag{2.17a}$$

$$\Delta_{\rm px} = (1/c)\varpi \equiv (1/c)\frac{r_\perp^2}{2d_p} \tag{2.17b}$$

$$\Delta_{{\rm R}IS} = (1/c)\Big(k_\parallel + \mathcal{S} - \mathcal{S}\frac{k_\parallel}{R_0}\Big)\,. \tag{2.17c}$$

Note that the parallax can be re-defined replacing R_0 with the parallax distance, d_p. This way, when fitting the timing model, the parallax effect can be separated from other effects with the $1/R_0$ dependency

and derive a value for the (conventional) astronomical parallax as $1\mathrm{AU}/d_p$. Further, note that from all the possible additional higher order terms from the second parenthesis in Equation 2.16, only the three appearing in these in Equations 2.17a and 2.17c. These are in fact the only higher order correction terms that are measurable for any present or planned pulsar timing observing system. The two last terms in Eq. 2.17a are the annual modulation of the Shklovskii effect from the Earth's orbital motion and the secular change of the pulsar's proper motion. The last term in Eq. 2.17c describes the secular change in the Shklovskii effect due to change in the radial distance to the pulsar (or BB).

2.3.3 Orbital Parameters: The Parametrised Post-Keplerian Formalism

As discussed in §2.1, the pulsar binary parameters are measured on the basis of the PPK parametrisation. In general, one describes the terms of Eq (2.13) as functions of a set of Keplerian parameters, and a set of post-Keplerian parameters that describe relativistic orbital effects. The latter divided into the two subcategories of parameters that can be measured independently and those which cannot (Damour & Taylor 1992).

The Keplerian parameters (see Figure 2.4) at reference time, t_0, are:
(i) the orbital period, P_b,
(ii) the time of periastron passage, T_0,
(iii) the eccentricity, e_0,
(iv) the longitude (or argument) of periastron, ω_0,
(v) the projected semi-major axis of the pulsar orbit, $x = (1/c)a_\mathrm{p}\sin(i)$ (see Fig. 2.5), where a_p is the semi-major axis of the pulsar orbit and i is the inclination angle, and
(vi) the longitude of the ascending node, Ω.
In principle, a and i cannot be measured separately. Ω is not always possible to be fitted. It becomes possible to do so in binary pulsars in wide orbits and small distances, where certain geometric delays due to the binary motion can be measured, as we explain below.

The second set of parameters, the post-Keplerian parameters for which we can achieve independent measurements are:
(i) k, a parameter that measures the secular precession and short-period nutation of ω,
(ii) the time dilation parameter, γ,
(iii) the secular change of the orbital period, $\dot{P}_\mathrm{b}$,
(iv) the 'range' of the Shapiro delay, r,
(v) the 'shape' of the Shapiro delay, s (which equals $\sin(i)$),
(vi) the dimensionless parameter, δ_θ, used to parametrise relativistic deformations of the orbit,
(vii) the secular change of the eccentricity, $\dot{e}$, and
(viii) the secular change of the projected semi-major axis, $\dot{x}$.

Additionally, post-Keplerian parameters that cannot be measured separately, are:
(i) The second dimensionless parameter for relativistic orbit deformations, δ_r,
(ii),(iii) The coefficients A and B that parametrise the delay from the rotating movement of the pulse beam
(iv) the Doppler factor due to the motion of the BB with respect to the SSB, D.

The PPK formalism connects the Keplerian and post-Keplerian parameters, and terms from Eq (2.13), namely the binary Roemer delay, Δ_BR, the aberration delay, $\Delta_{\mathrm{A}B}$, the binary Einstein delay, Δ_BE and the

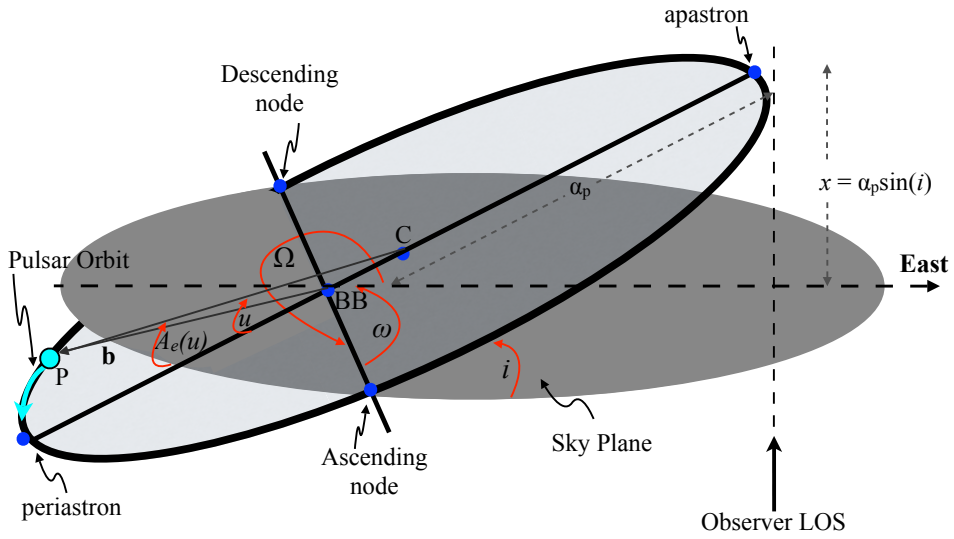

Figure 2.4: Diagram introducing the Keplerian parameters of pulsar's eccentric orbit. The orbit intersects the sky plane at the two orbital nodes, the ascending and descending nodes. The sky and orbital planes are separated by the inclination angle, i. The orbit's centre is denoted as C and the binary barycentre as BB. The vector **B** defines the position of the pulsar, P, with respect to BB. Marked in the diagram are the orbit's longitude of periastron ω, semi-major axis, a_p and it's projection to the line of sight, x, and the longitude of the ascending node, Ω, as well as the eccentric and true anomaly of the orbit, u and $A_e(u)$.

binary Shapiro delay, Δ_{BS}. Following Damour & Taylor (1992), the basic equations are:

$$\Delta_{RB} = x\sin(\omega)[\cos(u) - e(1+\delta_r)] + x[1 - e^2(1+\delta_\theta)^2]^{1/2}\cos(\omega)\sin(u) \tag{2.18a}$$
$$\Delta_{EB} = \gamma\sin(u) \tag{2.18b}$$
$$\Delta_{SB} = -2r\ln\{1 - e\cos(u) - s[\sin(\omega)(\cos(u) - e) + (1-e^2)^{1/2}\cos(\omega)\sin(u)]\} \tag{2.18c}$$
$$\Delta_{AB} = A\{\sin(\omega + A_e(u)) + e\sin(\omega)\} + B\{\cos(\omega + A_e(u)) + e\cos(\omega)\}\,. \tag{2.18d}$$

In these equations, the semi-major axis and eccentricity at a time epoch, t, are given by:

$$x = x_0 + \dot{x}(T - T_0) \tag{2.19a}$$
$$e = e_0 + \dot{e}(T - T_0)\,, \tag{2.19b}$$

where T denotes the pulsar proper time and T_0 the proper time of periastron passage. The term, u, is the

orbit's eccentric anomaly, derived directly from Kepler's equation expressed in terms of observables, as:

$$u - e\sin(u) = 2\pi\left[\frac{T - T_0}{P_\mathrm{b}} - \frac{1}{2}\dot{P}_\mathrm{b}\left(\frac{T - T_0}{P_\mathrm{b}}\right)^2\right], \tag{2.20}$$

where the right-hand-side term is the orbit's mean anomaly. The true anomaly, $A_e(u)$ and argument of periastron at any given time, ω are then defined as functions of u as:

$$A_e(u) = 2\arctan\left[\left(\frac{1+e}{1-e}\right)^{1/2}\tan\frac{u}{2}\right], \tag{2.21}$$

$$\omega = \omega_0 + kA_e(u)\ . \tag{2.22}$$

Since the radial motion of the BB cannot be measured independently from the rotational frequency, measured time epochs are in principle retarded from the real epoch by a Doppler factor $D = R_0/c$. As discussed in Damour & Taylor (1992), this means that D can be absorbed in the measurements of binary parameters, by renormalisation of the units of time, mass and length by a factor D. The outcome, is the relations connecting the observed Keplerian and post-Keplerian parameter values (superscript 'obs') to the intrinsic ones (superscript 'int') as a function of D, for example, $P_\mathrm{b}^\mathrm{obs} = (1/D)P_\mathrm{b}^\mathrm{int}$. Additionally, the aberration parameters, A and B, are not separately measurable since they can be absorbed via appropriate redefinitions of the Keplerian parameters.

Secular and periodic variation terms in the orbital parameters are induced by the change in the viewing angle from which we observe the binary. They can be derived using the vacuum propagation delays due to the orbital motion. We therefore revisit Equation (2.16) and keep only the binary terms and follow the same reasoning that led to Eq. (2.17) to derive a geometric equation for the binary Roemer delay, which includes these higher order term as:

$$\Delta'_{\mathrm{R}B} = (1/c)\Big(b_\parallel + (\tilde{\mu}_b - \varpi_{yr.b} + \varpi_b)\Big) \equiv (1/c)\Big(b_\parallel + (\tilde{\mu}_b - \frac{\mathbf{r}_\perp\cdot\mathbf{b}_\perp}{2d_{yr.b}} + \frac{b^2}{2d_b})\Big)\ . \tag{2.23}$$

Additional to the delay due to the radial component of the pulsar's displacement from the orbital motion, $b_\parallel/c$, which is described by to Eq. 2.18a, three higher order terms appear which may be in some cases measurable. The term $\tilde{\mu}_b \equiv (1/R_0)\mathbf{k}_\perp\cdot\mathbf{b}_\perp$ is equivalent to $\tilde{\mu}$ and describes the delay by change of the apparent viewing geometry to the binary induced by the its proper motion (Arzoumanian et al. 1996; Kopeikin 1996).

The orbital motion additionally induces two parallax terms, namely the orbital parallax, $\varpi_b \equiv (1/R_0)b_\perp^2/2$, and the annual-orbital parallax, $\varpi_{yr.b} \equiv (1/R_0)\mathbf{r}_\perp\cdot\mathbf{b}_\perp$ (Kopeikin 1995). The orbital parallax describes the delay induced by the change of the LOS due to the binary's transverse motion. This effect has not yet been measured to-date.

The annual-orbital parallax results from the change in the viewing angle by which we observe the

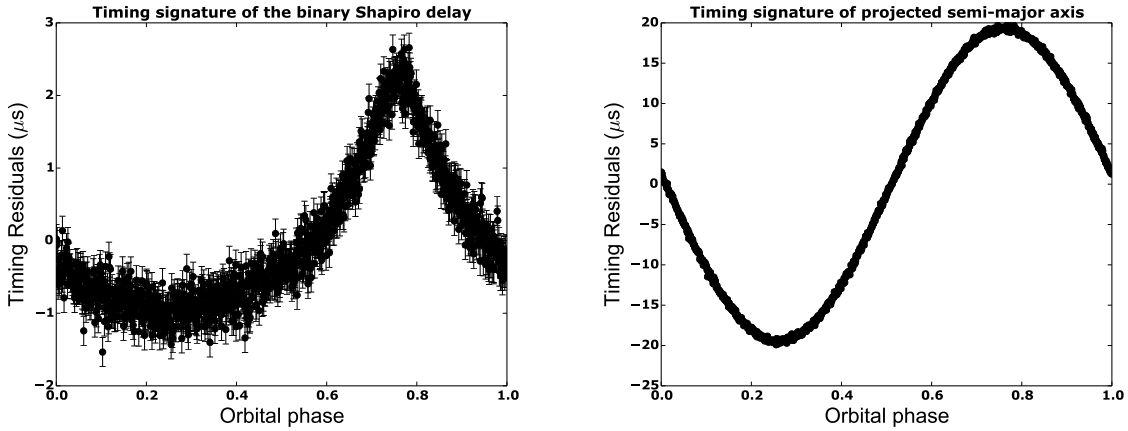

Figure 2.5: Timing residuals against the orbital period for simulated data based on the timing parameters of PSR J1713+0747. See §2.3.3 for a discussion on these parameters. *Left Panel:* The timing residual of the Shapiro delay, resulting from an erroneous value of the companion's mass in the timing model. The maximum value of the induced residuals corresponds to part of the orbit where the pulsar is behind the companion with respect to the observer. *Right Panel:* The timing signature of the pulsar's projected semi-major axis is a sin wave with amplitude equal to the semi-major of the pulsar orbit axis (divided by the speed of light).

binary's orbital motion due the Earth's orbit. It induces an annual periodic modulation to the signal of the binary Roemer delay. The three latter terms described, are often referred to as the "Kopeikin terms".

The annual-orbital parallax and delay from the binary's proper motion have measurable variations, periodic and secular respectively, on the projected semi-major axis and longitude of periastron, first measured by (van Straten et al. 2001). Measurements of these variations allow the derivation of the longitude of the ascending node, Ω, if an independent measurement of inclination angle exists, for example from Shapiro delay measurement (e.g. van Straten et al. 2001, see also §3.3.6).

Just as in the case of the annual parallax, we have redefined the annual-orbital and orbital parallaxes in Eq. 2.23 replacing the $1/R_0$ term with corresponding distance terms. The measurement of these parallaxes can in principle give independent measurements of the pulsar's distance.

2.3.3.1 Near-circular Orbits

The evolution of pulsar-WD binaries leads often to the circularisation of the orbit (see e.g Tauris 2011). When the eccentricity is very small, the use of (2.18a) leads to strong correlations between T_0 and and ω, because the effect of T_0 is small (Lange et al. 2001). An alternative parametrisation can be applied then for pulsars with near-circular orbits, by neglecting orbital terms of order e^2 and above, (Lange et al. 2001, Appendix A). In this parametrisation, commonly referred to as the 'ELL1' model, the five first post-Keplerian parameters are replaced by the time of ascending node, T_{asc} and the first and second

Laplace-Lagrange parameters, η and κ. By defining $n_b \equiv 2\pi/P_{\rm b}$, these parameters are calculated as:

$$T_{asc} = T_0 - \omega/n_b \tag{2.24a}$$
$$\eta = e\ \sin(\omega) \tag{2.24b}$$
$$\kappa = e\ \cos(\omega)\ . \tag{2.24c}$$

The binary Roemer delay is then approximately described by the following equation:

$$\Delta_{RB} \approx x(\sin(\Phi) + \kappa/2\ \sin(2\Phi) - \eta/2\ \cos(2\Phi))\ , \tag{2.25}$$

where $\Phi = n_b(T - T_{asc})$. As explained in Lange et al. (2001), these calculations take into account first-order eccentricity corrections only, as they are sufficient for most low-eccentricity binary pulsars, given the TOA uncertainties.

Based on the characteristics of nearly-circular pulsar binaries, Freire & Wex (2010) developed the "orthometric parametrisation" of the Shapiro delay, which uses a sum of harmonics of the binary's orbital period. For low inclination angles, one uses two new post-Keplerian parameters, h_3 and h_4, proportional to the third and fourth harmonics respectively, while for high inclinations angles, one uses h_3 and ς, the latter being the ratio of the amplitude of successive harmonics. The orbital-period harmonics are orthogonal functions, therefore h_3 and h_4 are uncorrelated, unlike the strongly correlated range and shape of the Shapiro delay, allowing easier and more robust Shapiro delay detections. We will return to the use of the formalism for low-eccentricity binary pulsars in Chapter 3 and again in Chapter 5, where we make use of this parametrisation for studying the low-eccentricity system PSR J1012+5307.

2.4 Beyond Least-Squares Fitting: Noise and non-Linearities in Pulsar-Timing Data

As noted in §2.1.3, the least-squares fitting of the timing parameters makes the explicit assumption that the TOAs are fully described by the timing model. This in turn has a number of underlying assumptions:

(1) We are assuming that our pre-fit parameter values are close to the true ones, since timing software typically use the linearised approximation to the effects of the residuals deviations on the timing model (e.g. Damour & Deruelle 1986; Hobbs et al. 2006).
(2) We do not consider strong non-linearities or covariances between timing parameters.
(3) It is assumed that the uncertainties of TOAs produced via template matching are solely due to white radiometer noise.
(4) It is also explicitly assumed that the TOAs are uncorrelated.

The above constitute good approximations and serve well into forming an initial, phase-connected timing solution. However, in high-precision timing, when average TOA uncertainties are at and below the μs level and when the data sets become sufficiently long, these solutions are not adequate, since subtle effects that are otherwise below noise levels, now become significant.

The first assumption is largely satisfied, since timing solutions are typically constructed iteratively, starting with a minimum of parameters, progressively adding more parameters if supported by the data,

and refining the model with additional data, thus always maintaining a phased-coherent solution.

For non-linear and highly-covariant parameters, methods have been developed to estimate their values and uncertainties using e.g. chi-squared mapping (see e.g. application in Lazarus et al. 2014) or Markov-Chain Monte-Carlo (MCMC) sampling (e.g. Lentati et al. 2015).

The third assumption can be broken down by a number of reasons. The basic calculations of TOA uncertainty estimation in the template-matching technique is described in Taylor (1992). In the low S/N regime this algorithm can underestimate the uncertainties, and more precise techniques have been developed, e.g. using MCMC, that produce more robust results. Other factors, however, such as the presence of un-excised radio frequency interference (RFI) can modify the pulse statistics and lead to incorrect uncertainty estimations. Additionally, there are cases where the pulsar is very bright (with respect to a given observing system), so that a high-S/N pulse is formed with short integration times and a small number of ($\lesssim$100) single pulses form the integrated profile. This can lead to the situation where the pulse profiles used for timing are dominated by single-pulse variability causing additional scattering of the timing residuals (see §4.3.1).

The fourth assumption is also known not to be generally valid. Correlated noise is known to exist in pulsar-timing data as a result of various effects, either intrinsic to the pulsar or extrinsic. One of the basic sources of correlated noise, is the temporal variations of the DM in the pulsar's LOS. Although the timing model allows for DM derivatives to be fitted, the variations can have periodic or stochastic components that need to mitigated separately (e.g. Keith et al. 2013; Lee et al. 2014). At the same time, possible rotational instabilities of the pulsar, analysis systematics and instrumental instabilities can add stochastic, time-correlated noise. As such, the noise analysis has become an integral part of high-precision pulsar timing. We will return to this in Chapter 4, where I will present the noise analysis of 42 MSPs.

CHAPTER 3

High-precision Pulsar Timing with the Effelsberg-Berkeley Pulsar Processor & the European Pulsar Timing Array

"World clocks tick and space gleams, everything changes place and order"

Harry Martinson

This chapter describes work that was previously published in
*Desvignes G., **Caballero R. N.**, Lentati L., Verbiest J. P. W., Champion D . J., Stappers B. W., Janssen G. H. et al. 2016, MNRAS, in press.*
In particular, my contribution to this publication was the reduction and timing analysis of the Effelsberg data as described in §3.2, the participation in the creation of the multi-telescope EPTA Data Release 1.0 described in §3.3.1 and the participation in the timing analysis of this data set described in §3.3.2, the results of which are presented in §3.3.3-§3.3.6.

In the previous chapter, I gave an overview of the pulsar timing technique, focusing mainly on the details of the timing model. In this chapter, I first give a description of pulsar timing instrumentation, followed by a description of the Effelsberg-Berkeley Pulsar Processor (EBPP) in particular. I will then elaborate on the reduction and analysis of EBPP data for 20 MSPs, which were recorded in the period 1996-2013 with the Effelsberg radio telescope, a fully-steerable, altazimuth, parabolic single-dish radio telescope, with a 100-meter diameter . After presenting the data products from this analysis, I will present the work done within the framework of the EPTA collaboration to combine the data from 18 of these pulsars with data from another three European telescopes to create the EPTA Data Release 1.0 (EPTA DR 1.0). This multi-telescope, multi-frequency data set, consisting of data on a total of 42 MSPs, was created primarily to be used for the EPTA's efforts for GW detection. I will conclude this chapter by presenting the EPTA results on the astrometric and astrophysical studies of the MSPs. The EPTA DR 1.0 data set, analysis methods and results, along with a detailed comparison of the results with those reported in the literature by independent work on a pulsar-by-pulsar basis, are fully described in Desvignes et al. (2016).

3.1 Pulsar-Timing Observing Systems

As discussed in Chapter 1, pulsars are faint radio sources, their emission is broadband and is affected by interstellar (and interplanetary) dispersion. Also, the pulsar timing application requires the TOAs to be measured at high precision. As such, pulsar timing is preferably undertaken on telescopes with large collecting areas, broadband receivers and high time and frequency resolution observing systems. In this section, I give a short overview of the standard observing setup for pulsar timing. Most of the data used for this thesis are form single-dish observing systems, and so the discussion is limited to these. This section summarises more detailed presentation of radio astronomical instrumentation, as found, for example, in Lorimer & Kramer (2005) and Rohlfs & Wilson (2004).

3.1.1 The Basic Signal Path

For pulsar observations, large collecting areas are preferred, so typically 100-m class radio telescopes are employed. The incoming radio waves are focused to a receiver, sometimes also called the frontend, where a waveguide leads the incoming radio waves to the polarisation feeds. Each of these feeds is sensitive to a polarisation sense orthogonal to the other one. Depending on the receiver, either linear or circular polarisation feeds are used. Modern receivers are cryogenically cooled to reduce the thermal noise.

The faint incoming radio signal at each feed needs to be amplified. Large amplifications are usually achieved by amplifier cascading, i.e. the sequential amplification of a signal passed through a series of amplifiers. To avoid instabilities that can occur, e.g. by power leakage from an amplifier's output, the amplified signal's frequency is converted by the use of a mixer. This unit has a local oscillator that produces a monochromatic signal which is mixed with the amplified signal to shift the incoming signal to a different frequency, a process known as *heterodyning'*. The common practice is to down-convert the data to the so-called *Intermediate Frequency'*, since at this lower frequency the signal is both easier to transmit and to be processed by the backends. As we have seen in §2.1.2, two of the main functions of the pulsar backends are de-dispersing and folding the pulses. We have explained that folding is performed with the help of a pulsar ephemeris that predicts the phase of each recorded pulse. In what follows, we briefly outline the process of de-dispersion, incoherent and coherent.

3.1.2 Incoherent De-dispersion

De-dispersion is performed on the basis of the dispersion law (Eq. 1.2), which states that the delay between the arrival time of the signal at two observing frequencies is proportional to the DM and the difference of the inverse squares of these frequencies. A straightforward way therefore to de-disperse the signal is to divide the signal into a number of channels of certain bandwidth with the use of a spectrometer. A widely used type of spectrometer in pulsar astronomy is the filterbank, an array of bandpass filters with frequency responses in a sub-band of the incoming signal. The backend applies the appropriate time delay to each sub-band and aligns them. Within each sub-band, however, the pulse smearing cannot be corrected. Therefore, the precision of the de-dispersion in this scheme is highly dependent on the bandwidth of each filterbank channel; the smaller the bandwidth of each sub-band, the more accurate the de-dispersion. In any case, the dispersive delay across each sub-band should be significantly smaller than the pulse period to avoid phase wraps. Filterbanks are either analogue or digital and de-dispersion can be performed either in hardware of software. This process is called

incoherent de-dispersion, because it does not account for the effects of dispersion on the phase of the incoming signal voltages.

3.1.3 Coherent De-dispersion

"Coherent de-dispersion" (Hankins & Rickett 1975) is a method that fully removes the effects of signal dispersion by making use of the phase of the incoming voltages from the observed signal and the known DM of the pulsar to recover the intrinsic (complex) voltages of the signal (i.e. the voltages that would be induced if the signal was not dispersed). The application of coherent de-dispersion results in sharp pulse profiles and consequently, increased timing precision. This method takes advantage of the fact that dispersion affects only the phases of the voltages. Therefore, in frequency domain the effect can be described by a transfer function, H, acting on the Fourier transform of the intrinsic voltages, $V_{\rm int}$, and resulting in the Fourier transform of the observed voltages $V_{\rm obs}$. For a band-limited signal at centre frequency $\nu_{\rm c}$, the effect of dispersion at frequency ν is:

$$V_{\rm obs}(\nu_c + \nu) = HV_{\rm int}(\nu_c + \nu) = \mathrm{e}^{\mathrm{i}\nu^2 \mathrm{DM}(2\pi K)/[(\nu+\nu_{\rm c})\nu_{\rm c}^2]}\, V_{\rm int}(\nu_{\rm c} + \nu), \tag{3.1}$$

where K is the dispersion constant. Based on the above formulation, it is easy to see that knowledge of the pulsar's DM allows determination of H, the inverse of which we apply to $V_{\rm obs}$ to retrieve $V_{\rm int}$ and completely de-disperse the signal.

In order to apply this technique, the observed signal has to be transformed to *complex-sampled data*. Complex sampling is a process during which one samples two related wave signals, say e.g. two identical signals with a phase difference. Through this process, one can sample the real and imaginary part of a time-domain voltage, which is mathematically expressed as:

$$v(t) = a(t)\mathrm{e}^{\mathrm{i}\phi(t)}\mathrm{e}^{\mathrm{i}2\pi\nu_c t}\ , \tag{3.2}$$

where $a(t)$ and $\phi(t)$ are the time-variable amplitude and phase. To achieve this, before being sent to the filterbanks, the signal undergoes a second mixing with the signal of another local oscillator. In particular, the signal is split in two, both mixed with the signal of the same local oscillator but with a $\pi/2$ phase shift, effectively one signal is multiplied with the cosine and the other with the sine branch of the local oscillator. The local oscillator frequency is chosen to be equal to the sub-band central frequency, $\nu_{\rm c}$. Therefore, frequencies below $-\Delta\nu/2$, where $\Delta\nu$ is the sub-band's bandwidth, are removed with the use of a low-pass filter. This is called *baseband sampling* because it shifts the bandpass to the range $[-\Delta\nu/2;+\Delta\nu/2]$, which is called the *baseband*. The resulting signals are cosines of $\phi(t)$ and sines of $-\phi(t)$ with amplitudes equal to $(1/2)a(t)$, which are the real part of the of the complex signal $v(t)$ in Eq. 3.2, and which give the full information on the amplitude and the phase of the complex voltage. These signals can now be used for coherent de-dispersion, i.e. H^{-1} can be applied on their Fourier transforms.

Coherent de-dispersion requires more computational resources than incoherent de-dispersion. The performance of a coherent de-dispersion system will be limited by the speed at which it can perform Fourier transforms and calculate $H^{-1}V_{\rm obs}$. While older systems were for this reason limited in the bandwidth they could process in real time, the advent of fast and inexpensive processing units such as

commercial graphics processing units (GPUs) has changed this. Modern pulsar backends can efficiently coherently de-disperse wide-band data with bandwidths of many hundreds of MHz in real time.

3.2 High-precision Timing of 20 MSPs with the EBPP

Much of the work described in this thesis relies on data recorded with the EBPP at Effelsberg. The EBPP (Backer et al. 1997) is a digital filterbank, online coherent de-dispersion backend. The signals from the two circular polarisation feeds of the receivers used at Effelsberg are down-converted to an intermediate frequency of 150 MHz. The backend converts this to an internal intermediate frequency of 440MHz. For each polarisation channel, the signal is then split into four parts and is mixed to baseband before being divided into the 32 channels (initially the system divided it into a maximum of 16 channels, but was later upgraded). The signal from each channel ends at the de-disperser boards, where real-time coherent de-dispersion is performed. The EBPP can process up to 112 MHz, depending on the pulsar's DM. The higher the DM, the more computational power is needed to perform the de-dispersion and less bandwidth can be processed. For the pulsars with the highest DM values, the bandwidth is limited to 44 MHz. Once de-dispersion is complete, the output signals are folded using the topocentric pulse period, which is calculated using a pulsar ephemeris, as described in §2.1.2. The backend can automatically adjust the power levels of the two polarisations prior to each observation using total-power detectors and computer controlled attenuators. At Effelsberg, the EBPP time-stamps the observations using an on-site H-maser clock. Each time the backend is started up, the user has to manually synchronise the backend with the clock. Synchronisation is at the nearest integer second to the user's input. It can therefore be the case, that some observations, upon imperfect synchronisation, have time-stamps that are offset by an integer number of seconds from the local atomic clock.

With continuous monitoring of pulsars since October 1996, the EBPP has the longest uniform set of coherently de-dispersed pulsar-timing data. Among the sources observed at Effelsberg with the EBPP are 18 MSPs that are part of the EPTA target list. Another two MSPs were analysed for separate, ongoing projects. In particular, these pulsars are PSR J1518+4904, a member of a DNS and PSR B1620-26, a member of a hierarchical triple system with a WD in the inner orbit and a Jupiter-mass planet in the outer orbit. Data from some of these MSPs were previously analysed and used for various applications (e.g. Lazaridis et al. 2009; van Haasteren et al. 2011). With this work, my aim was to develop a timing data set for all EPTA MSPs which is consistent among all pulsars in terms of reduction and analysis methods. This aspect is particularly important when using all pulsars simultaneously to search for spatially correlated signals across pulsars, for example when searching for GW signals. Consistency in the analysis methods becomes even more important when the data are combined with those from other telescopes (which was the end goal for these EBPP data), since the data set becomes inhomogeneous by default and minimising any inconsistency at least in data of each observing system increases the robustness of the results. (see §3.3.1). In order to provide a data set that could be reproduced by members of the pulsar community, I opted to make use of established general-use, state-of-the-art reduction and analysis software. To this end, I employed the `PSRCHIVE`[1] (Hotan et al. 2004b) and `Tempo2`[2] (Hobbs et al. 2006) software packages.

[1] Information on `PSRCHIVE` and analysis routines can be found at `http://psrchive.sourceforge.net/manuals/`
[2] `http://www.atnf.csiro.au/research/pulsar/tempo2/`

3.2.1 EBPP Data Reduction and Analysis

In the work described in this chapter, data with central frequencies at two bands were used. These are the L band, which covers frequencies in between 1-2 GHz, and the S band, with a frequency range 2-3 GHz. The L-band data are divided in two sub-sets, one with central frequency at 1410 MHz and another at 1360 MHz, due to a receiver change in 2009. The S-band data have a central frequency at 2639 MHz. As is commonly done, I followed an iterative approach in the data reduction and analysis, something which is quite common in pulsar timing. The following step-by-step discussion clarifies the reasons for this.

The first step is to perform RFI excision by zero-weighting parts of the data where the RFI signal is above the observation's noise levels, thereby modifying the statistics of the data and/or the shape of the pulse. In principle, RFI excision is possible both across the observing frequency and time. Therefore, persistent narrow-band RFI is better excised by zero-weighting the relevant frequency channels. On the other hand, a burst, but broadband RFI would be optimally excised by zero-weighting the affected sub-integrations. Compared to modern data, the EBPP data have long sub-integrations and most excision was performed across frequency. If a broadband RFI burst hit the receiver during any sub-integration, which are at least two minutes long, that sub-integration was not used. Modern observing systems are more robust against short-duration RFI, by damping sub-integration files on timescales of seconds.

At first, the excision is performed on individual sub-integrations. Automatic excision routines were first used. In particular, I used the `PSRCHIVE/paz` routine and more specifically the *Median Smoothed Difference Channel Zapping*. This routine zero-weights frequency channels that are above a specific tolerance level, which is determined in relation to a median-smoothed version of the bandpass. To create this smoothed version, the algorithm replaces each bin's intensity value with the median of its N surrounding neighbours. For the EBPP data, a 1-dimensional filter across frequency bins was used for various N values, depending on the total bandwidth of each pulsar's data. I have used a 5σ tolerance, i.e. any bin with intensity value more than five times the smoothed data's standard deviation is considered contaminated by an RFI spike and is zero-weighted.

The next stage was to combine sub-integrations to create average profiles with increased S/N. As explained in §2.1.2, the profiles must be properly phase-aligned. To improve the alignment, the timing parameters of the observed profiles were updated with those from a recent pulsar ephemeris using the `PSRCHIVE/pam` routine. We then combine sub-integrations using the `PSRCHIVE/psradd` routine, which uses the timing ephemeris of the data to predict the pulse phases, aligns the sub-integrations and then adds them. According to Equation 2.1, adding sub-integrations leads to a S/N increase that scales with the square root of the integration time (given the rest of the observational properties are the same among sub-integrations). Sub-integrations were added under the restriction that their start times were within one hour. This was to ensure that added observations were as uniform as possible in terms of the observing hardware settings, since at Effelsberg, each pulsar was typically observed for about 30 minutes during an observing run. After creating the ~30-minute-long profiles, the RFI excision process was repeated, since the increased S/N allows identification of faint RFI. At this stage, I also inspected the profiles manually and removed any RFI missed by the automatic routine, using the `PSRCHIVE/pazi` routine.

The next stage was to create an analytic profile for each of the three central observing frequencies. Even for the small difference between 1410 and 1360 MHz, for some pulsars there were measurable differences in the profiles. These are manifested as step offsets between the residuals from the two observing systems, when extracted with a single template. The analytic profiles were constructed using

the PSRCHIVE/paas routine, which uses combinations of von Mises functions to perform a least-squares fit to the observed profile. The fit was performed on a high-S/N profile, made by adding up to 10 high-S/N profiles, depending on the pulsar's brightness. To ensure that possible significant temporal variations of the pulse profile were not affecting the timing analysis, when possible, I created about three templates based on observations from different epochs, and verified that they produced statistically consistent TOAs.

The SATs were derived via Fourier-domain cross-correlation of the profiles with the template using the PSRCHIVE/pat routine. For most pulsars, the standard *Fourier phase gradient* method described in Taylor (1992) was used. For some pulsars where the profile's S/N is consistently low, e.g. PSR J0218+4232, the *Fourier-domain Markov-Chain Monte-Carlo TOA estimator* method was used instead. This routine employs MCMC methods to properly estimate the uncertainties which are underestimated by the standard method when working in the low-S/N regime (see also Verbiest et al. 2016, for a discussion on best timing practices). All TOAs were derived using time- and frequency-integrated, total-intensity (both polarisations added) profiles, in order to increase the S/N. The processes of integrating the profiles in time and frequency are referred to as time and frequency scrunching.

Once the SATs are formed, they are used to perform the timing analysis with Tempo2. Due to the exceptional rotational stability of MSPs compared to canonical pulsars, even a pulsar ephemeris that was produced many years before the present observations is usually sufficient to produce phase-connected residuals. This allowed the outlying points to be quickly identified for further inspection. In many cases, this led to finding further RFI or observations which were tagged with the wrong observing frequency or simply corrupted observations. More importantly, it also allowed to find outlying points due to integer-seconds offsets of the observatory's atomic clock. Once these issues were resolved, Tempo2 would converge after only a couple of iterations to an updated timing solution.

As we can see from the radiometer equation (Eq. 2.1), sharp profile features improve the precision of the TOA measurement. Improved measurements of timing parameters can lead to better alignment of added profiles, reducing in this way the pulse broadening from inaccuracies in the alignment, and finally leading to improved TOA precision. For this reason, I used the updated timing ephemeris to renew information in the profiles (using the pam routine) and repeated the process until the TOA precision would not further improve. For well-timed MSPs, typically, one to two iterations prooved sufficient.

3.2.2 EBPP Data Products

The final product of the EBPP data analysis consists of 4169 TOAs from 20 pulsars at two frequency bands. For each pulsar, three analytic profiles were created, one for each central frequency. The long data span is a key feature for GW searches, which was the central purpose for this work. Since pulsar timing data are used to search for nHz GWs, it is important to have long data spans so that low-frequency GW signals can be efficiently separated from the low-frequency signatures of the pulsar's rotational frequency and frequency derivative, and from the pulsar's intrinsic low-frequency noise. This is discussed in detail in Chapter 4. Furthermore, long time-span, high-precision data are essential for the measurement of long-term post-Keplerian timing parameters, such as secular changes of the orbital period or of the projected semi-major axis, which are especially important for certain tests of gravity theories (see e.g., §5.3). Finally, the S-band EBPP observations offer a large frequency range in combination with low frequency (< 600 MHz) EPTA data for better DM measurements and corrections of the noise induced by their temporal variations.

3.3 High-Precision Timing of 42 MSPs with the EPTA

In the framework of a co-ordinated effort within the EPTA to create a combined, multi-telescope data set, the EBPP data set was combined with pre-2015 data from the other three EPTA telescopes. Each telescope data were reduced and analysed by EPTA members, following the same idea of creating data sets that are homogeneous in terms of analysis methods. The end result is the EPTA DR 1.0, composed of data from 42 MSPs. Apart from the Effelsberg radio telescope, data were provided from the Nançay Radio Telescope (NRT) in France, the Lovell Telescope of the Jodrell Bank Observatory in the UK and the Westerbork Radio Synthesis Telescope (WSRT) in the Netherlands. The respective backends used at these telescopes are the Berkeley-Orléans-Nançay (BON), the Pulsar Machine I (PuMaI) and the Digital Filterbank (DFB) respectively. Below, we first briefly describe these instruments and the reduction techniques used, followed by a description of the methodology used to perform the timing analysis of this complex data set. Finally the chapter reviews the astrometric and astrophysical results of the analysis. The combined data set and timing-analysis results are fully presented in Desvignes et al. (2016). This data set was primarily designed for nHz GW searches within the EPTA collaboration. The data set was used to characterise the noise properties of these MSPs (Caballero et al. 2016, see Chapter 4), to place upper limits on the strain amplitude of GWs from individual supermassive black-hole binaries (Babak et al. 2016) and stochastic GW backgrounds (Lentati et al. 2015) and to place upper limits on possible anisotropies of the stochastic background (Taylor et al. 2015). Subsets of the data set is also being used for various studies, some of which are presented in Chapter 5. The EPTA DR 1.0 set is now publicly available[3].

3.3.1 The EPTA Data Release 1.0

The data of the EPTA DR 1.0 were categorised based on unique combinations of observatory, receiver and backend. Additionally, we gave a different system code to WSRT data before and after an (undetermined) observatory clock offset which occurred in early 2001. In total, the data set contains 18 observing systems with a frequency coverage from 300 to 2640 MHz. We have already discussed the details of the EBPP backend and the reduction and analysis of its data. Let us now see some details on these aspects for the data from the other three EPTA telescopes. The key properties for the data of all four telescopes are summarised in Table 3.1.

Table 3.1: Backend characteristics and data reduction software.

	EFF-EBPP	NRT-BON	WSRT-PuMaI	JBO-DFB
Obs. Freq. (GHz)	1.4/1.36/2.64	1.4/1.6/2.0	0.3/0.4/0.84/1.38/2.3	1.4/1.52
Max. Ban dwidth (MHz)	112	128	160	512
De-despersion	Coherent	Coherent	Incoherent	Incoherent
Clock	H-Maser	GPS	H-Maser	H-Maser
Polarisation Calibration	Auto (attenuators)	Full (Noise diode)	Phased-Array calibration	Auto (attenuators)
Data reduction	`PSRCHIVE`	`PSRCHIVE`	PuMa soft	`PSRCHIVE`
Cross-correlation template	Analytic (`paas`)	noiseless obs (`psrsmooth`)	high S/N obs -	high S/N obs -
TOA generation	`pat`	`pat`	PuMa soft	`pat`

[3] http://www.epta.eu.org/aom.html

The NRT is a meridian telescope with a collecting area equivalent to a 94-m parabolic dish. The BON backend is a member of the ASP-GASP coherent de-dispersion backend family (Demorest 2007). The BON data have a bandwidth of 64 MHz in the period 2004-2008 and 128 MHz from 2008 onwards. Since the change in bandwidth, the data were also polarisation calibrated. The data were recorded on a 2-minute sub-integrations basis and were time-stamped with a GPS-disciplined clock. BON data were reduced using `PSRCHIVE` and TOA extraction was performed with the `pat` routine, using observations fully scrunched in frequency and time. Exceptions were made for the short-period MSPs J0751+1807, J0610−2100, J1738+0333 and J1802−2124. The data were time-integrated to form 6, 12, 16 and 8 min profiles respectively to better sample the orbit. The integration times were adjusted according the orbital period and the brightness of the pulsar, to have a good orbital sampling and sufficient S/N. The profiles used for each TOA were used by folding all observations taken in a specific day. The observation profiles were cross-correlated with a noiseless template, created by removing the noise from a high S/N profile with the `PSRCHIVE`/`psrsmooth` routine (see Demorest et al. 2013). Exceptionally for PSR J1939+2134, the EPTA data set contains archival L-band data recorded with a swept-frequency local oscillator at the NRT[4] in the period 1990-1999 (Cognard et al. 1995).

The WSRT is an aperture synthesis interferometer, consisting of fourteen, 25-m dishes. For pulsar timing observations it is used in phased-array mode, with an equivalent size of a 94-m dish. It is an East-West array with equatorial mount. The PuMaI backend is an incoherent de-dispersion, digital filterbank machine (Voûte et al. 2002) and provides data starting from 1999. Apart from data in the L- and S-bands PuMaI has data at 350, 840 MHz. These low-frequency data provide vital information for measuring the DM, especially in the first half of the data set where there is a lack of S-band data. The bandwidth of the data ranges from 10 MHz for the lowest frequencies to 160 MHz for L- and S-band data. For the offline de-dispersion and folding of the profiles as well as the data reduction, custom PuMaI software was used. For TOA extraction, high S/N observations were used as templates. Since the WSRT is an interferometer, calibration of the two polarisation signals is by-default performed during the phased-array calibration of the dishes.

The Lovell Telescope is a 76-m dish at the Jodrell Bank Centre for Astrophysics. The DFB backend onboard the Lovell is a clone of the Parkes DFB (Hobbs et al. 2004). DFB data are recorded since early-2009, first at a central frequency of 1400 MHz and bandwidth of 128 MHz and since September of the same year at and later at 1520 MHz with 512 MHz of bandwidth[5]. Incoherent de-dispersion and folding is performed online in hardware. Data reduction was performed with `PSRCHIVE` and high-S/N observations were used as templates for TOA extraction.

When combining the data, arbitrary phase offsets, commonly referred to as "JUMPs", were fitted between the various observing systems. These offsets include, for example, the difference in instrumental delays, the results from using different templates and the choice for the fiducial point on the template. To bring these offsets to a minimum, we have measured the delays from the phase between the various templates used to extract the TOAs. Most of the remaining delays are then due to the difference in instrumental delays. Between the different observing frequencies, the profile shape is also significantly different for some pulsars, which contributes to larger remaining offsets, since it becomes difficult to define a common fiducial point.

The data from the different telescopes used are highly complementary, creating a data set that is vastly superior to that of each telescope alone, increasing the scientific output of the observing cam-

[4] Unlike the case of the BON data, these data are time-stamped with an on-site Rubidium atomic clock, which is corrected to UTC using recorded offsets from the Paris Observatory Universal Time.

[5] Of the 512 MHz, about 380 MHz of the bandwidth is usable due to the local RFI conditions

paigns. The Effelsberg data offer a long baseline of data. Even when forming a long data set with combinations of shorter data sets, the numbers of degrees of freedom are effectively increased for analysis of the data, unless the time offsets between the residuals of the different observing systems are known by direct measurements. The long baseline of the Effelsberg data are essential, as we have mentioned, to measure long-term timing parameters and to search for low-frequency GW signals. The various L-band data are important in that they verify each other. Overlapping data at the same frequency bands are paramount to detect and remove problematic data, since otherwise it is at times impossible to decide whether outlying points are due to a problem in the data or due to an underlying physical process. Further, data gaps exist in most data sets, e.g. during periods of telescope upgrades or instrumental failures and overlapping data ensure the number of these gaps is minimised. The NRT data offer the highest timing precision points in the data set, which boost the precision with which short term orbital parameters are measured. These are also aided by the high cadence of these data. Similarly, the high-cadence JBO data improve these measurements even further.

Another example of how these data are complementary is the way they increase the sensitivity of the data set to low-frequency stochastic signals, discussed in Chapter 5. When such a signal is present in the data, it can only be sampled thanks to the long span of the Effelsberg data. However, it is in many cases only thanks to the highly densely sampled L-band data from the combination of all telescopes and the high precision of the NRT data points that overall precision of the data set is high enough to detect a weak, slow variation in the data. Finally, the broad observing frequency coverage of the telescopes gives information to measure and remove interstellar medium effects from the timing residuals.

3.3.2 Timing-Analysis Methods

The timing analysis of the EPTA data set was performed using `Tempo2` and the Bayesian inference pulsar timing package `TempoNest` (Lentati et al. 2014). This is the first large-scale pulsar timing analysis performed using Bayesian inference methods. As such, great effort was made to ensure that the results were statistically consistent with those derived using established and well-tested methods, and made extensive comparisons of our results with those derived by other groups using independent methods and data sets.

Timing analysis with `TempoNest` is a combination of the `Tempo2` timing model and fitting method and Monte-Carlo sampling of the model parameters using the Bayesian inference tool `MultiNest` (Feroz & Hobson 2008). This approach allows to go beyond the linear model of `Tempo2` and performs a non-linear fit of the timing data. One can show via simulations (e.g. Lentati et al. 2014) that for intermediate to low S/N, the linear model, which creates updated timing model through linear perturbations of the timing-parameters pre-fit values, can lead to erroneous values for the timing parameters and underestimations of the their uncertainties. These effects are further amplified with the presence of correlated noise in the data.

The effect of the presence of correlated noise in pulsar data on the estimations of timing parameters and their uncertainties, were already known by previous studies (Coles et al. 2011; van Haasteren & Levin 2013), which assumed time-stationary correlated signals in the residuals. Coles et al. (2011) proposed a solution which is an extension of the `Tempo2` least-squares fit to a generalised least-squares that includes the information form the covariance matrix of the residuals. This follows an iterative process, where a first fit is perform to get a set of timing residuals, of which one calculates the covariance matrix and uses it in a new fit. On the other hand van Haasteren & Levin (2013) discussed the problem from a Bayesian approach, where they argued in favour of solving the timing and stochastic noise para-

meters simultaneously, based on the fact that the fit itself breaks down the stationarity of the correlated signal. In van Haasteren & Levin (2013), a linear approximation to the timing model was performed, while in contrast, `TempoNest` allows a non-linear fit of the timing model simultaneously with the noise parameters.

For the EPTA timing analysis, we considered time-correlated and uncorrelated noise terms that have already been identified in pulsar timing data. I will discuss in depth this noise budget paradigm and its justification in §4.3.1. Here, I only briefly overview the used noise terms and their physical origin. These are:

- *1 EFAC (f) per observing system*: An EFAC is a multiplicative factor on the TOA uncertainty derived from the cross-correlation TOA extraction method. It is used to correct for errors in the uncertainty calculations which can occur when one or more of the underlying assumptions, e.g. that the statistics of the profile are purely Gaussian, break down.
- *1 EQUAD (q) per observing system*: A second correction factor for the TOA uncertainty, added in quadrature. This correction is needed for the possibility that uncorrelated noise components may exist in the TOAs additional to the measurement uncertainty. A well known effect that creates this effect is pulse phase jitter (see §1.2.1). Eventually, the corrected TOA uncertainty is equal to $\sqrt{\sigma^2 f^2 + q^2}$.
- *1 achromatic, time-stationary, stochastic signal per pulsar*: The timing residuals of pulsar, especially canonical ones, show time-correlated stochastic variations known as "timing noise". These may be formed by various mechanisms, e.g. by instabilities in the pulsar's rotation. These variations typically have signals with red power-law spectra. We therefore include one achromatic, power-law-spectrum signal.
- *1 DM variations component per pulsar*: I have already discussed the effects on the pulse from its propagation via the IISM in §1.2.3, where the IISM dispersion law and the temporal variations of DM were discussed. DM variations induce a stochastic timing signal, which we model as a frequency-dependent, time-stationary, stochastic signal which obeys the IISM dispersion law (i.e. Eq. 1.2).

As discussed in Chapter 2, the timing model used a Solar system ephemeris to predict the locations of the planets and the SSB. In this work, we have made use of the planetary ephemeris DE421 (Folkner et al. 2009). The final referencing of the TOAs to the SSB were made using the BIPM2011 standard. Binary orbits were modelled using `Tempo2` implementations of the PPK formalism discussed in §2.3.3. We either used the `Tempo2` implementation of the model developed by Damour & Deruelle (1985, 1986), commonly referred to as the 'DD' model or we used the implementation of the 'ELL1' model by Lange et al. (2001), for quasi-circular orbits. The Shapiro delay was either modelled using the standard shape and range PK parameters of the 'DD' model or the orthometric parametrisation of the Shapiro delay, using the h_3 and ς parameters, as discussed in §2.3.3.1. Table 3.2 summarises the main properties of the 42 pulsars in the EPTA data set and for binary pulsars, the binary model Shapiro delay parametrisation used.

The timing analysis of the EPTA DR 1.0 has provided many interesting astrometric and astrophysical results. Compared with similar previously published results, there are expected improvements not only due to the improved TOA precision and longer time-spans, but also from the use of Monte-Carlo sampling for all timing parameters, the simultaneous modelling of stochastic-noise processes and the use of updated and improved Solar system ephemeris and time-standards. In the next paragraphs, the timing results are presented with separate discussions on distance estimations, kinematic properties,

Table 3.2: Summary of the EPTA DR 1.0 data set. Figures in parentheses represent the 68.3% confidence-level (C.L.) uncertainties in the last digit quoted, as derived from the 1-dimensional marginalised posterior distribution of each parameter. The columns present the pulsar name in the J2000 coordinate system, the observatories that contributed to the data set, the number of TOAs, the time-span, the median TOA uncertainty ($\sigma_{\rm TOA}$, after applying white-noise corrections), the RMS timing residual after subtracting the maximum-likelihood (ML) signal. the spin period and orbital period, the median flux density of the pulsar at 1400 MHz and the used binary model. The binary model is either the DD or ELL model. The use of the orthometric parametrisation of the Shapiro delay instead of the standard range and shape parameters is noted with an 'DDH' and 'ELLH' for the two binary models, respectively. Solitary pulsar are noted with '-' in the binary model column. Adapted version of Table 1 from Desvignes et al. (2016).

PSR JName	Observatories	$N_{\rm TOA}$	$T_{\rm span}$ (yr)	$\sigma_{\rm TOA}$ (μs)	RMS (μs)	$P_{\rm Spin}$ (ms)	$P_{\rm Orb}$ (d)	S_{1400} (mJy)	Binary Model
J0030+0451	EFF, JBO, NRT	907	15.1	3.79	4.1	4.9	—	0.8	-
J0034−0534	NRT, WSRT	276	13.5	8.51	4.0	1.9	1.59	0.01	ELL1
J0218+4232	EFF, JBO, NRT, WSRT	1196	17.6	10.51	7.4	2.3	2.03	0.6	ELL1
J0610−2100	JBO, NRT	1034	6.9	8.14	4.9	3.9	0.29	0.4	ELL1
J0613−0200	EFF, JBO, NRT, WSRT	1369	16.1	2.57	1.8	3.1	1.20	1.7	ELL1
J0621+1002	EFF, JBO, NRT, WSRT	673	11.8	9.43	15.6	28.9	8.32	1.3	DD
J0751+1807	EFF, JBO, NRT, WSRT	1491	17.6	4.33	3.0	3.5	0.26	1.1	ELL1H
J0900−3144	JBO, NRT	875	6.9	4.27	3.1	11.1	18.74	3.2	ELL1
J1012+5307	EFF, JBO, NRT, WSRT	1459	16.8	2.73	1.6	5.3	0.60	3.0	ELL1
J1022+1001	EFF, JBO, NRT, WSRT	908	17.5	4.02	2.5	16.5	7.81	2.9	DDH
J1024−0719	EFF, JBO, NRT, WSRT	561	17.3	3.42	8.3	5.2	—	1.3	-
J1455−3330	JBO, NRT	524	9.2	7.07	2.7	8.0	76.17	0.4	DD
J1600−3053	JBO, NRT	531	7.7	0.55	0.46	3.6	14.35	2.0	DDH
J1640+2224	EFF, JBO, NRT, WSRT	595	17.3	4.48	1.8	3.2	175.46	0.4	DD
J1643−1224	EFF, JBO, NRT, WSRT	759	17.3	2.53	1.7	4.6	147.02	3.9	DD
J1713+0747	EFF, JBO, NRT, WSRT	1188	17.7	0.59	0.68	4.6	67.83	4.9	DD
J1721−2457	NRT, WSRT	150	12.8	24.28	11.7	3.5	—	1.0	-
J1730−2304	EFF, JBO, NRT	285	16.7	4.17	1.6	8.1	—	2.7	-
J1738+0333	JBO, NRT	318	7.3	5.95	3.0	5.9	0.35	0.3	ELL1
J1744−1134	EFF, JBO, NRT, WSRT	536	17.3	1.21	0.86	4.1	—	1.6	-
J1751−2857	JBO, NRT	144	8.3	3.52	3.0	3.9	110.75	0.4	DD
J1801−1417	JBO, NRT	126	7.1	3.81	2.6	3.6	—	1.1	-
J1802−2124	JBO, NRT	522	7.2	3.38	2.7	12.6	0.70	0.9	ELL1
J1804−2717	JBO, NRT	116	8.4	7.23	3.1	9.3	11.13	1.0	DD
J1843−1113	JBO, NRT, WSRT	224	10.1	2.48	0.71	1.8	—	0.5	-
J1853+1303	JBO, NRT	101	8.4	3.58	1.6	4.1	115.65	0.5	DD
J1857+0943	EFF, JBO, NRT, WSRT	444	17.3	2.57	1.7	5.4	12.33	3.3	DD
J1909−3744	NRT	425	9.4	0.26	0.13	2.9	1.53	1.1	ELL1
J1910+1256	JBO, NRT	112	8.5	3.39	1.9	5.0	58.47	0.5	DD
J1911+1347	JBO, NRT	140	7.5	1.78	1.4	4.6	—	0.6	-
J1911−1114	JBO, NRT	130	8.8	8.82	4.8	3.6	2.72	0.5	ELL1
J1918−0642	JBO, NRT, WSRT	278	12.8	3.18	3.0	7.6	10.91	1.2	DDH
J1939+2134	EFF, JBO, NRT, WSRT	3174	24.1	0.49	34.5	1.6	—	8.3	-
J1955+2908	JBO, NRT	157	8.1	14.92	6.5	6.1	117.35	0.5	DD
J2010−1323	JBO, NRT	390	7.4	2.89	1.9	5.2	—	0.5	-
J2019+2425	JBO, NRT	130	9.1	26.86	9.6	3.9	76.51	0.1	DD
J2033+1734	JBO, NRT	194	7.9	18.24	12.7	5.9	56.31	0.1	DD
J2124−3358	JBO, NRT	544	9.4	5.57	3.2	4.9	—	2.7	-
J2145−0750	EFF, JBO, NRT, WSRT	800	17.5	2.64	1.8	16.1	6.84	4.0	ELL1
J2229+2643	EFF, JBO, NRT	316	8.2	11.18	4.2	3.0	93.02	0.1	DD
J2317+1439	EFF, JBO, NRT, WSRT	555	17.3	7.78	2.4	3.4	2.46	0.3	ELL1
J2322+2057	JBO, NRT	229	7.9	12.47	5.9	4.8	—	0.03	-

mass measurements and constraints on the geometry of binary pulsar orbits.

A number of newly measured parameters resulted from this analysis. In particular, we achieved new measurements for seven timing parallaxes, nine proper motions, six apparent changes of the semi-major axis and one pulsar mass. For many other parameters, we improved on previous measurements[6].

3.3.3 Timing Results I: Parallax Distances

In §2.3.2, we saw how the wavefront curvature of the pulse signal induces an annual periodic signal on the residuals while the Earth orbits around the SSB. We can rewrite Eq. 2.17b, as:

$$\Delta_{\rm px} = \frac{d_\odot^2 \cos^2\beta}{2cd_p}\,, \tag{3.3}$$

where the vector of the Earth's barycentric position is expressed in terms of the distance between Earth and the SSB, $d_\odot$, and the pulsar's ecliptic latitude, β. We have applied the correction of Verbiest et al. (2010) for the Lutz-Kelker bias (LKb; §2.3.2) on the measured parallax values and derived the LKb-corrected parallax distance measurements. For the LKB correction, we used the mean flux densities of the pulsars at 1400 MHz, which were measured using NRT observations with the NUPPI backend (see §5.3.3), which was used simultaneously with the BON backend. The used data set allowed such distance measurements for 25 MSPs. Absolute flux calibration was made using the quasar 3C48 as the standard calibrator. For seven pulsars there was no prior measurement of their parallaxes but, as noted in Desvignes et al. (2016), they have at best a 3σ detection, therefore still severely biased. For another ten pulsars, our measurements have improved precision from previous reported values. For only one pulsar, specifically for PSR J1738+0333, we did not achieve a measurement while there is a significant measurement in the literature from a timing campaign that followed this pulsar for 10 years with the Arecibo and GBT (Freire et al. 2012b).

In Desvignes et al. (2016), we present a comparison of the LKb-corrected parallax distances with the distances estimated from their DM values, using Galactic electron content models (§1.5). In particular, we compared with the "NE2001" model of Cordes & Lazio (2002) and the "M2" and "M3" models of Schnitzeler (2012).

The NE2001 is the most widely used model to estimate pulsar distances from their DMs. It was created to expand and improve the model by Taylor & Cordes (1993) which models large-scale Galactic components smoothly, i.e. without local structures of enhanced or reduced electron density, and generally overestimates distances for distant objects. Using a wealth of newer data, the NE2001 was constructed based on observational data from pulsar DM, multi-path scattering pulse broadening and distance measurements (e.g. parallax or via associations with globular clusters), as well as data from other radio, optical and X-ray observations that offer information on local interstellar structures (voids or clumps, the Galactic centre, spiral arms etc). The model has several Galactic structure components; an outer thick disc with a large Galactocentric scale-height, an inner, annular thin disk, the Galactic centre, the spiral arms and several localised ISM components.

[6] While Desvignes et al. (2016) was under review, similar work with independent methods and comparable overall timing precision were published from the PPTA (Reardon et al. 2016) and NANOGrav (The NANOGrav Collaboration et al. 2015; Matthews et al. 2016). collaborations. Some of the newly measured parameters reported in this chapter, were independently measured also by these groups.

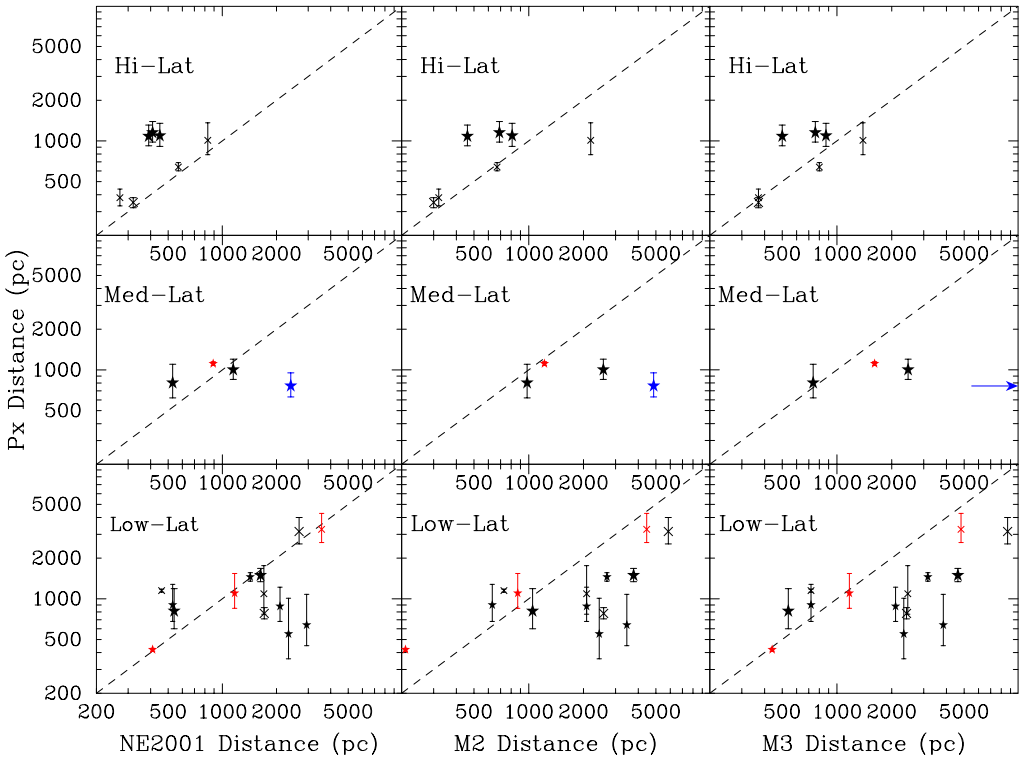

Figure 3.1: Comparison between the Lutz-Kelker bias corrected parallax distances (in ordinates) and the DM distances (in abscissa) for different Galactic latitudes b on logarithmic scales. The DM distances in the left, middle and right panels are derived from the NE2001, M2 and M3 models respectively. Top panels: the stars show pulsars with $b > 40^\circ$ and the crosses pulsars with $b < -40^\circ$. Middle panels: the stars show pulsars with $40^\circ > b > 20^\circ$ and the crosses pulsars with $-40^\circ < b < -20^\circ$. Bottom panels: the stars show pulsars with $20^\circ > b > 0^\circ$ and the crosses pulsars with $-20^\circ < b < 0^\circ$. The red symbols indicate pulsars with a known parallax before NE2001 was created, namely PSRs J1713+0747, J1744−1134, J1857+0943 and J1939+2134. The blue symbol indicates PSR J1643−1224 where its corresponding M3 distance is infinite and represented by an arrow. Figure from Desvignes et al. (2016).

The M2 and M3 models are two of the four models introduced in Schnitzeler (2012). They were developed in order to examine possible improvements to the two aforementioned models, by using carefully selected data to create new, simple descriptions of thick disc component. In particular, DM information from pulsar in 45 LOSs were selected, excluding LOSs near the Galactic plane (in particular excluding Galactic latitudes $b < 5^\circ$), LOSs with reported strong H_α emission from structures in the interstellar medium. These selection criteria were made to ensure that only well understood LOSs were used to calibrate the models. The updated thick-disc models in the M2 and M3 models have single-component discs, with exponential scale-heights of 1.59 and 1.31 kpc respectively, in contrast to the multi-component NE2001 model. Figure 3.1 show schematically the comparison of our parallax distance measurements with the distance predicted by the NE2001, M2 and M3 models. The comparison is divided in three Galactic latitude regimes, low ($|b| < 20^\circ$), medium ($20^\circ < |b| < 40^\circ$) and high ($|b| > 40^\circ$).

The NE2001 model outperforms the M2/M3 models at medium and low latitudes, while the opposite occurs for high latitudes. The NE2001model underperforms particularly at high latitudes and large distances, i.e. above 2 kpc. The M2/M3 models appear to have somewhat benefitted from the careful selection of the LOSs used. However, the exclusion of low-Galactic-latitude pulsars causes them to systematically underestimate the electron content at lower latitudes, with the M3 model leading even to infinite distance for one of the pulsars in this study, the high-DM PSR J1643−1224. On average, the NE2001 performs better, despite its shortcomings at high latitudes.

An important finding of our analysis, is the implied level of uncertainties that these electron density model require to be statistically consistent with our distance measurements. We find that for low, middle and high Galactic latitudes the NE2001 requires mean uncertainties of 64%, 55% and 117% respectively, an average of 80%. This is significantly higher than the 25% mean uncertainty that is usually assumed in the literature when using the NE2001, and the fractional distance uncertainties presented in Cordes & Lazio (2002) (their Fig. 12). The required mean uncertainties for the other two models we investigated are 95%, 200% and 53% for the M2 model and 113%, 202% and 41% for the M3 model.

3.3.4 Timing Results II: Kinematics

Pulsars have large proper motions (§2.3.2), showing velocities larger than those of their progenitor massive (of OB spectral type) stars (e.g. Gunn & Ostriker 1970). Pulsar proper motion measurements can provide significant observational constraints on the formation mechanisms of pulsars and the recycling process through which MSPs are thought to be formed (§1.4). For example, a key prediction of some stellar evolution models for the MSP formation, predict smaller spatial velocities for MSPs than for canonical pulsars (Tauris & Bailes 1996; Cordes & Chernoff 1997). Various studies have attempted to identify such a difference in the distributions of transverse velocities, $\overline{V}_T$, of the different pulsar populations. Using a sample of 23 MSPs, Toscano et al. (1999) derived a transverse velocity distribution for MSPs of $\overline{V}_T$ =85±13 km s^{-1}, noting that this value was about four times lower than typical transverse velocities of canonical pulsars. Toscano et al. also reported an apparent difference in the velocity distributions of binary and solitary MSPs, the latter having velocities which were about 66% smaller than those of binary MSPs. Later work, however, have revised this last result using larger MSP samples (Hobbs et al. 2005; Lommen et al. 2006; Gonzalez et al. 2011). All studies showed that the two MSP populations do not have statistically different transverse velocity distributions.

Our work with the EPTA data set has led to seven new proper motion measurements, three out of which are for solitary pulsars. For another seven MSPs, we have improved the precision of the proper motion measurements by an order of magnitude. Combining the proper motion and distance measurements, one may derive the transverse velocity via the relation:

$$\overline{V}_T = 4.74\,\mathrm{km\,s^{-1}} \times \mu \times d_\mathrm{p}\,, \tag{3.4}$$

where μ is the composite proper motion value in mas yr^{-1} and d is the distance to the pulsar in kpc. We have used the most precise distance estimate, either from the LKb-corrected parallax distance measurements or the NE2001 distance estimate. We combined our results with available information from the ATNF pulsar catalogue and revisited the transverse distribution of MSPs, looking for statistical differences between the velocity distribution of binary and solitary MSPs. In doing so, we have excluded MSPs in globular clusters (since their velocities are strongly affected by gravitational interactions with

cluster objects) and DNSs (due to the dynamical interactions of the pulsars with their companions). We limited our study to MSPs with rotational periods below 20 ms, resulting in a sample of 57 binary and 19 solitary MSPs, which is a great improvement to the sample of 27 binary and 10 solitary MSPs used in the most recent past study by Gonzalez et al. (2011).

The average value of the transverse velocity distribution for our full sample is $\overline{V}_T = 92\pm10\,\mathrm{km\,s^{-1}}$. For binary and solitary MSPs, the average values are $\overline{V}_T = 93\pm13\,\mathrm{km\,s^{-1}}$ and $\overline{V}_T = 88\pm17\,\mathrm{km\,s^{-1}}$ for the binary and solitary MSPs respectively. These values are consistent with those derived by Hobbs et al. (2005) and Gonzalez et al. (2011). We investigated the possibility that the transverse velocity distributions of the two MSPs populations are drawn from different parent distributions using the Kolmogorov-Smirnoff (KS) test, which concluded in that our data do not reject the null hypothesis that the two velocity distributions are drawn from the same parent distribution. We repeated the same process using only MSPs with parallax distance measurements (21 binary and 8 solitary MSPs). The average velocity values were then $56\pm3\,\mathrm{km\,s^{-1}}$ and $75\pm10\,\mathrm{km\,s^{-1}}$ for binary and solitary MSPs respectively and the KS test again did not reject the null hypothesis.

A final study on the kinematic properties of MSPs in Desvignes et al. (2016), is the derivations of the kinematic contributions to the measured derivatives of the rotational and orbital periods. In §2.3.2 and §2.3.3, I introduced the Shklovskii effect, i.e. the apparent radial motion component induced by the binary's transverse motion, and explained that the acceleration by the Galactic gravitational potential is absorbed in the terms describing the pulsar's radial motion. Two such terms are the pulsar's rotational period derivative, $\dot{P}$, and orbital period derivative, $\dot{P}_\mathrm{b}$. We can express the intrinsic values of these parameters with respect to their observed values and the various contributions to the latter as:

$$\dot{P}^\mathrm{int} = \dot{P}^\mathrm{obs} - \dot{P}^\mathrm{Shk} - \dot{P}^\mathrm{dgr} - \dot{P}^\mathrm{kz} \tag{3.5a}$$

$$\dot{P}^\mathrm{int}_\mathrm{b} = \dot{P}^\mathrm{obs}_\mathrm{b} - \dot{P}^\mathrm{Shk}_\mathrm{b} - \dot{P}^\mathrm{dgr}_\mathrm{b} - \dot{P}^\mathrm{kz}_\mathrm{b} - \dot{P}^{\dot{m}}_\mathrm{b} - \dot{P}^\mathrm{relat}_\mathrm{b}\,, \tag{3.5b}$$

The additional term superscripts 'Shk', 'dgr', 'kz', and 'GW' denote contributions to the observed parameter values from the Shklovskii effect, the acceleration towards the Galactic disc, the acceleration from the differential rotation of the Galaxy and from GW emission. The mathematical details of these terms are discussed separately in Chapter 5. For systems without mass transfer one can fully attribute the observed rotational frequency derivative to the Shklovskii effect and Galactic contributions to derive an upper limit on the pulsar's distance. In Desvignes et al. (2016), we present these upper limits for the 19 pulsars where the values are below 15 kpc, which is reasonable limit given the Galactic size and typical distances at which we can observe MSPs. For nine of these sources we have parallax distance measurements. For all but one case, PSR J1024−0719, the parallax distance is consistent with the kinematic upper limit. The DM distances from the NE2001 and M3 electron density models are ruled out by the kinematic distance upper limits for two and three pulsars respectively. The case of J1024−0719 warranted some additional attention. While rotationally-powered pulsars have a positive intrinsic period derivative (§1.2.4), this MSP has a negative one. The measured parallax distance is about four standard deviations further from the upper limit. The most likely explanation, is that J1024−0719 is a member of a hierarchical triple system, much like PSR B1620-26 (Arzoumanian et al. 1996). The outer star would be in a wide orbit, applying on the pulsar a relative acceleration along the LOS of at least $1.7\times10^{-9}\,\mathrm{m\,s^{-2}}$. Notably, Sutaria et al. (2003) have reported a candidate companion in optical.

Finally, one can also use Eq. 3.5b to repeat the same exercise, but using the measured derivative of the orbital period, $\dot{P}_\mathrm{b}$, instead of the rotational period derivative (Bell & Bailes 1996). In this case, $\dot{P}^\mathrm{relat}_\mathrm{b}$

denotes additional relativistic effects, such as energy loss from GW radiation damping and temporal variations in the gravitational constant. Some of these terms are predicted by GR and some only by alternative theories of gravity. We will see these terms in more detail in Chapter 5.

We have measured $\dot{P}_b$ for four MSPs in our sample, namely PSRs J0613−0200, J0751+1807, J1012+5307, J1909−3744. For the case of J1012+5307, the optical observations of the companion allowed a derivation of the pulsar and companion masses and orbital inclination angle (van Kerkwijk et al. 1996; Callanan et al. 1998). Assuming GR, one can calculate the contribution to $\dot{P}_b$ (Taylor & Weisberg 1982). Following Damour & Taylor (1991), the Galactic components are also estimated, allowing the independent derivation of the distance, which agrees with both the measured parallax distance and the optical distance derived from Callanan et al. (1998). For PSR J1909−3744, based on the Shapiro delay measurement information, we found the $\dot{P}_b^{obs}$ of PSR J1909−3744 to be dominated by the Shklovskii effect contribution and derived a distance in agreement to the parallax distance and, in fact, about 30 times more precise. For PSR J0613−0200 we have no information on the mass or inclination angle either from optical or Shapiro delay measurements. We can only make an estimate for the radiation damping contribution, using canonical values of the pulsar mass and orbital inclination of $1.4 M_\odot$ and 60° respectively. We derived a distance in agreement with the parallax distance on the 2.2σ level. Finally, PSR J0751+1807 has a negative $\dot{P}_b$, which implies that the Shklovskii contribution is not the dominant factor. As such, instead of making a distance estimate, we use the $\dot{P}_b$ and Shapiro delay measurements to increase the mass measurement precision, as discussed below.

3.3.5 Timing Results III: Mass Measurements

The current EPTA data set has allowed the measurements of the pulsar mass in seven cases. For PSR J1918−0642, this is the first measurement achieved while for PSRs J0751+1807 and J1600−3053 we have significantly increased the mass measurement precision from the last published values.

The three mass measurements reported were derived using the orthometric parametrisation of the Shapiro delay. Following Freire & Wex (2010), assuming GR, the amplitude of the third harmonic of the orbital period can be expressed, in seconds, as:

$$h_3 = \left(\frac{\sin(i)}{1 + \cos(i)} \right)^3 m_c T_\odot \ , \ T_\odot \equiv M_\odot G c^{-3} = 4.925490947 \mu s \ . \tag{3.6}$$

Here, $T_\odot$ is the mass of the sun expressed in units of time, G is the gravitational constant, c is speed of light, $M_\odot$ is the solar mass, i is the orbital inclination and m_c is the companion's mass. We use this relation and the posterior distributions of the Shapiro delay parameters from the timing analysis to plot the 2-D posterior density function of the companion mass against the (cosine of the) orbital inclination. We then plot the *mass-mass diagram*, by using the mass function to calculate the pulsar mass. This is given by:

$$\mathcal{F}(m_p, m_c) = \frac{4\pi^2}{G} \frac{(a_p \sin(i))^3}{P^2} = \frac{(m_c \sin(i))^3}{m_p + m_c} \ , \tag{3.7}$$

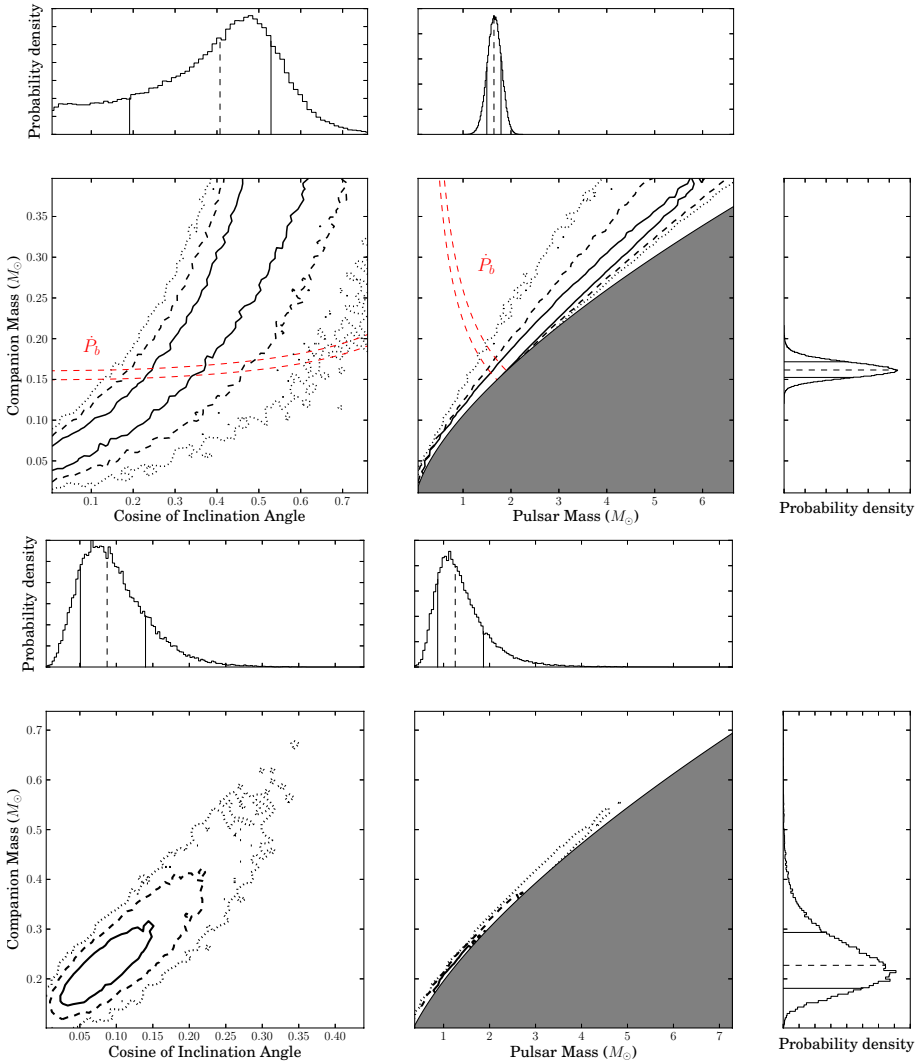

Figure 3.2: Figure caption. Figures from Desvignes et al. (2016).

where m_p is the pulsar mass. The mass-mass diagram is a very important diagram that shows whether a gravity theory is consistent with the binary pulsar orbit or not. Each post-Keplerian parameter is described as a function of the masses and therefore defines their probability distributions can be projected on the mass-mass diagram All measured post-Keplerian parameter distributions must intersect at a specific point, which due to the uncertainties is an area, the size of which reflects how precise is the verification of the theory by the binary orbit, as first demonstrated by Taylor et al. (1979). By projecting the posterior distribution of $\dot{P}_b$ on the mass-mass and the mass-inclination angle diagrams, we not only confirm GR with the pulsar, but more importantly for this discussion, we improve the precision of the orbital inclination and masses measurements. These diagrams are shown in the top panel of Fig. 3.2 for PSR J0751+1807, for which $\dot{P}_b$ is measured. In the bottom panel of Fig. 3.2 one can see these plots also for PSR J1918−0642, for which the mass was not previously measured. Table 3.3 summarises the mass measured pulsar and companion masses and the previous measured values.

Table 3.3: Table of pulsar and companion masses. The columns indicate the pulsar name, the previously published pulsar and companion mass (Prev. m_p and Prev. m_c) with the corresponding publication. The last 2 columns show our new measurements, m_p and m_c. † Nice et al. (2008) did not report on the companion mass in their proceedings. ‡ The pulsar masses were not reported by Verbiest et al. (2009) so we quote the pulsar mass value based on the mass function and their companion mass. Table from Desvignes et al. (2016).

PSR JName	Prev. $m_{\rm p}$ ($M_\odot$)	Prev. $m_{\rm c}$ ($M_\odot$)	Ref.	$m_{\rm p}$ ($M_\odot$)	$m_{\rm c}$ ($M_\odot$)
J0751+1807	1.26 ± 0.14	—†	Nice et al. (2001, 2008)	$1.64^{+0.15}_{-0.15}$	$0.16^{+0.01}_{-0.01}$
J1600−3053	0.87‡	0.6 ± 0.7	Verbiest et al. (2009)	$1.22^{+0.50}_{-0.35}$	$0.21^{+0.06}_{-0.043}$
J1713+0747	1.31 ± 0.11	0.286 ± 0.012	Zhu et al. (2015)	$1.33^{+0.09}_{-0.08}$	$0.289^{+0.013}_{0.011}$
J1802−2124	1.24 ± 0.11	0.78 ± 0.04	Ferdman et al. (2010)	$1.25^{+0.6}_{-0.4}$	$0.80^{+0.21}_{-0.16}$
J1857+0943	1.61‡	0.270 ± 0.015	Verbiest et al. (2009)	$1.59^{+0.21}_{-0.18}$	$0.268^{+0.022}_{-0.019}$
J1909−3744	1.53‡	0.212 ± 0.002	Verbiest et al. (2009)	$1.54^{+0.027}_{-0.027}$	$0.213^{+0.0024}_{-0.0024}$
J1918−0642	—	—	—	$1.25^{+0.61}_{-0.38}$	$0.227^{+0.066}_{-0.046}$

3.3.6 Timing Results IV: Constrains on Orbital Geometry

In §2.3.3 and Eq. 2.23, I introduced the secular and periodic variation terms of the binary Roemer delay, induced by the changes in the viewing angle to the binary. Here, we show how we searched for the annual-orbital parallax in systems where the Shapiro delay is measured in an effort to place additional constraints on the orbital geometry.

Keeping the convention of using the superscripts 'obs' and 'int' for the observed and intrinsic values of timing parameters, the effect of the annual-orbital parallax is described by the following equations (Kopeikin 1995):

$$x^{\rm obs} = x^{\rm int}\Big[1 + \frac{\cot(i)}{d_{psr}}(\Delta_{I_0}\sin(\Omega) - \Delta_{J_0}\cos(\Omega)\Big] \tag{3.8a}$$

$$\omega^{\rm obs} = \omega^{\rm int} - \frac{\csc(i)}{d_{psr}}(\Delta_{I_0}\cos(\Omega) + \Delta_{J_0}\sin(\Omega))\,, \tag{3.8b}$$

where $\Delta_{I_0} = -X\sin(\alpha) + Y\cos(\alpha)$ and $\Delta_{J_0} = -X\sin(\delta)\cos(\alpha) - Y\sin(\delta)\sin(\alpha) + Z\cos(\delta)$, and X,Y,Z are the cartesian components of Earth's barycentric position, $\mathbf{r}$. The equivalent relations for the case of the effects from the binary's proper motion are (Arzoumanian et al. 1996; Kopeikin 1996):

$$x^{\rm obs} = x^{\rm int}\Big[1 + \frac{1}{\tan(i)}(-\mu_\alpha\sin(\Omega) + \mu_\delta\cos(\Omega)(t - t_0)\Big] \tag{3.9a}$$

$$\omega^{\rm obs} = \omega^{\rm int} + \frac{1}{\tan(i)}(\mu_\alpha\cos(\Omega) + \mu_\delta\sin(\Omega)(t - t_0))\,, \tag{3.9b}$$

where μ_α and μ_δ are the right ascension and declination components of the measured proper motion. In Desvignes et al., we present $\dot{x}$ measurements for 13 MSPs. For six of these cases, this constituted the first measurements. The $\dot{x}$ and $\dot{\omega}$ effects are taken into account by the `Tempo2` timing model via the

'KOM' and 'KIN' parameters, which are the Ω and i. A detection of KIN provides a measurement of the inclination angle without the 90° ambiguity from the measurement of $\sin(i)$ through the Shapiro delay. When we have a measurement of the inclination angle from the Shapiro delay and an $\dot{x}$ measurement, we can combine these information to derive or constrain Ω. For three of the 13 MSPs with $\dot{x}$ measurement, namely PSRs J0751+1807, J1600−3053 and J1857+0943, we also have a Shapiro delay measurement and can attempt to use constrain Ω and i.

The KOM and KIN parameters are highly covariant and the their parameter space is complex and can be multi-modal. For this reason, we set `TempoNest` to do a the sampling of these parameters with higher sampling efficiency. To moderate the computational cost, we marginalised analytically over the rotational and astrometric timing parameters, and fixed the white-noise correction factors (EFACs/EQUADs) to their ML values, as derived previously from the full timing analysis.

We did not achieve an unambiguous measurement of these parameters for any of the three MSPs. The data are simply not sufficient to distinguish between different symmetric solutions of the orbits, as one can see for example in Fig. 3.3, for PSR J1600−3053. For this pulsar we have (at the 68% C.L.) three solutions, namely $219^\circ < \Omega < 244^\circ$ and $63^\circ < i < 71^\circ$ or $303^\circ < \Omega < 337^\circ$ and $61^\circ < i < 72^\circ$ and the preferred (the ML) solution, $37^\circ < \Omega < 163^\circ$ and $105^\circ < i < 122^\circ$. For PSR J1909−3744 the non-detection of $\dot{x}$ constrains Ω to $-2^\circ < \Omega < 33^\circ$ or $181^\circ < \Omega < 206^\circ$. The ML solution is $-2^\circ < \Omega < 33^\circ$ and $93.78^\circ < i < 93.95^\circ$. For PSRs J0751+1807 and J1857+0943 we did not achieve any significant constraints.

3.4 Conclusions and Discussion

The results from the timing analysis of the 42 MSPs using EPTA data was the end result of a co-ordinated effort at four major radio astronomical facilities in Europe towards GW-detection with pulsar-timing data. The power this data set is demonstrated by the many interesting astrometric and astrophysical results. The high timing precision and long time-spans have given access to precise measurements of short- and long-term timing parameters. Several parameters were measured for the first time. These were seven timing parallaxes, nine proper motions, six apparent changes in the orbital semi-major axis and one new Shapiro delay measurement. The current results show that further observations of PSR J1600−3053 will likely yield the detection of the advance of periastron, dramatically improving the mass measurement and improving the constraints on the binary's orbit geometry. We have searched for signatures of the annual-orbital parallax in three systems and managed a marginal detection for PSR J1600−3053.

We used a set of 26 timing parallax measurements from our pulsar sample and compared them with the distances predicted by electron-density models for the Galaxy. An important finding, is the most widely used model, the NE2001 by Cordes & Lazio (2002) requires on average an 80%-level uncertainties to account for our measurements, in contrast to the standard 25% mean uncertainty assumed in the literature. We also showed, that the NE2001 performed better overall by comparison to other widely used models and demonstrated that a change in the scale-height of the thick disc in the electron density models also dramatically affects the distance estimations for pulsars located in the Galactic plane.

Using an extended sample of MSP 2-D velocity measurements, we have also verified that the velocity distributions of solitary and binary MSPs are statistically consistent, as suggested already by studies such as Hobbs et al. (2005) and Gonzalez et al. (2011). The sample we used, however, was significantly larger than these previous studies.

This work has highlighted the quality of the data recorded with the previous generation of pulsar

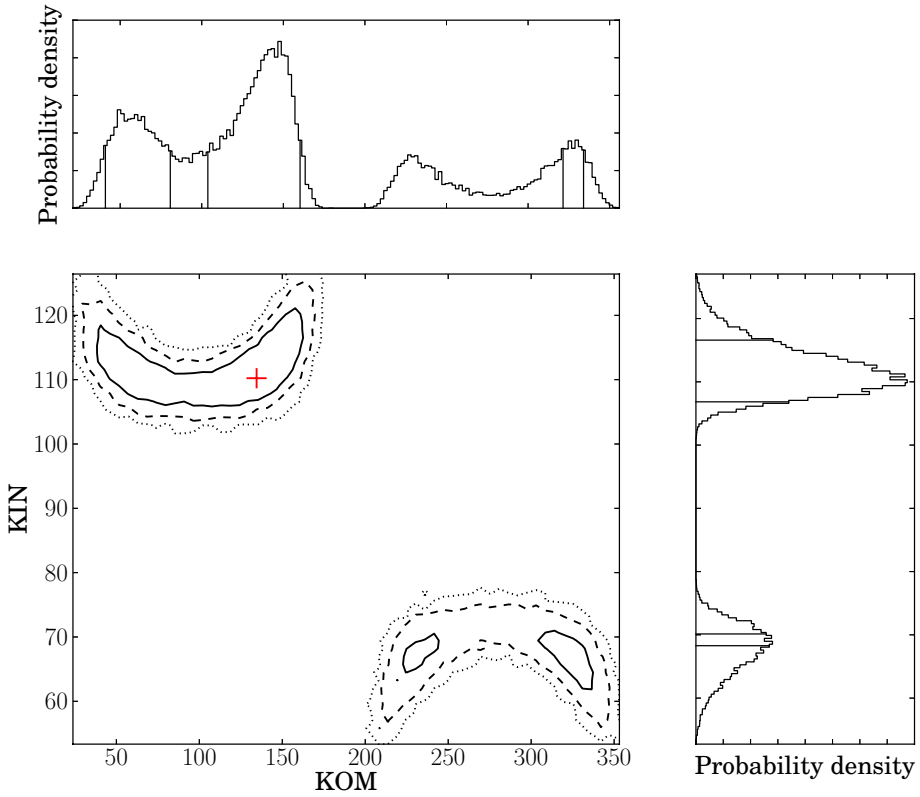

Figure 3.3: One and two-dimensional marginalized posterior distributions of the longitude of ascending node Ω (KOM) and inclination angle i (KIN) for PSR J1600−3053. The continuous black line, the dashed line and the dotted line represent, respectively, the 68.3%, 95.4% and 99.7% C.L. of the 2-D probability density function. The red cross indicates the ML-solution values. The continuous lines in the panels of the marginalised 1-D distributions of KOM and KIN show the 68.3% C.L. for each parameter. Figure from Desvignes et al. (2016).

processors. The lower TOA precision by comparison to newer instrumentation was partially compensated by the data set's long time-span and the good frequency coverage. With this study, we have also demonstrated the potential of using new timing-analysis algorithms based on Bayesian methods, non-linear timing analysis and extensive sampling of the timing parameters, thanks to the advent of supercomputing facilities.

At all EPTA observatories, the new generation of backends have already been recording data for about 5 years, and have now sufficiently long time-spans to contribute to the various scientific projects. The result from the analysis presented in this chapter and in Desvignes et al. (2016) of this large data set will serve as an excellent starting point when extending our data sets. EPTA DR 1.0 data have been thoroughly examined and corrected and new data can be compared to these in order to test their quality (see e.g. Lazarus et al. 2016). The analysis results from EPTA DR 1.0, including the extensive noise analysis discussed in the next chapter guides the work towards revisiting our observing strategies and priority target lists.

CHAPTER 4

The Noise Properties of 42 Millisecond Pulsars from the European Pulsar Timing Array and Their Impact on Gravitational-Wave Searches

"One person's data is another person's noise"

K. C. Cole

This chapter was previously published as
***Caballero R. N.**, Lee K. J., Lentati L., Desvignes G., Champion D . J., Verbiest J. P. W., Janssen G. H., Stappers B. W., et al. 2016, "The noise properties of 42 millisecond pulsars from the European Pulsar Timing Array and their impact on gravitational-wave searches", MNRAS, 457, 4421*
Small modifications were made to for the inclusion in this thesis, in order to keep consistency in style and cross-referencing to other sections.
The algorithms and codes described in §4.3.3, §4.6 and §4.7 were developed together with Dr. K.J. Lee.

As explained in the previous chapter, the primary purpose of the EPTA DR 1.0 was to be used for GW searches. In this chapter, we focus on the noise analysis of the individual pulsar data of this data set, which is an integral part of this process. The results are then used to examine the limitations that the noise imposes on the sensitivity of the EPTA DR 1.0 to GWs.

4.1 Introduction

We saw in §1.5 that one of the primary scientific applications of pulsar timing, is the use of long-term PTA observations for direct GW observation at nHz frequencies. The expected effects of GW propagation on the TOAs were first examined by Sazhin (1978). Later, the idea of using a PTA for unambiguous direct detection of low-frequency (nHz regime) GWs based on the predicted cross-correlation of the residuals of pulsars in various sky positions was proposed by Hellings & Downs (1983). Subsequent work

has identified the potential of modern timing data for detecting nHz GWs and formulated the detection methodologies (e.g. Jenet et al. 2004, 2005; Sanidas et al. 2012).

PTAs are sensitive to the stochastic GW background (GWB) resulting from the incoherent superposition of the GW signals from the cosmic population of unresolved inspiralling supermassive black-hole binaries (SMBHBs) (e.g. Rajagopal & Romani 1995), continuous GWs (CGWs) from individual, resolvable SMBHB systems (e.g. Estabrook & Wahlquist 1975), the GWB created from the decaying loops of a cosmic string network that may have formed in the early Universe (e.g. Kibble 1976), a cosmological relic GWB from the Universe's inflationary era (e.g. Grishchuk 2005) and the memory term (long-term change in the GW's amplitude) from GW bursts from SMBHB mergers (e.g. Favata 2009). Prior to the detection, upper limits on the GW amplitudes can impose limits on the properties of the cosmic SMBHB population (e.g Shannon et al. 2015), and rule out the presence of nearby SMBHBs proposed by independent observations (Jenet et al. 2004). In the era of GW astronomy, PTAs using future, hyper-sensitive telescopes will also be able to test theories of gravity in the radiative regime. The GW polarisation modes predicted by GR or alternative theories result in different spatial cross-correlations of the pulsar timing residuals (e.g. Chamberlin & Siemens 2012). These cross-correlations can be further modified if the graviton is not massless as predicted by GR (e.g. Lee 2013).

The sensitivity of a given PTA to GWs is mainly limited by the uncertainties of the TOA measurements, the number of observations and the data time-span, the number of pulsars, their sky distribution and the presence of low-frequency noise in the data (see e.g. Lee et al. 2012; Siemens et al. 2013). While improvements in the instrumentation, increase of the allocated telescope time to PTAs and discoveries of new pulsars can address the first three factors, low-frequency noise needs to be characterised and understood on a pulsar-by-pulsar basis.

A number of methods have been developed to mitigate the dominant sources of noise in pulsar timing. DM variations along the line of sight to the pulsar is a primary source of low-frequency stochastic noise. DM time delays, however, depend on the observing frequency, ν, as $t_{DM} \propto DM\nu^{-2}$, and therefore DM variations can be, to a large degree, corrected using multi-frequency data, (e.g. Keith et al. 2013; Lee et al. 2014). Improper calibration of the gain of the two receiver feeds or cross-coupling between the two feeds can potentially lead to distortions of the total intensity profiles. These instrumental artefacts will introduce additional non-stationary noise components in the timing residuals (van Straten & Bailes 2003; van Straten 2006). By performing standard calibration observations during every observing run, we can minimise the presence of such noise in the data (e.g. Britton 2000). By comparing the noise properties of the same pulsars using overlapping data from from different telescopes, uncorrected noise from instrumental instabilities can potentially be identified (Lentati et al. 2016).

Unfortunately, pulsar timing data also exhibit some levels of "timing noise" (TN), low-frequency, stochastic, achromatic noise, the physical origin of which is unknown and, as such, cannot be mitigated. TN is primarily thought to be caused by pulsar rotational instabilities from various mechanisms. One approach is to consider simultaneous random walks and discrete jumps (caused, e.g., by micro-glitches) in the pulsar's spin frequency and the spin-down rate (e.g. Cordes & Downs 1985; D'Alessandro et al. 1995; Shannon & Cordes 2010). Based on observational evidence, it is also suggested that TN can result from accumulated periodic and quasi-periodic changes in the spin-down rates due to magnetospheric state switching (Kramer et al. 2006a; Lyne et al. 2010). In addition, intrinsic noise has also been proposed to be the result of undetected (and therefore unmodelled) bodies in orbit, such as asteroid belts (Shannon et al. 2013) or planetary-mass objects in long, decadal orbits (Thorsett et al. 1999). Clearly, the measured TN in pulsar timing data can be a superposition of noise intrinsic to the pulsar, and any of the above non-intrinsic noise which is not properly mitigated, e.g. noise by DM variations not properly

corrected due to the lack of sufficient multi-frequency data.

While young pulsars show large amounts of low-frequency noise, MSPs typically show very low levels of such noise (Verbiest et al. 2009). Their highly stable rotations, short periods and absence of significant temporal changes in their pulse profile shapes (see e.g. Shao et al. 2013) make them excellent celestial clocks which can be timed to sub-100 ns precision over decades. MSPs are therefore the observed sources for GW-detection experiments, and indeed for all high-precision pulsar timing applications.

Despite their demonstrated rotational stability, some MSPs show significant amounts of TN. While their TN is considerably weaker than that of non-recycled pulsars, it can be significant enough to hinder GW detection. PSR B1937+21 (J1939+2134), the first ever discovered MSP, is a notable example of an MSP with strong TN (Kaspi et al. 1994; Shannon et al. 2013). Other MSPs show more moderate noise levels, comparable to the predicted strength of the targeted GWs signals (e.g. PSR J1713+0747; see Zhu et al. 2015). The characterisation of TN is therefore of central importance in high-precision pulsar timing applications.

The measured TN will also contain signals from spatially correlated low-frequency noise (e.g. Tiburzi et al. 2016). Primary examples are the long sought-after stochastic GWB, the signal caused by errors in the reference terrestrial time-standards (see e.g. Hobbs et al. 2012) and errors in the Solar-system ephemeris (see Champion et al. 2010). These signals can be distinguished by the spatial cross-correlations they induce on the timing residuals. The GWB induces a quadrupole signature (see §4.7.1). Errors in the terrestrial time-standards produce a fully correlated signal in all pulsars (see §4.6) while errors in the Solar-system ephemeris can potentially produce a superposition of dipolar correlations between pulsars, each produced by the error in the predicted location of a Solar-system body. PTAs allow such correlated signals to be recovered or put upper limits on their power.

Different methods have been proposed and employed to characterise the statistical properties of TN in pulsar-timing data and to perform timing analysis in the presence of correlated noise. These cover techniques based on frequentist (Matsakis et al. 1997; Coles et al. 2011) and Bayesian statistics (e.g. van Haasteren et al. 2009; Lentati et al. 2014), both in the time- and frequency-domain. As part of the efforts to detect GWs, an increasing number of algorithms are being used by the various PTAs to determine the TN properties of MSPs, motivating work to examine the possible biases inherent to different methods. In this context, we perform characterisation of the TN using two established methods based on different statistical analyses, Bayesian and frequentist, and make a comparison of their performance and results. We subsequently use the measured TN properties to search for the presence of TN unique to specific observing systems, place an upper limit on the contribution of clock errors to the measured noise and investigate the impact of the TN on the data set's sensitivity to GWs.

This chapter is organised as follows. A brief overview of the used data is given in §5.3.3, followed by a presentation of the methods used to calculate the noise parameters in §4.3. The results from both methods are presented in §4.4. In §4.5, a search for TN present only in individual data subsets is presented, followed by a search for a correlated clock error signal in §4.6. In §4.7, the effects of the TN present in our data on their sensitivity to GWBs and CGWs are evaluated and finally in §4.8 the results and their implications are discussed.

4.2 Key Properties of the Data Set

We use the EPTA DR 1.0 described in §3.3.1. As we have seen, the data set includes TOAs from 42 MSPs. Table 4.1 summarises the properties which are central in noise analysis. As in the previous chapter, we keep the identification of observing systems as unique combinations of telescope, backend and central observing frequency. The EBPP L-band data have the longest time-span, with a maximum of 18 years, starting from October 1996, divided into two observing systems, due to a change in the receiver in 2009. For most of the sources with EBPP data, all other instruments started recording from 2007 onwards, dividing our longest pulsar data sets into two subsets: the first, with single-telescope, single-frequency data and the second, with multi-telescope, multi-frequency data. The lack of multi-frequency data in the first half of the data set makes direct measurements and corrections of the DM variations impossible. It is however possible to extrapolate the signal measured in the second epoch to the first, under the assumption that the DM variations signal is stationary (see Lee et al. 2014). This is performed using the Bayesian analysis methods described in §4.3.2. For a number of MSPs (e.g. PSR J1713+0747, PSR J1012+5307), multi-telescope coverage begins in 1999 with PuMaI data, which contain good quality low-frequency data, allowing direct measurements of the DM variations almost throughout the data set. We note that four MSPs (see Table 4.1) suffer from a gap in the Effelsberg L-band data for the period between April 1999 and October 2005. The gap is due to changes in the observing priorities.

4.3 Methods for Estimating Noise Properties

For the estimation of the noise properties, we use two different methods. The first method follows a Bayesian approach, in the time-frequency domain and is described in Lentati et al. (2014). The second method uses frequentist statistics based on power-spectral estimation of the residuals and using algorithms described in §4.3.3, which are an extension of those introduced in Coles et al. (2011). We first discuss the noise model components, which we use for both approaches, and then present the details of each method used.

4.3.1 Noise Modelling

We form the timing residuals using the pulsar timing analysis package `Tempo2` (Hobbs et al. 2006), which iteratively performs a weighted least-squares (wLS) fit of the model to the TOAs until the reduced chi-squared of the residuals is minimised. Timing models are gradually improved over many years by incorporating more data. These solutions will often result in timing residuals scattered beyond what would be expected based on their formal uncertainties, due to the absence, at this point, of the stochastic signals in the model. As briefly introduced in §3.3.2, these signals are in general divided into the time-correlated and uncorrelated components. We now discuss these components in detail.

The uncorrelated (white-noise) components correct the uncertainties of the timing residuals. The formal uncertainties of the TOAs are derived by the cross-correlation of the recorded integrated pulse profile with a reference template, which is constructed using the best available observations. These uncertainties are correct if the recorded profiles are characterised solely by (white) radiometer noise and the profile template precisely represents the intrinsic shape of the integrated profile. However, possible presence of un-excised RFI, temporal variations in the pulse profile, artefacts in the profiles from instrumental instabilities or imperfect profile templates can lead to errors in the uncertainty estimations

Table 4.1: General characteristics of the EPTA DR 1.0. For each pulsar we note the total time-span, T, the ranges of the observing frequencies, ν, the number of observing systems and the number of TOAs. Sources marked with a star suffer from a gap of ~6 years (1999-2005) in the Effelsberg 1410 MHz data.

PSR J-Name	T (yrs)	ν range (MHz)	number of systems	number of TOAs
J0030+0451⋆	15.1	1345-2678	7	907
J0034−0534	13.5	323-1628	6	276
J0218+4232	17.6	323-2683	13	1196
J0610−2100	6.9	1365-1632	3	1034
J0613−0200	16.1	323-2636	14	1369
J0621+1002	11.8	323-2635	10	673
J0751+1807	17.6	1352-2695	9	796
J0900−3144	6.9	1365-2303	5	875
J1012+5307	16.8	323-2636	15	1459
J1022+1001	17.5	323-2634	10	908
J1024−0719⋆	17.3	1346-2628	9	561
J1455−3330	9.2	1367-1698	3	524
J1600−3053	7.6	1366-2298	4	531
J1640+2224	17.3	1335-2636	8	595
J1643−1224	17.3	1353-2639	11	759
J1713+0747	17.7	820-2637	14	1188
J1721−2457	12.7	1335-1698	4	150
J1730−2304⋆	16.7	1352-2629	8	268
J1738+0333	7.3	1366-1630	3	318
J1744−1134	17.3	323-2634	9	536
J1751−2857	8.3	1397-1631	3	144
J1801−1417	7.1	1395-1697	3	126
J1802−2124	7.2	1366-2048	4	522
J1804−2717	8.1	1374-1698	3	116
J1843−1113	10.1	1335-1629	5	224
J1853+1303	8.4	1397-1698	3	101
J1857+0943	17.3	1335-2632	9	444
J1909−3744	9.4	1367-2681	3	425
J1910+1256	8.5	1366-1630	3	112
J1911−1114	8.8	1397-1630	4	130
J1911+1347	7.5	1365-1698	3	140
J1918−0642	12.8	1372-1630	6	278
J1939+2134	24.1	820-2278	12	3172
J1955+2908	8.1	1395-1629	4	157
J2010−1323	7.4	1381-2298	5	390
J2019+2425	9.1	1365-1629	3	130
J2033+1734	7.9	1367-1631	4	194
J2124−3358	9.4	1365-2298	5	544
J2145−0750	17.5	323-2683	12	800
J2229+2643	8.2	1355-2637	6	316
J2317+1439⋆	17.3	1352-2637	8	555
J2322+2057	7.9	1395-1698	4	229

(e.g. Liu et al. 2011). Furthermore, additional scatter in the TOAs caused by statistically independent physical processes, such as pulse phase jitter noise (e.g. Shannon et al. 2014). We therefore use the two error correction terms described in §3.3.2, namely the multiplicative correction factor, EFAC, and the term added in quadrature, EQUAD. We do not investigate the physical origin of the noise included in the EQUADs. This requires a more detailed analysis of the white noise; for example, jitter noise is dependent on the integration time of the observation and this needs to be properly taken into consideration if one wants the EQUAD number to describe an underlying physical process.

Following the same approach as in the timing analysis presented in the previous chapter, we include one EFAC and one EQUAD term per observing system to mathematically model the uncorrelated noise from all possible processes. The white-noise correction factors should be such that the data satisfy the central assumption of pulsar timing, that they are drawn from a random Gaussian process. In other words, when subtracting the waveforms (induced residuals) of all calculated stochastic signals from the residuals, their uncertainties should be such that the residuals are white and the timing solution has a reduced chi-squared of unity. The original TOA uncertainty, σ, EFAC (f), EQUAD (q) and corrected uncertainy, $\hat{\sigma}$, are related[1] as:

$$\hat{\sigma}^2 = (\sigma \cdot f)^2 + q^2 \tag{4.1}$$

We include two stationary time-correlated noise components, namely the chromatic low-frequency noise from DM variations and the achromatic TN. Previous studies (e.g. Shannon & Cordes 2010; Coles et al. 2011) have shown that the low-frequency power spectra of pulsar timing residuals can be adequately modelled with single power-laws for the majority of MSPs. This does not mean that the TN is necessarily a pure power-law, but rather that this functional form is sufficient to describe the data, given the measurement precision. We examined whether deviations from the single power-law model are supported by the data using the Bayesian analysis method. In particular, we performed the noise analysis with two additional models for the TN spectrum: (i) a model that allows the power of individual frequency bins to vary independently from the power law model and (ii) a model that includes the power-law and an additional sinusoid signal of varying frequency, amplitude and phase. We evaluated the results using the Bayes factor, i.e. the ratio of the Bayesian evidence of two competing models (see also §4.3.2). A common interpretation of the Bayes factor is given by Kass & Raftery (1995), based on which we required a value equal or greater than 3 to justify the addition of any extra model parameter. This was not the case for any of the models we compared to the simple single power-law model.

In this work, we have followed the single power-law formalism for both analysis methods in order to facilitate their comparison and the comparison of the measured TN parameters with those usually used as GW stochastic parameters in the PTA literature. For isotropic GW signals (see §4.7) one of the most important properties is the characteristic strain spectrum, $h_c(f)$, of the GWB on the one-sided power spectrum of the induced timing residuals. For most models of interest, this can be written as a power-law function of the GW frequency (e.g. Jenet et al. 2005), f as:

[1] This definition is not unique. `Tempo2` by default defines the correction as $\hat{\sigma}^2 = f^2 \cdot (\sigma^2 + q^2)$

$$h_c(f) = A\Big(\frac{f}{f_r}\Big)^{\alpha} \tag{4.2}$$

where A is the (dimensionless) amplitude of the wave, α is the spectral index[2] and f_r is the reference frequency, typically set to 1 yr^{-1}. The one-sided power spectral density of the signal is then given by:

$$S(f) = \frac{A^2}{12\pi^2}\Big(\frac{f}{f_r}\Big)^{-\gamma} \tag{4.3}$$

where the power spectrum and strain spectral indices are related as $\gamma \equiv 3 - 2\alpha$. This is the functional form we use to model the TN. We set a cut-off at frequency 1/T, where T is the time-span of the data. The cut-off arises naturally because the fitted pulsars' spin and spin-down absorb the power from any achromatic low-frequency signal below the cut-off frequency. It has been shown (van Haasteren et al. 2009; Lee et al. 2012) that if the spectral index is $\gamma \lesssim 7$ (which is the case for all MSPs in this study), the cut-off at frequency 1/T is sufficient.

The DM variations have been mitigated using first- and second-order DM derivatives in the timing model (which are first- and second-order polynomials) and additionally a power law equivalent to Eq. (4.3). The DM derivatives absorb any power from the stochastic DM component below the cut-off frequency, in the same way the spin and spin-down do for the achromatic TN (Lee et al. 2014). The observing frequency dependence of the DM variations signal is measured in the time-domain via the (multi-frequency) timing residuals, as we show in §4.3.2. The choice of a power-law spectrum for the DM variations is motivated by the fact that, across a wide spatial frequency range, the electron density fluctuation spectrum usually follows a power-law (Armstrong et al. 1995).

4.3.2 Noise Parameter Estimation Using Bayesian Inference

The first Bayesian investigation of the GWB detectability with PTAs was performed by van Haasteren et al. (2009). The algorithms were later applied on EPTA data to derive the EPTA GWB upper limit (van Haasteren et al. 2011). In that analysis, the timing noise parameters of the MSPs were simultaneously estimated with the GWB parameters. Further work on Bayesian analysis methods for pulsar timing provided more algorithms, both in time- and time-frequency-domains, to characterise the properties of timing noise and DM variations and to perform robust pulsar timing analysis in the presence of correlated noise (e.g. van Haasteren et al. 2011; Lentati et al. 2013; Lee et al. 2014).

Bayes' theorem, which is the central equation for these analysis methods, states that:

$$Pr(\Theta) = \frac{L(\Theta)\pi(\Theta)}{Z}, \tag{4.4}$$

[2] We define the index positive, but note that in the literature it is sometimes defined as a negative number

where Θ is the model's parameters, $Pr(\Theta)$ is the posterior probability distribution (PPD) of the parameters (probability distribution of the parameters given the model and the data), $\pi(\Theta)$ is the prior probability distribution (pPD) of the parameters (the initial hypothesis of the probability distribution of the parameters for a given model), $L(\Theta)$ is the likelihood function (which gives the probability that the data are described by a given model) and Z is the Bayesian evidence. Z is only a normalising factor independent of Θ and can therefore be ignored when one is interested only in parameter estimation, such that $Pr(\Theta) \propto L(\Theta)\pi(\Theta)$. On the other hand, when one is interested in model selection, the ratio of the evidence between two different models, $\mathcal{R}$, known as the Bayes factor, is used. The probability, $\mathcal{P}$, of a model compared to another, can the expressed (Kass & Raftery 1995) as:

$$\mathcal{P} = \frac{\mathcal{R}}{1+\mathcal{R}} \tag{4.5}$$

The various Bayesian analysis algorithms are distinguished by the mathematical description of the model parameters and the computational methods used to sample the unnormalised PPD.

Lentati et al. (2014) introduced `TempoNest`, a Bayesian software package for the analysis of pulsar timing data, available to use as a `Tempo2` plug-in. The timing solution and the additional stochastic parameters such as EFACs, EQUADs, DM variations and the TN (referred to as "excess red noise") can be determined simultaneously. `TempoNest` uses the Bayesian inference tool MultiNest (Feroz & Hobson 2008) to explore this joint parameter space, whilst using `Tempo2` as an established means of evaluating the timing model at each point in that space. For the PPD sampling, `TempoNest` uses the nested sampling Monte-Carlo method (Skilling 2004).

We perform a joint analysis for the timing model and the stochastic parameters. Both the TN and the DM variations are modelled as Gaussian stochastic signals with power-law spectra as described by Eq. (4.3). `TempoNest` employs the time-frequency analysis described in Lentati et al. (2013). The TN waveform is expressed as (here, and henceforth, we use boldface characters in equations to denote matrices) $\mathbf{t}_{\rm TN} = \mathbf{F}_{\rm TN}\mathbf{a}$, where $\mathbf{F}_{\rm TN}$ is the Fourier transform with elements $\mathsf{F} = \sin(2\pi f) + \cos(2\pi f)$ and corresponding coefficients, $\mathbf{a}$, which are free parameters. The Fourier frequencies take values $f = n/\mathrm{T}$, with n integers ranging from 1 up to the value necessary to sample frequencies as high as 1/14 days^{-1}. The covariance matrix of the TN is then described by the following equation (see Lentati et al. 2015):

$$\mathbf{C}_{\rm TN} = \mathbf{C}_{\rm w}^{-1} - \mathbf{C}_{\rm w}^{-1}\mathbf{F}_{\rm TN}\left[(\mathbf{F}_{\rm TN})^{\mathbf{T}}\mathbf{C}_{\rm w}^{-1}\mathbf{F}_{\rm TN} + (\Psi)^{-1}\right]^{-1}(\mathbf{F}_{\rm TN})^{\mathbf{T}}\mathbf{C}_{\rm w}^{-1}. \tag{4.6}$$

Here, $\Psi = \langle \mathrm{a}_i \mathrm{a}_j \rangle$, is the covariance matrix of the Fourier coefficients and $\mathbf{C}_{\rm w}$ is the covariance matrix of the white noise component, a diagonal matrix with the main diagonal populated by the residual uncertainties squared, $\hat{\sigma}^2$ (as in Eq. 4.1). The superscript $\mathbf{T}$ denotes the transpose of the matrix.

The covariance matrix for the DM variations, $\mathbf{C}_{\rm DM}$, is equivalent to Eq. (4.6), but including an observing frequency dependence. This is achieved by replacing the $\mathbf{F}$ elements with $\mathsf{F}_{ij}^{DM} = \mathsf{F}_{ij}D_iD_j$, where the i,j indices denote the residual numbers, $D_i = 1/K\nu_i^2$, where ν_i is the observing frequency of the TOA, typically set as the central frequency of the observing band, and K=2.41×10^{-16} Hz^{-2}cm^{-3}pc

s^{-1}, is the dispersion constant.

The likelihood function is the probability that the data (the TOAs), noted as $\mathbf{t}$, are fully described by the timing model signal, $\boldsymbol{\tau}(\boldsymbol{\epsilon})$, with parameters $\boldsymbol{\epsilon}$ and the stochastic noise. The latter is encoded in the residuals' total covariance matrix,

$$\mathbf{C} = \mathbf{C}_{\mathrm{w}} + \mathbf{C}_{\mathrm{DM}} + \mathbf{C}_{\mathrm{TN}}. \tag{4.7}$$

Following van Haasteren et al. (2009), and noting that the difference $\mathbf{t} - \boldsymbol{\tau}(\boldsymbol{\epsilon})$ gives the timing residuals vector, we can write the likelihood function as:

$$L = \frac{1}{\sqrt{(2\pi)^n |\mathbf{C}|}} e^{-\frac{1}{2}(\mathbf{t}-\boldsymbol{\tau}(\boldsymbol{\epsilon}))^{\mathrm{T}} \mathbf{C}^{-1} (\mathbf{t}-\boldsymbol{\tau}(\boldsymbol{\epsilon}))}. \tag{4.8}$$

After the noise properties are estimated, we produce the TN waveforms, which can be estimated from the data using the ML value of its statistical model parameters, A and γ. As shown in Lee et al. (2014), the ML waveform, $\mathbf{t}_{\mathrm{TN}}$, and its uncertainties, σ_{TN}, are optimally estimated as

$$\mathbf{t}_{\mathrm{TN}} = \mathbf{C}_{\mathrm{TN}} \mathbf{C}^{-1} \mathbf{t}\,, \tag{4.9}$$

with uncertainties estimated as:

$$\sigma_{\mathrm{TN}} = \mathbf{C}_{\mathrm{TN}} - \mathbf{C}_{\mathrm{TN}} \mathbf{C}^{-1} \mathbf{C}_{\mathrm{TN}}. \tag{4.10}$$

The uncertainties are estimated as the standard deviation of the estimator. However, as noted in Lee et al. (2014), since the components of TN waveforms are correlated, their interpretation in terms of uncertainties is meaningless, since this is only valid under the assumption that the noise is uncorrelated. The uncertainties can therefore only be used as an indication of the variance of each point.

We have performed the Bayesian inference analysis twice using different combination of pPDs. The pPDs on the timing parameters are always uniform, centred around the value from the wLS fit of the timing model by `Tempo2` with a range of 10 to 20 times their 1-σ `Tempo2` uncertainties. This range was chosen after testing verified that is sufficient for all timing parameters PPDs to converge. For the noise parameters, the ranges are from 0 to 7 for spectral indices, -20 to 8 for the logarithm of the amplitudes, -10 to -3 for the logarithm of the EQUADs and 0.3 to 30 for the EFACs. For EQUADs, TN and DM variations amplitudes we used two different types of pPDs. The first is a uniform distribution in log space (log-uniform) and the second is a uniform distribution in linear space (uniform). Log-uniform pPDs assume that all orders of magnitude are equally likely for the parameter value while for uniform pPDs, we assign the same probability for all values. The uninformative log-uniform pPDs will result in PPDs for the parameters that are the least affected by the pPD and therefore are what we consider as the

parameter measurement. If no significant noise can be detected in the data, the PPDs are unconstrained and the distribution's upper limit is dependent on the lower limit of the pPD. Therefore, a separate analysis is required using uniform pPDs in order to obtain robust upper limits. If the signal is strong and the result from a log-uniform-pPD analysis is a well-constrained PPD, then the change of the pPD should not affect the result significantly and the PPDs should be almost identical. As a result, we performed the analysis with the following combination of pPDs:
a) Uniform EQUAD pPDs and log-uniform pPDs for TN and DM variation amplitudes. This set of pPDs results in upper limits for EQUADs. As such, the solutions have the highest possible timing residuals uncertainties, resulting in weaker TN and DM variations detections. The TN and the DM variations are treated in the same way, giving no prior information that can favour the one over the other when multi-frequency data are not sufficient to de-couple them. In the absence of multi-frequency data one can therefore expect that their PPDs will not be well-constrained.
b) Uniform TN amplitude and log-uniform pPDs for EQUADs and DM variation amplitudes: The total white noise levels of these solutions are lower, since EQUAD PPDs can be flat if the data do not support them to be measurable. The use of uniform pPDs for the TN amplitude and log-uniform for the DM variations results in solutions in favour of the TN against the DM variations in the absence of multi-frequency data. This set of pPDs will provide the strictest upper limits on the TN amplitudes. We used the PPDs from this analysis to calculate the amplitude upper limits at the 95% C.L.

4.3.3 Noise Parameter Estimation Using Power-Spectral Analysis

Power-spectral analysis of pulsar timing data using standard discrete Fourier transforms is complicated by highly variable error bars, irregular sampling, data gaps (due to difficulties in being granted telescope time at exact regular intervals but also due to loss of data from technical difficulties, weather conditions, telescope maintenance or from weak pulses on particular days due to unfavourable interstellar scintillation) and the presence of TN which has a steep red spectrum. Fourier transforms require equispaced data points. Interpolation of data points on regular grids introduces time-correlations in data points and the presence of strong TN introduces spectral leakage. In order to bypass such problems, Coles et al. (2011) introduced an algorithm for pulsar-timing analysis in the presence of correlated noise which employs the use of generalised least-squares (GLS) analysis of the timing data using the covariance matrix of the residuals (as described in §4.3.2). In brief, the covariance matrix of the residuals is used to perform a linear transformation that whitens both the residuals and the timing model. The transformation is based on the Cholesky decomposition of the covariance matrix.

For this algorithm, initial estimates of the residuals covariance matrix are necessary, and are obtained using the Lomb-Scargle periodogram (LSP), which can calculate the power spectrum of irregularly sampled data. Spectral leakage in the presence of strong TN with steep power-law spectra is mitigated with pre-whitening using the difference filter. The difference pre-whitening filter of any order, k, can be described by $y_{w,k} = y_{w,k-1}(t_i) - y_{w,k-1}(t_{i-1})$, where t_i is the i-th sampling time and $y_{w,k}$ is the whitened residual of difference order k ($k = 0$ corresponds to the original residuals). It was suggested to use the lowest order necessary to whiten the data enough to mitigate spectral leakage. Effectively, this filter is equivalent to multiplying the power spectrum by a filter (e.g. for first order difference, the filter is the square of the transfer function). After the spectrum is estimated using the pre-whitened data, one corrects the power spectrum by dividing it with the same filter, a process known as post-darkening. The low-frequency spectrum can be fitted with a power-law model leading to the first estimation of the covariance matrix. Through an iterative process, new estimates of the spectrum can be achieved by

Table 4.2: Timing-noise characteristics of EPTA MSPs based on Bayesian inference for a single power-law model as described by Equation (4.3). The results are divided based on the quality of the posterior probability distributions (PPDs) as described in §4.4.1. We tabulate the maximum likelihood (ML) and median (med) values of the dimensionless amplitude, A, at reference frequency of 1 yr^{-1} and the spectral index, γ. For A, we also tabulate the 95% confidence upper limits. The 1-σ uncertainties are calculated such that the 68% of the area under the 1-dimensional marginalised PPS of the parameter is symmetrically distributed around the median. As described in §4.4.1, for unconstrained PPDs we only consider the upper-limits analysis results.

PSR J-Name	$\log(A_{ML})$	$\log(A_{med})$	$\log(A_{UL}^{95\%})$	γ_{ML}	γ_{med}
			Well-constrained PPDs		
J0621+1002	−12.029	$-12.07^{+0.06}_{-0.06}$	−11.9	2.5	$2.4^{+0.3}_{-0.2}$
J1012+5307	−13.20	$-13.09^{+0.07}_{-0.07}$	−12.94	1.7	$1.7^{+0.3}_{-0.2}$
J1022+1001	−13.2	$-13.0^{+0.1}_{-0.2}$	−12.8	2.2	$1.6^{+0.4}_{-0.4}$
J1600−3053	−13.35	$-13.28^{+0.06}_{-0.06}$	−13.11	1.2	$1.7^{+0.3}_{-0.2}$
J1713+0747	−14.7	$-15.2^{+0.5}_{-0.5}$	−13.8	4.8	$5.4^{+0.9}_{-1.0}$
J1744−1134	−13.7	$-13.8^{+0.2}_{-0.3}$	−13.3	2.2	$2.7^{+0.7}_{-0.6}$
J1857+0943	−13.3	$-13.3^{+0.2}_{-0.3}$	−12.9	2.6	$2.4^{+0.7}_{-0.6}$
J1939+2134	−14.2	$-14.5^{+0.3}_{-0.3}$	−13.7	5.9	$6.2^{+0.5}_{-0.6}$
			Semi-constrained PPDs		
J0030+0451	−14.9	$-14.9^{+0.8}_{-2.1}$	−13.0	6.3	$5.2^{+1.2}_{-2.1}$
J0218+4232	−13.1	$-14.1^{+1.0}_{-1.7}$	−12.4	2.7	$3.9^{+1.7}_{-1.6}$
J0610−2100	−18.7	$-16.0^{+2.9}_{-2.7}$	−12.4	1.4	$2.7^{+2.8}_{-2.1}$
J0613−0200	−13.7	$-14.4^{+0.7}_{-0.9}$	−13.0	2.8	$4.1^{+1.6}_{-1.5}$
J0751+1807	−18.8	$-15.9^{+2.6}_{-2.7}$	−12.9	6.5	$3.0^{+2.0}_{-1.4}$
J1024−0719	−14.0	$-16.3^{+2.1}_{-2.4}$	−13.1	5.3	$3.9^{+2.0}_{-2.5}$
J1455−3330	−19.8	$-14.2^{+1.0}_{-3.7}$	−12.7	0.8	$3.6^{+1.9}_{-1.6}$
J1640+2224	−13.2	$-13.1^{+0.2}_{-3.4}$	−12.8	0.01	$0.4^{+1.7}_{-0.3}$
J1643−1224	−17.7	$-13.3^{+0.6}_{-2.4}$	−12.5	1.8	$1.7^{+0.9}_{-0.6}$
J1721−2457	−11.7	$-13.5^{+1.7}_{-4.5}$	−11.5	1.1	$1.9^{+2.7}_{-1.0}$
J1730−2304	−12.8	$-14.7^{+1.7}_{-3.6}$	−12.6	1.8	$2.9^{+1.9}_{-1.3}$
J1801−1417	−14.4	$-15.1^{+2.5}_{-3.4}$	−12.2	6.3	$3.3^{+2.2}_{-1.8}$
J1802−2124	−17.0	$-15.6^{+3.2}_{-3.0}$	−12.2	4.5	$2.3^{+2.9}_{-0.8}$
J1843−1113	−13.0	$-12.9^{+0.2}_{-3.3}$	−12.5	0.6	$1.5^{+3.1}_{-0.5}$
J1909−3744	−14.1	$-14.1^{+0.2}_{-1.9}$	−13.8	2.4	$2.3^{+1.0}_{-0.6}$
J1918−0642	−16.9	$-14.5^{+0.7}_{-0.5}$	−12.6	1.7	$5.4^{+1.1}_{-1.6}$
J2145−0750	−14.4	$-14.0^{+0.6}_{-0.8}$	−12.9	5.2	$4.1^{+1.6}_{-1.3}$
			Unconstrained PPDs		
J0034−0534	-	-	−12.3	-	-
J0900−3144	-	-	−12.7	-	-
J1738+0333	-	-	−12.7	-	-
J1751−2857	-	-	−12.4	-	-
J1804−2717	-	-	−12.3	-	-
J1853+1303	-	-	−12.4	-	-
J1910+1256	-	-	−12.1	-	-
J1911−1114	-	-	−12.1	-	-
J1911+1347	-	-	−12.9	-	-
J1955+2908	-	-	−12.1	-	-
J2010−1323	-	-	−12.8	-	-
J2019+2425	-	-	−11.9	-	-
J2033+1734	-	-	−12.0	-	-
J2124−3358	-	-	−12.8	-	-
J2229+2643	-	-	−12.7	-	-
J2317+1439	-	-	−13.1	-	-
J2322+2057	-	-	−12.3	-	-

Table 4.3: Timing-noise characteristics of EPTA MSPs based on power-spectral analysis for a single power-law model as described by Equation (4.3). We tabulate the dimensionless amplitude, A, at reference frequency of $1\mathrm{yr}^{-1}$, the spectral index, γ, and the white-noise power level, S_{W}, and their respective 1-σ uncertainties. We also tabulate the pre-whitening level used ($\mathrm{level_{pw}}$). For the pulsars where the measurement of timing noise was not possible, we quote the 95% confidence upper limits for the amplitude. The table is divided as Table 4.2 for easier comparison.

Measured				
PSR J-Name	log(A)	γ	$\log(S_{\mathrm{W}}(\mathrm{yr}^3))$	$\mathrm{level_{pw}}$
J0621+1002	−12.3±0.1	2.8±0.6	−26.94±0.04	1
J1012+5307	−13.01±0.07	1.7±0.3	−28.60±0.02	1
J1022+1001	−13.2±0.2	2.0±0.6	−27.97±0.03	0
J1600−3053	−13.6±0.1	1.3±0.5	−29.36±0.05	0
J1713+0747	−14.2±0.2	4.9±0.6	−30.146±0.02	2
J1744−1134	−13.6±0.2	3.0±0.6	−28.90±0.03	1
J1857+0943	−13.2±0.2	2.3±0.7	−27.97±0.04	1
J1939+2134	−14.3±0.1	6.7±0.5	−30.27 ± 0.02	2
J0030+0451	−13.2 ± 0.4	4.5 ± 1.0	−27.78±0.03	2
J0218+4232	−12.6±0.2	2.3±0.6	−26.69±0.03	0
J0610−2100	-13.6±0.1	2.1±0.6	−29.62±0.03	0
J0613−0200	-14.9±0.9	5.2±1.8	−28.45±0.03	0
J0751+1807	-14.3±0.7	5.2±1.6	−27.86±0.03	1
J1024-0719	−13.0±0.1	4.1±0.5	−28.15±0.03	2
J1455−3330	−13.4±0.4	3.5±1.2	−27.59±0.03	0
J1640+2224	−13.0±0.1	1.4±0.4	−27.96±0.05	0
J1643−1224	−13.2±0.1	3.5±0.4	−28.25±0.03	0
J1721−2457	−12.3±0.3	2.7±0.8	−26.01±0.09	0
J1730−2304	−12.8±0.2	1.7±0.5	−27.31±0.06	0
J1801−1417	−13.3±0.3	2.4±1.1	−28.41±0.10	0
J1802−2124	−12.8±0.2	2.9±0.7	−27.93±0.04	0
J1843−1113	−12.8±0.1	3.0±0.6	−27.93±0.05	1
J1909−3744	−14.5±0.7	1.6±1.7	−30.05±0.04	0
J1918−0642	−13.0±0.2	2.8±0.8	−27.72±0.05	1
J2145-0750	−13.7±0.3	3.5±0.7	−28.36 ± 0.03	0
Upper Limits				
PSR J-Name	$\log(A_{\mathrm{UL}}^{95\%})$		$\log(S_{\mathrm{W}}(\mathrm{yr}^3))$	$\mathrm{level_{pw}}$
J0034−0534	−12.4	-	−27.02 ± 0.05	0
J0900−3144	−12.8	-	−28.0 ± 0.1	0
J1738+0333	−12.6	-	−27.36 ± 0.04	0
J1751−2857	−12.1	-	−27.3 ± 0.6	0
J1804−2717	−12.2	-	−26.57 ± 0.09	0
J1853+1303	−12.7	-	−27.7 ± 0.1	0
J1910+1256	−12.6	-	−27.38 ± 0.06	0
J1911−1114	−12.2	-	−26.7 ± 0.1	0
J1911+1347	−12.8	-	−27.88±0.1	0
J1955+2908	−12.1	-	−26.46 ± 0.06	0
J2010−1323	−12.9	-	−27.95 ± 0.04	0
J2019+2425	−12.0	-	−26.14 ± 0.08	0
J2033+1734	−12.0	-	−26.15 ± 0.06	0
J2124−3358	−12.8	-	−27.69 ± 0.04	0
J2229+2643	−12.7	-	−27.66 ± 0.05	1
J2317+1439	−12.8	-	−27.678 ± 0.03	0
J2322+2057	−12.3	-	−26.78 ± 0.05	0

using LSP after whitening the data using the Cholesky decomposition of the covariance matrix.

Coles et al. (2011) have demonstrated that the implementation of this method allows better timing solutions with more robust timing parameters and uncertainty calculations. In particular the measured spin and spin-down of the pulsar show the largest improvements, since they have low-frequency signatures in the Fourier domain and correlate with TN. However, this method is not optimised to accurately estimate the TN properties through detailed fitting of a noise model to the power-spectrum. The algorithm described in Coles et al. (2011) focuses on obtaining a linear, unbiased estimator of the timing parameters. For this purpose, they demonstrate that using the GLS timing solutions using the covariance matrices of any TN models which whiten the data sufficiently to remove spectral leakage, are statistically consistent. In this work, we extend the algorithms of Coles et al. (2011), focusing on the precise evaluation of the power spectra and the power-law model parameters. To this end, we have developed an independent power spectral analysis and model fitting code.

A fully frequentist analysis should include a white-noise and DM-correction analysis. However, in order to focus on comparing the methods with regards to the estimation of the TN properties, we use the ML EFAC and EQUAD values and subtract the ML DM-variations waveforms derived from the Bayesian analysis.

Our spectral analysis code calculates a generalised LSP, i.e. it performs a wLS fit of sine and cosine pairs at each frequency. We follow an iterative procedure as follows: (1) We first use `Tempo2` to obtain the wLS post-fit residuals, while subtracting the ML DM variations signal estimated with the Bayesian methods described in §4.3.2. (2) We calculate the spectrum of these residuals using a chi-squared minimisation fit on all frequency points. (3) `Tempo2` is re-run using the covariance matrix of the initial noise model to perform a GLS fit. (4) Finally, we re-run the spectral analysis code on the residuals from the GLS timing solution to update the TN model and repeat steps 3 and 4 until the solution converges. Typically, this required no more than one iteration.

Our code implements a generalised LSP to account for the timing residual uncertainties. Denoting each pair of time and residual as (t_i, y_i), the LSP is formed by fitting sine-cosine pairs of the form $\hat{y}(\omega_k, t_i) = a_k \cos(\omega_k t_i) + b_k \sin(\omega_k t_j)$ at all angular frequencies, $\omega_k = 2\pi f_k$, with f_k the frequency. The solution is obtained by minimising the chi-squared for each ω_k, weighted by the summed uncertainties of the timing residuals as:

$$\chi^2_k = \sum_i \left(\frac{y_i - a\sin(\omega t_i) - b\cos(\omega t_i)}{\hat{\sigma}_i} \right)^2. \tag{4.11}$$

Once the LSP is calculated, noting the number of timing residuals as N, the spectral density is finally computed as:

$$S(f) = \frac{2|\hat{y}|^2 T}{N^2}. \tag{4.12}$$

We examine whether spectral leakage is present following the same routine as in Coles et al. (2011). Visual inspection of the original spectrum allows to approximately define the frequency where the red component of the spectrum intersects the flat, white component. We apply a low-pass filter in time-domain to separate the high-frequency from the low-frequency residuals and calculate their individual spectra. The high-frequency spectrum should be consistent with the high-frequency part of the spectrum of the original data. If that is not the case, and instead the high-frequency spectrum is significantly weaker, then leakage is important and we need to apply the pre-whitening filter. The code allows for any order of difference whitening. For this data set, we required only up to second order. We then proceed with calculating the LSP as before and finally post-darken the spectrum before calculating the final spectral density.

We fit the power spectrum with the following function:

$$S(f) = S_0\Big(\frac{f}{f_r}\Big)^{-\gamma} + S_{\rm W}, \;\; S_0 = \frac{A^2}{12\pi^2}. \tag{4.13}$$

Here, $S_{\rm W}$ is the spectral density of the high-frequency (white) component. The power-law description of the low-frequency component is equivalent to Eq. (4.3), with S_0 the spectral density at reference frequency, f_r, which is set to $1\mathrm{yr}^{-1}$. A fit of only the low-frequency component is proven difficult; due to the steepness of the spectrum at low frequencies and moderate power of the TN in many MSPs, only about five frequency points would be included in a pure power-law fit of only the red part of the spectrum. This leads to unstable fits without meaningful error estimations.

The fit minimises the chi-squared, χ^2_S. Chi-squared minimisation assumes that the spectrum is normally distributed. In principle, the power spectrum is a chi-squared distribution. However, in logarithmic space, the distribution is approximately Gaussian with variance of order unity. Therefore this is a good approximation if we fit the power-law model to the spectrum in logarithmic space. By doing so, we minimise the chi-squared defined as:

$$\chi^2_S = \sum_{i=1}^{N} \left\{ \log S_i - \log\left(S_0 \left(\frac{f_i}{f_r}\right)^{-\gamma} + S_{\rm W} \right) \right\}^2, \tag{4.14}$$

where S_i and f_i define the points of the spectrum for each frequency bin, i, while simultaneously fitting for S_0, γ, and $S_{\rm W}$. We first fit the spectrum while setting the uncertainties of the LSP points to one and then scale the uncertainties to achieve a reduced chi-squared of unity.

Once we obtain the values for the noise parameters, we construct the covariance matrix of the TN, $\mathbf{C}_{\rm TN}$. The Fourier transform of the TN power-law model gives the covariance function, $c_{\rm TN}(\tau) = \langle \mathrm{t}_{TN,i}\mathrm{t}_{TN,j}\rangle$. The i and j indices refer to the time epoch of the observation and $\tau = t_i - t_j$. The TN covariance matrix is then formed by the elements $C_{{\rm TN},ij} = c(\tau_{{\rm TN},ij})$, where $\tau_{ij} = |t_i - t_j|$. Using the total covariance matrix (Eq. 4.7), we then perform a `Tempo2` GLS fit on the TOAs, repeat the power-spectrum analysis and power-law fit to update the model parameter values and iterate these steps until we converge to a stable solution.

For the cases where the spectra are white-noise dominated and no measurement of the TN parameters can be achieved on a 3-σ level, we derived upper limits for the TN amplitude. The limits are at the 95% C.L. and are calculated as the 2-σ upper limit of the white-noise level ($S_{\rm W}$ in Eq. (4.13) and Table 4.3).

4.4 Results

Table 4.2 summarises the results of the noise properties determined using `TempoNest`, while Table 4.3, summarises the results from the power spectral analysis. The reader can find online[3] the PPDs of the TN properties from the Bayesian analysis, the power spectra and the TN waveforms from both methods. In the rest of this section, we first discuss the framework under which we compare the results from the two methods and then proceed with the comparison of the results in more detail. We conclude this section by presenting and discussing the results on the white noise parameters from the Bayesian analysis.

4.4.1 Comparing Bayesian and Frequentists Results

Bayesian analysis is based on the principle that we test a hypothesis (model) given the data and a pPD. The latter is essential in Bayesian inference and states our prior degree of confidence on what the PD of the parameter is. The inference results in the PPD, which is the updated probability distribution for the unknown parameter, based on the information provided by the data. Bayesian inference also assigns the likelihood value for each model (i.e. for each set of values for all unknown parameters), providing a measure of how well the model describes the data. To evaluate the `TempoNest` results, we report in Table 4.2 the ML values of the TN parameters and the median value and 1-σ uncertainties of the one dimensional marginalised PPDs. The uncertainties are calculated such that 68% of the area under the distribution is symmetrically distributed around the median. The asymmetry of many PPDs will result in asymmetric error bars.

We sort the PPDs in three categories, and show representative examples in Figure 4.1. We name the first category of distributions “well-constrained”; this represents cases where the data were sufficient to obtain good measurements of the noise parameters. As seen in Figure 4.1 for the case of PSR J1012+5307, the PPDs are well defined and very close to symmetric. As a result, the median values of the 1-dimensional PPDs coincide well with the ML solution. There are cases where the PPD of at least one of the TN parameters suffers from long tails due to strong covariances between unknown parameters (e.g. amplitude of TN and amplitude of DM variation noise in the absence of sufficient multi-frequency data). We refer to these distributions as “semi-constrained”. As seen for the case of PSR J0751+1807 in Figure 4.1, the two-dimensional distribution shows a main area of high probability as well as many smaller regions of local maxima. The tails in the one dimensional distribution of amplitude (which in general extend to $\pm\infty$), causes the median values to vary significantly from the ML values. Moreover, the large amount of area under the curve, along the tail, causes the uncertainties around the median to have large and very asymmetric values. Finally, when the data do not support any evidence of TN, the PPDs are flat. We refer to these as “unconstrained”. As seen for the case of PSR J2229+2643 in Figure 4.1, the reported median and ML values do not hold a strong significance. The only meaningful result to report in such cases is the upper limits for the amplitude, as seen in the bottom right panel of Figure 4.1.

[3] http://www.epta.eu.org/aom/DR1noise.html

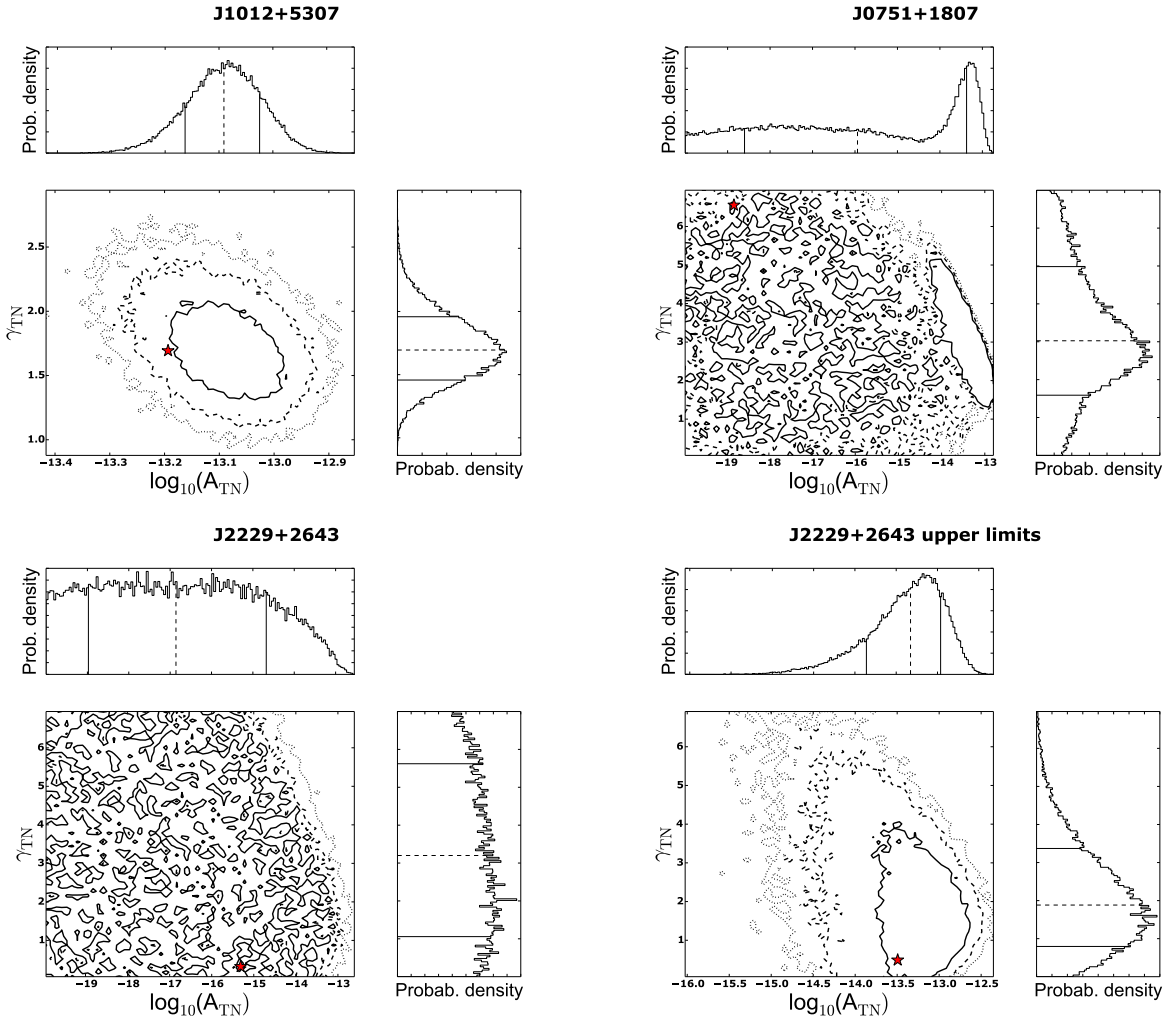

Figure 4.1: Two- and one-dimensional marginalised PPDs for the timing noise parameters of three pulsars: J1012+5307, J0751+1807, and J2229+2643. In the two-dimensional distributions, the solid, dashed and dotted contours represent the 68%, 95% and 99.7% (1-, 2- and 3-σ) confidence intervals and the red star marks the maximum likelihood solution. The 1-dimensional distributions have the median and 1-σ uncertainties marked as dashed and solid lines respectively. For J2229+2643, the right figure shows the distribution of the noise parameters from the upper limits analysis. Note the different ranges on the amplitude axes. See text in §4.4.1 for discussion.

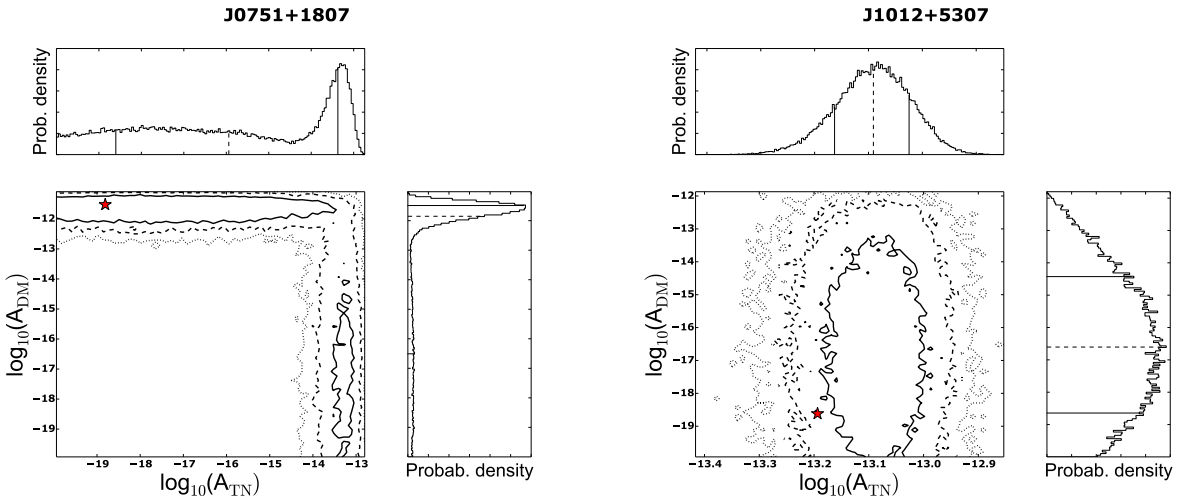

Figure 4.2: Two- and one-dimensional marginalised PPDs for the timing noise and DM variations amplitudes for J0751+1807 and J1012+5307. In the two-dimensional distributions, the solid, dashed and dotted contours represent the 68%, 95% and 99.7% (1-, 2- and 3-σ) confidence intervals and the red star marks the maximum likelihood solution. The 1-dimensional distributions have the median and 1-σ uncertainties marked as dashed and solid lines respectively. Note the different ranges on the amplitude axes. See text in §4.4.1 for discussion.

Power-spectral analysis provides single-value resultsfrom the power-law model fit to the power spectrum. This fit is performed under the assumption of Gaussian statistics. As discussed above, in the case of power spectra, this is only an approximation. Finally, the fit is dependent on the estimation of the uncertainties of the power spectrum points, which was ensured to be properly calculated by pre-whitening the data when TN caused spectral leakage. The comparison of the results derived with these two methods should also consider the effects of the Bayesian ML DM variations waveform subtraction from the residuals before performing the power-spectral analysis. In the case of semi-constrained PPDs, the amplitude parameters for the two TN and DM variations are naturally highly correlated. When this is the case, the ML parameter estimates are not as reliable, as the particular ML solution might correspond to either significant DM variations and no TN, or significant TN and no DM variations. This can lead to over- or under-estimations of the DM variations which will lead to either part of the TN being subtracted as well or part of the DM signal leaking into the TN.

As an example, we show in the left panel of Figure 4.2 the two- and one-dimensional marginalised PPDs for the amplitudes of the timing noise and DM variations for PSR J0751+1807 (semi-constrained PPDs case). One can see the strong covariance between the two parameters. The data support that the TN amplitude is more likely to be very low (the TN tail has more probability than the DM tail), however, there is still a non-zero probability that the DM variations signal is weaker than the ML model suggests. For well-constrained PPDs, DM variations and TN are de-coupled, as seen in the right panel of Figure 4.2 for the case of J1012+5307, and the DM ML waveform subtraction is more reliable. If the statistical assumptions of the Bayesian and frequentist analysis are valid, the results for the TN of pulsars with well-constrained PPDs should be consistent between the two methods.

4.4.2 Timing-Noise Parameters

Out of the 42 sources, the Bayesian analysis resulted in well-constrained PPDs for both the amplitude and the spectral index of the TN power-law model for eight sources. For these, the Bayesian ML and median values are always consistent at the 1-σ level. The two methods are always consistent at the 1-σ level for the spectral index, while for the amplitude, three sources show deviations, though consistency remains at the 2-σ level. (Figure 4.3, top row).

For 17 MSPs, the PPDs of at least one of the timing noise parameters is semi-constrained. The Bayesian ML and median values show inconsistencies at the 1-σ level in four pulsars (Figure 4.3, middle row). The power-spectral analysis results are in agreement with the Bayesian median values. All Bayesian upper limits are in agreement with the rest of the results. We note that for PSR J1909−3744, we did not achieve a 3-σ measurement for the spectral index with the power-spectral analysis.

The rest of the sources, 17 in total, show flat, unconstrained PPDs. The bottom row of Figure 4.3 shows the 95% C.L. upper limits from the two methods. Given the low significance of the TN measurement in these cases, inconsistencies in the amplitudes do not have statistically significant effects on the timing solutions when using the total covariance matrix to perform GLS timing analysis.

The agreement between the two methods for the sources with statistically significant TN measurements, supports the confidence in the methods and the results. When covariances between noise properties cannot be decoupled by the data, the interpretation of the results requires more attention. For this reason, we propose that cross-checks of the results with various methods should become common practice.

4.4.3 White-Noise Parameters

Radiometer noise estimation is typically robust when the pulse has a medium to high S/N (Taylor 1992), so EFACs are expected to be close to unity for most observing systems. The EQUADs results indicate for which observing systems there may be additional scatter in the residuals from physical processes related to the pulsars (e.g. pulse phase jitter) or RFI.

Figure 4.4 shows the distribution of the ML EFAC values. As expected, the distribution strongly peaks around unity. A few systems show EFAC values up to ∼5. These are typically high-frequency observations with very weakly detected pulses. The cases where EFACs take values significantly lower than one are either due to strong overestimation of the uncertainties or when a system's EFAC and EQUAD are highly correlated.

We examine in a similar way the distribution of EQUAD values. Figure 4.5 shows the distribution of the measured ML EQUAD values from the analysis using log-uniform EQUAD pPDs, and the distribution of their upper limits. As expected, in the vast majority of cases, the EQUADs are much below the TOA precision, which typically ranges from 0.5-10μs (see Table 3.2).

We have examined the EQUAD PPDs from the analysis with log-uniform pPDs to determine the cases where EQUADs have well-constrained PPDs and therefore show measurable EQUADs. For some of these cases, this could reflect signs of jitter noise present in the data. We list these pulsars and observing systems in Table 4.4. We note that there are 49 cases where the EQUAD PPDs are semi-constrained and significantly covariant with EFACs, and therefore cannot be considered as significant EQUAD measurements. From Table 4.4 we can see that the vast majority of EQUADs come from L-band systems, which typically have the most sensitive data. For each pulsar there are usually only one

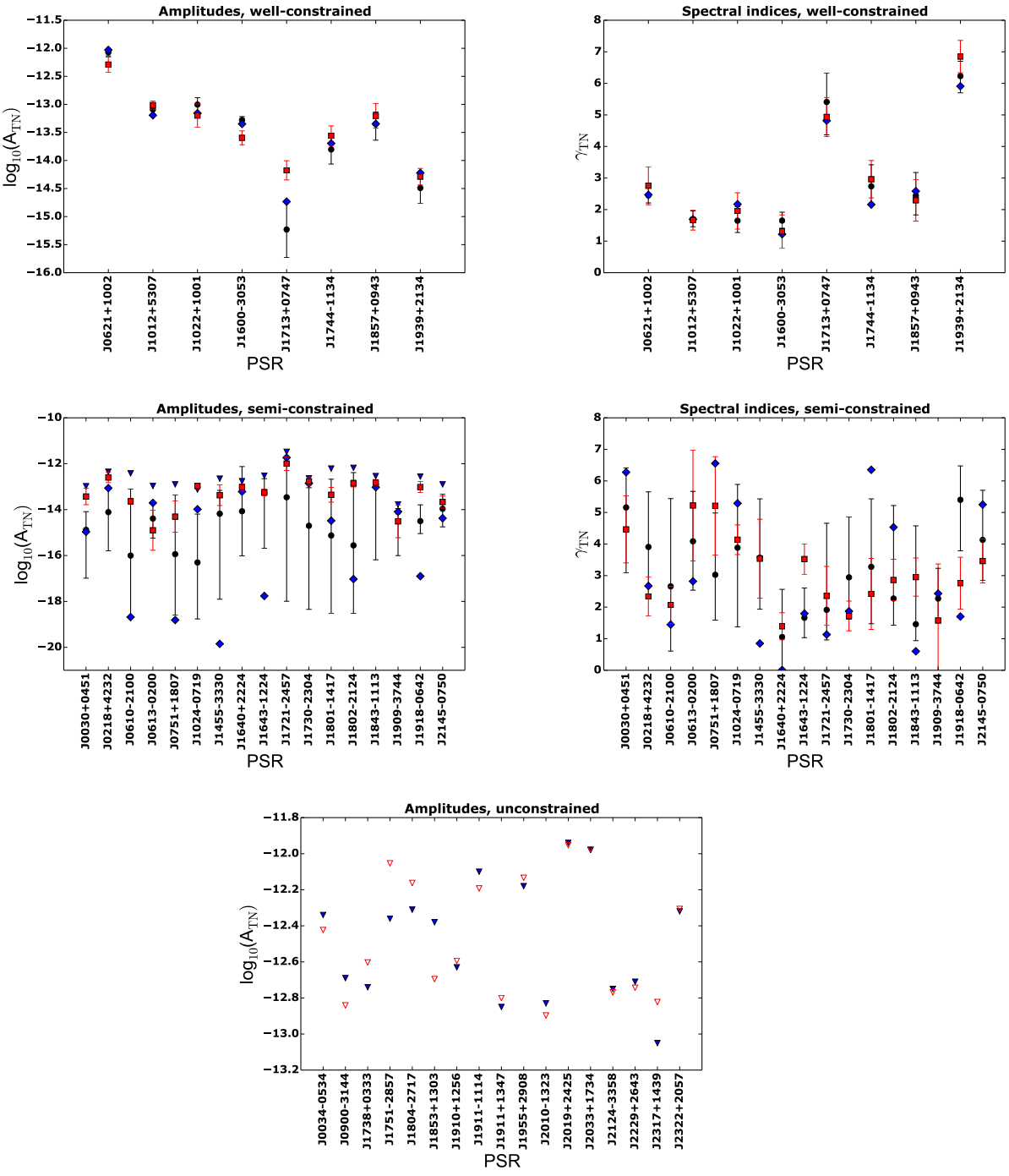

Figure 4.3: Comparison of the timing noise parameters estimated with the Bayesian (blue, filled diamonds for the maximum likelihood values, black, filled circles for the median values with 1-σ error bars and blue, filled triangle for upper limits) and frequentist method (red, filled squares and red, open triangles for upper limits). *Top Row*: Results for the cases where the Bayesian analysis resulted in well-constrained posterior probability distributions for both parameters. *Middle Row*: Results for the cases where the Bayesian analysis resulted in semi-constrained posterior probability distributions for at least one of the parameters. *Bottom Row*: Results for the cases where the Bayesian code resulted in unconstrained posterior probability distributions for at least one of the parameters.

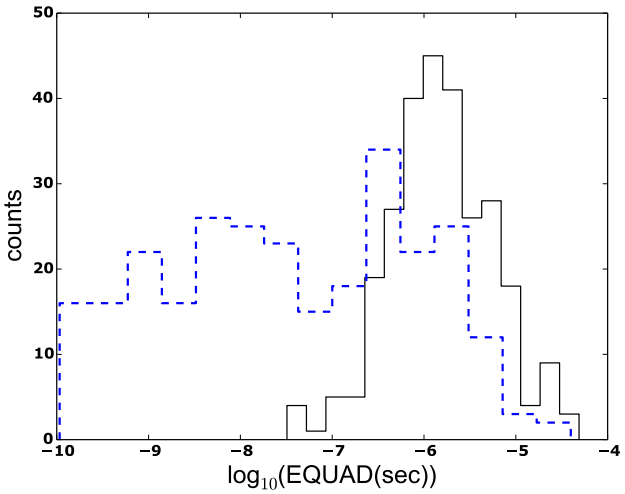

Figure 4.4: Distribution of EFAC values for all MSPs and observing systems. The black, solid line refers to the results of the Bayesian analysis for which the EQUAD priors are set to uniform to get their upper limit values, while the blue, dashed line is for the analysis were EQUAD priors are uninformative log-uniform.

or two systems with clear EQUAD measurement with the exception of PSR J1022+1001. This source is known to require a high level of polarimetric calibration (van Straten 2013) and to show phase jitter noise (Liu et al. 2015). Only part of the NRT data were fully calibrated and this may explain the high levels of EQUADs in this source. We stress once again, that more detail investigation is required to comment on the origin of the EQUAD measurements. It is likely that EQUADs could reflect additional scatter in the residuals from instrumental instabilities or analysis systematics, which could explain the EQUAD measurements in systems where the TOA precision is too low to expect any measurements of pulse jitter noise (as in the case e.g. of PSR J2033+1734, see Table 4.4.)

4.5 Timing Noise from Individual Observing Systems

For MSPs which have large enough data span with overlapping data from various observing systems we examine whether part of the measured TN is present only in specific observing systems. We perform the noise analysis on selected pulsars with data from one telescope removed at a time. For the Effelsberg data, this is more complicated for many MSPs where it is the only telescope with data in the first half of the data set, so removing its data automatically means a loss of about half the data span. We note that this test may not be feasible in some cases with this data set, e.g. when a significant fraction of the residuals sensitivity to the TN is lost when removing a set of dominant, very precise data points. When the TN was absent after removing data from one telescope, we confirmed that the rest of the data would be sufficient to detect the noise by simulating realisations of the new data and performing the noise analysis after injecting TN with the measured properties.

Our analysis shows evidence for TN specific to the NRT data. Figure 4.6 shows the PPDs for the TN parameters when using the full data set and when excluding the NRT data, and the respective ML TN waveforms. For PSR J1022+1001 the PPDs become significantly broader when excluding the NRT data. The mean value of the amplitude reduces by two orders of magnitude and the TN waveform becomes

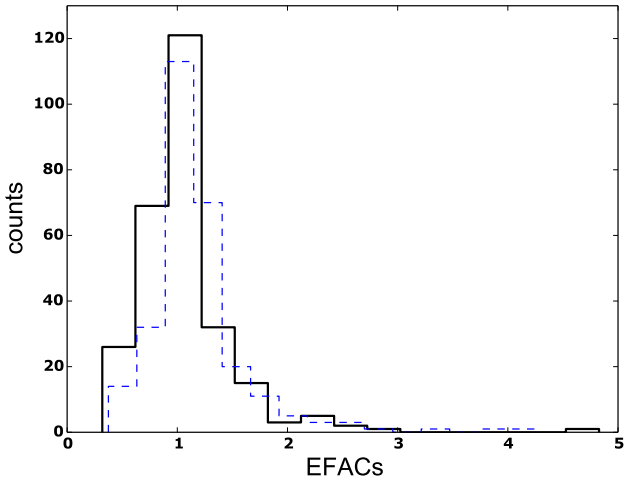

Figure 4.5: Distribution of EQUAD values for all MSPs and observing systems. The solid line refers to the results of the Bayesian analysis for which the EQUAD priors are set to uniform to get their upper limit values, while the dashed line is for the analysis were EQUAD priors are uninformative log-uniform.

Table 4.4: List of the pulsars and observing systems for which we have well-constrained posterior probability distributions for the EQUADs. The last column shows the EQUADs maximum likelihood values from a Bayesian analysis with log-uniform EQUAD prior distribution. The telescope and backend acronyms are as introduced in §5.3.3.

PSR J-Name	Telesc.	Backend	Freq. (MHz)	EQUAD_{ML} (μs)
J0751+1807	EFF	EBPP	1360	5.0
J1012+5307	EFF	EBPP	1360	3.4
J1022+1001	JBO	DFB	1520	1.4
	NRT	BON	1400	1.3
	EFF	EBPP	1410	3.9
J1643−1224	JBO	DFB	1520	2.5
J1744−1134	JBO	DFB	1520	1.0
J1857+0943	NRT	BON	1400	0.9
J1939+2134	NRT	DDS	1400	0.3
	EFF	EBPP	1410	0.3
J2033+1734	NRT	BON	1400	25
J2145−0750	NRT	BON	2000	0.3
	JBO	DFB	1520	0.9

smoother, although the waveform has almost unchanged peak-to-peak variations. The TN parameters PPDs of PSR J2145−0750 show a bimodality, which is not present when removing the NRT data. The two TN waveforms are almost identical, apart from the fact that the waveform of the full data set shows a bump around MJD 56000, which is not present when removing the NRT data. These effects are most likely caused either by additional noise in the NRT data from instrumental instabilities or by some additional non-instrumental noise component that only the NRT data are sensitive to, having indeed the highest precision TOAs. We stress that since we have assumed the TN to be stationary, the properties of instrumental noise during a specific time-interval can leak into the estimated TN waveform throughout the pulsar data set. We note that there were known instrumental instabilities at the NRT during the period between MJD 54300-54500 (July 2007 to February 2008).

This analysis can be better performed using the IPTA data set (Verbiest et al. 2016) where data from another 3 telescopes are included, offering a larger amount of multi-telescope overlapping data. The presence of observing system-dependent noise is more extensively investigated in the paper examining the noise properties of the IPTA data set (Lentati et al. 2016).[4]

4.6 Timing Noise from Errors in Terrestrial Time Standards

As discussed in §2.2.1 the SATs must be referenced to the BIPM time-standard in order to achieve the targeted timing precision. Unless the time-stamping during observations was performed using a GPS clock, the SATs are converted to GPS-based Universal Coordinated Time (UTC) time, using the clock correction files. This is then converted to UTC and subsequently to the TAI standard. TAI is formed by the weighted average of the time-scales of several hundred atomic clocks around the world and subsequent frequency adjustments using primary frequency standards. These adjustments are made over timescales of years, a process known as "steering". As a result, TAI can have errors during the steering periods which are never retroactively corrected. For these reasons, for pulsar timing we use the corrections on TAI provided by the Bureau International des Poids et Mesures (BIPM)[5]. These corrections are made through measuring offsets between various clock pairs to achieve the best possible precision and are regularly updated.

Any possible remaining errors in the BIMP terrestrial time-standard or error propagated to the TOAs by systematics when referencing the TOAs to the various time-standards, will lead to a "clock error" signal, a monopolar correlated signal in the PTA sources, i.e. a signal with the same waveform in all pulsars and observing systems. As discussed in Tiburzi et al. (2016), the mitigation of the clock-error signal is of central importance in PTA efforts for GW detection. In this section, we search for a terrestrial clock error in the data set to determine how much of the measured noise can be attributed to clock error noise. Previously, Hobbs et al. (2012) presented their measurement of the clock error using data from the PPTA and discussed how pulsars can serve as an independent, non-terrestrial time-standard.

4.6.1 Methodology and Results

We use a maximum likelihood estimator to infer the clock error signal. The clock-error noise is modelled as a red-noise process power-law with power spectral density described by Eq. (4.3), with amplitude $A_{\rm clk}$

[4] In that paper, which has recently been published, this type of *System noise* was searched in the data, and we have shown that there is a measurable noise term associated with NRT-BON L-band data in 8 of the MSPs, including PSRs J1022+1001 and J2145−0750.

[5] http://www.bipm.org/

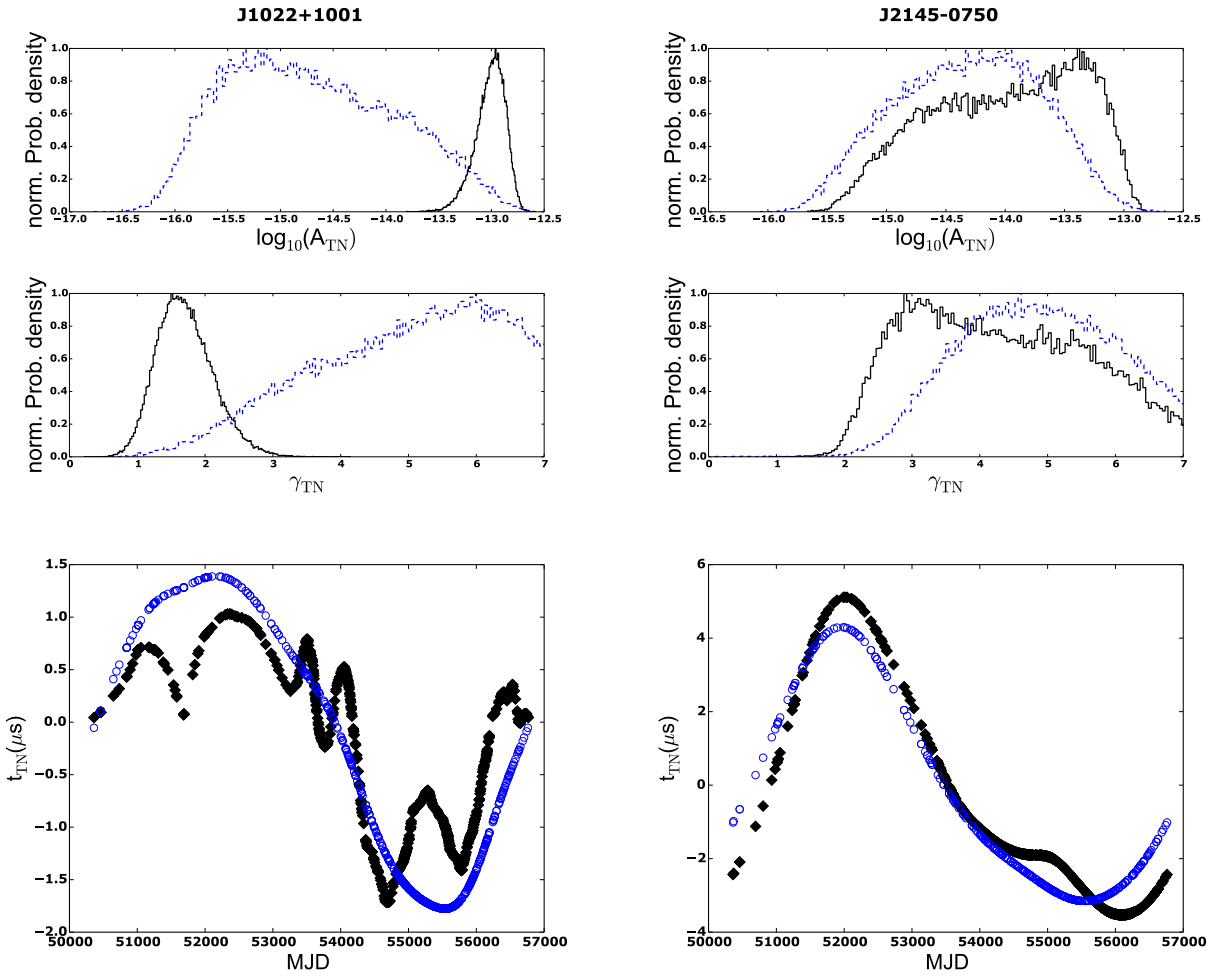

Figure 4.6: *Top panel:* Comparison of the 1-dimensional marginalised posterior probability distributions of the timing noise parameters when using the full EPTA data set (solid, black lines) and the data subset which does not include any NRT-BON data (blue, dashed lines). *Bottom panel:* Comparison of the timing noise waveforms ($\mathbf{t}_{\rm TN}$) when performing the noise analysis on the full EPTA data set (filled black diamonds) and the data subset which excludes the NRT-BON data (open blue circles). See §4.5 for a discussion.

and spectral index $\gamma_{\rm clk}$. Using the results on these parameters, we subsequently construct the ML signal waveform.

For this analysis, we set the TN parameters of the MSPs to the ML values from the Bayesian analysis with uniform pPDs on the TN amplitude (as described in §4.3.2). In this way, we derive the ML solution for the clock-error noise with the higher possible amplitude, given our TN results. We use the residuals after subtracting the ML DM variations signal as in §4.3.3, to focus on the TN only. The likelihood function is similar to Eq. (4.8) but with the extension to multiple pulsars to investigate the clock signal, which is identical among all pulsars, as:

$$L \propto \frac{1}{\sqrt{|\mathbf{C}|}} e^{-\frac{1}{2}\sum_{i,j,I,J}(t_{I,i}-\tau_{I,i})C^{-1}_{I,J,i,j}(t_{J,j}-\tau_{J,j})}, \tag{4.15}$$

where the index I, J are for pulsars, and index i, j are for the time epoch. The total covariance matrix now includes the covariance matrix of the clock error signal, $\mathbf{C}_{\rm clk}$, while not including the matrix of the DM variations such that, $\mathbf{C} = \mathbf{C}_{\rm w} + \mathbf{C}_{\rm TN} + \mathbf{C}_{\rm clk}$. The intrinsic noise of pulsars is not correlated between pulsar pairs, so $\mathrm{C}_{\mathrm{w}\,I,J} = 0$ and $\mathrm{C}_{\mathrm{TN}\,I,J} = 0$ for $I \neq J$. The clock error waveform is identical in all pulsars, therefore its covariance matrix elements can be expressed as $C_{\mathrm{clk\,I,J,i,j}} = C_{\rm clk}(t_i - t_j)C_{\mathrm{clk}\,I,J}$, with $\mathrm{C}_{\mathrm{clk}\,I,J} = 1$ for all I,J pairs. The likelihood function shows that for the estimation of the clock noise parameters we consider both the clock error signal on the residuals of each pulsar (autocorrelation effect) and the cross-correlation of the residuals between pulsar pairs.

We make the linear approximation of the timing model as described in van Haasteren et al. (2009), i.e. considering linear deviations of the true timing parameter values, $\boldsymbol{\epsilon}$, from the least-square-fit timing model values, $\boldsymbol{\epsilon_0}$, via the linear relation $\delta(\boldsymbol{\epsilon}) = \boldsymbol{\epsilon}$ - $\boldsymbol{\epsilon_0}$. We therefore substitute the expression for the residuals in Eq. (4.15), $\mathbf{t} - \boldsymbol{\tau}(\boldsymbol{\epsilon})$, with $\delta\mathbf{t} = \delta\mathbf{t}_{post} - \mathbf{M}\delta(\boldsymbol{\epsilon})$; $\delta\mathbf{t}_{post}$ are the post-fit timing residuals and $\mathbf{M}$ is the design matrix of the timing parameters. We marginalise analytically over all timing parameters and get the reduced likelihood function:

$$L \propto \frac{1}{\sqrt{|\mathbf{C}|}} e^{-\frac{1}{2}\sum_{i,j,I,J}(\delta t_{I,i})C'^{-1}_{I,J,i,j}(\delta t_{J,j})}, \tag{4.16}$$

with $\mathbf{C}' = \mathbf{C}^{-1} - \mathbf{C}^{-1}\mathbf{M}(\mathbf{M}^{\mathbf{T}}\mathbf{C}^{-1}\mathbf{M})^{-1}\mathbf{M}^{\mathbf{T}}\mathbf{C}^{-1}$. Going one step further, we split the deterministic signal between that of parameters for which we want to marginalise over (usually the timing model parameters), $\delta\mathbf{t}'$ and the signal of parameters we assume unknowns of the likelihood function (see e.g. §4.7.2). We note the latter parameters with the vector lambda, and assume their waveforms to be described by the $\boldsymbol{S}(\boldsymbol{\lambda})$. The likelihood function is then re-written as:

$$L \propto \frac{1}{\sqrt{|\mathbf{C}|}} e^{-\frac{1}{2}\sum_{i,j,I,J}(\delta t'_{I,i}-S(\lambda)_{I,i})C'^{-1}_{I,J,i,j}(\delta t'_{J,j}-S(\lambda)_{J,j})}, \tag{4.17}$$

We sample A_{clk} and γ_{clk} over a uniform grid of values and search for the model that maximises the likelihood. The amplitude is sampled with values of $\log(\mathrm{A}_{clk})$ ranging from -17.0 to -14.0 with a step of 0.1, while the spectral index values range from 0.5 to 5 with a step of 0.1. Due to the large condition number of the clock error's covariance matrix, the individual likelihood computations are unstable. As such, the direct search for the ML solution with uniform grids produces non-desirable artefact (non-

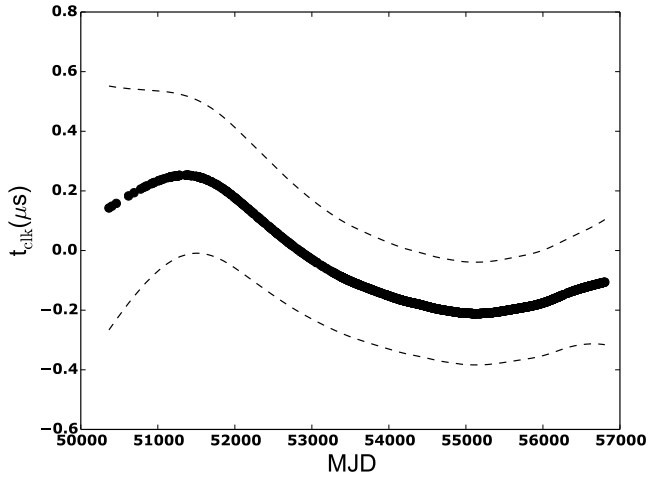

Figure 4.7: The estimated waveform of the clock-error noise. The filled circles is the maximum likelihood waveform ($\mathbf{t}_{\rm clk}$). The dashed lines indicate the 68% confidence intervals. For the estimation of the waveform, we used the upper limits for the values of the individual pulsar timing noise parameters providing upper limits for the clock error noise parameters.

physical likelihood maxima). To avoid these effects, we performed a large number of trials by dithering noise parameters with randomised offset values within each search grid. The likelihood value of the grid is taken to be the maximum of all trials.

To reduce the computational cost of the analysis we use the "restricted data set" proposed in Babak et al. (2016). This consists of six MSPs from the full data set, which give 90 % of the sensitivity to CGWs. This "restricted data set" has also been used in the derivation of upper limits to the amplitude of GWs with the EPTA DR 1.0 (Lentati et al. 2015; Taylor et al. 2015; Babak et al. 2016). The "restricted data set" contains the pulsars PSRs J0613−0200, J1012+5307, J1600−3053, J1713+0747, J1744−1134, and J1909−3744.

We find a ML solution at $A_{clk} = -15.2$ and $\gamma_{clk} = 4.8$. We use these values to calculate the ML waveform of the signal, shown in Fig. 4.7. The clock signal waveform can be estimated in the same way we did for TN:

$$\mathbf{t}_{\rm clk} = \mathbf{C}_{\rm clk}\mathbf{C}^{-1}\mathbf{t}\,. \tag{4.18}$$

with uncertainties estimated as:

$$\sigma_{\rm clk} = \mathbf{C}_{\rm clk} - \mathbf{C}_{\rm clk}\mathbf{C}^{-1}\mathbf{C}_{\rm clk} \tag{4.19}$$

The upper limit clock error waveform has an rms value of $0.17\mu s$. By integrating Eq. (4.3) from the lowest to the highest spectral frequency for the clock error noise we derive the average power of the signal. We can compare this to the average power of the noise for each MSP, which is calculated by adding the TN average power and the white noise average power ($S_{\rm W}$, as in Eq. 4.13). We find that the

contribution of the clock error noise to the total noise levels of the individual pulsars is less than 1%.

4.7 Effects of Timing Noise on Prospects for GW Detection

Various studies have examined the sensitivity of PTAs to GWB signals (e.g. Jenet et al. 2005; Lee et al. 2012; Siemens et al. 2013). These studies focus on making detection significance estimations and projections based on analytic formulae or scaling laws, which are derived assuming a given detection technique. These estimates are usually made based on specific assumptions, such as: the TOAs are regularly sampled and simultaneous across pulsars, that the measurement precision is constant and identical for all pulsars and the absence of low frequency noise. The detection significance is usually expressed as the precision by which the dimensionless amplitude can be measured for a given spectral index.

In this chapter we make use of the Crámer-Rao lower bound (CRLB) to investigate the limitations of the present data set in detecting GWs, both for stochastic isotropic GWBs and CGWs from SMBHBs. The advantage of this method is that it takes into account all the observational properties of the data, such as cadence, white and TN levels, while still using analytic calculations that demand very few computational resources and does not require data simulations. The impact of the TN present in the data on the PTA's sensitivity to GWs can then be estimated by comparing the CRLB when using the full covariance matrix and when omitting the TN component.

The CRLB states that, for any unbiased estimator, the variance is equal to or higher than the inverse of the Fisher information matrix, $\mathcal{I}$. When the equality is valid the estimator is also "fully efficient" (Fisz 1963). As discussed in Vallisneri (2008), the ML estimator (which we use in this analysis for the GW amplitude as described below) can achieve the bound in the high S/N regime. For the amplitude of GW signals, the CRLB represents the lowest uncertainties (in case of detection) or upper limits (in case on non-detection) any unbiased estimator can achieve. We note, that although the CRLB is underperformed by all unbiased estimator, in principle it can be outperformed by a biased estimator (Vallisneri 2008). The interpretation of the bound as the amplitudes upper limit in the non-detection case warrants more caution, since by default it assumes we are outside the high S/N regime. Nevertheless, it is unlikely that other estimators can provide lower upper limits than the CRLB under the same assumptions. For the purpose of evaluating the role of TN on the data's sensitivity to GWs, we are primarily interested in the ratio of the CRLB when assuming only white noise in the data and when the TN is taken into account. Therefore, even if the individual CRLB results are not optimal, their ratio should be representative of the effects of TN. The CRLB calculated in the presence of TN are in fact comparable[6] to the amplitude limits derived in Lentati et al. (2015) and Babak et al. (2016) using more rigorous algorithms.

In its general form, the CRLB is formulated as follows. Given a likelihood function, $f(\boldsymbol{\lambda}, \mathbf{x})$, where $\mathbf{x}$ is the data and $\boldsymbol{\lambda}$ are the model parameters, the CRLB is:

$$\mathrm{Cov}(\boldsymbol{\lambda}) = \langle \sigma_{\lambda_i} \sigma_{\lambda_j} \rangle \geq \mathcal{I}_{ij}^{-1}, \tag{4.20}$$

where the indices i and j denote the different parameters and $\mathcal{I}_{ij}$ is:

[6] Note that the CRLB refers to the equivalent of a 68% C.L. Typically, the 95% C.L. is reported in the PTA literature for the amplitude of GWs.

$$\mathcal{I}_{ij} = \left\langle \frac{\partial \ln f(\boldsymbol{x}, \boldsymbol{\lambda})}{\partial \lambda_i} \frac{\partial \ln f(\boldsymbol{x}, \boldsymbol{\lambda})}{\partial \lambda_j} \right\rangle \equiv - \left\langle \frac{\partial^2 \ln f(\boldsymbol{x}, \boldsymbol{\lambda})}{\partial \lambda_i \partial \lambda_j} \right\rangle \tag{4.21}$$

It is well-known that $\mathcal{I}$ can be analytically calculated for Gaussian likelihood functions (as is Eq. 4.8), and results in the so-called Slepian-Bangs formula (Slepian 1954; Bangs 1971):

$$\mathcal{I}_{ij} = \frac{1}{2} \Big\{ \mathbf{tr} \Big[\mathbf{C}^{-1} \frac{\partial \mathbf{C}}{\partial \beta_i} \mathbf{C}^{-1} \frac{\partial \mathbf{C}}{\partial \beta_j} \Big] + \frac{\partial \mathbf{S}(\lambda)^{\mathbf{T}}}{\partial \lambda_i} \mathbf{C}^{-1} \frac{\partial \mathbf{S}(\lambda)}{\partial \lambda_j} \Big\} . \tag{4.22}$$

Here, β_i are the model parameters describing the covariance matrix, λ_i, are the parameters describing the unknown waveform $\mathbf{S}$ and $\mathbf{tr}$ is the matrix trace.

We make use of the same maximum likelihood estimator as in §4.6 (Eq. 4.17), but we replace the stochastic clock error signal with that of a stochastic and isotropic GWB and we set $\boldsymbol{S}(\boldsymbol{\lambda})$ to be the CGW signal from a single SMBHB, as detailed in §4.7.2. The likelihood function (Eq. 4.17) uses a total covariance matrix which includes the covariance matrix of the GWB, such that $\mathbf{C} = \mathbf{C}_{\mathrm{w}} + \mathbf{C}_{\mathrm{TN}} + \mathbf{C}_{\mathbf{gwb}}$. The GWB's covariance matrix, is dictated by the expected correlation coefficient in the residuals of every pulsar pair, described by the overlap reduction function (Finn et al. 2009), $\Gamma(\zeta)$, defined as:

$$\Gamma(\zeta) = \frac{3}{8} \Big[1 + \frac{\cos\zeta_{IJ}}{3} + 4(1 - \cos\zeta_{IJ}) \ln\Big(\sin\frac{\zeta_{IJ}}{2}\Big) \Big] (1 + \delta_{IJ}). \tag{4.23}$$

Here, ζ_{IJ} is the angular separation between the I-th and the J-th pulsar, and δ_{IJ} is the Kronecker delta. In principle, both an Earth and a pulsar term contribute to the correlation and δ_{IJ} accounts for the latter. In the short-wavelength approximation, i.e. when the pulsars are separated from the Earth and from each other by many GW wavelengths, the overlap reduction function is also known as the Hellings-Downs curve (Hellings & Downs 1983). The elements of the covariance matrix of the GWB are then expressed as $\mathrm{C}_{\mathrm{gwb}I,J,i,j} = \mathrm{C}_{\mathrm{gwb}}(t_i - t_j)\Gamma(\zeta_{IJ})$. As in the case of the clock error covariance matrix (§4.6.1), the form of the covariance matrix allows the calculation of the CRLB to include both the autocorrelation and cross-correlation effects of the GW.

For this analysis, we use the same six MSPs that we used to estimate the clock error noise parameters in §4.6.1 and we set the TN properties to their ML values as estimated with the Bayesian pulsar noise analysis described in §4.3.2 and presented in Table 4.2. As discussed in §4.6.1, the estimation that the sensitivity loss to GWs when using this data subset is below 10 % was made for the case of CGWs. For low-frequency stochastic signals such as the GWB or the clock error signal, the sensitivity loss should be less. For CGWs, adding a pulsar with precise data only in part of its data span can increase the S/N of a detection significantly if the SMBHB orbit is fully sampled. In the case of the GWB, however, the targeted correlated signal must be found in cross-correlations of TOAs across a long time-span of order equal to the inverse of the GW frequency, with sufficient precision. We have verified this by calculating

the CRLB for the GWB using 40 MSPs and noting an improvement in the amplitude limit of order 2 %. The scaling of the sensitivity to GWs with the number of MSPs, the S/N regime of the targeted signal and other factors have been studied elsewhere (e.g. Babak & Sesana 2012; Siemens et al. 2013) and is outside the scope of this work.

In order to focus on the impact of TN only, we mitigate the DM variations beforehand by subtracting the ML DM-variations waveforms from the residuals. For detailed derivations and astrophysical interpretations on GW limits using the EPTA DR 1.0, we refer the reader to Lentati et al. (2015), Taylor et al. (2015) and Babak et al. (2016) for the cases of a stochastic and isotropic GWB, the anisotropy in the GWB and the CGW from individual SMBHBs respectively.

4.7.1 Stochastic Gravitational-Wave Background

When estimating the CRLB for the GWB amplitude, the terms with partial derivatives of **S** are zero and Eq. (4.22) reduces to

$$\mathcal{I}_{ij} = \frac{1}{2}\mathbf{tr}\Big[\mathbf{C}^{-1}\frac{\partial \mathbf{C}}{\partial \beta_i}\mathbf{C}^{-1}\frac{\partial \mathbf{C}}{\partial \beta_j}\Big]. \tag{4.24}$$

We calculate the CRLB for the GWB amplitude, keeping each time the GWB spectral index fixed. We do so for a range of spectral indices, from −2 to 1, which covers GWB signals often discussed in PTAs literature, e.g. from SMBHBs, cosmic strings and the relic GWB from the inflationary era.

This simplified approach intends to provide an understanding of the difficulties the TN imposes on the detection of the various GWBs probed by PTAs. It is not exhaustive, since each of these GWBs can in general have a range of possible spectral index values. In the case of SMBHBs, this depends on the orbital eccentricities and whether the SMBHBs are coupled to their stellar and gaseous environment or they are driven by GW emission only (Sesana 2013). The often used power-law index of $-2/3$ refers to circular, GW-driven SMBHBs (Rajagopal & Romani 1995; Jaffe & Backer 2003). Strong environment coupling and high orbital eccentricities can cause a turnover of the spectrum at low-frequencies (e.g. Fig. 2 in Sesana 2013). The value -7/6 we have used for the spectral index of the cosmic string GWB has been analytically derived using a simplified approximation of the loop number density and assuming cusp emission (e.g. Damour & Vilenkin 2005). However, especially in the frequencies probed by PTAs, a wide range of spectral indices is possible, depending on some characteristic parameters used to describe the evolution of the network and the details of the dominant GW emission mechanism, and one typically sets limits on the amplitude for a range of these parameters (Sanidas et al. 2012) For the cosmological relic GWB, a spectral index of −1 is often cited (Grishchuk 2005). For more details on the sources of the various GWBs and details on the derivation of amplitude limits as function of the spectral index and other physical parameters, we refer the reader to Lentati et al. (2015); Arzoumanian et al. (2015)

The CRLBs are calculated using the TN parameters from the two Bayesian analyses, using different types of pPDs on the TN noise amplitude. For each set of TN results, we calculate the CRLB for two cases, namely assuming the presence of the measured white and TN, or assuming only the measured white noise levels, and finally, calculate their ratios. Figure 4.8 shows the results for both cases. The results for the spectral indices representative of GWBs from SMBHBs, cosmic strings and relic GWs

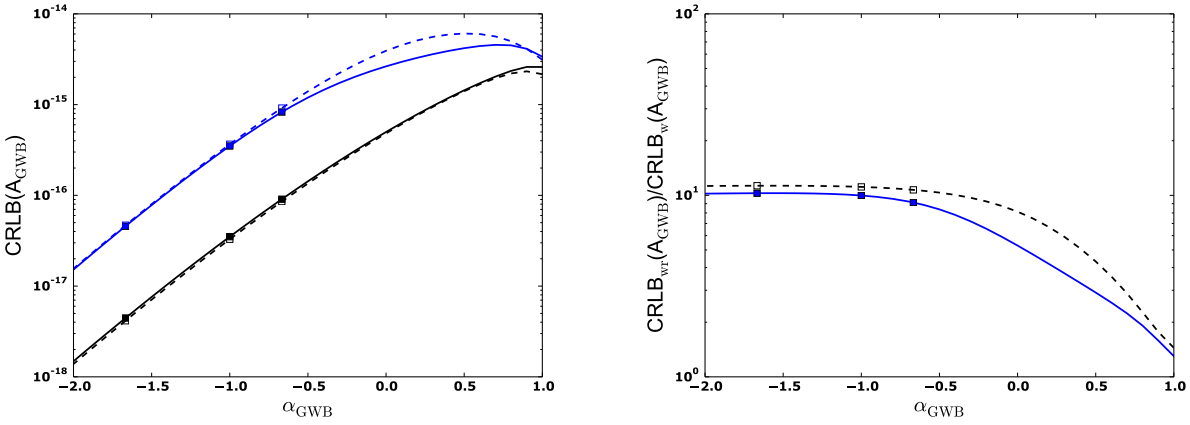

Figure 4.8: Crámer-Rao lower bounds (CRLBs) for the strain amplitude of GWBs, A_{GWB} for a range of spectral indices, α_{GWB}. Squares denote the values shown in Table 4.5. *Left panel:* CRLBs calculated using the timing-noise ML parameters from the Bayesian analysis using log-uniform priors on the TN amplitude (solid lines and filled squares) and using uniform priors on the timing-noise amplitude (upper limits; dashed lines with open squares). Blue (grey for black and white prints) symbols are for limits calculated assuming timing and white noise, while black symbols when only the white noise levels are taken into account. *Right panel:* The ratio of the CRLBs when considering the white- and timing-noise levels of the data and when assuming no timing noise present in the data. The blue solid line is when using the timing-noise properties the analysis with log-uniform priors and the while the black dashed line is for the analysis with uniform priors.

are presented in Table 4.5. The improvement factor on the lower bound when assuming no TN in the data is about an order of magnitude, ranging from 9.1 to 11.4. These results demonstrate how strongly TN can reduce the data's sensitivity to stochastic GWBs. To stress this even further, we note that the upper limits on the GWB amplitude by SMBHBs (spectral index $-2/3$) by PTAs have improved by a factor of ten over the past ten years.

4.7.2 Gravitational Waves from single SMBHBs

Here we focus on CGWs from resolvable, GW-driven SMBHBs with circular orbits and without measurable frequency evolution of the signal due to energy loss from the binary by GW emission over the observing interval (an effect known as frequency chirping, see e.g. Hughes (2009)). The waveform ($\mathbf{S}$) of CGWs has been calculated by many independent studies (e.g. Wahlquist 1987; Blanchet 2006; Hughes 2009). For each SMBHB, the waveform is characterised by seven parameters, namely the GW amplitude, frequency and phase, the SMBHB's sky co-ordinates (right ascension and declination), orbital inclination, and direction of the binary's ascending node on the sky. Clearly, the terms with partial derivatives of $\mathbf{C}$ are zero for the single SMBHB signal and Eq. (4.22) reduces to

$$\mathcal{I}_{ij} = \frac{1}{2}\frac{\partial \mathbf{S}^{\mathbf{T}}}{\partial \lambda_i}\mathbf{C}^{-1}\frac{\partial \mathbf{S}}{\partial \lambda_j}\,. \tag{4.25}$$

Table 4.5: Results for the Crámer-Rao bound (CRLB) on a GWB for the expected signals from SMBHBs ($\alpha = -2/3$), cosmic strings ($\alpha = -7/6$) and cosmological relic GWs ($\alpha = -1$) (see §4.7.1 for a discussion on the noted spectral indices). We tabulate the CRLB when considering both the white- and timing-noise levels, ($A_{GWB_{\rm wr}}$) and when assuming no timing noise present in the data ($A_{GWB_{\rm w}}$). Results were derived using the noise parameters from both Bayesian analyses, with uniform (ML TN) and log-uniform priors (TN upper limits) on the timing-noise amplitude.

α_{GWB}	$A_{GWB_{\rm wr}}$	$A_{GWB_{\rm w}}$	$\frac{A_{GWB_{\rm wr}}}{A_{GWB_{\rm w}}}$
ML TN			
-2/3	8.3×10^{-16}	9.1×10^{-17}	9.1
-7/6	4.6×10^{-17}	4.4×10^{-18}	10.3
-1	3.5×10^{-16}	3.5×10^{-18}	10.0
TN upper limits			
-2/3	9.2×10^{-16}	8.5×10^{-17}	10.7
-7/6	4.7×10^{-17}	4.1×10^{-18}	11.4
-1	3.7×10^{-16}	3.3×10^{-17}	11.1

Due to the seven parameters, the covariance matrix for the single GW source is a 7×7 matrix. The CRLB of the single source amplitude depends on the GW frequency, source position, orbital inclination and orientation. It has been shown (Lee 2013) that the precision estimation of the GW source position using CRLB would be poor, due to the lack of a unique un-biased estimator for the single source problem. The statistics of the amplitude estimator, on the other hand, can be well described by the CRLB, which determines the sensitivity of a PTA as function of frequency. The sensitivity depends on the GW source position. We estimate the CRLB for three scenarios: placing the SMBHB at the sky position where the PTA has the minimum and maximum sensitivity as well as the average of all positions on the sky. Our results are given in Fig. 4.9. The low-frequency sensitivity extends to values lower than the frequency resolution (1/T) because the GW low frequency signal still leaks power into the observing window after the pulsars' spin and spin-down fitting. This causes the curve to rise below the frequency resolution. The rise of the curve at high GW frequencies is due to the PTA frequency response, as the GW induced timing residuals are the time integral of the GW strain. The peak at 1 $\rm yr^{-1}$ (3.17×10^{-8} Hz) is caused by the pulsar sky position fitting.

The improvement in the PTA sensitivity at low frequencies is obvious from Fig. 4.9. One can clearly notice how the presence of TN flattens the sensitivity below ∼10 nHz, which, in contrast, keeps improving in the case of timing data free of TN. In the absence of TN, the sensitivity at low GW frequencies is only limited by the PTA's frequency resolution. Table 4.6 summarises the CRLBs for the CGWs amplitude at frequencies of 5 and 7 nHz and the improvement factors to the sensitivity when the data do not have TN, which range from 2.3 to 5.6.

4.8 Conclusions and Discussion

In this chapter, we have characterised the noise properties for 42 MSPs, using the EPTA DR 1.0. While the central focus is on the timing noise properties, we have also characterised the white noise properties of the data. The long time-spans of the pulsar data sets (the shortest being 6.9 years and the longest 24.1 years long) of high-quality timing data, are especially valuable for determining the timing noise. In order to increase our confidence in the results, we have employed two established methods, one based

Table 4.6: Results for the Crámer-Rao lower bound (CRLB) on the strain amplitude of continuous GWs from resolvable SMBHBs with circular orbits and without measurable frequency chirping. We quote the limits for the cases when the SMBHB is at the sky location where the PTA has the maximum (max) and minimum (min) sensitivity, and the average of all sky positions (avg) at GW frequencies of 5 and 7 nHz. For each case we quote the limits when accounting for the white and the TN of the data, $A_{\mathrm{CGW_{wr}}}$ and for the white noise only, $A_{\mathrm{CGW_{w}}}$. The last column shows the ratio of the limits for these two cases.

GW freq. (nHz)	$A_{\mathrm{CGW_{wr}}}$	$A_{\mathrm{CGW_{w}}}$	$\frac{A_{\mathrm{CGW_{wr}}}}{A_{\mathrm{CGW_{w}}}}$
	Min PTA sensitivity		
5	1.2×10^{-14}	2.1×10^{-15}	5.6
7	9.1×10^{-15}	3.8×10^{-15}	2.4
	Avg PTA sensitivity		
5	4.0×10^{-15}	8.1×10^{-16}	5.0
7	2.7×10^{-15}	1.1×10^{-15}	2.4
	Max PTA sensitivity		
5	1.3×10^{-15}	2.4×10^{-16}	5.3
7	1.0×10^{-15}	4.4×10^{-16}	2.3

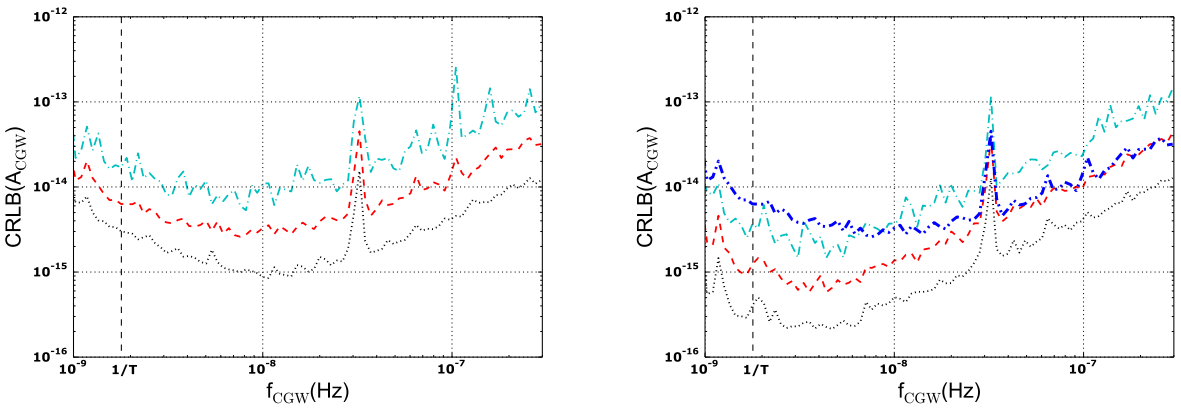

Figure 4.9: Results for the Crámer-Rao lower bound (CRLB) on the strain amplitude of continuous GWs, A_{CGW}, against the CGW frequency, f_{CGW}, from resolvable SMBHBs with circular orbits and without measurable frequency chirping. The different curves are for the cases where the SMBHB is at the sky location where the PTA has the minimum (cyan, dot-dashed lines) and maximum (black, dotted lines) sensitivity, and the average of all positions on the sky (red, solid lines). The vertical line show the frequency resolution of the PTA, 1/T, where T is time-span of the pulsar with the longest data set. *Left panel:* Sensitivity curves when accounting for the white and the timing noise of the data. *Right panel:* Sensitivity curves when only accounting the white noise of the data. The additional blue, thick double dot-dashed line is the case for mean PTA sensitivity when including the timing noise as in the left panel (red, solid line) for better comparison.

on Bayesian and the other one on power-spectral analysis. We used the Bayesian pulsar timing analysis package `TempoNest` to simultaneously determine the time-correlated timing noise, DM variations and uncorrelated noise (white-noise) properties. In order to focus the comparison between the methods on the timing noise characterisation, we used the maximum likelihood `TempoNest` results on DM variations and white-noise parameters as a priori known information when performing the frequentist analysis, based on a developed power-spectral analysis code described in this chapter. For pulsars with statistically significant timing noise measurements, the two methods give statistically consistent results.

The lack of sufficient multi-frequency data in 17 pulsars where timing noise is detected leads to strong covariances between the timing noise and DM variations, causing the posterior distributions of the noise parameters derived from the Bayesian analysis to have probability tails extending to $\pm\infty$. These reflect the small probabilities of the noise amplitude to be zero, causing some deviations between the maximum likelihood and mean values of the parameters. The values of the ML and mean parameters as well as the parameter values estimated with the power-spectral analysis, are still however statistically consistent. Upper limit analysis is performed in these cases to set robust upper limits on the timing noise amplitude.

Our analysis shows evidence of timing noise specific to the NRT data, which are likely linked to improper polarisation calibration in a roughly six-month-long epoch. We have also placed an upper limit on clock-error timing noise and find that it contributes at most 1% to the total noise in the MSPs under examination. Finally, we assessed the role of timing noise in the efforts for GW detection using PTAs. We did so by estimating the Crámer-Rao lower bound on the strain amplitude of a stochastic GWB and CGWs from resolvable SMBHBs, accounting only for the measured white noise first and then adding the measured timing noise properties. We find that, for GWBs, the timing noise in this data set reduces the sensitivity of this data set by a factor of 9.1 to 11.4, depending on the GWB spectral index. For CGWs, the sensitivity reduces by a factor of 2.3 to 5.6, depending on the GW frequency and the sky position of the SMBHB with respect to the sky position where the PTA is most sensitive.

The results of this chapter stress in a clear way the imperative need of PTAs to improve the noise characterisation and mitigation techniques and the development of good observing and data reduction practices to avoid introducing timing noise due to systematics. It also demonstrates the demand for new discoveries of MSPs that are not only bright, but also exhibit stable rotation. The rotational stability of pulsars can only be evaluated via timing-noise characterisation on data sets that are at least five years long, making the long-term follow-up timing observations of newly discovered MSPs essential for PTA observing campaigns.

CHAPTER 5

Two Tests of Theories of Gravity with Pulsar-Timing Data

> "Wie kommt uns da das die pedantische Genauigkeit der Astronomy zu Hilfe, über die ich mich im Stillen früher oft lustig machte!"
>
> *Albert Einstein, letter to A. Sommerfeld, Dec. 9, 1915*

Section 5.2 of this chapter describes work that was previously published in
*Shao L., **Caballero R. N.**, Kramer M., Wex N., Champion D . J., and Jessner A. 2013, "A new limit on local Lorentz invariance violation of gravity from solitary pulsars", Class. and Quant.Grav., 30, 165019*
In particular, my work for this publication focused on the observational aspects, i.e. the reduction of radio pulsar data and analysis of the pulse profiles temporal stability, as described in §5.2.2.
Work described in §5.3 will be used in the future for planned publication. The Nançay "NUPPI" data used in addition to those described in §3.3.1 were reduced by collaborators.

In this chapter, I discuss work related to tests of gravity theories in the quasi-stationary, strong-field regime using pulsar-timing data. After providing an overview on the possible ways that pulsar timing data can be employed for such tests, I present two such studies. The first, discussed in 5.2, is the derivation of the best limit to-date on one of the three PPN parameters that describes local Lorentz invariance of gravity, using EBPP data from two solitary MSPs, namely PSR B1937+21 and PSR J1744−1134. The second, discussed in 5.3 concerns gravitational-radiation-damping tests, where we place a limit on the existence of dipolar-GW radiation, using EPTA timing data of PSR J1012+5307.

5.1 Introduction: Probing Gravity in the Quasi-Stationary Strong Field Regime with Pulsars

Unlike the other three fundamental interactions, electromagnetic, strong nuclear, and weak nuclear, gravitational interaction is the only one not yet compatible with quantum physics. Owing to the very small relative strength of the gravitational interaction, weaker by more than 25 orders of magnitude from

the rest of the fundamental interactions, the experimental tests of gravity theories are largely performed by studying celestial objects. The experiments are in this sense, not only limited by the measurement precision of our instruments, but by nature itself, as we cannot create our own experimental set-up. In that respect, we are extremely fortunate that pulsars exist.

So far, GR has not been falsified by any direct experiment. However, there is a lot of motivation for development of alternative theories of gravity. Pure theoretical considerations, such as GR's prediction of gravitational singularities, points of infinite density, as well as its incompatibility with quantum mechanics, contrary to the other three fundamental forces, lead to the expectation that at some scale of the field's intensity or some length-scale, GR breaks down and becomes incompatible with observations, an event which will lay the foundations for the new description of gravity. At the same time, there are some observational results that have further motivated this research field. For example, the hypothesis for the existence of dark matter to explain observations such the rotation curves of galaxies and weak lensing is still lacking experimental verification through a detection of dark matter particles.

Tests of gravity theories are divided into four regimes, defined by the degree of the space-time curvature and the velocity of the mass, as shown in Figure 5.1. In these type of graphical illustrations, the 4-dimensional space-time is represented in three dimensions, by reducing the space dimensions from three to two, defined by the x-y plane. The z-axis defines the time dimension. In panels I-III, space-time is curved by the presence of self-gravitating bodies, while in panel IV, accelerated self-gravitating bodies at the centre of the diagram produce the propagating GWs, which are illustrated as co-centric space-time ripples.

The curvature of space-time can be understood as the degree of the space-time properties from the Minkowski space-time. The latter is basically a four-dimensional space-time from the combination of flat Euclidian space and time which obeys to the rules of special relativity. The space-time curvature caused by the gravitational field of a self-gravitating body, relates with its gravitational binding energy, $U \simeq GM^2/R$, where M and R are the body's mass and radius respectively, and G is the gravitational constant. Velocities associated with the different gravity regimes are with respect to the speed of light. For the regimes i-iii below, the velocity refers to the velocity of the motion of the self-gravitating object. The four regimes are therefore, (i) the *quasi-stationary, weak-field regime* (weakly curved space-time, $u/c \ll 1$), (ii) *the quasi-stationary, strong-field regime* (strongly curved space-time,$u/c \ll 1$), (iii) *the highly-dynamical, strong field strong* (strongly curved space-time,$u/c \sim 1$), and (iv) *the radiative, or GW regime* ($u/c = 1$).

We have already outlined in the last chapter some of the ways that GWs can contribute in limiting the parameter space of gravity theories. The GW regime is of course not completely separated from the other three. In particular, the motion of compact objects in the second and third regime can produce observable GWs. But even without the direct observation of GWs, pulsars provide access to a wealth of gravity theory tests in the quasi-stationary, strong-field regime, through comparison of their orbital and rotational behaviour and that predicted by the equations of motion of various gravity theories. This includes changes in the pulsar orbital motion by emission of GWs as discussed in §1.5. We will see more on this also later in §5.3. As already introduced in §2.3.3, these tests are based on the post-Newtonian approximation and the PPN and PPK formalisms.

The PN approximation allows to produce approximate solutions to the equation of motion of gravitationally interacting massive bodies. In Newtonian gravity, the relative acceleration at distance r (in

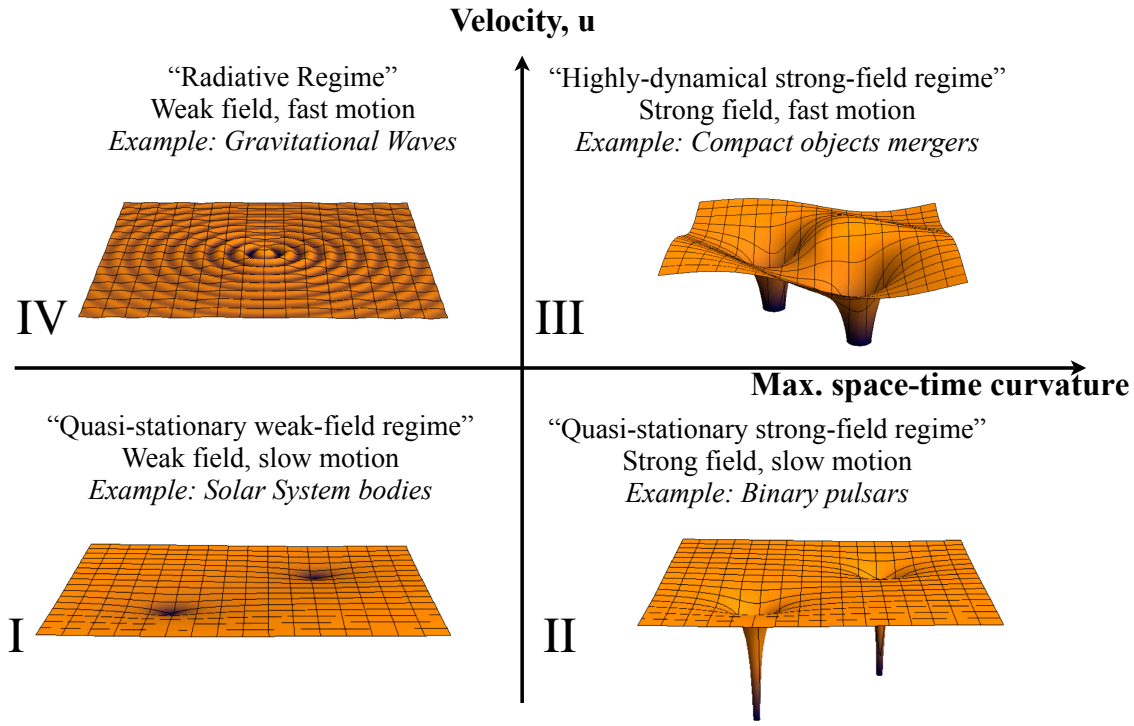

Figure 5.1: The various regimes of gravity theories tests. In the horizontal direction we show the classification based on the degree by which space-time is curved. In the vertical direction, we classify the experiment regime based on the velocity of the self-gravitating body, u, or that of GWs, which equal that of the speed of light, c. The graphical illustrations are from Wex (2014), and show the curvature of space-time in the different regimes. See discussion in §5.1 for more details.

the frame co-moving with the centre of mass) of bodies in orbit with total mass M, $\ddot{\mathbf{r}}$, is:

$$\ddot{\mathbf{r}} = -\frac{GM\hat{\mathbf{r}}}{r^2}\,, \tag{5.1}$$

where $\mathbf{r}$ is the vector connecting the two point masses, $\hat{\mathbf{r}} = \mathbf{r}/r$, is the unit vector in the direction of the vector, and r is the magnitude or $\mathbf{r}$. In the PN approximation, this equation of motion is expressed in a relation of the form (e.g Blanchet 2014):

$$\ddot{\mathbf{r}} = -\frac{GM}{r^2}\left[(1 + A_2 + A_3 + ...)\frac{\mathbf{r}}{r} + (B_2 + B_3 + ...)\dot{\mathbf{r}}\right]. \tag{5.2}$$

The A_k and B_k are the coefficients that describe deviations from Newtonian gravity of increasing order

$(u/c)^{-k}$, where c and u are the speed of light and the velocity of the massive body, respectively. The PN correction orders are often described in pulsar timing literature with the by the number $k/2$. For example, for $k = 2$ we have the 1PN order, for $k = 3$ we have the 1.5PN order and so on.

The 1PN corrections are valid for the quasi-stationary, weak-field regime and have been widely used for experimental verification of GR in the Solar system (see e.g. Will 2014b, for a review). However, observation in this regime alone can verify physically motivated theories, and deviations from GR are sought where higher order PN terms can be probed. As nicely put by Damour & Taylor (1992), this situation is similar to studying the behaviour of a function $f(x)$ in the neighbourhood of $x = 0$, with various solutions of an approximate function, for example, $f(x) \approx \alpha + \beta x + \gamma x^2 + O^+$, where the latter term describes terms of higher order. Many solutions (i.e. combinations of the x-terms coefficients) can approximate each other at such a small range of the x parameter, even though they can be very different away from x.

To measure the effect of the higher order terms, one needs to examine the behaviour of $f(x)$ for a wider range of x values. This is possible when it comes to gravity theories, when moving to the strong-field regime. The PN approximation has solutions that can very well predict the equation of motion of binary pulsars in the quasi-stationary, strong-field regime using up to the 2.5 PN term (see e.g. Wex 2014). The highly-dynamical regime, on the other hand, requires much higher order corrections and full numerical solutions based on GR and alternative theories are developed to fully solve the equations of motion (e.g. Baker et al. 2006; Shibata et al. 2014). Such detailed models are particularly useful to predict the GW waveform by merging compact objects, as demonstrated by the study of the recent GW detection announcement we discussed in the previous chapter (The LIGO Scientific Collaboration & the Virgo Collaboration 2016).

When it comes to gravity-theory tests with pulsars, the measurements (or placed upper limits) of post-Keplerian orbital parameters are central. The measurement of N post-Keplerian parameters allows $N-2$ independent tests of a theory (see e.g. Damour 2009). Any given theory, predicts relations between the Keplerian and post-Keplerian parameters and the unknown, in principle, masses of the pulsar and companion (Equations 2.18a-2.19). A classic test is performed with the use of the so-called mass-mass diagrams, as we have already seen in §3.3.5. In more detail, and following the review in (Wex 2014) the general categories of tests provided by pulsar observations (mostly with binaries but also solitary pulsars) are:

(1) Gravitational-wave damping: Due to the accelerated motion of the bodies in a binary pulsar, the system loses energy via GW emission. The back-reaction from the emission results in orbital decay, mensurable via $\dot{P}_{\rm b}$, i.e. the (negative) secular change of the orbital period, the value of which is gravity-theory dependent. As mentioned in §1.5, this test gave the first clear evidence for the existence of GWs (Taylor & Weisberg 1989). Certain alternatives theories predict additional GW radiation to that the GR predicts for masses orbiting in a binary system, which give rise to additional $\dot{P}_{\rm b}$ components. This effect will discuss in more detail in §5.3.

(2) Spin effects: Relativistic gravity theories predict interactions between the rotational spin-spin effects, i.e. between the spins of the two orbiting bodies, and spin-orbit interactions, where the spin of each member individually interacts with the orbital angular momentum (e.g. Barker & O'Connell 1975). Only spin-orbit effects are observable in binary pulsars with contemporary observing systems via the geodetic precession of the binary members, i.e. the secular change in their rotation axis orientation.

(3) Universality of free fall of strongly self-gravitating bodies: In GR, the motion of a self-gravitating body by an external gravitational filed is independent of its gravitational binding energy or chemical

composition (i.e. independent of its EOS). Many alternative theories of gravity violate this principle, predicting different accelerations for two bodies with large binding energy difference that are attracted by the same external gravitational field. NS-WD systems with small eccentricities are excellent for these test, since the different accelerations will lead to an observed polarisation of the orbit in the projected direction of the external field, allowing direct tests (Freire et al. 2012a). The external field can be that of the Galaxy. Triple systems, however, with a NS-WD in an inner orbit and a third companion in the outer orbit, such as the hierarchical triple system PSR J0337+1715 (Ransom et al. 2014) can serve as the best testbeds for these tests.

(4) Local Lorentz Invariance of gravitational interaction (LLI): Some alternative gravity theories do not conform with the LLI. Unlike GR, they predict that the outcome of an experiment depends on the reference frame. The existence of a preferred (or privileged) frame induces the so-called "preferred-frame effects" (PFEs). In the PPN formalism they are described by three parameters which have null values in GR and non-zero in any theory that predicts LLI. The relative velocity of the solitary or binary pulsars with respect to the preferred frame induces secular variations in the longitude of periastron, orbital angular momentum precession which results in secular changes of the projected semi-major axis as well as pulsar spin precession that can limit the relevant PPN parameters. We will return to LLI violation tests in §5.2.

(5) Local Position Invariance (LPI): Similar to the case of LLI, LPI is valid in GR but can be violated by some theories of gravity. The LPI states that the result of a locally conducted gravitational experiment is independent on the location of the reference frame and the time that the experiment takes place. Consequently, in such theories the gravitational field of a self-gravitating body depends on the location with with respect to an external gravitational field. Due to the Galactic matter distribution, this would imply that the gravitational constant depends on the position self-gravitating body. Apart from variations in G, this also produces the same qualitative effects on binary and solitary pulsars as LLI, i.e. orbital angular momentum and pulsar spin precessions.

(6) Variations in the gravitational constant: We have already seen that LPI induces a $\dot{G}$ and can be derived by limiting the LPI observable effects on binary and pulsar spin effects. Alternative gravity theories, predict variations in the gravitational constant on cosmological time-scales and present-day variations. Binary pulsars can, in particular NS-WD systems, i.e. binaries consisting of bodies with a large difference in their gravitational binding energies can limit the $\dot{G}$ through measurements of secular variations of the orbital period.

In this chapter, we present results for two tests of gravity theories using pulsar timing data. The first test (§5.2.2) examines LLI violation by placing limit of the existence of PFEs via the study of the long-term temporal stability of solitary MSP pulse profiles. The second (§5.3) is a GW-radiation-damping test, where we impost limits on the existence of dipolar-GW radiation.

5.2 A Limit on Local Lorentz Invariance Violation of Gravity from Solitary MSPs

Violations of the LLI in the gravitational sector are predicted by various classes of gravity theories. For example, the vector-tensor theory in Will & Nordtvedt (1972), TeVeS (Tensor-Vector-Scalar) gravity (Bekenstein 2004; Sagi 2009), Einstein-Æther theory (Jacobson & Mattingly 2001), Hořava-Lifshitz gravity (Hořava 2009), and the standard model extension (SME) of gravity (Kostelecký 2004; Bailey &

Kostelecký 2006). A possible way to asses the validity of such theories, is to search for the PFEs they imply, with respect to possible preferred reference frames.

Violations of the LLI can be separately studied in the weak- and the strong-field gravity regimes. In the PPN formalism, PFEs are described by three parameters introduced in Will & Nordtvedt (1972). The idea is that when a theory singles out a preferred frame in relation to the mean rest-frame of the Universe, they will induce motion effects with respect to the preferred frame. It is shown that three parameters suffice to fully describe these effects. These parameters are noted as α_1, α_2 and α_3 when dealing with the weak-gravity field. The latter, in fact, has a double role, since it also probes possible violations in the global conservation laws for total momentum (see e.g. Will 2014a). Their strong-field counterparts are noted as $\hat{\alpha}_1$, $\hat{\alpha}_2$ and $\hat{\alpha}_3$. In GR and other theories, where PFEs are absent, all these parameters have null values.

Experimental efforts to measure these parameters have been carried out with observations in the Solar system and using pulsar timing. The tightest limits on the first and third parameter were already produced earlier with pulsar timing observations. Shao & Wex (2012) have derived the lowest limit on the first parameter from the orbital dynamics of PSR J1738+0333, using the high-precision timing data presented in Freire et al. (2012b). The best limit on the third parameter was recently derived by Zhu et al. (2015), using the data from PSR J1713+0747 to constrain the predicted effects of $\hat{\alpha}_3$ on the eccentricity. This limit surpassed the previous that was derived by statistical analysis of the orbital dynamics of a set of binary pulsars (Stairs et al. 2005). Until recently, the best limit on the second parameter was the one placed by Nordtvedt (1987), via solar system observations. With the work presented in this section and fully described in Shao et al. (2013), we have derived a new limit on $\hat{\alpha}_2$, which is the best limit to-date on this parameter. With this result, now all three PPN parameters describing the PFEs have their tightest limits from pulsar-timing observations (see Will 2014a, for a review on all experimental limits on PPNs).

5.2.1 Methodology of the Experiment

The α_2 PPN parameter is associated with a precession of the spin (rotational) axis of a self-gravitating object. In particular, α_2 induces a precession of the spin axis, defined by the unit vector $\hat{\mathbf{s}}$, around the direction of the pulsar's motion with respect to the preferred frame, defined by the unit vector $\hat{\mathbf{w}}$, as illustrated in Figure 5.2. Following Nordtvedt (1987) and Damour & Esposito-Farèse (1992b), the post-Newtonian Lagrangian for the N-body α_2-induced effects can be written as:

$$L_{\alpha_2} = \frac{\alpha_2}{4} \sum_{i \neq j} \frac{G m_i m_j}{c^2 r_{ij}} \left[(\mathbf{v}_i^0 \cdot \mathbf{v}_j^0) - (\hat{\mathbf{n}}_{ij} \cdot \mathbf{v}_i^0)(\hat{\mathbf{n}}_{ij} \cdot \mathbf{v}_j^0) \right] . \tag{5.3}$$

Here, $\mathbf{v}_i^0$ is the velocity of the i-th body with respect to the preferred frame, r_{ij} is the coordinate separation of the i-th and j-th bodies, and $\hat{\mathbf{n}}_{ij} \equiv (\mathbf{r}_i - \mathbf{r}_j)/r_{ij}$. In Nordtvedt (1987), it has been shown that the spin axis of a massive body precesses around the velocity of the centre-of-mass of the many-body system. Denoting the latter as $\mathbf{w}$, the massive body precesses with an angular velocity of

$$\Omega_{\hat{\alpha}_2}^{\mathrm{prec}} = -\frac{\alpha_2}{2} \left(\frac{2\pi}{P} \right) \left(\frac{w}{c} \right)^2 \cos(\psi) , \tag{5.4}$$

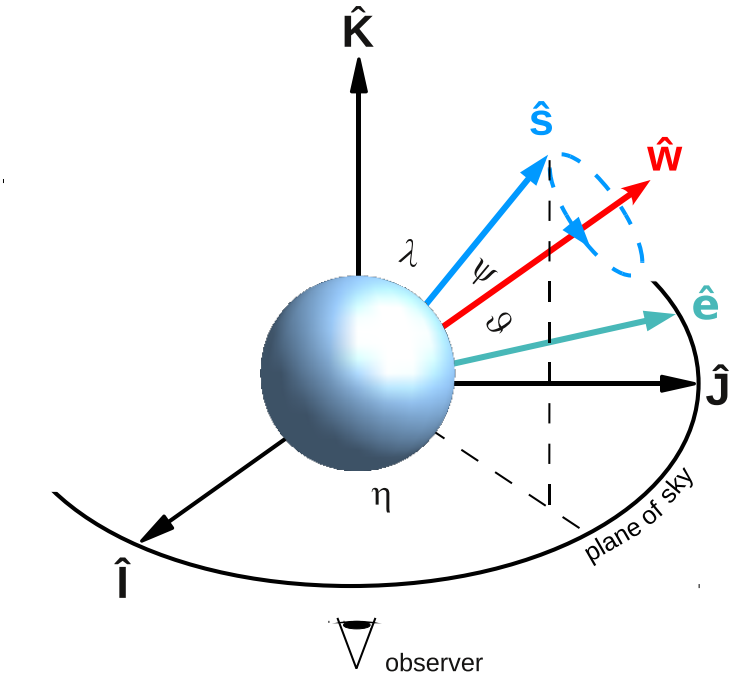

Figure 5.2: The geometry of the pulsar's rotation with respect to the observer, and the related quantities for testing the hypothesis of $\hat{\alpha}_2$-induced precession of the pulsar spin axis $\hat{\mathbf{s}}$. The relative velocity of the pulsar with respect to the preferred frame, $\hat{\mathbf{w}}$, induces the precession of $\hat{\mathbf{s}}$ around $\hat{\mathbf{w}}$. The coordinate system ($\hat{\mathbf{I}}$, $\hat{\mathbf{J}}$, $\hat{\mathbf{K}}$) is defined with $\hat{\mathbf{I}}$ pointing to east, $\hat{\mathbf{J}}$ pointing to the north celestial pole, and $\hat{\mathbf{K}}$ pointing along the line of sight. The unit vector $\hat{\mathbf{e}} \equiv \hat{\mathbf{K}} \times \hat{\mathbf{s}}/|\hat{\mathbf{K}} \times \hat{\mathbf{s}}|$ is in the sky plane. The geometry's unit vectors are related via the angles λ, ϑ, ψ and η. See §5.2.1 for details. Figure from Shao et al. (2013).

where P is the self-gravitating body's spin period, ψ is the angle between $\mathbf{w}$ and $\hat{\mathbf{s}}$, and $w \equiv |\mathbf{w}|$, is the magnitude of the velocity towards the preferred frame. This formulation was the basis of the derivation of the best α_2 limit from Solar system observation (Nordtvedt 1987). Under the assumption that the Sun's spin orbit and the Solar systems's angular momentum were aligned soon after the Sun's formation, a limit on α_2 is placed due their current alignment. The Sun was formed $\gtrsim 10^9$ yr ago which provides the experiment with a very long baseline that can boost the limit significantly. At the same time, however, this is an assumption that cannot be verified and is, as such, the largest source of uncertainty as well. The limit derived by this experiment stands at $|\alpha_2| < 2.4 \times 10^{-7}$. Note that in the Solar system, another limit on α_2 is placed at $|\alpha_2| = (1.8 \pm 5.0) \times 10^{-5}$ (at the 95% confidence level) by the Lunar Laser Ranging experiment (Müller et al. 2008). This experiment is based on highly accurate measurements of the distance between the Earth and the Moon using reflectors that were placed on the Moon by manned and unmanned space missions. The presence of LLI would induce periodic modulation in the lunar orbit around the Earth which can be used to limit a number of post-Newtonian parameters, including α_1 and α_2. Although significantly weaker than the Nordtvedt limit, this limit does not rely on assumptions and is therefore more robust.

One may notice from Eq. 5.4, that the experimental limits on α_2 can benefit from a small spin period. MSPs rotate at millisecond periods, about 10^8 times faster than the Sun, which rotates with a period of about 28 days. The way we can use pulsars for this experiment relies on our empirical

knowledge that a pulsar's precessing spin axis can have observable changes in the pulse profile. In §1.2.1, I already discussed that the pulse profile shape is formed by the cross-section of the radiation and the telescope beams, and that in highly relativistic orbits, we observe changes in the profile that are attributed to relativistic spin precession. Solitary pulsars, on the other hand, are not expected to ever suffer from such precessions. They are therefore excellent test beds for the α_2 experiment. In particular, following the geometric configuration of Fig. 5.2, we can relate Eq. 5.4 with the rate of change of the angle λ as (Bailes 1988):

$$\frac{\mathrm{d}\lambda}{\mathrm{d}t} = \Omega^{\mathrm{prec}}_{\hat{\alpha}_2}\, \hat{\mathbf{w}} \cdot \left(\frac{\hat{\mathbf{K}} \times \hat{\mathbf{s}}}{|\hat{\mathbf{K}} \times \hat{\mathbf{s}}|} \right) \equiv \Omega^{\mathrm{prec}}_{\hat{\alpha}_2} \cos(\vartheta)\,, \tag{5.5}$$

where $\hat{\mathbf{K}}$ is the unit vector defining the LOS, ϑ is the angle between $\hat{\mathbf{w}}$ and $\hat{\mathbf{e}}$. The unit vector, $\hat{\mathbf{e}}$, gives the line of nodes associated with the intersection of the sky plane and the equatorial plane of the pulsar.

We now need to connect this relation with the observed (non-)change of a pulse profile over time. To do so, we have to assume a model for the radiation beam. We use a simple cone model (Gil et al. 1984). The only assumption that this simple geometric model makes is that the beam is centred at the magnetic axis, avoiding model-dependent aspects of pulsar emission while sufficiently reproducing the basic features of the profiles we used for this study. The selection of this model is also motivated by its use by Manchester et al. (2005) to search for a change in the profile of the MSP member of the Double Pulsar, PSR J0737−3039A. In that paper, it was shown that the profile data are equally well described by circular and elliptical beams (the circular beam is then preferred as it is a simpler model). Following geometrical argument, once can derive a relation between the pulse width and the geometry of the pulsar as (Manchester et al. 2005; Lorimer & Kramer 2005):

$$\sin^2\left(\frac{W}{4}\right) = \frac{\sin^2(\rho/2) - \sin^2(\beta/2)}{\sin(\alpha+\beta)\sin(\alpha)}\,, \tag{5.6}$$

where W is the width of the pulse, α is the angle between $\hat{\mathbf{s}}$ and the magnetic axis, $\beta \equiv 180^\circ - \lambda - \alpha$ is the impact angle, and ρ is the semi-angle of the opening radiating region. The basic assumption that we have to make, is that the radiation properties of the pulse, described by α and ρ, have not changed over the 15-year time-span of the used observations. This is a plausible assumption since there is no evidence in the data to the contrary. This assumption is expressed as $\mathrm{d}\alpha/\mathrm{d}t = \mathrm{d}\rho/\mathrm{d}t = 0$, and ultimately leads to (see Cordes et al. 1990):

$$\frac{\mathrm{d}\lambda}{\mathrm{d}t} = \frac{1}{2}\,\frac{\sin(W/2)}{\cot(\lambda)\cos(W/2) + \cot\alpha}\,\frac{\mathrm{d}W}{\mathrm{d}t} \equiv \mathcal{A}\,\frac{\mathrm{d}W}{\mathrm{d}t}\,, \tag{5.7}$$

where we have compacted the equation introducing the notation $\mathcal{A} \equiv \sin(W/2)/[2\cot(\lambda)\cos(W/2) + 2\cot\alpha]$. By combining this equation with Eqs. 5.4 and 5.5, we derive a relation that allows to translate the limits on the profile changes to limits of $\hat{\alpha}_2$:

$$\hat{\alpha}_2 = -2\,\mathcal{A}\left[\frac{2\pi}{P}\left(\frac{w}{c}\right)^2 \cos(\psi)\cos(\vartheta)\right]^{-1} \frac{\mathrm{dW}}{\mathrm{dt}}\,. \tag{5.8}$$

The height of the pulse where the width is measured is a free parameter. We chose the classic full width at half maximum, for which analytic formulas to describe it exist for various distributions. We use the notation W_{50} to explicitly state the use of this width measure. Before proceeding to describe the implementation of this idea, we note that in binary pulsars the spin axis precession effect of $\hat{\alpha}_2$ would induce long-term periodic variations on the projected semi-major axis that will be observed on shorter timescales as secular changes. These predictions were used by Shao & Wex (2012) for two binary MSPs to derive a limit in the strong-field regime of $|\hat{\alpha}_2| < 1.8 \times 10^{-4}$.

5.2.2 Data Analysis: Temporal Pulse Profile Stability

We examine the profiles of two solitary MSPs, namely PSR B1937+21 (a.k.a. J1939+2134) and PSR J1744−1134. The best way to perform this experiment is by using long-term data recorded with the same observing system, which should however also record the profiles with sufficient precision. The EBPP data, recorded with the 100-m Effelsberg radio telescope and presented in Chapter 3, are perfectly suited for this. It is a coherent de-dispersion backend, therefore offers sharply sampled pulse profiles and the observing configuration underwent minimal changes for over 15 years in the L-band. No other data set, in fact, existed with these characteristics. We note, that all data used for this and the second experiment described in this chapter were recorded primarily for the EPTA timing campaign, demonstrating how the recorded data can produce other equivalently important scientific results while working on a long-term project, such as the GW detection effort.

We discuss the profile characteristics and the derivations of their upper limits on their variability separately for each profile. Four were the main aspects of the radio pulse profiles that were investigated. First, for each pulsar we had to fit an analytic model. Second, we used these fits to quantify as as many profiles characteristics as possible, such as the width or the distance between components. The third part was to quantify any possible profile frequency evolution (§1.2.1, Fig. 1.4), due to the change of the central frequency from 1360 to 1410 MHz. This also led to an investigation for possible profile changes between the two bands due to IISM effects (§1.2.3). The data reduction methods are described in §3.2.1.

5.2.2.1 PSR B1937+21 Pulse Profile

PSR B1937+21 is the first ever discovered MSP (Backer et al. 1982). It has a rotational period of 1.6 ms and it's one of the brightest MSPs that is systematically observed (see mean flux measurements in Table 3.2). Although it suffers from significant timing noise, as we saw in Chapter 4, its brightness, and the fact that its sky location is accessible to all PTAs, make it a source that is useful to check the individual observing systems and the relative performance of different ones. It is also an excellent pulsar to study the mechanisms of timing noise. Owing to the pulsar's brightness, for almost every observing run that it was observed we have a high S/N ratio profile. The pulse profile of PSR B1937+21 is presented in Fig. 5.3, where two profiles recorded 12 years apart are shown. The profile has a strong main-pulse (`MP1`) with a secondary, weaker component (`MP2`) and a strong interpulse (`IP`), with about half the intensity of the main pulse. The main and the interpulse are separated by about 180°. As discussed in §1.2.1, such a separation can be explained by a pencil-beam model, with the pulsar in such orientation that we observe emission from both magnetic poles or with a model of a wide, hollow cone emission pattern.[1] The "dips" of the baseline around the pulses are due to instrumental effects. We have

[1] Note that, in fact, γ-ray observations discussed in §5.2.3 do not support the hollow-cone model.

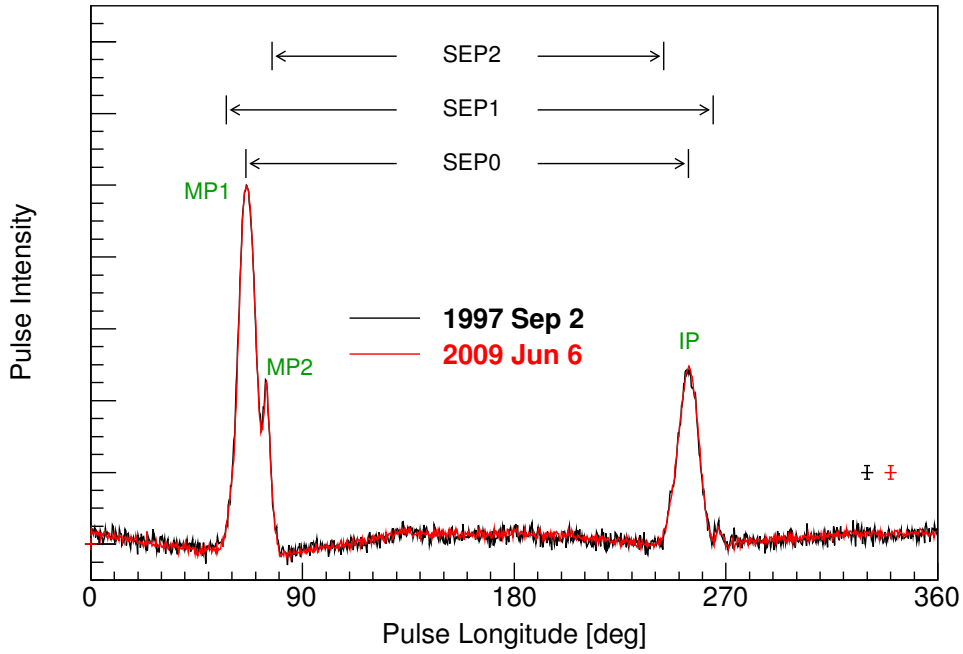

Figure 5.3: Comparison of two pulse profiles of PSR B1937+21 recorded at two different epochs – the black one is from September 2, 1997, while the red one was from June 6, 2009. The profiles were scaled and aligned to allow a direct comparison. Uncertainties in pulse profiles are illustrated at the right bottom corner, defines as the average off-pulse fluctuactions. The profiles is composed of the first component of the main-pulse (`MP1`), the second component of the main-pulse (`MP2`), the interpulse (`IP`), the separation between `MP1` and `IP` (`SEP0`), the separation between leading `MP1` and trailing `IP` (`SEP1`), and the separation between trailing `MP2` and leading `IP` (`SEP2`). Figure from Shao et al. (2013)

not removed these effects since they remain unchanged over the time-span and do not introduce any bias in profile temporal variation measurements.

All components of this profile are quite symmetric, and fitting of all components was achievable with simple parabolic functions, one for each component. The fitting was performed with custom `FORTRAN` routines. The symmetry of the fitted functions allowed to preserve the linearity of the fitting procedure and a straightforward error-propagation-based calculation of the uncertainties assigned to the measured quantities. Prior to the fit, the profiles are normalised with respect to their peak flux and rotated to a fixed phase. For each of the three components we calculated the peak intensity and its corresponding phase location as well as its W_{50} width. We investigated the time stability of the pulse profile using seven different diagnostics, based on measurements of components widths, separations and peak flux ratios (see Fig.5.3). The derivation of the $\hat{\alpha}_2$ limit is only based on the temporal behaviour of W_{50}, however, the rest of the diagnostics are used to demonstrate the stability of the profile in multiple ways, since all these parameters have been observed to change in binary pulsars with spin axis precession from spin-orbit couplings. The results from fitting are plotted in figure 5.4 as a function of time. The difference in the central frequency is noted with the change in colour, from black to blue.

The limit on the changes of the width over time is derived by fitting the measured widths with a

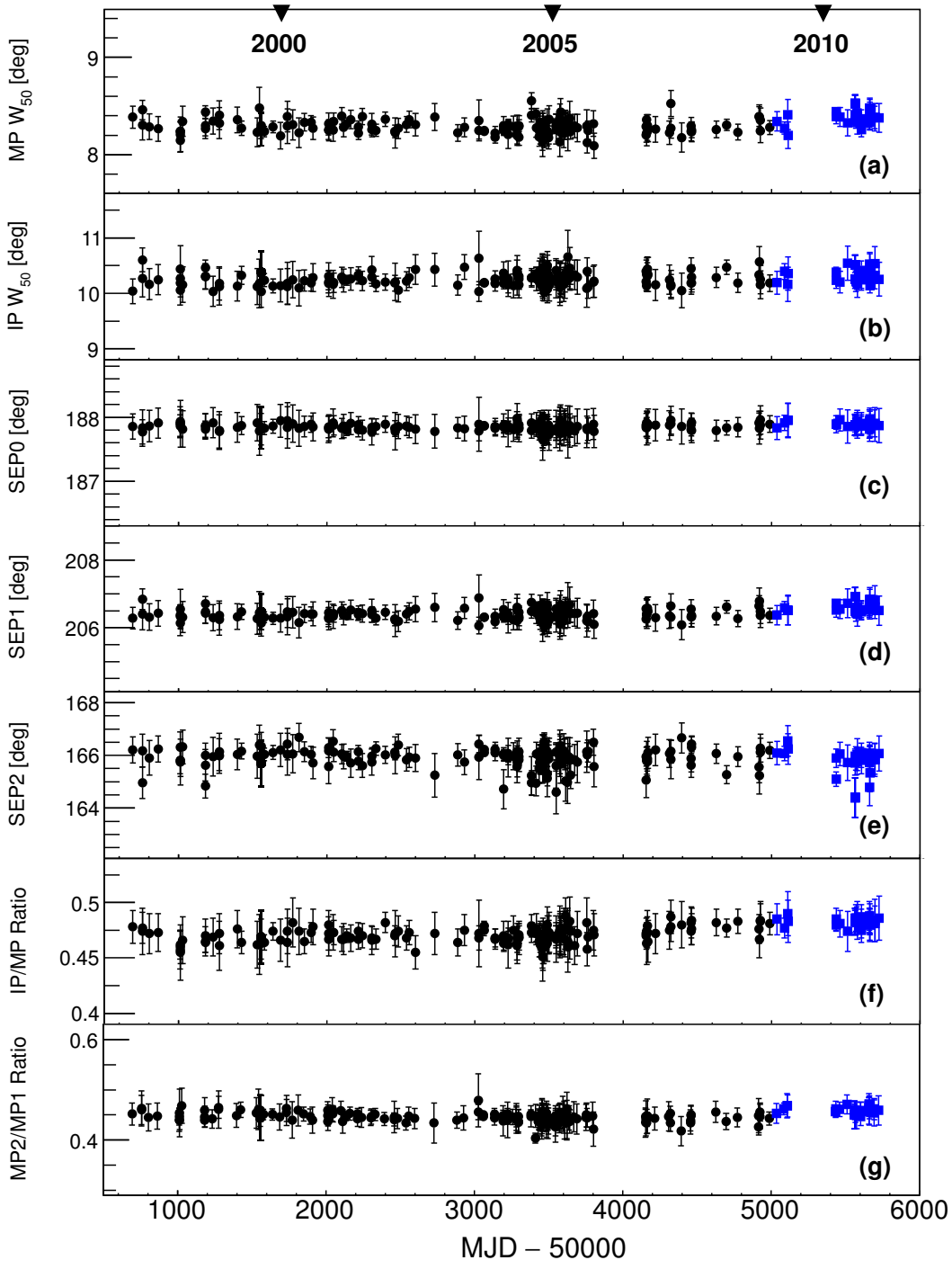

Figure 5.4: Pulse profile characteristics of PSR B1937+21, as a function of modified Julian date (MJD); see figure 5.3 for notations. The amplitude ratios in (f–g) are measured from peak to peak. Black circles are observations made at 1410 MHz, while blue squares are observations made at 1360 MHz. Years of observations are indicated at the top of the figure. Figure from Shao et al. (2013)

3-parameter function of time, t, as:

$$W_{50}(t) = W_{50} + \frac{\mathrm{d}W_{50}}{\mathrm{d}t}\, t + \Delta W_{50}\, \Theta(t - t_0)\ . \tag{5.9}$$

The first two right-hand-side terms denote the width at an arbitrarily selected epoch and the a linear change of the width in time. The third term, models a possible change in the width after the central frequency change on time t_0, which is known for each data set. This will manifest as an offset and is therefore modelled with a width difference, ΔW_{50} multiplied with a Heaviside step function $\Theta(t - t_0)$. We simultaneously fit for W_{50}, $\mathrm{d}W_{50}/\mathrm{d}t$, and ΔW_{50}.

In order to measure the values and quantify the uncertainties of these width parameters, we used Monte-Carlo methods to create 10^6 realisations of the W_{50} sample, which we each fitted with Eq. 5.9 via a wLS fit. The results were used to construct the probability distributions for each parameter, which were symmetric and very well approximated by Gaussian distributions. We used the distributions' central values and standard deviations as the width values and their 1σ uncertainties. The uncertainties were rescaled with the square root of the mean reduced chi-squared from all the wLS fits.

The results are summarised in Table 5.1 and are consistent with no time evolution of the width for both the main pulse and the interpulse. We did, however, examine if the data can still support the hypothesis of the necessity of a non-zero width time-derivative. To this end, we performed an F-tests which used a *null hypothesis* that the data do not require a non-zero $\mathrm{d}W_{50}/\mathrm{d}t$ to be fully modelled. For the main pulse and the interpulse the p-values are 0.22 and 0.31 respectively, so the inclusion of an additional parameter (i.e. the width time-derivative) does not significantly improve the fit.

On the other hand, the results from the PSR B1937+21 analysis give a measurable small jump between the two frequencies for the main pulse width at a value $\Delta W_{50} = 0.12° \pm 0.03°$. This is approximately on third of the profiles time bin, demonstrating that the data and methods used are in fact sensitive to very tiny changes on the profile. Such a change is not observed for the interpulse.

Profile Frequency Evolution & IISM Effects

We examined the possible origin of the measured difference in the main pulse width in the data from the slightly different frequency bands. PSR B1937+21 has a high DM value and it is logical to investigate the probability that the change is due to interstellar medium effects.

The first effect we have investigated is that of pulse broadening by multi-path ray scattering (§1.2.3.2, Fig. 1.6). We calculated the expected broadening, τ_d based on the empirical relation by Cordes & Lazio (2003) and the updated constants and coefficients as defined observationally by Bhat et al. (2004):

$$\log(\tau_d)(\mathrm{ms}) = -6.46 + 0.154(\log(\mathrm{DM})) + 1.07(\log(\mathrm{DM}))^2 - (3.86 \pm 0.16)\log(\nu)\ , \tag{5.10}$$

where the broadening is calculated in ms, and ν is as usual the observing frequency. We find that the difference in the broadening width between the two central frequencies is 0.004°. This is two orders of magnitude smaller than the measured value, and the broadening width itself at these frequencies in an order of magnitude below the measured ΔW_{50}. Scattering therefore does not appear to be a viable explanation, even when accounting for the uncertainties of the used empirical relation.

The next possibility, is to have a profile broadening because of imperfect DM de-dispersion (§1.2.3.1, Fig 1.5). The DM value is registered in the pulsar ephemeris that the EBPP is using to perform the on-

line coherent de-dispersion, and could had been out of date, since PSR B1937+21 is known to suffer from significant temporal DM variations (e.g. Ramachandran et al. 2006; You et al. 2007). We have calculated the width difference between the two frequency bands for a DM value that deviates as much as 0.05 cm^{-3} pc from the correct value. This is a large deviation that would occur only after decades without updating the DM value of the ephemeris. Even for this extreme case, we found that the ΔW_{50} between the 1410 MHz and 1360 MHz bands are below a few times 0.001°, using the cold plasma dispersion law (Eq 1.2). Therefore, the effects from DM variation are also negligible. Note that the used ephemeris files were also inspected and verified that the DM values, although updated only in intervals of some years, it never deviated from the correct value enough to cause the measured width difference. Finally, the expected change width due to the assumed incorrect DM values from analytic calculations, was also reproduced in the data, by updating the timing parameter information with fake, erroneous DM values and de-dispersing the signal.

All evidence pointed out that this was a true profile evolution across the frequency. A way to test this hypothesis, was to compare the EBPP data, with data recorded simultaneously at Effelsberg with the PSRIX backend. The latter has a wider bandwidth at 200 MHz, by comparison the 44 MHz of the EBPP for a high-DM pulsar such as PSR B1937+21. Further, the pulsar ephemeris at PSRIX was more recently updated, the data quality is higher and the pulse better sampled. Importantly, the PSRIX frequency range covers both frequency bands of the EBPP backend. We split the PSRIX profile into two frequency bands corresponding the EBPP bands and found a difference in the two pulse profile widths of $\Delta W_{50} \simeq 0.07° \pm 0.03°$, in agreement with the width jump from the EBPP data. Consequently, we conclude that ΔW_{50} reflects an evolution of the pulsar profile width with frequency. This finding is agreement with observations in the literature (see Kramer et al. 1999, their Fig. 13). that noted the frequency evolution of this pulsar's profile across wider frequency ranges, also using the EBPP.

5.2.2.2 PSR J1744−1134 Pulse Profile

PSR J1744−1134 was discovered in 1997 in data from the Parkes 436 MHz survey (Bailes et al. 1997), along with another three solitary MSPs. It spins at a 4.07-ms period and it has been continuously observed at Effelsberg ever since it was discovered. The pulse profile in the L-band has a single, sharp component with a width of $W_{50} \sim 12.5°$.

Although at first glance this looks like a simple profile, a closer inspection reveals a highly asymmetric profile, which proved more challenging to model and fit than the multi-component profile of PSR B1937+21. Figure 5.5 shows the pulse profile at two epochs separated by 10 years. The inset shows a zoomed view to the on-pulse region. Following a similar approach to the PSR B1937+21 profile fitting proved unstable. We found that one could use a minimum number of components by using three components of different distributions. We used one Gaussian and two Landau functions with opposite orientations. The fitting code used custom C++ routines based on routines from the data analysis framework ROOT[2].

Fitting the profile with this combination of distributions did not allow an analytic estimation of the fit uncertainties. For this reason, we employed Monte-Carlo methods to simulate 10^4 realisations of each profile, perform a wLS fit for each realisation with the 3-component model, and derive the W_{50} from the analytical sum of these components. The W_{50} distribution for each 10^4 profile realisations were used to derive the central value and uncertainties, with the uncertainties rescaled with the square root of the mean reduced chi-squared from the wLS profiles fit. The results are shown in Fig. 5.6.

[2] https://root.cern.ch/

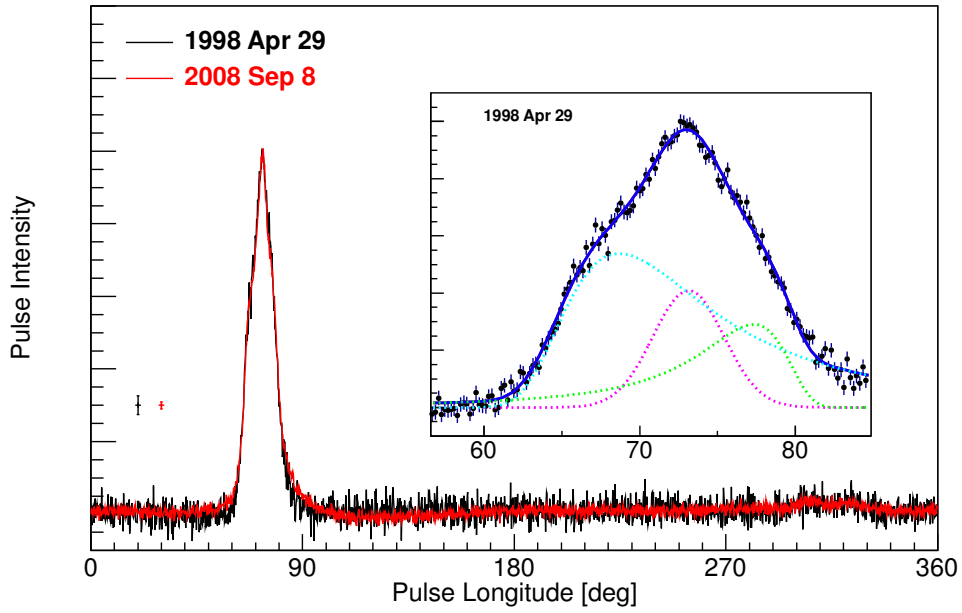

Figure 5.5: A comparison of two pulse profiles of PSR J1744−1134 recorded at two different epochs – the black one was obtained on April 29, 1998, while the red one was obtained on September 8, 2008. The peak is aligned and scaled to have the same intensity. Uncertainties in pulse profiles are illustrated at the left bottom corner. The inset shows the zoom-in of the main pulse (corresponding to the black profile in the main figure), and the three components used for the analytical fitting to the pulse. Figure from Shao et al. (2013)

We followed the same procedure as with PSR B1937+21 to search for variations in the pulse width with null results, summarised in Table 5.1. The ΔW_{50} is consistent with zero for this pulsar. The overall lower precision of the results with this pulsar is due to the fewer available high S/N ratio observations.

5.2.3 Derivation of a New Limit on the $\hat{\alpha}_2$ PPN Parameter

We now proceed to derive the limits on $\hat{\alpha}_2$, using our results and Eq. 5.8. We have defined the widths and the limits of the time derivatives, and so we still need information on the emission property parameters, namely the angle between the rotation and magnetic axes, α, and the impact angle, λ. Fortunately, these information were observationally defined by combining radio and γ-ray observations of these pulsars from the Fermi Gamma-ray Space Telescope (Guillemot et al. 2012; Johnson 2012).

The last step, is to define w, i.e. the velocity of the pulsar with respect to the preferred frame and the angle, ψ, between that velocity and the spin axis. To this end, we need to define a preferred frame. A widely used frame, is that where the Cosmic Microwave Background (CMB) is isotropic. The preferred frame is then assumed to be determined by the global matter distribution in the Universe. The PFEs are therefore caused by the fields the gravitational interaction which must have ranges much larger that the Hubble radius[3]. All values of PFE parameters discussed in this chapter refer to the CMB frame. Note

[3] The Hubble radius defines a sphere around a point in the Universe, beyond which a local observer sees objects moving away at a rate greater than the speed of light.

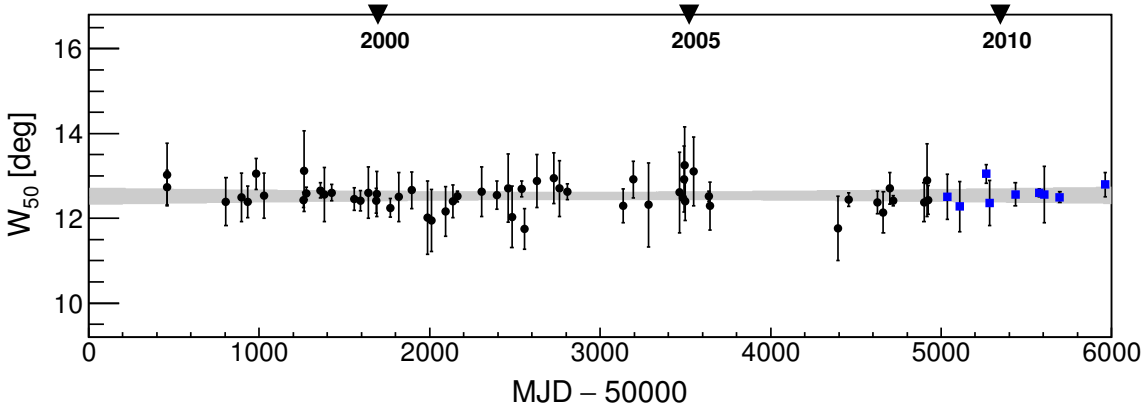

Figure 5.6: Pulse width at 50% intensity level of PSR J1744−1134, as a function of time. Black circles are observations made at 1410 MHz, while blue squares are observations made at 1360 MHz. Errors are rescaled by the square root of the fitting $\chi^2_{\rm red}$. The grey region shows the 3σ band of our linear fitting. The years of observations are indicated at the top of the figure. Figure from Shao et al. (2013)

Table 5.1: A summary of the results for the measurements of the pulse profiles widths and rate of change. The spin periods and dispersion measures (reference epoch MJD 55000) are from Desvignes et al. (2016). Parenthesised numbers represent the 1σ uncertainty in the last quoted digit.

Pulsar	B1937+21		J1744−1134
Spin period, P (ms)	1.55780653910(3)		4.074545940854022(8)
Dispersion measure, DM ($\rm cm^{-3}\,pc$)	71.0227(5)		3.1380(3)
Time span of data used in this work (MJD)	50693–55725		50460–55962
Number of points used	189		65
Pulse width at 50% intensity, W_{50} (deg)	8.281(9)	10.245(17)	12.53(3)
Time derivative of W_{50}, $\mathrm{d}W_{50}/\mathrm{d}t$ (10^{-3} deg yr^{-1})	−3.2(34)	3.5(66)	1.3(72)
Jump between two frequencies, ΔW_{50} (deg)	0.12(3)	0.04(6)	–

that other local frames have also been used in the literature, e.g. the Barycentric Celestial Reference System (e.g. Soffel et al. 2008).

The velocity of the SSB with respect to the CMB has been measured with the Wilkinson Microwave Anisotropy Probe to be $|\mathbf{w}_{\rm SSB}| = 369.0 \pm 0.9\,{\rm km\,s^{-1}}$, and the direction of the relative SSB movement in Galactic coordinates is $(l, b) = (263.99^\circ \pm 0.14^\circ, 48.26^\circ \pm 0.03^\circ)$ (Hinshaw et al. 2009; Jarosik et al. 2011). The velocity of the pulsar with respect to the CMB can be derived simply via the vector relation relation $\mathbf{w} = \mathbf{v}_{\rm PSR-SSB} + \mathbf{w}_{\rm SSB}$, where $\mathbf{v}_{\rm PSR-SSB}$ is the 3D motion of the pulsar with respect to SSB. Distance and kinematic parameters from Verbiest et al. (2009) where available. The distance to the PSR B1937+21 was not well constrained at that time and therefore a range of 3.6 to 4.8 kpc was used based on DM distances from the NE2001 and M3 (§3.3.3) Galactic electron density models. The parallax distance from the latest EPTA timing model (Desvignes et al. 2016, Chapter 3) places this MSP at a distance between 2.61 and 4.29 kpc, making the choice used a rather conservative one. Because the composite proper motion of PSR B1937+21 is small ($\simeq 0.42\,{\rm mas\,yr^{-1}}$) the error of the 2D velocity is less than $10\,{\rm km\,s^{-1}}$ even if we underestimate or overestimate the distance by a few kpc.

As explained in Chapter 2, The radial velocity ($v_r \equiv \hat{\mathbf{K}} \cdot \mathbf{v}_{\rm PSR-SSB}$) of pulsars is not measurable in general with pulsar timing. The effects of the radial velocity enter the experiment's result via the velocity's component along the spin axis ($\mathbf{w} \cdot \hat{\mathbf{s}}$). Fortunately, as shown from the γ-ray observations, the spin axis of both pulsars lie close to the sky plane (i.e. $\zeta \approx 180^\circ$) so the effects from the uncertainty in the radial velocity are small. We found that even for unphysical radial velocities of the order of $10^3{\rm km\,s^{-1}}$ (recall from Chapters 2 and 3 that the observed velocities of pulsars are of the order of $10^2{\rm km\,s^{-1}}$), the $\hat{\alpha}_2$ limit alters by about $\sim 40\%$. A reasonable range of radial velocities can be derived through the plausible assumption that pulsars are gravitationally bound to the Galaxy. Using the Galactic potential model from Kuijken & Gilmore (1989), an estimation of reasonable ranges of the radial velocities were estimated to be between -600 and $+200\,{\rm km\,s^{-1}}$ for PSR B1937+21 and between -400 and $+250\,{\rm km\,s^{-1}}$ for PSR J1744−1134. It turned out that the $\hat{\alpha}_2$ test results are affected by the range of the velocities at most by $\sim 15\%$ with these ranges.

Unfortunately, the last remaining parameter, the azimuthal angle of the pulsar spin around the LOS, η, is not observationally constrained. We therefore considered this as a free parameter. This, in fact, is the biggest source of uncertainty of this experiment and inevitably leads to a constrain of the $\hat{\alpha}_2$ which is not direct, but probabilistic in nature. To reach the end result of this study, we employ Monte-Carlo methods to fit the data of each pulsar with Eq 5.3, accounting for the measurement errors, and the unknown parameters, namely the angle η and the radial velocity, v_r. The prior probability distribution for v_r is a zero-mean Gaussian with a $100\,{\rm km\,s^{-1}}$ standard deviation. For η, we use an uninformative prior, uniformly distributed in the range $[0^\circ, 360^\circ]$. Using 10^8 simulations, we finally resulted in the two posterior probability distributions of the $\hat{\alpha}_2$, one per pulsar. It was already known Shao & Wex (2012), that the posterior distributions have very long tails, which result from the probabilities associated with highly unfavourable geometrical configurations where $\cos(\psi) \simeq 0$ and/or $\cos(\vartheta) \simeq 0$, which cannot constrain $\hat{\alpha}_2$. However, this was exactly the reason for which this experiment was set up from the beginning using two pulsars (more pulsar would be better, but two is the minimum requirement, and no other pulsar data we had available would significantly improve our results). Statistically, it is quite improbable to have randomly selected pulsars in such an unfavourable geometry. We can make the reasonable assumption that the pulsars are independent, and that their posterior distributions are drawn from the same parent distribution, i.e. they both measure the same $\hat{\alpha}_2$ (see §5.2.4 for a discussion on this and other assumptions made). This allows a combined probability distribution that suppress the tails, enabling an improved limit. The individual and combined $\hat{\alpha}_2$ distributions are shown in Fig. 5.2.3, The

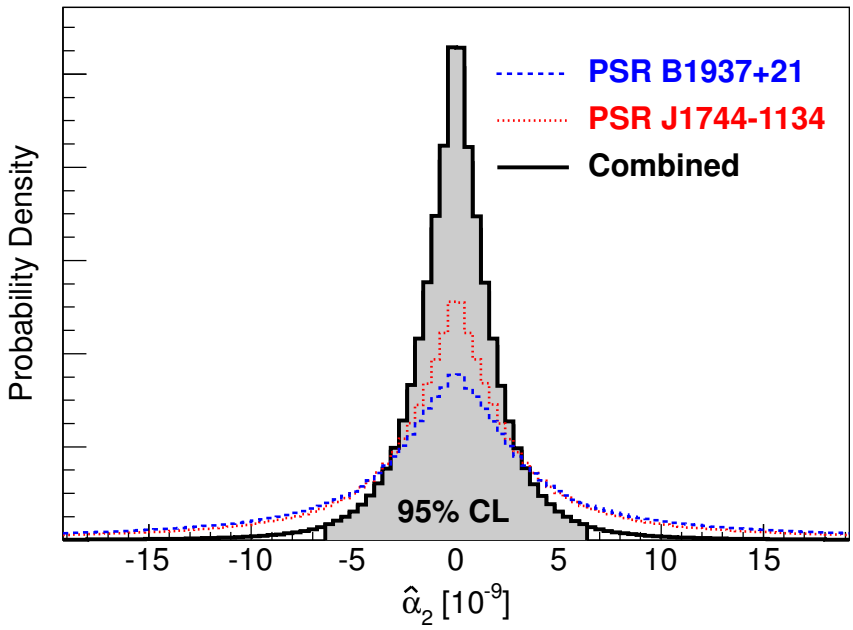

Figure 5.7: Probability density functions of $\hat{\alpha}_2$ from PSR B1937+21 (blue dashed histogram), PSR J1744−1134 (red dotted histogram), and their combination (black solid histogram). At 95% confidence level, $|\hat{\alpha}_2|$ is constrained to be less than 1.6×10^{-9} from the combined probability distribution. Figure from Shao et al. (2013)

new $\hat{\alpha}_2$ limits, at the 95% confidence level are:

$$\begin{aligned} \text{PSR B1937+21:} \quad & |\hat{\alpha}_2| < 2.5 \times 10^{-8}, \quad (95\%\ \text{CL}), \\ \text{PSR J1744−1134:} \quad & |\hat{\alpha}_2| < 1.5 \times 10^{-8}, \quad (95\%\ \text{CL}). \\ \\ \text{Combined:} \quad & |\hat{\alpha}_2| < 1.6 \times 10^{-9}, \quad (95\%\ \text{CL}). \end{aligned}$$

The combined $\hat{\alpha}_2$ upper limit is four orders of magnitude better than the limit from the Lunar Laser Ranging experiment (Müller et al. 2008), over two orders of magnitude better than the Nordtvedt limit, and about five orders of magnitude better than the previous best strong-field limit by Shao & Wex (2012).

5.2.4 Conclusions and Discussion

The new limit on the $\hat{\alpha}_2$ parameter is significantly improved than all previous limits, so it is important to look at some details of the experiment and assumptions, and how these fit into the framework of gravity theories.

Observationally, the limit depends strongly on the measurements of the profile stability of solitary pulsars. The data set used from the EBPP, was the best for this purpose due to the fact that is was produced by the same observing system over a long time-span. The only change was a small shift

in frequency due to the replacement of the receiver towards the end of the time under consideration. This added one additional free parameter in the problem, which turned out to be only measurable for PSR B1937+21, due to a small evolution of the main pulse across the observing frequency. Thanks to available data from the PSRIX backend, we verified that our measurement of the change in width is robust. The profile PSR B1937+21 has three components which allowed for measurements of components separations and peak flux ratios, none of which show any variability within the measurement errors, adding more confidence in the result of non-detection of temporal profile variations. We did in fact verify that by using the width measurement of the interpulse width of PSR B1937+21 instead of the main pulse, the result was consistent, and in fact even a bit improved. We made the choice to use the main pulse, to keep the experiment results on the more conservative side.

The method used also needs the adoption of an emission beam geometry. The radio pulse profile of PSR B1937+21 could imply a wide, hollow cone shape for the beam instead of the simple cone model. However, γ-ray data came to the rescue to reject this model. Nevertheless, under the assumption of this geometry the results are similar. The γ-ray data, were also instrumental in reducing the free parameters of the problem, since in combination with the radio data were able to define the magnetic axis inclination and impact angle, leaving only one angle, the azimuthal angle of the pulsar spin around the LOS, to be a geometric free parameter. We are also limited by the unknown radial velocity of the pulsars, which add another free parameter. Due to these, the $\hat{\alpha}_2$ limit we produced is a probabilistic one, and the combination of the probability distributions of more than one pulsars, has improved the individual-pulsar limits by an order of magnitude.

It is interesting to note, that although PSR B1937+21 has a smaller period and a narrower main pulse component, more data points and profiles with better overall sampling precision, PSR J1744−1134 produces a better $\hat{\alpha}_2$ limit. Although the remarkably short spin periods of MSPs are a without question what gives a great improvement in the precision of the test by comparison the Solar system limit from Nordtvedt (1987), when it comes to comparing the limits from different MSPs, the geometry of the spin and magnetic axes and the inclination angle by which we see the pulsar can be more important for the $\hat{\alpha}_2$ limit.

Finally, we note that a strong feature of the PFEs tests with pulsars, is that they have the potential of improving significantly over time. Specifically, the $\hat{\alpha}_2$ limit precision scales with $P\,\mathrm{d}W/\mathrm{d}t$, which approximately translates in a scaling relation with the data time-span, T, as $P\,T^{-3/2}$. Even without improvement in instrumentation the limit can improve with more observations that extent the baseline of our sample. The observational technology however is improving. Newer observing systems offer already superior data to that of the EBPP and future ones will improve the pulse width measurement precision even further. Long-term monitoring of many MSPs is already ongoing, mainly because they are PTA sources, just as in the case of the two MSPs we used in this work. Although in principle data from newer systems can provide better limits on the $\hat{\alpha}_2$ limit, note that this will be possible only if the observing systems remain unchanged for decadal time-scales, as was the case with the EBPP data. We also note, that new limits from other pulsars can be combined with the ones we present here to improve the overall limits to $\hat{\alpha}_2$ even further.

To conclude the presentation of this work, it is necessary to discuss the implications of the results of this experiment to the study of gravity theories. It is noteworthy that the α_i and $\hat{\alpha}_i$ ($i = 1, 2, 3$) parameters probe different regimes of gravity. As such, any comparison between $\hat{\alpha}_2$ and α_2 is phenomenological, since they describe, in general, different aspects of the Lorentz symmetry. The reason why we keep different notations for these parameters in the strong and the weak gravity regime, is because in principle the PPN parameters can differ between the different gravity regimes (e.g. Yagi et al. 2014). We must

therefore be cautious with the assumption we made that the two pulsars measure the same $\hat{\alpha}_2$ value in order to combine their results. A steep compactness factor would mean that even for two NSs with different masses, this assumption may break down and we would have to rely only on the, already very good, single-pulsar limits.

5.3 A Limit on the Existence of Dipolar Gravitational Waves in a New Mass Range using PSR J1012+5307

As introduced in §5.1, one of the ways that pulsar timing observations can limit the parameter of gravity theories is via the effects on the orbit by the emission of GW radiation. The basic effect, is that energy is lost from the binary and therefore the orbit will decay, which eventually leads to the mergers of compact objects. The effects of GW-radiation damping are more prominent the tighter the orbit is (faster motion) and the more massive the objects are (see e.g. Wex 2014, their Fig. 6). In this respect, it is quite difficult to find a pulsar that can verify with greater precision the predictions of GR for GW emission than the Double Pulsar. However, the results from the Double Pulsar is not the final word, when it comes to testing gravity theories based on GW damping. Even when intending to test the predictions of GR, it is important to probe gravity at various masses, since strong-field effects may show deviations from GR at higher masses than the ≈ 1.2–$1.4 M_\odot$ of the Double Pulsar or the Hulse-Taylor Pulsar members. Such an observational validation of GR came with PSR J0348+0432, which has a 2-solar-mass pulsar in orbit with a WD (Antoniadis et al. 2013). There are however more effects that need to be tested, and which have different figures-of-merit for the best pulsars to use.

We have noted that in many alternative theories of gravity, the compactness of the self-gravitating bodies leads to predictions of additional, observable in some cases, effects. In GR, GWs are described by the quadrupole formula (Einstein 1918), and the back-reaction to the orbit enters the equation of motion at the 2.5PN order. In alternative theories, it can already enter at the 1.5PN order via the existence of dipolar GWs (e.g. Will 1993). This type of gravitational radiation becomes, however, significant only when the two orbiting bodies have a significant difference in their gravitational binding energies. As an example, we can use a physically motivated family of gravity theories, the *quadratic, mono-scalar-tensor* theories of gravity (Damour & Esposito-Farèse 1993; Damour 2009). In general, scalar-tensor (also tensor-scalar in the literature) theories describe gravitation using both a tensor and a scalar field. Simply put (following Freire et al. 2012b), the well-known metric $g_{\mu\nu}$ in GR that defines the gravitational field becomes $\bar{g}_{\mu\nu} = A^2(\varphi) g_{\mu\nu}$ in scalar-tensor gravity, with $A(\varphi)$ a (non-vanishing) function that describes the coupling between matter and the scalar field.

5.3.1 Limiting Dipolar-GW Emission with Binary Pulsars

In the framework of scalar-tensor theories, "scalarisation" effects are possible (Damour & Esposito-Farèse 1993), where the dynamical coupling between a compact object and the extra scalar field depends on the compactness of the compact object, and as a consequence on their EOS. This is measured through the *effective scalar coupling parameters*, usually denoted as α; in the rest of this chapter we use the notations α_p and α_c for the pulsar and its binay companion respectively. These parameters depend on fundamental constants of each theory that describe the coupling of matter to the scalar field. The lower-order terms, α_0 and β_0, are typically used in pulsar-timing applications, which define the linear and quadratic matter-scalar coupling constants (see e.g. Damour & Esposito-Farèse 1993, 1996). These,

together with the scalar field define a theory from the mono-scalar-tensor family, and are noted in the literature as $T_1(\alpha_0, \beta_0)$, where the subscript 1 denotes that it the theory includes a single scalar field. What was first noted by Damour & Esposito-Farèse (1993), is that even for extremely small values of α_0, α_p can in fact be significant (of order unity), owing to the non-linear interaction between matter and the gravitational field near strongly self-gravitating bodies, an effect which is called "strong-field scalarisation".

Significant work has been done within the scalar-tensor theory framework to predict the expected behaviour of post-Keplerian parameters in binary pulsars (e.g. Damour & Esposito-Farèse 1996). For example, it is expected that the emission of dipolar GWs in the 1.5PN order predicted by such theories causes a contribution (to leading order) to the secular change of the orbital period as:

$$\dot{P}_{\rm b}^{\rm dGW} = -2\pi \frac{m_{\rm p} m_{\rm c}}{M^2} \frac{1 + e^2/2}{(1-e^2)^{5/2}} \frac{\mathcal{V}_b^3}{c^3} \frac{(\alpha_{\rm p} - \alpha_{\rm c})^2}{1 + \alpha_{\rm p}\alpha_{\rm c}} \,. \tag{5.11}$$

Here, $\mathcal{V}_b = (\mathcal{G} M n_b)^{1/3}$. The total mass of the binary system is $M = m_{\rm p} + m_{\rm c}$. The term $\mathcal{G}$ is the *effective gravitational constant*. Such a modified gravitational constant is necessary to describe the dependency of the gravitational interaction between two of self-gravitating bodies due to the strong-field effects. It is given by $\mathcal{G} = G_*(1 + \alpha_{\rm p}\alpha_{\rm c})$ (Damour & Esposito-Farèse 1992a), where G_* is the *bare gravitational constant*[4]. One can see in this equation, that binary systems with short binary periods and members with a large difference in their effective scalar coupling parameters are best suited to search for dipolar GWs. Approximately, the $(\alpha_p - \alpha_c)$ is three orders of magnitude larger in NS-WD systems than DNSs (see e.g. Wex 2014). Equation 5.11 is derived for quasi-circular orbits, which is expected for binaries with fully-recycled MSPs (§2.3.3.1). In some cases, the WD is bright enough to be observed at optical wavelengths, making the binaries dual-line systems. When photometric and high-resolution spectroscopic data are available for the WD, independent measurements of the distance, the mass ratio and the WD mass are possible. These allow the estimation of kinematic contributions to the post-Keplerian parameter and the recovery of their intrinsic values.

Among the different NS-WDs, it is interesting to place limits on dipolar-GW emission and use that to constrain the value of the effective scalar coupling parameters at different pulsar masses. Since α_p depends on the internal structure of the pulsar, stringent limits of this parameter across the full spectrum of pulsar masses can exclude the existence of spontaneous scalarisation effects within various families of gravity theories and for EOSs permitted by the known masses of the pulsars. The best limits on α_p so far come from Freire et al. (2012b) and Antoniadis et al. (2013), for the PSRs J1738+0333 and J0348+0432. For Jordan-Fierz-Brans-Dicke scalar-tensor theories (Jordan 1959; Fierz 1956; Brans & Dicke 1961), $\beta_0 = 0$. WDs are weakly self-gravitating bodies, as such their effective scalar coupling are very close to α_0, which has been already very well constrained with experiments in the Solar systerm (Bertotti et al. 2003) to $|\alpha_0| < 3 \times 10^{-3}$ at the 95% C.L. For these theories, PSRs J1738+0333 and J0348+0432 give limits at the 95% C.L. of $|\alpha_{\rm p} - \alpha_0| < 2 \times 10^{-3}$ and $|\alpha_{\rm p} - \alpha_0| < 5 \times 10^{-3}$.

Complementary to these two results, is the one from the NS-WD binary PSR J1012+5307, which has a mass in-between the two. First measured by Lange et al. (2001) at $|\alpha_{\rm p} - \alpha_0| < 2 \times 10^{-2}$, it was most recently updated by Lazaridis et al. (2009) at $|\alpha_{\rm p} - \alpha_0| < 7.7 \times 10^{-3}$. With this work, we attempt to improve on the limit from PSR J1012+5307 using an updated data set, which offers longer time-span and higher overall timing precision. In what follows, I will show the current results from this effort

[4] G_* is related to the gravitational constant measured in a Cavendish experiment, G, as G=$G_*(1 + \alpha_0^2)$

and discuss the problems that still need to be overcome to reach a conclusive result. Finally, I will explain how the results from this binary pulsar can potentially contribute significantly to excluding the possibility of the existence of strong-field scalarisation for physically motivated pulsar EOSs and how such results affect the GW observations of ground-based detectors.

5.3.2 PSR J1012+5307: An Overview

The binary pulsar PSR J1012+5307, was discovered by Nicastro et al. (1995), using the 76-m Lovell radio telescope at the Jodrell Bank Observatory. It has a 5.3 ms spin period and it is in a NS-WD binary system in a quasi-circular orbit with a period of 14.4 hours. The WD companion is observable at optical wavelengths, first reported by Lorimer et al. (1995), where the mass of the WD companion was first estimated to be $\approx 0.15\,M_\odot$. Further optical observations by van Kerkwijk et al. (1996) and Callanan et al. (1998) have given WD mass measurements of m_c=0.16±0.02 $M_\odot$. Apart from estimating the same mass for the WD, these two publications reached to different values for the WD's radial velocity and surface gravity. As explained in van Kerkwijk et al. (2005) the differences were due to a data reduction error by van Kerkwijk et al. and differences in the used atmosphere models respectively. Once those are taken into account, the two groups have consistent results. Despite the difference in the surface gravity estimation, the errors from the two approaches compensated each other leading by chance to the same estimate of the WD mass. For the calculations in this work, I will be using the values from Callanan et al., being the latest of the two. The mass ratio is estimated at $q = m_p/m_c = 10.5 \pm 0.5$, and hence a pulsar mass at $m_p = 1.64 \pm 0.22 M_\odot$.

Extensive pulsar timing observations and analysis on PSR J1012+5307 have been previously presented in Lange et al. (2001) and Lazaridis et al. (2009). Using data from the Effelsberg and Lovell telescopes, Lange et al. determined an upper limit of 1.3×10^{-6} for the intrinsic value eccentricity (95% C.L.),and served as the test ground to develop the 'ELL1' model for quasi-circular orbits (§2.3.3.1). In that paper, it was demonstrated how the Shapiro delay signal cannot be separated from the orbital Roemer delay and gets absorbed by first Laplace-Lagrange parameter, $\eta = e\,\sin(\omega)$. In order therefore to derive the intrinsic eccentricity value, one needs to apply the necessary corrections to η. By taking into account the distributions of the Laplace-Lagrange parameters, η and κ, the projected semi-major axis and the companion and pulsar mass (via the mass ratio), one can derive a probability distribution for the intrinsic value of the eccentricity. In the same work, it was first discussed how PSR J1012+5307 can also serve as a laboratory for testing gravity theories, placing the most stringent limits on α_p at the time.

Using an extended data set that used a data from four EPTA telescopes, Lazaridis et al. improved the timing solution and also achieved the first measurements of the timing parallax at $\varpi = 1.2 \pm 0.3$ mas, the orbital period derivative at $\dot{P}_b = 5.0 \pm 1.4 \times 10^{-14}$, and the secular change of the projected semi-major axis at $\dot{x} = (2.3 \pm 0.8) \times 10^{-15}$. The derived parallax distance was consistent with the optical distance of the WD. In that paper, not only the limits on dipolar GWs and α_p were improved, but the data were also combined with timing data from PSR J0437−4715 to place an upper limit on the variation of the gravitational constant. The $\dot{x}$ measurement was found to be fully caused by the change in the apparent viewing angle to the pulsar induced by the its proper motion, which was introduced in §2.3.3 and discussed in more detail in §3.3.6 (Eqs. 3.9). Kinematic contributions as well as contributions from the energy loss by GW emission, from mass transfer and geodetic precession where found to be negligible. This allowed to derive limit limitations in the binary's orientation via limits on the longitude of the ascending node, Ω. The upper limits on the eccentricity where further improved to $e < 8.4\times10^{-7}$ at the

95% C.L.

The latest update in the timing of PSR J1012+5307 from the EPTA, is presented in Desvignes et al. (2016), which is discussed in Chapter 3. The timing parallax measurement was at $\varpi = 0.71 \pm 0.17$ mas which was used to derive a LKb-corrected distance of $1.15^{+0.24}_{-0.17}$ kpc. As described in §3.3.4, using the updated measurement of the orbital period change at $\dot{P}_b = 0.94 \pm 0.03$, Desvignes et al. also derived an independent estimate of the distance assuming GR and using the inclination angle and mass measurements from the optical data. The latter, is more consistent the WD optical distance and the previous EPTA parallax distance by comparison to the new parallax distance, although still statistically consistent at the 2-σ level. In what follows, we present a new timing analysis of PSR J1012+5307, using an extension to the data EPTA DR 1.0 data that attempts to investigate these last results in more detail. Finally, in Desvignes et al., the $\dot{x}$ measurement was at $2.0 \pm 4 \times 10^{-15}$. The intrinsic value of the eccentricity was not quoted.

In what follows, we focus an the timing solutions, distance estimates and derivations of limits to the existence of dipolar-GW emission. For the purpose of this work, we did not attempt to further restrict the value of Ω from the $\dot{x}$, since the measurement hasn't improved by comparison to the Lazaridis et al. (2009) results.

5.3.3 Data, Reduction and Timing Analysis

The data set used for this analysis is an extension of the EPTA DR 1.0 (Desvignes et al. 2016) described in §3.3.1. Additional to the EPTA DR 1.0, we have added data from the new generation backend of the NRT, NUPPI (Desvignes et al. 2011). The NUPPI backend is based on a Casper[5] ROACH board, feeding data to 4 nodes, with 2 GPUs each. It became operational in November 2011 and is regularly used for pulsar timing observations at the NRT at central frequencies of $\sim$ 1.4 GHz and $\sim$ 2 GHz with 512 MHz of bandwidth. All observations are polarisation calibrated, using standard polarisation calibration observations. The data reduction was performed using `PSRCHIVE`. Due to the large NUPPI bandwidth, we have employed the channelized discrete Fourier transform method Liu et al. (2014) for the 1.4 GHz receiver data. We did not do so for the 2 GHz because the signal-to-noise ratio of the data in this band is not high enough to allow this type of analysis to improve the results. This type of TOA extraction is necessary when the bandwidth is over a couple of hundreds of MHz, since then effects such as frequency pulse profile evolution (§1.2.1), interstellar medium effects such as diffractive scintillation and DM temporal variations (§1.2.3) can affect the profile across frequency and its temporal stability significantly. The NUPPI data were strategically chosen to be added to the EPTA DR 1.0 data set to increase the precision in the measurement of the parallax distance. Since knowledge of the distance is of high importance for this test, the aim was to have a as precise-as-possible comparison between the optical derived distance, and that derived with pulsar timing.

A joint timing and noise analysis of the full data set was performed using `TempoNest`. From the timing and the noise analysis of the EPTA DR 1.0, we know that the noise properties of PSR J1012+5307 are well defined and that the choice of the noise-parameters pPDs will not significantly alter the timing solution. Nevertheless, the uncertainties of the timing parameters may change, since some pPD choices will lead to larger uncertainties on the residuals (recall the discussion on pPDs in §4.3.2). We have performed two analyses. The first (model M1) uses log-uniform pPDs on EQUADs and stochastic noise amplitudes, as in the timing analysis in Desvignes et al. (2016). The second (model M2), differs in that the EQUADs have a uniform pPD that favours higher residual uncertainties, as explained in §4.3.2. Due

[5] https://casper.berkeley.edu

to the binary's very low eccentricity, we employ the ELL1 binary model, as we did with the EPTA DR 1.0 data.

Table 5.2: Timing solutions for J1012+5307, using the M1 noise model as described in §5.3.3. The 'Mean' and 'ML' in parentheses denote whether the tabulated values are the mean vale as derived from the 1-dimensional marginalised posterior probability distributions of the timing parameters, or the values from the ML model.

Parameter	M1(Mean)	M1(ML)
MJD range	50647 — 57088	50647 — 57088
Number of TOAs	1815	1815
RMS Timing residual (μs)	1.195	1.191
Reference epoch (MJD)	55000	55000
Measured parameters		
Right ascension, α	10:12:33.437527(4)	10:12:33.437523(4)
Declination, δ	53:07:02.30001(5)	+53:07:2.29998(5)
Proper motion in α (mas yr^{-1})	2.616(7)	2.618(7)
Proper motion in δ (mas yr^{-1})	−25.479(9)	−25.478(9)
Period, (ms)	5.255749101970089(15)	5.255749101970091(13)
Period derivative	$1.712726(11)\times10^{-20}$	$1.712719(11)\times10^{-20}$
Parallax, ϖ (mas)	0.78(15)	0.81(15)
DM (cm^{-3}pc)	9.0171(13)	9.0176(13)
DM1 (cm^{-3}pc yr^{-1})	$1.58(20)\times10^{-4}$	$1.53(20)\times10^{-4}$
DM2 (cm^{-3}pc yr^{-2})	$1.6(3)\times10^{-5}$	$1.5(3)\times10^{-5}$
Orbital period, P_b (d)	0.604672722912(9)	0.604672722902(9)
Epoch of periastron, T_0 (MJD)	50700.244(9)	50700.249(9)
Projected semi-major axis, x (lt-s)	0.58181708(11)	0.58181709(11)
Longitude of periastron, ω_0 (deg)	97(5)	100(6)
$\eta = e\sin(\omega_0)$	$1.28(11)\times10^{-6}$	$1.22(11)\times10^{-6}$
$\kappa = e\cos(\omega_0)$	$-1.5(12)\times10^{-7}$	$-2.1(12)\times10^{-7}$
Orbital eccentricity, $e = \sqrt{\eta^2+\kappa^2}$	$1.29(11)\times10^{-6}$	$1.24(11)\times10^{-6}$
Time of asc. node (MJD)	50700.08174602(3)	50700.08174606(3)
Orbital period derivative, $\dot{P}_b$	$5.8(3)\times10^{-14}$	$6.0(3)\times10^{-14}$
First derivative of x, $\dot{x}$ (10^{-12})	$1.6(3)\times10^{-15}$	$1.6(3)\times10^{-15}$
Periastron advance, $\dot{\omega}$ (deg/yr)	—	—
Sine of inclination angle,sin i	—	—
Companion mass, m_c ($M_\odot$)	—	—
Derived parameters		
Gal. Longitude (deg)	160.3	»
Gal. Latitude (deg)	50.9	»
Composite PM (mas yr^{-1})	25.613(9)	25.612(9)
Intrinsic eccentricity (95% C.L.)	$< 6.1\times10^{-7}$	$< 4.6\times10^{-7}$
LKb-corr. parallax distance (kpc)	$1.11^{+0.20}_{-0.15}$	$1.09^{+0.20}_{-0.15}$
$\dot{P}_b$ distance (kpc)	0.750(0.034)	»

Table 5.3: Timing solutions for J1012+5307, using the M2 noise model as described in §5.3.3. The 'Mean' and 'ML' in parentheses denote whether the tabulated values are the mean vale as derived from the 1-dimensional marginalised posterior probability distributions of the timing parameters, or the values from the ML model.

Parameter	M2(Mean)	M2(ML)
MJD range	50647 — 57088	50647 — 57088
Number of TOAs	1815	1815
RMS Timing residual (μs)	1.292	1.262
Reference epoch (MJD)	55000	55000
Measured parameters		
Right ascension, α	10:12:33.437527(5)	10:12:33.437528(5)
Declination, δ	53:07:02.30001(5)	+53:07:2.30003(5)
Proper motion in α (mas yr^{-1})	2.615(8)	2.615(8)
Proper motion in δ (mas yr^{-1})	−25.480(10)	−25.473(10)
Period, (ms)	5.255749101970096(15)	5.255749101970089(15)
Period derivative	$1.712724(13)\times10^{-20}$	$1.712724(13)\times10^{-20}$
Parallax, ϖ (mas)	0.79(17)	0.86(17)
DM (cm^{-3}pc)	9.0164(16)	9.0164(16)
DM1 (cm^{-3}pc yr^{-1})	$1.6(3)\times10^{-4}$	$1.7(3)\times10^{-4}$
DM2 (cm^{-3}pc yr^{-2})	$1.6(3)\times10^{-5}$	$1.8(3)\times10^{-5}$
Orbital period, P_b (d)	0.604672722913(11)	0.604672722927(11)
Epoch of periastron, T_0 (MJD)	50700.245(10)	50700.245(10)
Projected semi-major axis, x (lt-s)	0.58181709(12)	0.58181699(12)
Longitude of periastron, ω_0 (deg)	97(6)	97(6)
$\eta = e\sin(\omega_0)$	$1.30(13)\times10^{-6}$	$1.25(13)\times10^{-6}$
$\kappa = e\cos(\omega_0)$	$-1.6(13)\times10^{-7}$	$-1.5(13)\times10^{-7}$
Orbital eccentricity, $e = \sqrt{\eta^2+\kappa^2}$	$1.31(13)\times10^{-6}$	$1.25(13)\times10^{-6}$
Time of asc. node (MJD)	50700.08174602(3)	50700.08174598(3)
Orbital period derivative, $\dot{P}_b$	$5.7(3)\times10^{-14}$	$5.4(3)\times10^{-14}$
First derivative of x, $\dot{x}$ (10^{-12})	$1.6(3)\times10^{-15}$	$1.8(3)\times10^{-15}$
Periastron advance, $\dot{\omega}$ (deg/yr)	—	—
Sine of inclination angle,sin i	—	—
Companion mass, m_c ($M_\odot$)	—	—
Derived parameters		
Gal. Longitude (deg)	160.3	»
Gal. Latitude (deg)	50.9	»
Composite PM (mas yr^{-1})	25.614(10)	25.607(10)
Intrinsic eccentricity (95% C.L.)	$< 4.5\times10^{-7}$	$< 4.4\times10^{-7}$
LKb-corr. parallax distance (kpc)	$1.08^{+0.22}_{-0.16}$	$1.01^{+0.19}_{-0.14}$
$\dot{P}_b$ distance (kpc)	0.750(0.034)	»

We have examined the noise properties from this analyses and we have confirmed that they are consistent with the ones from the EPTA DR 1.0. Any deviation would suggest that the newly added NUPPI data may be suffering from analysis systematics that would need to be investigated. We discuss

the results from the analysis below, after a discussion on our estimates of the kinematic contributions to timing parameters of interest. The timing solutions The timing solution are presented in Tables 5.2 and 5.3, where we tabulate both the mean values with 68% C.L. uncertainties as derived from the 1-dimensional marginalised PPDs for each parameter as well as the ML model values. For the latter, we assume the same uncertainties as the mean values. The tables also include the derived Galactic co-ordinates, composite proper motion, the upper limits to the intrinsic value of the eccentricity, the LKb-corrected parallax distances as well as the $\dot{P}_{\rm b}$ distances.

5.3.3.1 Kinematic Contributions to Timing Parameters

In §3.3.4, I introduced the kinematic contributions to $\dot{P}$ and $\dot{P}_{\rm b}$ that needs to be taken into account in order to derive the intrinsic values of the parameters (Damour & Taylor 1991). Here, I discuss these in more detail and give the details of how they are calculated. The same methods and codes as in Desvignes et al. (2016) were used.

The sum of kinematic terms constitute a Doppler shift to a measured parameter from the radial motion of the pulsar. We therefore used $\dot{P}_{\rm b}$ to write the equation describing the kinematic terms. For other parameters such as $\dot{P}$ and $\dot{x}$, the relations are equivalent.

The first kinematic contribution is that caused by the Shklovskii effect §2.3.2 and is given by:

$$\frac{\dot{P}_{\rm b}^{\rm Shk}}{P_{\rm b}} = \frac{\mu^2 d}{c}, \tag{5.12}$$

where as usual, c is the speed of light, μ is the composite proper motion and d is the distance to the pulsar. Two kinematic contributions result from the accelerated motion of the pulsar in the Galaxy, one due to the Galactic differential rotation and one due to the acceleration towards the Galactic centre (Damour & Taylor 1991; Nice et al. 2005). For the first term, we use the relation from Nice & Taylor (1995):

$$\frac{\dot{P}_{\rm b}^{\rm dgr}}{P_{\rm b}} = -\cos(b)\left(\frac{\Theta_0^2}{R_0}\right)\left(\cos(l) + \frac{\beta}{\sin^2(l)+\beta^2}\right). \tag{5.13}$$

The values for the Sun's distance to the Galactic centre, R_0, and the Galactic-rotation velocity at the position of the Sun, Θ_0, are taken from (Reid et al. 2014). As usual, l and b are the Galactic co-ordinates of the pulsar and $\beta \equiv (d/R_0)\cos(b) - \cos(l)$ (Damour & Taylor 1991). For the acceleration towards the Galactic disk, we have used the vertical component, K_z of the Galactic acceleration model by Holmberg & Flynn (2004), and is calculated as:

$$\frac{\dot{P}_{\rm b}^{\rm kz}}{P_{\rm b}} = -\frac{K_z|\sin(b)|}{c}. \tag{5.14}$$

We denote the sum of the kinematic contributions as $\dot{P}_{\rm b}^{\rm D}$, using the D superscript to denote a Doppler shift. We have calculated the kinematic corrections for five different estimates of the distance, namely the optical distance of the WD by Callanan et al. and the parallax distances from the mean and ML

Table 5.4: Kinematic and relativistic contributions to the measured values of the orbital period derivative, $\dot{P}_b$. Figures in parentheses represent the 68.3% confidence uncertainties in the last digit quoted. Results are derived using the for different models presented in Tables 5.2 and 5.3, and using the corresponding LKb-corrected parallax distances and the optical distance to the WD companion by Callanan et al. (1998).

	M1(Mean)	M1(ML) using d_{px}	M2(Mean)	M2(ML)
Shklovskii	$+9.3(1.7)\times10^{-14}$	$+9.1(1.6)\times10^{-14}$	$+9.0(1.8)\times10^{-14}$	$+8.4(1.6)\times10^{-14}$
Acc. to Gal. disc	$-7.5(6)\times10^{-15}$	$-7.5(5)\times10^{-15}$	$-7.5(6)\times10^{-15}$	$-7.3(6)\times10^{-15}$
Diff. Gal. Rot.	$+1.52(29)\times10^{-15}$	$+1.48(28)\times10^{-15}$	$+1.48(30)\times10^{-15}$	$+1.39(27)\times10^{-15}$
	M1(Mean)	M1(ML) using d_{opt}	M2(Mean)	M2(ML)
Shklovskii	$+7.0(7)\times10^{-14}$	$+7.0(7)\times10^{-14}$	$+7.0(7)\times10^{-14}$	+7.0(7)e-14
Acc. to Gal. disc	$-6.69(32)\times10^{-15}$	$-6.69(32)\times10^{-15}$	$-6.69(32)\times10^{-15}$	-6.69(32)e-15
Diff. Gal. Rot.	$+1.16(15)\times10^{-15}$	$+1.16(15)\times10^{-15}$	$-1.16(15)\times10^{-15}$	+1.16(15)e-15

values of the timing parallax from the timing analyses described in the previous paragraph, and presented in Tables 5.2 and 5.3. The values of the individual kinematic corrections and their sum or all distance estimates are shown in Table 5.4.

5.3.4 Limits on Dipolar-Gravitational-Wave Emission

Having at hand the corrections for the kinematic contributions, noted as $\dot{P}_b^D$ below, we finally use $\dot{P}_b$ to get upper limits on the existence of dipolar gravitational radiation emission from PSR J1012+5307. Apart from kinematic and GW-emission terms, the secular change of the orbital period has, in principle some additional contributions:

$$\dot{P}_b^{int} = \dot{P}_b^{obs} - \dot{P}_b^D - \dot{P}_b^T + \dot{P}_b^{\dot{m}} + \dot{P}_b^{rel} \tag{5.15}$$

Lazaridis et al. have already shown that terms due to mass loss from the binary system, $\dot{P}_b^{\dot{m}}$, and from tidal forces, $\dot{P}_b^T$, are negligible. The last term, which accounts for all relativistic effects can be expanded as $\dot{P}_b^{rel} = \dot{P}_b^{mGW} + \dot{P}_b^{dGW} + \dot{P}_b^{qGW} + \dot{P}_b^{\dot{G}}$. The first three terms are from monopole, dipole and quadrupole GW emission respectively, and the last is from variations in the gravitational constant. Monopolar and quadrupolar (additional to the quadrupolar GWs from the tensor field) GWs also enter at the 2.5PN level in tensor-scalar theories due to the scalar field (Damour & Esposito-Farèse 1992b). However, monopolar GWs are negligible for near-circular orbits (Damour & Esposito-Farèse 1992b) and scalar-field contributions to the quadrupolar GW from PSR J1012+5307 are shown to be negligible (Lazaridis et al. 2009). Therefore, the change in $\dot{P}_b$ from quadrupole GW emission can be estimated according to GR, which for small eccentricities is calculated as (Peters 1964):

$$\dot{P}_b^{qGW} = -\frac{192\pi n_b^{3/5}}{5}\frac{(T_\odot m_c)^{3/5} q}{(q+1)^{1/3}}\,, \tag{5.16}$$

where $T_\odot \equiv M_\odot G c^{-3} = 4.925490947 \mu s$ (as in Eq. 3.6) and $n_b \equiv 2\pi/P_b$, as already introduced in §2.3.3.1. From experiments in the Solar system, very tight limits are imposed on $\dot{G}$, which is found to be consistent with zero at the $10^{-12}\,\mathrm{yr}^{-1}$ precision level (e.g. Hofmann et al. 2010). The $\dot{P}_b^{\dot{G}}$ term is therefore negligible. We now connect the observational results with the theoretical predictions for dipolar-GW contribution to the orbital decay. Following Freire et al. (2012b), we rewrite Eq. 5.11 as:

$$\dot{P}_b^{\mathrm{dGW}} = -2\pi n_b \frac{G_* m_c}{c^3} \frac{q}{q+1} (\alpha_p - \alpha_c)^2 \,, \tag{5.17}$$

We can define the 'excess' orbital period derivative $\dot{P}_b^{\mathrm{exc}} = \dot{P}_b^{\mathrm{obs}} - \dot{P}_b^{\mathrm{D}} - \dot{P}_b^{\mathrm{qGW}}$. Denoting in compact notation the proportionality constant as $C = -2\pi n_b (G_* m_c / c^3) q/(q+1)$, we derive the relation:

$$\frac{\dot{P}_b^{\mathrm{exc}}}{C} = \frac{\dot{P}_b^{\mathrm{dGW}}}{C} = (\alpha_p - \alpha_c)^2 \simeq (\alpha_p - \alpha_0)^2 \,, \tag{5.18}$$

where the last approximation is due to the weak gravitational field of the WD, as explained above. We derived limits on $|\alpha_p - \alpha_0|$ at the 95% C.L. using the four different sets of timing-parameter values to derive the limits this radiation-demping test. The precision of distance from timing-parallax measurements are still considerably lower than that from optical observations and the limits using the optical distance are about five times better. The lowest limit was derived for the M1(Mean) model and is $|\alpha_p - \alpha_0| < 4.6 \times 10^{-3}$, which is a slight improvement of a factor 0.6 over the Lazaridis et al. result and it is slightly better than the limit from PSR J0348+0432 presented in Antoniadis et al. (2013).

5.3.5 Discussion and Future Work

It is clear from the discussion in this section that the accurate measurement of the distance and the pulsar mass are essential for the robustness of the dipolar gravitational radiation test. Since the optical distance measurement of the WD companion depends on the models for its atmosphere, having an independent distance from timing parallax measurements can help increase our confidence to the used distance value. It is therefore of interest to examine the various distance measurements for PSR J1012+5307.

The first timing-parallax measurement of PSR J1012+5307 was reported by Lazaridis et al. (2009) using EPTA data, and was 1.2 ± 0.3 mas which corresponds to a distance of 0.82 ± 0.18 kpc and was consistent with the optical distance of 0.840 ± 0.090 kpc that was reported by Callanan et al. (1998). That parallax distance was derived without applying the LKb correction. In Desvignes et al. (2016), the parallax was measured at 0.71 ± 0.17 mas (which give a LKb-corrected distance of $1.15^{+0.24}_{-0.17}$ kpc), which deviates more from the optical distance. In this work, after adding the NUPPI data to the EPTA DR 1.0 data set, we have performed the timing analysis using two different sets of noise parameter pPDs. The case where the analysis is identical to that of Desvignes et al. resulted in parallax distance of $1.11^{+0.20}_{-0.15}$ kpc. The closest to the optical distance from this analysis is $1.01^{+0.19}_{-0.14}$ kpc. In general, maximum likelihood solutions give results that are more consistent with the optical distance than the values from the mean of the 1-dimensional marginalised PPDs.

It is obvious that the parallax distance is difficult to improve such that it can compete with the optical distance measurements in terms of precision. Nevertheless, since the distance estimation from optical observations of the companion depends on the used atmosphere models and consistent independent

distance measurements from radio data increase the confidence in the optical results. The central value of the parallax distance appears to have moved away from the optical value by comparison to Lazaridis et al.. However, the timing solutions reported here and in Desvignes et al. benefit from the use of the JPL planetary ephemeris DE421, which is improved by comparison to the DE405, by more detailed mitigation of the DM variations and by modelling the timing noise. The reported parallax distances are also LKb-corrected, which is not the case in Lazaridis et al.. We note, however, that applying the LKb correction to the Lazaridis et al. results leads to a distance of $0.70^{+17}_{-0.12}$ kpc. An interesting finding, is that the NUPPI data alone, which probe parallax better than any other of the data sub-sets due to their high precision and cadence, support a parallax of 0.98 mas. Therefore, an investigation is ongoing as to whether additional time-span and higher complexity of the multi-telescope combined data set, may introduce some bias to the parallax measurement.

Interestingly, the $\dot{P}_b$ distance, which is much more precise than the parallax distance, is 0.750 ± 0.034 kpc, in stronger agreement with the optical distance measurement. The $\dot{P}_b$ distance obviously depends on the assumption of the validity of GR and the optical mass measurement. The first condition appears to be safe to use, given the negative results on the existence of dipolar GWs. The mass value may need to be updated, however, the kinematic contributions to $\dot{P}_b$ are dominant in the case of PSR J1012+5307 and changes in the mass value of up to 2σ does not affect the derived $\dot{P}_b$ distance. It is therefore logical to deduce that the $\dot{P}_b$ distance is a better estimate of the distance than the parallax distance. This motivates further investigation of the effects of noise modelling and multi-telescope data combination to the parallax measurements, since as discussed in §3.3.3, these measurements are also crucial to the development of Galactic electron-density models.

The result from the dipolar-GW test have improved the limit on the effective scalar coupling of the pulsar by a factor 0.6 from the previous limit with PSR J1012+5307. The improvement may seem small, and the data show that we will not have large improvement with this pulsar over the next years. However, we stress that the reasoning behind trying to get the best possible limit with PSR J1012+5307 has to do with the significant improvement it can provide on tests of scalar-tensor theories when combining this limit with those from other pulsars. It has been repeatedly emphasised in this chapter that due to the compactness-dependent effects found in many alternative theories of gravity, it is important to limit the space of parameters for various pulsar masses. PSR J1738+0333 provides the tightest limit on α_p at the moment, but the limits from the 2-solar-mass pulsar PSR J0348+0432 and PSR J1012+5307 are of the same order. PSR J0348+0432 permitted to test and rule out a family of scalar-tensor theories that predict significant deviations from GR at very high neutron-star masses, where the gravitational field is highly non-linear. These, could not be tested with the 1.4-solar-mass pulsar, PSRs J1738+0333. The gap between 1.4 and 2.1 solar masses, allows for scalarisation effects to be predicted by scalar-tensor theories (Shibata et al. 2014). PSR J1012+5307 can in fact close that gap depending on what the exact mass is and the precision of its measurement.

A recent re-analysis of the optical data using more recent, improved WD atmosphere models, have suggested that the mass of PSR J1012+5307 needs to be updated (J. Antoniadis, private communication). For this reason, new optical observations of the WD companion have been scheduled to take place with the "Gemini North" telescope (J. Antoniadis, private communication). The aim is a more precise and robust measurement of the WD mass with the analysis of newer, high-quality optical data using the improved WD-atmospheres models. We forsee that the analysis of the new optical data will provide a clear derivation of the pulsar mass. PSR J1012+5307 will then unambiguously provide dipolar radiation limits on a mass range that has not yet been probed. By additionally using more pulsars for which we now have good estimates of the distance (Chapter 3) we should be able to exclude the existence of

strong-field scalarisation effects for a very wide range of physically motivated EOSs.

Such a result would be of particular interest to ground-based GW detectors. One of the primary targets of the advanced LIGO and Virgo detectors are GWs from DNS mergers. The GW signals are expected at noise levels and therefore template-matching filtering methods are needed to detect the GWs (Sathyaprakash & Schutz 2009). If pulsar timing experiments manage to rule out the existence of strong-field scalarisation in NSs, then GW-waveform templates based on GR PN-approximations can be used for the final inspiral stages with more confidence. However, the implications can even go further. It has been shown (Barausse et al. 2013) that even in the absence of spontaneous scalarisation, *dynamical scalarisation* can occur in the highly-dynamical strong-field regime, when the NSs come close before the merger. The ruling-out of families of scalar-tensor theories by pulsar timing experiments however, can potentially also significantly limit the chances for such effects to exists. If the experimental limitations request significant and non-physically motivated fine-tuning of the theory parameters to allow scalarisation, then it would be a strong indication that such effects do not exist as predicted by scalar-tensor theories. These results could be further supported by the GWs from merging NSs that ground-based detectors are anticipated to observe.

CHAPTER 6

Summary and Discussion

The research conducted for the purposes of this thesis is focused on applications of high-precision radio pulsar timing. In particular, pulsar timing, which is explained in Chapter 2, is employed as a tool to primarily study aspects of gravity. Most of the work described in the thesis has been conducted as part of a co-ordinated effort within the EPTA. While the collaboration focuses on detection of low-frequency GWs, the data collected are also used, among others, for astrometric and astrophysical studies and tests of gravity theories based on individual-pulsar data.

Chapter 3 describes the instrumentation used for pulsar timing at the Effelsberg observatory over the course of almost two decades. The chapter presents the reduction and analysis methods used for the data recorded with the EBPP. These data were combined with data from the other EPTA telescopes to form the first EPTA data release, which contains data from 42 MSPs. In Chapter 3, we give an overview of the astrometric and astrophysical studies we have performed using this data set and which appear in Desvignes et al. (2016). This work was the first one to use a fully Bayesian approach to perform timing analysis for an extended timing data set. The analysis was performed while simultaneously modelling stochastic noise in the data, resulting in probability distributions for all timing parameters and robust parameter and uncertainty estimations. This work has led to a wealth of newly measured parameters such as pulsar proper motions, timing parallaxes, apparent changes of orbital semi-major axes and pulsar masses.

The timing-analysis results, combined with those for other MSPs from the literature, were used to statistically study the pulsar-distance estimations and the kinematics of binary and solitary MSPs. We have made a comparison of the pulsar distances derived using timing parallax and kinematic information, and have compared these to the distance predictions using Galactic electron-density models, which predict the pulsar distance based on the measurement of the dispersion measure, i.e. the number density of free electrons along the line-of-sight. With this quantitative analysis, we show that the mean uncertainties used in the literature for distances derived using the NE2001 model, the most widely used model, are too small by a factor of about 3. The quantitative study of 2-dimensional velocities of MSPs via proper-motion measurements, has led to an updated and larger sample of MSP velocities, by which we have confirmed previous studies that have suggested that solitary and binary pulsars have the same velocity distribution.

The timing-analysis of the EPTA data set has also confirmed, and in some cases significantly improved, pulsar-mass measurements and has provided one new mass measurement. We have also attempted to constrain the orbital geometry of three pulsar for which we have combined information from

measurements of changes in the semi-major axis and Shapiro delay, through a search for annual-orbital parallax signatures. The data, however, were not yet sufficient to have conclusive results, resulting only in multi-modal solutions for the orbit's longitude of the ascending node, Ω, which can restrict the orbit's orientation if measured.

The EPTA data set, was primarily created to be used for searches of nHz GWs. An essential part of this effort is the detailed characterisation of the noise on a pulsar-by-pulsar basis. In Chapter 4, the noise analysis of the 42 MSPs is presented. In this work, which appears in Caballero et al. (2016), we have performed the a comprehensive noise analysis which focused on low-frequency noise but included white-noise analysis and search for instrumental and analysis-systematics noise. For the achromatic low-frequency noise, which is also referred to as "timing noise" in pulsar-timing literature, we made the first comparison of results from two analyses based on different statistical approaches. The results from the time-frequency Bayesian analysis and a power-spectral analysis produced statistically consistent results. However, both methods have certain limitations in the intermediate to low signal-to-ratio regime, and we have demonstrated that safer conclusions can be reached when performing noise analysis with multiple methods and independent codes.

The derived low-frequency noise properties were then used to quantify the limitations they impose on the EPTA data set on their sensitivity to GWs. We investigated the sensitivity loss for both a stochastic GWB and continuous CGWs from single, resolved supermassive black-hole binaries. By employing the Crámer-Rao lower bound, we have calculated that the timing noise present in the pulsar data reduce the sensitivity to a gravitational-wave background by a factor of ten and by a factor of up to 5.6 for continuous gravitational waves in the frequency range of 5-7 nHz.

In Chapter 5 two pulsar timing experiments are presented which focus on testing theories of gravity. The first, which is appears in Shao et al. (2013), takes advantage of the high-quality EBPP data from two solitary pulsars, namely PSRs B1937+21 and J1744−1134. The key element of these data is that data recording setup was only slightly changed over the course of over 15 years, which allowed a direct measurement of the pulse-profile stability. This feature was not available for any other data from coherent de-dispersion backends for such a long period of time. In the absence of relativistic effects that can cause a precession in the spin axis of pulsars in binary systems, solitary pulsars are expected to have stable profiles. Our analysis showed no evidence of temporal changes in the profile shapes of the two MSPs. Under the assumption of a non-detection we have derived a new limit for $\hat{\alpha}_2$, one of the three post-Newtonian parameter which describe violations of Local Lorentz Invariance in the gravitational sector in the strong-field regime of gravity. This type of violations result from preferred-frame effects and are predicted by many alternative theories of gravity. The limit we have derived is the best to-date and supports the validity of General Relativity.

The second test is based on the detailed analysis of orbital parameters of the binary pulsar PSR J1012+5307. In this work, which is part of an ongoing EPTA project, we used a timing data set formed using the EPTA data set described in Chapter 3 and additional data recorded with NUPPI, a new generation timing backend at the Nançay Radio Telescope. The addition of these highly precise data points was made to increase the precision of the parallax-distance measurement, since knowledge of the distance is required in order to recover the intrinsic values of the timing parameters of interest. Based on the measurement of the secular change of the orbital period of this neutron star-white dwarf binary, we conducted a radiation-damping test. The observed orbital decay of PSR J1012+5307 is compatible with General Relativity, which only predicts emission of quadrupole GW radiation. We have placed an upper limit on the existence of dipolar GWs as predicted by physically motivated alternative theories of gravity, specifically the Jordan-Fierz-Brans-Dicke scalar-tensor theories.

The goal of this work is to improve the limits as much as possible in this pulsar's mass regime. Since dipolar radiation depends on the compactness of the self-gravitating object, it is important to derive these limits for binaries with pulsars at different masses. This work is based on combined information from radio pulsar timing observations and photometric and spectroscopic observations of the white-dwarf companion at optical wavelengths. In Chapter 5, we have used the results from previous published optical-data analysis to confirm their distance measurements. The pulsar mass information also relies heavily on the optical data. It is important to measure the mass with the best possible precision and so this work will be finalised after new, higher-quality optical data will be recorded in the near future, which will be analysed with recent and more reliable state-of-the art white-dwarf atmosphere models.

6.1 Further Work

Apart from the NUPPI data used in Chapter 5, all work that is presented in this thesis was based on data recorded with the previous generation of pulsar timing data processors, or backends. Despite their limited time and frequency resolution, bandwidth and overall data quality compared to the data from the newer backends, these historical data have provided an excellent data set to put our analysis methods, algorithms and computing facilities, to test and have produced exciting scientific results, largely aided by the data set's long time-span.

All radio astronomical observatories with pulsar-timing campaigns have been using new-generation backends already for some years. Due to the larger bandwidth and larger data volumes, analysis of these new data is more complicated and requires significantly increased amounts of computing resources. Significant amount of effort goes into optimising our timing-analysis algorithms and in finding ways to more optimally make use of supercomputing facilities. Such work has begun with the timing analysis of the first combined data set from the IPTA, presented in Verbiest et al. (2016). Although that data set comprised only from historical backend data, the analysis of such a large volume of data which were analysed with different methods was a prelude to the difficulties we are going to face in the future. For the detailed analysis of the IPTA data set's noise properties, the `Polychord` algorithm (Handley et al. 2015) was employed, which extends on the capabilities of `MultiNest` and allows efficient Bayesian analysis for problems with very high dimensionalities.

PTA applications are long-term projects and as such require good planning. The demonstrated impact of noise on the efforts to detect GWs and their systematic observation in the future, make the results from our noise analyses are cornerstone of PTAs. Recent upper limits placed on the strain amplitudes of GWs (e.g. Babak et al. 2016; Arzoumanian et al. 2015) and theoretical predictions for the expected signals from astrophysical sources (e.g. Sesana 2013), suggest that GW signals are expected in the intermediate to low signal-to-noise (S/N) regime for the current and near-future PTA instrumentation. With limited observing resources and available telescope time, PTAs need to optimise their observing scheduling, for example in terms of integration times on a pulsar-by-pulsar basis and frequency coverage. The noise properties of the pulsars are central in such planning (e.g. Lee et al. 2012; Christy et al. 2014). As demonstrated by the results in Chapter 4, performing the noise analysis of a given data set with multiple methods is essential for increasing one's confidence on the results. The power-spectral analysis algorithms described in §4.3.3 are planned to be expanded to include white-noise analysis and non-stationary noise to provide fully independent results. A central aspect of this work and all similar projects, is to also computationally improve the algorithm in order to analyse future, complex data in reasonable time-scales.

Finally, the results from the tests on the existence of dipolar GWs using PSR J1012+5307, will be used to place stringent limits on scalar-tensor theories of gravity. It is important to extend this test to more pulsars for which we now have sufficient data, in an attempt to exclude the existence of scalarisation effects, which predict modifications in the gravitational interaction between compact objects by comparison to the predictions of General Relativity. Such a result will have a strong impact on the development and use of GW templates by ground-based detectors, which aim to also study mergers of DNSs. Within our research group, we aim to experimentally confront the predictions of scalar-tensor theories for a wide range of pulsars masses and EOSs. Such tests can be complimentary to the anticipated observations of GWs from DNS by ground-based detectors. Gravity theories and the EOS of the NS interiors can be better constrained with combination of complementary results from pulsar timing and the ground-based GW observations. This research can serve as a basis to connect these two fields in the newly-emerged era of GW astronomy.

Bibliography

Alpar, M. A., Cheng, A. F., Ruderman, M. A., & Shaham, J. 1982, Nature, 300, 728

Anderson, P. W. & Itoh, N. 1975, Nature, 256, 25

Antoniadis, J., Freire, P. C. C., Wex, N., et al. 2013, Science, 340, 448

Archibald, A. M., Stairs, I. H., Ransom, S. M., et al. 2009, Science, 324, 1411

Armstrong, J. W., Rickett, B. J., & Spangler, S. R. 1995, ApJ, 443, 209

Arzoumanian, Z., Brazier, A., Burke-Spolaor, S., et al. 2015, ArXiv e-prints:1508.03024v1

Arzoumanian, Z., Joshi, K., Rasio, F. A., & Thorsett, S. E. 1996, in Astronomical Society of the Pacific Conference Series, Vol. 105, IAU Colloq. 160: Pulsars: Problems and Progress, ed. S. Johnston, M. A. Walker, & M. Bailes, 525–530

Baade, W. & Zwicky, F. 1934, Physical Review, 46, 76

Babak, S., Petiteau, A., Sesana, A., et al. 2016, MNRAS, 455, 1665

Babak, S. & Sesana, A. 2012, Phys. Rev. D, 85, 044034

Backer, D. C. 1976, ApJ, 209, 895

Backer, D. C., Dexter, M. R., Zepka, A., et al. 1997, PASP, 109, 61

Backer, D. C. & Hellings, R. W. 1986, ARA&A, 24, 537

Backer, D. C., Kulkarni, S. R., Heiles, C., Davis, M. M., & Goss, W. M. 1982, Nature, 300, 615

Bailes, M. 1988, A&A, 202, 109

Bailes, M., Johnston, S., Bell, J. F., et al. 1997, ApJ, 481, 386

Bailey, Q. G. & Kostelecký, V. A. 2006, Phys. Rev. D, 74, 045001

Baker, J. G., Centrella, J., Choi, D.-I., Koppitz, M., & van Meter, J. 2006, Physical Review Letters, 96, 111102

Bangs, G. W. 1971, PhD thesis, Yale University

Barausse, E., Palenzuela, C., Ponce, M., & Lehner, L. 2013, Phys. Rev. D, 87, 081506

Barker, B. M. & O'Connell, R. F. 1975, Phys. Rev. D, 12, 329

Bekenstein, J. D. 2004, Phys. Rev. D, 70, 083509

Bell, J. F. & Bailes, M. 1996, ApJ, 456, L33

Bertotti, B., Iess, L., & Tortora, P. 2003, Nature, 425, 374

Bhat, N. D. R., Cordes, J. M., Camilo, F., Nice, D. J., & Lorimer, D. R. 2004, ApJ, 605, 759

Bhat, N. D. R., Tingay, S. J., & Knight, H. S. 2008, ApJ, 676, 1200

Bhattacharya, D. & van den Heuvel, E. P. J. 1991, Physics Reports, 203, 1

Bilous, A., Kondratiev, V., Kramer, M., et al. 2015, ArXiv e-prints

Blanchet, L. 2006, Living Reviews in Relativity, 9, 4

—. 2014, Living Reviews in Relativity, 17

Blandford, R. D. & Romani, R. W. 1988, MNRAS, 234, 57P

Brans, C. & Dicke, R. H. 1961, Phys. Rev., 124, 925

Britton, M. C. 2000, ApJ, 532, 1240

Burgay, M., D'Amico, N., Possenti, A., et al. 2003, Nature, 426, 531

Caballero, R. N., Lee, K. J., Lentati, L., et al. 2016, MNRAS, 457, 4421

Callanan, P. J., Garnavich, P. M., & Koester, D. 1998, MNRAS, 298, 207

Chadwick, J. 1932, Nature, 129, 312

Chamberlin, S. J. & Siemens, X. 2012, Phys. Rev. D, 85, 082001

Champion, D. J., Hobbs, G. B., Manchester, R. N., et al. 2010, ApJ, 720, L201

Christy, B., Anella, R., Lommen, A., et al. 2014, ApJ, 794, 163

Cognard, I., Bourgois, G., Lestrade, J.-F., et al. 1995, A&A, 296, 169

Coles, W., Hobbs, G., Champion, D. J., Manchester, R. N., & Verbiest, J. P. W. 2011, MNRAS, 418, 561

Cordes, J. M. 1978, ApJ, 222, 1006

Cordes, J. M. & Chernoff, D. F. 1997, ApJ, 482, 971

Cordes, J. M. & Downs, G. S. 1985, ApJS, 59, 343

Cordes, J. M. & Lazio, T. J. W. 2002, ArXiv Astrophysics e-prints

—. 2003, ArXiv Astrophysics e-prints

Cordes, J. M., Wasserman, I., & Blaskiewicz, M. 1990, ApJ, 349, 546

Cordes, J. M., Weisberg, J. M., & Boriakoff, V. 1985, ApJ, 288, 221

D'Alessandro, F., McCulloch, P. M., Hamilton, P. A., & Deshpande, A. A. 1995, MNRAS, 277, 1033

Damour, T. 2009, in Astrophysics and Space Science Library, Vol. 359, Physics of Relativistic Objects in Compact Binaries: From Birth to Coalescence, ed. M. Colpi, P. Casella, V. Gorini, U. Moschella, & A. Possenti, p. 1–42. Available as eprint: 0704.0749v1

Damour, T. & Deruelle, N. 1985, Ann. Inst. Henri Poincaré Phys. Théor., Vol. 43, No. 1, p. 107 - 132, 43, 107

—. 1986, Ann. Inst. Henri Poincaré Phys. Théor., Vol. 44, No. 3, p. 263 - 292, 44, 263

Damour, T. & Esposito-Farèse, G. 1992a, Classical and Quantum Gravity, 9, 2093

—. 1992b, Phys. Rev. D, 46, 4128

—. 1993, Physical Review Letters, 70, 2220

—. 1996, Phys. Rev. D, 54, 1474

Damour, T. & Taylor, J. H. 1991, ApJ, 366, 501

—. 1992, Phys. Rev. D, 45, 1840

Damour, T. & Vilenkin, A. 2005, Phys. Rev. D, 71, 063510

Davis, J., Lawson, P. R., Booth, A. J., Tango, W. J., & Thorvaldson, E. D. 1995, MNRAS, 273, L53

Demorest, P. B. 2007, PhD thesis, University of California, Berkeley

Demorest, P. B., Ferdman, R. D., Gonzalez, M. E., et al. 2013, ApJ, 762, 94

Demorest, P. B., Pennucci, T., Ransom, S. M., Roberts, M. S. E., & Hessels, J. W. T. 2010, Nature, 467, 1081

Desvignes, G., Barott, W. C., Cognard, I., Lespagnol, P., & Theureau, G. 2011, in American Institute of Physics Conference Series, Vol. 1357, American Institute of Physics Conference Series, ed. M. Burgay, N. D'Amico, P. Esposito, A. Pellizzoni, & A. Possenti, 349–350

Desvignes, G., Caballero, R. N., Lentati, L., et al. 2016, MNRAS, 458, 3341

Eatough, R. P., Falcke, H., Karuppusamy, R., et al. 2013, Nature, 501, 391

Eddington, A. S. 1922, The mathematical theory of relativity, 1st edn. (Cambridge University Press)

Edwards, R. T., Hobbs, G. B., & Manchester, R. N. 2006, MNRAS, 372, 1549

Einstein, A. 1918, Sitzungsberichte der Königlich Preußischen Akademie der Wissenschaften (Berlin), Seite 154-167.

Espinoza, C. M., Lyne, A. G., Stappers, B. W., & Kramer, M. 2011, MNRAS, 414, 1679

Estabrook, F. B. & Wahlquist, H. D. 1975, General Relativity and Gravitation, 6, 439

Favata, M. 2009, Phys. Rev. D, 80, 024002

Ferdman, R. D., Stairs, I. H., Kramer, M., et al. 2010, ApJ, 711, 764

Feroz, F. & Hobson, M. P. 2008, MNRAS, 384, 449

Fienga, A., Laskar, J., Verma, A., Manche, H., & Gastineau, M. 2012, in SF2A-2012: Proceedings of the Annual meeting of the French Society of Astronomy and Astrophysics, ed. S. Boissier, P. de Laverny, N. Nardetto, R. Samadi, D. Valls-Gabaud, & H. Wozniak, 25–33

Fierz, M. 1956, Helv. Phys. Acta, 22, 489

Finn, L. S., Larson, S. L., & Romano, J. D. 2009, Phys. Rev. D, 79, 062003

Fisz, M. 1963, Probability Theory and Mathematical Statistics, ed. Geisser, S. (John Wiley and Sons)

Folkner, W. M., Williams, J. G., & Boggs, D. H. 2009, Interplanetary Network Progress Report, 178, 1

Folkner, W. M., Williams, J. G., Boggs, D. H., Park, R. S., & Kuchynka, P. 2014, Interplanetary Network Progress Report, 196, 1

Foster, R. S. & Backer, D. C. 1990, ApJ, 361, 300

Freire, P. C. C., Kramer, M., & Wex, N. 2012a, Classical and Quantum Gravity, 29, 184007

Freire, P. C. C. & Wex, N. 2010, MNRAS, 409, 199

Freire, P. C. C., Wex, N., Esposito-Farèse, G., et al. 2012b, MNRAS, 423, 3328

Gardner, F. F. & Davies, R. D. 1966, Australian Journal of Physics, 19, 129

Gil, J., Gronkowski, P., & Rudnicki, W. 1984, A&A, 132, 312

Gonzalez, M. E., Stairs, I. H., Ferdman, R. D., et al. 2011, ApJ, 743, 102

Grishchuk, L. P. 2005, Physics Uspekhi, 48, 1235

Guillemot, L., Johnson, T. J., Venter, C., et al. 2012, ApJ, 744, 33

Gunn, J. E. & Ostriker, J. P. 1970, ApJ, 160, 979

Handley, W. J., Hobson, M. P., & Lasenby, A. N. 2015, MNRAS, 453, 4384

Hankins, T. H. & Rickett, B. J. 1975, in Methods in Computational Physics. Volume 14 - Radio astronomy, ed. B. Alder, S. Fernbach, & M. Rotenberg, Vol. 14, 55–129

Hellings, R. W. & Downs, G. S. 1983, ApJ, 265, L39

Hewish, A., Bell, S. J., Pilkington, J. D. H., Scott, P. F., & Collins, R. A. 1968, Nature, 217, 709

Hewish, A. & Okoye, S. E. 1965, Nature, 207, 59

Hinshaw, G., Weiland, J. L., Hill, R. S., et al. 2009, The Astrophysical Journal Supplement Series, 180, 225

Hobbs, G. 2013, Classical and Quantum Gravity, 30, 224007

Hobbs, G., Coles, W., Manchester, R. N., et al. 2012, MNRAS, 427, 2780

Hobbs, G., Lorimer, D. R., Lyne, A. G., & Kramer, M. 2005, MNRAS, 360, 974

Hobbs, G., Lyne, A. G., & Kramer, M. 2010, MNRAS, 402, 1027

Hobbs, G., Lyne, A. G., Kramer, M., Martin, C. E., & Jordan, C. 2004, MNRAS, 353, 1311

Hobbs, G. B., Edwards, R. T., & Manchester, R. N. 2006, MNRAS, 369, 655

Hofmann, F., Müller, J., & Biskupek, L. 2010, A&A, 522, L5

Holmberg, J. & Flynn, C. 2004, MNRAS, 352, 440

Hotan, A. W., Bailes, M., & Ord, S. M. 2004a, MNRAS, 355, 941

Hotan, A. W., van Straten, W., & Manchester, R. N. 2004b, PASA, 21, 302

Hořava, P. 2009, Phys. Rev. D, 79, 084008

Hughes, S. A. 2009, ARA&A, 47, 107

Hulse, R. A. & Taylor, J. H. 1975, ApJ, 195, L51

Irwin, A. W. & Fukushima, T. 1999, A&A, 348, 642

Issautier, K., Meyer-Vernet, N., Moncuquet, M., & Hoang, S. 1998, J. Geophys. R., 103, 1969

Izvekova, V. A., Kuzmin, A. D., Malofeev, V. M., & Shitov, I. P. 1981, Ap&SS, 78, 45

Jacobson, T. & Mattingly, D. 2001, Phys. Rev. D, 64, 024028

Jaffe, A. H. & Backer, D. C. 2003, ApJ, 583, 616

Jarosik, N., Bennett, C. L., Dunkley, J., et al. 2011, The Astrophysical Journal Supplement Series, 192, 14

Jenet, F. A., Hobbs, G. B., Lee, K. J., & Manchester, R. N. 2005, ApJ, 625, L123

Jenet, F. A., Lommen, A., Larson, S. L., & Wen, L. 2004, ApJ, 606, 799

Johnson, T. J. 2012, ArXiv e-prints

Johnston, S., Nicastro, L., & Koribalski, B. 1998, MNRAS, 297, 108

Jordan, P. 1959, Zeitschrift fur Physik, 157, 112

Kaspi, V. M., Taylor, J. H., & Ryba, M. F. 1994, ApJ, 428, 713

Kass, R. E. & Raftery, A. E. 1995, J. Amer. Stat. Assoc., 90, 773

Keith, M. J., Coles, W., Shannon, R. M., et al. 2013, MNRAS, 429, 2161

Kibble, T. W. B. 1976, Journal of Physics A Mathematical General, 9, 1387

Komesaroff, M. M. 1970, Nature, 225, 612

Kondratiev, V. I., Verbiest, J. P. W., Hessels, J. W. T., et al. 2016, A&A, 585, A128

Kopeikin, S. M. 1995, ApJ, 439, L5

—. 1996, ApJ, 467, L93

Kostelecký, V. A. 2004, Phys. Rev. D, 69, 105009

Kramer, M. 1994, A&AS, 107

—. 1998, ApJ, 509, 856

Kramer, M. & Champion, D. J. 2013, Classical and Quantum Gravity, 30, 224009

Kramer, M., Lange, C., Lorimer, D. R., et al. 1999, ApJ, 526, 957

Kramer, M., Lyne, A. G., O'Brien, J. T., Jordan, C. A., & Lorimer, D. R. 2006a, Science, 312, 549

Kramer, M., Stairs, I. H., Manchester, R. N., et al. 2006b, Science, 314, 97

Kramer, M., Xilouris, K. M., Jessner, A., Wielebinski, R., & Timofeev, M. 1996, A&A, 306, 867

Kramer, M., Xilouris, K. M., Lorimer, D. R., et al. 1998, ApJ, 501, 270

Kuijken, K. & Gilmore, G. 1989, MNRAS, 239, 605

Kuzmin, A. D. & Losovsky, B. Y. 1999, A&A, 352, 489

Landau, L. D. & Lifshitz, E. M. 1960, Electrodynamics of continuous media

Lange, C., Camilo, F., Wex, N., et al. 2001, MNRAS, 326, 274

Lazaridis, K., Wex, N., Jessner, A., et al. 2009, MNRAS, 400, 805

Lazarus, P., Karuppusamy, R., Graikou, E., et al. 2016, MNRAS, in press; ArXiv e-prints:1601.06194

Lazarus, P., Tauris, T. M., Knispel, B., et al. 2014, MNRAS, 437, 1485

Lee, K. J. 2013, Classical and Quantum Gravity, 30, 224016

Lee, K. J., Bassa, C. G., Janssen, G. H., et al. 2014, MNRAS, 441, 2831

—. 2012, MNRAS, 423, 2642

Lentati, L., Alexander, P., Hobson, M. P., et al. 2014, MNRAS, 437, 3004

—. 2013, Phys. Rev. D, 87, 104021

Lentati, L., Shannon, R. M., Coles, W. A., et al. 2016, MNRAS

Lentati, L., Shannon, R. M., Coles, W. A., et al. 2016, Monthly Notices of the Royal Astronomical Society

Lentati, L., Taylor, S. R., Mingarelli, C. M. F., et al. 2015, MNRAS, 453, 2576

Link, B., Epstein, R. I., & van Riper, K. A. 1992, Nature, 359, 616

Liu, K., Desvignes, G., Cognard, I., et al. 2014, MNRAS, 443, 3752

Liu, K., Karuppusamy, R., Lee, K. J., et al. 2015, MNRAS, 449, 1158

Liu, K., Verbiest, J. P. W., Kramer, M., et al. 2011, MNRAS, 417, 2916

Livingstone, M. A., Kaspi, V. M., Gavriil, F. P., et al. 2007, Ap&SS, 308, 317

Löhmer, O., Kramer, M., Mitra, D., Lorimer, D. R., & Lyne, A. G. 2001, ApJ, 562, L157

Lommen, A. N., Kipphorn, R. A., Nice, D. J., et al. 2006, ApJ, 642, 1012

Lorimer, D. R. & Kramer, M. 2005, Handbook of Pulsar Astronomy, ed. Lorimer, D. R. & Kramer, M. (Cambridge University Press)

Lorimer, D. R., Lyne, A. G., Festin, L., & Nicastro, L. 1995, Nature, 376, 393

Lutz, T. E. & Kelker, D. H. 1973, PASP, 85, 573

Lyne, A., Hobbs, G., Kramer, M., Stairs, I., & Stappers, B. 2010, Science, 329, 408

Lyne, A. G., Burgay, M., Kramer, M., et al. 2004, Science, 303, 1153

Lyne, A. G. & Graham-Smith, F. 1998, Pulsar astronomy

Lyne, A. G. & Lorimer, D. R. 1994, Nature, 369, 127

Lyne, A. G. & Manchester, R. N. 1988, MNRAS, 234, 477

Malofeev, V. M. & Malov, I. F. 1980, Sov. Astronomy, 24, 90

Manchester, R. N., Hobbs, G. B., Teoh, A., & Hobbs, M. 2005, AJ, 129, 1993

Manchester, R. N., Kramer, M., Possenti, A., et al. 2005, The Astrophysical Journal Letters, 621, L49

Maron, O., Kijak, J., Kramer, M., & Wielebinski, R. 2000, A&AS, 147, 195

Matsakis, D. N., Taylor, J. H., & Eubanks, T. M. 1997, A&A, 326, 924

Matthews, A. M., Nice, D. J., Fonseca, E., et al. 2016, ApJ, 818, 92

McLaughlin, M. A. 2013, Classical and Quantum Gravity, 30, 224008

Mitra, D., Wielebinski, R., Kramer, M., & Jessner, A. 2003, A&A, 398, 993

Müller, J., Williams, J. G., & Turyshev, S. G. 2008, in Astrophysics and Space Science Library, Vol. 349, Lasers, Clocks and Drag-Free Control: Exploration of Relativistic Gravity in Space, ed. H. Dittus, C. Lammerzahl, & S. G. Turyshev, 457

Nicastro, L., Lyne, A. G., Lorimer, D. R., et al. 1995, MNRAS, 273, L68

Nice, D. J., Splaver, E. M., & Stairs, I. H. 2001, ApJ, 549, 516

Nice, D. J., Stairs, I. H., & Kasian, L. E. 2008, in American Institute of Physics Conference Series, Vol. 983, 40 Years of Pulsars: Millisecond Pulsars, Magnetars and More, ed. C. Bassa, Z. Wang, A. Cumming, & V. M. Kaspi, 453–458

Nice, D. J. & Taylor, J. H. 1995, ApJ, 441, 429

Nice, D. J., Weisberg, J. M., & Taylor, J. H. 2005, in Bulletin of the American Astronomical Society, Vol. 37, American Astronomical Society Meeting Abstracts, 1468

Nordtvedt, K. 1987, ApJ, 320, 871

Noutsos, A., Johnston, S., Kramer, M., & Karastergiou, A. 2008, MNRAS, 386, 1881

Noutsos, A., Schnitzeler, D. H. F. M., Keane, E. F., Kramer, M., & Johnston, S. 2013, MNRAS, 430, 2281

Oort, J. H. & Walraven, T. 1956, BAIN, 12, 285

Pacini, F. 1967, Nature, 216, 567

Papitto, A., Ferrigno, C., Bozzo, E., et al. 2013, Nature, 501, 517

Pennucci, T. T., Demorest, P. B., & Ransom, S. M. 2014, ApJ, 790, 93

Peters, P. C. 1964, Phys. Rev., 136, B1224

Radhakrishnan, V. & Srinivasan, G. 1982, Current Science, 51, 1096

Rajagopal, M. & Romani, R. W. 1995, ApJ, 446, 543

Ramachandran, R., Demorest, P., Backer, D. C., Cognard, I., & Lommen, A. 2006, ApJ, 645, 303

Ransom, S. M., Stairs, I. H., Archibald, A. M., et al. 2014, Nature, 505, 520

Rawley, L. A. 1986, PhD thesis, Princeton Univ., NJ.

Reardon, D. J., Hobbs, G., Coles, W., et al. 2016, MNRAS, 455, 1751

Reid, M. J., Menten, K. M., Brunthaler, A., et al. 2014, ApJ, 783, 130

Rickett, B. J., Coles, W. A., & Bourgois, G. 1984, A&A, 134, 390

Rohlfs, K. & Wilson, T. L. 2004, Tools of radio astronomy

Sagi, E. 2009, Phys. Rev. D, 80, 044032

Sanidas, S. A., Battye, R. A., & Stappers, B. W. 2012, Phys. Rev. D, 85, 122003

Sathyaprakash, B. S. & Schutz, B. F. 2009, Living Reviews in Relativity, 12

Sazhin, M. V. 1978, Soviet Astronomy, 22, 36

Schnitzeler, D. H. F. M. 2012, MNRAS, 427, 664

Sesana, A. 2013, Classical and Quantum Gravity, 30, 224014

Shannon, R. M. & Cordes, J. M. 2010, ApJ, 725, 1607

Shannon, R. M., Cordes, J. M., Metcalfe, T. S., et al. 2013, ApJ, 766, 5

Shannon, R. M., Osłowski, S., Dai, S., et al. 2014, MNRAS, 443, 1463

Shannon, R. M., Ravi, V., Lentati, L. T., et al. 2015, Science, 349, 1522

Shao, L., Caballero, R. N., Kramer, M., et al. 2013, Classical and Quantum Gravity, 30, 165019

Shao, L. & Wex, N. 2012, Classical and Quantum Gravity, 29, 215018

Shibata, M., Taniguchi, K., Okawa, H., & Buonanno, A. 2014, Phys. Rev. D, 89, 084005

Shklovskii, I. S. 1970, Sov. Astronomy, 13, 562

Sieber, W. 1973, A&A, 28, 237

—. 1982, A&A, 113, 311

Siemens, X., Ellis, J., Jenet, F., & Romano, J. D. 2013, Classical and Quantum Gravity, 30, 224015

Skilling, J. 2004, in American Institute of Physics Conference Series, Vol. 735, Bayesian inference and maximum entropy methods in science and engineering, ed. R. Fischer, R. Preuss, & U. von Toussaint, 395–405

Slepian, D. 1954, in Transactions of the IRE Professional Group on Information Theory, Vol. 3, Transactions of the IRE Professional Group on Information Theory, 68–89

Soffel, M., Klioner, S., Müller, J., & Biskupek, L. 2008, Phys. Rev. D, 78, 024033

Spitler, L. G., Lee, K. J., Eatough, R. P., et al. 2014, ApJ, 780, L3

Spruit, H. C. 2008, in American Institute of Physics Conference Series, Vol. 983, 40 Years of Pulsars: Millisecond Pulsars, Magnetars and More, ed. C. Bassa, Z. Wang, A. Cumming, & V. M. Kaspi, 391–398

Stairs, I. H., Faulkner, A. J., Lyne, A. G., et al. 2005, ApJ, 632, 1060

Sutaria, F. K., Ray, A., Reisenegger, A., et al. 2003, A&A, 406, 245

Tauris, T. M. 2011, in Astronomical Society of the Pacific Conference Series, Vol. 447, Evolution of Compact Binaries, ed. L. Schmidtobreick, M. R. Schreiber, & C. Tappert, 285

Tauris, T. M. & Bailes, M. 1996, A&A, 315, 432

Taylor, J. H. 1992, Philosophical Transactions of the Royal Society of London Series A, 341, 117

Taylor, J. H. & Cordes, J. M. 1993, ApJ, 411, 674

Taylor, J. H., Fowler, L. A., & McCulloch, P. M. 1979, Nature, 277, 437

Taylor, J. H. & Weisberg, J. M. 1982, ApJ, 253, 908

—. 1989, ApJ, 345, 434

Taylor, S. R., Mingarelli, C. M. F., Gair, J. R., et al. 2015, Physical Review Letters, 115, 041101

The LIGO Scientific Collaboration & the Virgo Collaboration. 2016, ArXiv e-prints

The NANOGrav Collaboration, Arzoumanian, Z., Brazier, A., et al. 2015, ApJ, 813, 65

Thorsett, S. E., Arzoumanian, Z., Camilo, F., & Lyne, A. G. 1999, ApJ, 523, 763

Tiburzi, C., Hobbs, G., Kerr, M., et al. 2016, MNRAS, 455, 4339

Torne, P., Eatough, R. P., Karuppusamy, R., et al. 2015, MNRAS, 451, L50

Toscano, M., Sandhu, J. S., Bailes, M., et al. 1999, MNRAS, 307, 925

Vallisneri, M. 2008, Phys. Rev. D, 77, 042001

van Haasteren, R. & Levin, Y. 2013, MNRAS, 428, 1147

van Haasteren, R., Levin, Y., Janssen, G. H., et al. 2011, MNRAS, 414, 3117

van Haasteren, R., Levin, Y., McDonald, P., & Lu, T. 2009, MNRAS, 395, 1005

van Kerkwijk, M. H., Bassa, C. G., Jacoby, B. A., & Jonker, P. G. 2005, in Astronomical Society of the Pacific Conference Series, Vol. 328, Binary Radio Pulsars, ed. F. A. Rasio & I. H. Stairs, 357

van Kerkwijk, M. H., Bergeron, P., & Kulkarni, S. R. 1996, ApJ, 467, L89

van Straten, W. 2003, PhD thesis, Swinburne University Of Technology

—. 2006, ApJ, 642, 1004

—. 2013, ApJS, 204, 13

van Straten, W. & Bailes, M. 2003, in Astronomical Society of the Pacific Conference Series, Vol. 302, Radio Pulsars, ed. M. Bailes, D. J. Nice, & S. E. Thorsett, 65

van Straten, W., Bailes, M., Britton, M., et al. 2001, Nature, 412, 158

Verbiest, J. P. W., Bailes, M., Coles, W. A., et al. 2009, MNRAS, 400, 951

Verbiest, J. P. W., Lentati, L., Hobbs, G., et al. 2016, MNRAS, 458, 1267

Verbiest, J. P. W., Lorimer, D. R., & McLaughlin, M. A. 2010, MNRAS, 405, 564

Voûte, J. L. L., Kouwenhoven, M. L. A., van Haren, P. C., et al. 2002, A&A, 385, 733

Wahlquist, H. 1987, General Relativity and Gravitation, 19, 1101

Weisberg, J. M., Romani, R. W., & Taylor, J. H. 1989, ApJ, 347, 1030

Weisberg, J. M. & Taylor, J. H. 2005, in Astronomical Society of the Pacific Conference Series, Vol. 328, Binary Radio Pulsars, ed. F. A. Rasio & I. H. Stairs, 25

Wex, N. 2014, ArXiv e-print (1402.5594). Appears in "Frontiers in Relativistic Celestial Mechanics, Vol. 2, Applications and Experiments", edited by Sergei Kopeikin. XIX+288 pp., De Gruyter, 2014

Wijnands, R. & van der Klis, M. 1998, Nature, 394, 344

Will, C. M. 1981, Theory and experiment in gravitational physics

—. 1993, Theory and Experiment in Gravitational Physics, 396

—. 2014a, Living Reviews in Relativity, 17, 4

—. 2014b, ArXiv e-prints; Appears in "General Relativity and Gravitation: A Centennial Perspective", eds. A. Ashtekar, B. Berger, J. Isenberg and M. A. H. MacCallum (Cambridge University Press), 2015.

Will, C. M. & Nordtvedt, Jr., K. 1972, ApJ, 177, 757

Wolszczan, A. 1994, Science, 264, 538

Wolszczan, A. & Frail, D. A. 1992, Nature, 355, 145

Xilouris, K. M., Kramer, M., Jessner, A., Wielebinski, R., & Timofeev, M. 1996, A&A, 309, 481

Yagi, K., Blas, D., Barausse, E., & Yunes, N. 2014, Phys. Rev. D, 89, 084067

You, X. P., Hobbs, G., Coles, W. A., et al. 2007, MNRAS, 378, 493

Yu, M., Manchester, R. N., Hobbs, G., et al. 2013, MNRAS, 429, 688

Zhu, W. W., Stairs, I. H., Demorest, P. B., et al. 2015, ApJ, 809, 41

APPENDIX A

List of Units, Constants and Abbreviations

Table A.1: List of Units and Constants

Unit	Symbol	Numerical Value
Solar Mass	$M_\odot$	1.9891×10^{33} gr
Jansky	Jy	10^{-23} erg s^{-1} cm^{-2} Hz^{-1}
Astronomical Unit	AU	1.4960×10^{13} cm
Parsec	pc	3.0857×10^{18} cm
Year	yr	3.1558×10^{7} s
Gauss	G	10^{-4}kg C^{-1} s^{-1}
Speed of light	c	2.99792458×10^{8} m s^{-1}

Table A.2: List of frequently used abbreviations

Abbreviation	Term
BAT	Barycentric time-of-arrival
BB	Binary Barycentre
BH	Black Hole
BIPM	Bureau International des Poids et Mesures
CGW	Continuous Gravitational Wave
DM	Dispersion Measure
DNS	Double Neutron Star
EOS	Equation-of-State
GLS	Generalised Least-squares
GPS	Global Positioning System
GR	General Relativity
GW	Gravitational Wave
GWB	Gravitational-Wave Background
IISM	Ionised Interstellar Medium
LKb	Lutz-Kelker bias
LLI	Local Lorentz Invariance
LOS	Line-of-sight
LPI	Local Position Invariance
LSP	Lomb-Scargle periodogram
MCMC	Markov-Chain Monte-Carlo
ML	Maximum Likelihood
MSP	Millisecond Pulsar
NS	Neutron Star
PFE	Preferred-frame effect
PN	post-Newtonian
PPD	Posterior Probability Distribution
PPK	Parametrised post-Keplerian
PPN	Parametrised post-Newtonian
PTA	Pulsar Timing Array
RFI	Radio Frequency Interference
RM	Rotation Measure
S/N	signal-to-noise ratio
SAT	Site (topocentric) time-of-arrival
SMBHB	Supermassive Black-Hole Binary
SNR	Supernova Remnant
SSB	Solar system Barycentre
TAI	International Atomic Time
TN	Timing Noise
TOA	Time-of-arrival
UTC	Coordinated Universal Time
WD	White Dwarf
pPD	prior Probability Distribution
wLS	Weighted Least-squares

List of Figures

List of Tables